

# **Observations of Sporadic-E Utilising High Frequency Oblique Sounding Techniques**

Thesis submitted for the degree of  
Doctor of Philosophy  
at the University of Leicester

by

**Paul J. Rylah**  
Department of Physics and Astronomy  
University of Leicester

December, 1998

UMI Number: U534326

All rights reserved

INFORMATION TO ALL USERS

The quality of this reproduction is dependent upon the quality of the copy submitted.

In the unlikely event that the author did not send a complete manuscript and there are missing pages, these will be noted. Also, if material had to be removed, a note will indicate the deletion.



UMI U534326

Published by ProQuest LLC 2014. Copyright in the Dissertation held by the Author.  
Microform Edition © ProQuest LLC.

All rights reserved. This work is protected against  
unauthorized copying under Title 17, United States Code.



ProQuest LLC  
789 East Eisenhower Parkway  
P.O. Box 1346  
Ann Arbor, MI 48106-1346

# Observations of Sporadic-E

## Utilising High Frequency Oblique Sounding

### Techniques

Paul J. Rylah

#### Abstract

Sporadic-E is an 'abnormal', altitude-confined intensification of the E-region plasma density. Its presence may both enable and disable an oblique propagation circuit, depending on the prevalent propagation path geometry, the ambient ionospheric conditions, and the plasma structure of the layer itself. This thesis studies the plasma characteristics of sub-auroral sporadic-E layers, utilising oblique HF 'Chirp' sounders, deployed during times of both quiet and disturbed geomagnetic activity.

During largely quiet geomagnetic conditions, a relationship is established between the sporadic-E top frequency,  $fE_s$ , and the layer's signal strength (SS), at a fixed sounder 'Probing Frequency' (PF) such that  $SS \propto (fE_s/PF)^n$ , with values of 'n' varying between  $\sim$  zero and  $\sim$  20. The resulting 'curve' is derived primarily for 'overdense' sporadic-E reflections and is interpreted in terms of the sporadic-E plasma 'cloud' model. A gaussian distribution of differing cloud plasma densities is demonstrated to best model the observed sporadic-E signal strength characteristics. However, this signal strength relationship is increasingly inapplicable to the minority of sporadic-E layers arising from equivalent vertical top frequency ( $\nu fE_s$ ) growth rates, greater than  $\sim$  0.6 MHz per five minute time interval. Indeed, for  $\nu fE_s$  growth rates greater than  $\sim$  1.2 MHz per five minutes, the signal strength is independent of the top frequency. These observations are again consistent with the plasma cloud model, though field-aligned irregularities and off great circle path propagation may account for some of the more temporary  $\nu fE_s$  growths.

The thesis concludes with a study of correlated observations of sporadic-E layers and  $\sim$  1 m scale plasma irregularities, as detected by the Wick receiver of the SABRE (Sweden And Britain Radar-aurora Experiment) VHF backscatter radar. The correlated occurrence of the two plasma features, coincided, primarily, with substorm activity. On occasions it was also noted that the backscatter S/N ratio correlates closely with the sporadic-E top frequency, the observation being interpreted in terms of the enhanced auroral electric fields.

*To Cathy and my parents*

# Acknowledgements

I firstly wish to thank the Radio and Space Plasma Physics Group, headed by Prof. Stan Cowley, and formerly Prof. Tudor Jones, for supporting my Ph.D. studentship, and P.P.A.R.C. (formerly S.E.R.C.) for providing me with a research grant.

I am extremely grateful to Mark Lester for being my adopted supervisor, for supporting my countless requests for registration extensions, and for being the busiest goalkeeper in the five-a-side league. He has always been available for advice and guidance and is an example for PhD supervisors everywhere.

I thank the Defence Research Agency (formerly the Royal Aerospace Establishment) for the CASE studentship they offered me, and in particular Paul Cannon, Anil Shukla and Adrian Dickson for the procurement of HF sounders and assistance in operation.

I am indebted to Britvic Soft Drinks for granting me flexible working arrangements and unpaid leave, without which this thesis would have taken even longer! I would particularly like to thank Gary Tyrell, Andrew Storey, Bob Darby and Ian Ferguson (SGi) for supporting my requests for study leave.

I thank Prof. Terry Robinson and Dr. Tim Yeoman for helpful, clarification discussions, Chris Thomas, Roderick Maude and Nigel Wade for all their help relating to radar and computing matters and Dave Milling (University of York) for the prompt provision of SAMNET data.

A special word of thanks goes to Neil Arnold, Jackie Davies, Steve Milan, John Taylor and Darren Wright for their friendship and willing assistance during the writing of this thesis and particularly to John for being the best landlord I (n)ever had. I would also like to thank Martin Pople for keeping me sane during the 'dark' years and for teaching me the finer points of snooker.

Over the long duration of my studies, I have received technical assistance and friendship from countless people within my research group and beyond. I believe that everyone I have had association with has aided me in some way or another, and in wishing not to offend by inadvertent omission, I simply take this opportunity to thank you all.

But my sincerest gratitude goes to Cathy, for her unwavering support, unlimited patience and ever consoling love. I apologise wholeheartedly for what I have put her through over the seemingly unending years in pursuit of this thesis, and by some means of consolation, promise never to write another one!

# Contents

<b>CHAPTER 1 THE SOLAR-TERRESTRIAL ENVIRONMENT .....</b>	<b>1</b>
1.1 Introduction .....	1
1.2 The Solar and Geomagnetic Environment .....	1
1.2.1 The Sun .....	1
1.2.2 The Solar Wind and Interplanetary Magnetic Field .....	2
1.2.3 The Magnetosphere .....	3
1.2.4 Solar Wind and Magnetospheric Coupling .....	5
1.2.5 Magnetospheric Substorms .....	6
1.3 The Earth's Atmosphere .....	7
1.3.1 The Neutral Atmosphere .....	7
1.3.2 The Ionosphere .....	8
1.4 Radio Wave Propagation .....	11
1.4.1 Ionospheric Influences .....	11
1.4.2 High Frequency Radio Waves .....	12
1.5 The Current Investigation .....	13
<b>CHAPTER 2 A REVIEW OF SPORADIC-E OBSERVATIONS AND THEORY .....</b>	<b>14</b>
2.1 Introduction .....	14
2.2 Observations of Sporadic-E .....	15
2.2.1 Scaling Parameters .....	15
2.2.2 Geographical Distribution and Morphology .....	16
2.2.3 The Effects of Magnetic Activity .....	16
2.3 The Theory of Sporadic-E Generation .....	17
2.3.1 Introduction .....	17
2.3.2 E-region Conductivities, Mobilities and Collision Frequencies .....	17
2.3.3 The Windshear Theory .....	19
2.3.4 Mid-Latitude Approximations of the General Windshear Theory .....	21
2.3.5 High-Latitude Approximations of the General Windshear Theory .....	22
2.3.6 E-Region Tides and Gravity Waves .....	24
2.3.7 Ion Composition of Sporadic-E Layers .....	25
2.3.8 Sporadic-E layers in the Equatorial and Polar Regions .....	26
2.4 Sporadic-E Profiles and Internal Plasma Structure and Composition .....	26
2.4.1 Sporadic-E Profiles .....	26
2.4.2 Inhomogeneities Within Sporadic-E layers .....	27
2.5 Summary .....	31
<b>CHAPTER 3 EXPERIMENTAL AND ANALYSIS TECHNIQUES .....</b>	<b>32</b>
3.1 Introduction .....	32
3.2 Propagation Theory .....	32
3.2.1 In the beginning .....	32

3.2.2	The Appleton-formula.....	33
3.2.3	Approximate Solutions of the Appleton Formula.....	34
3.2.4	Phase and Group Velocity.....	36
3.2.5	Phase and Group Paths.....	37
3.2.6	Practical Oblique Propagation.....	38
3.2.7	Attenuation of Radio Waves.....	40
3.3	<i>Ionosondes and Ionograms</i> .....	41
3.3.1	Vertical Ionosondes.....	41
3.3.2	Oblique Ionosondes and the Chirp Sounder.....	42
3.4	<i>Further Ionospheric Diagnostic Equipment</i> .....	47
3.4.1	The SABRE Radar.....	47
3.4.2	SAMNET Magnetometer Data.....	48
3.5	<i>Summary</i> .....	49

**CHAPTER 4 AN INTRODUCTION TO THE BODØ/WICK OBLIQUE PROPAGATION  
CIRCUIT AND ASSOCIATED SPORADIC-E RECORDINGS.....50**

4.1	<i>Introduction</i> .....	50
4.2	<i>Campaign Details</i> .....	51
4.2.1	Radar Deployments.....	51
4.2.2	Radar Antennas.....	52
4.3	<i>Morphological Studies of Sporadic-E Layers, Observed on the Bodø/Wick Propagation Path, during the August Campaign</i> .....	53
4.3.1	Phillips' Rule.....	53
4.3.2	The Diurnal Occurrence of Sporadic-E Layers.....	54
4.3.3	Discussion.....	56
4.4	<i>Summary</i> .....	58

**CHAPTER 5 THE SPORADIC-E SIGNAL STRENGTH PROFILE.....60**

5.1	<i>Introduction</i> .....	60
5.2	<i>Analysis Procedure</i> .....	62
5.3	<i>Introductory Observations</i> .....	64
5.3.1	The General Signal Strength versus $f^oE_s$ Relationship.....	64
5.3.2	Diurnal Observations of Sporadic-E Signal Strength and $f^oE_s$ .....	65
5.4	<i>The Partial Transparency Region of Sporadic-E</i> .....	66
5.4.1	Introduction.....	66
5.4.2	Data Definition.....	66
5.4.3	Results and Analysis.....	67
5.4.4	Discussion.....	68
5.5	<i>A Comparison with Model Signal Strength Profiles</i> .....	70
5.5.1	Introduction and Data Definition.....	70
5.5.2	Results and Analysis.....	72
5.5.3	Discussion.....	74
5.5.4	Summary.....	77

5.6	<i>Examining the Cause of the Sporadic-E Signal Strength Profile</i> .....	78
5.6.1	The Influence of the Sporadic-E Cloud Structure .....	78
5.6.2	The Influence of E-Region Densities .....	83
5.7	<i>Summary</i> .....	86

**CHAPTER 6 AN INVESTIGATION INTO THE EFFECT OF *VFTES* GROWTH RATES  
ON THE SPORADIC-E SIGNAL STRENGTH PROFILE .....87**

6.1	<i>Introduction</i> .....	87
6.2	<i>Data Description</i> .....	88
6.3	<i>Introductory Observations of <i>vftEs</i> Growth Rates</i> .....	89
6.3.1	Typical Daily Variations of <i>vftEs</i> .....	89
6.3.2	<i>vftEs</i> Growth rate Distribution .....	89
6.4	<i>The Relationship between Sporadic-E Signal Strengths and Top Frequency Growth Rates</i> .....	90
6.4.1	Introduction.....	90
6.4.2	Analysis Procedure.....	91
6.4.3	Signal Strength Observations of the Sporadic-E ‘Common’ Region .....	91
6.4.4	‘Common’ Signal Strength Differences Between Consecutive Sporadic-E Layers .....	93
6.4.5	Signal Strength Observations of the Sporadic-E ‘Growth’ Region .....	96
6.5	<i>Discussion</i> .....	97
6.5.1	Schematic Representation of Sporadic-E <i>vftEs</i> Growths.....	98
6.5.2	A Cloud Model Explanation of the <i>vftEs</i> Growth Characteristics .....	99
6.5.3	Other Possible Causes of <i>vftEs</i> Growth Rates .....	104
6.6	<i>Summary</i> .....	105

**CHAPTER 7 CORRELATION STUDIES OF SPORADIC-E LAYERS AND E-REGION  
PLASMA IRREGULARITIES .....107**

7.1	<i>Introduction</i> .....	107
7.2	<i>Ionogram Observations of Sporadic-E Layers</i> .....	108
7.3	<i>Analysis Procedure</i> .....	109
7.4	<i>Correlation Studies of SABRE Backscatter and Sporadic-E Top Frequency Data</i> .....	111
7.4.1	Introduction.....	111
7.4.2	Case Study (a): 12:00 – 24:00 UT, Day 344 .....	111
7.4.3	Case Study (b): 00:00 – 06:00 UT, Day 345 .....	114
7.4.4	Case Study (c): 22:00 UT, Day 338 – 02:00 UT, Day 339.....	115
7.4.5	Case Study (d): 18:00 UT, Day 343 - 06:00 UT, Day 344 .....	116
7.4.6	Case Study (e): 18:00 UT, Day 75 – 03:00 UT, Day 76.....	118
7.5	<i>Summary of the Case Study Observations</i> .....	119
7.6	<i>Discussion</i> .....	120
7.6.1	The Correlation of SABRE backscatter observations with Substorm Events.....	120
7.6.2	The Correlation of Sporadic-E Occurrence with Substorm Events .....	121
7.6.3	The Correlation of SABRE Backscatter S/N Ratio and <i>vftEs</i> Magnitudes .....	123
7.7	<i>Summary and Conclusions</i> .....	130

<b>CHAPTER 8</b>	<b>SUMMARY AND SUGGESTION FOR FURTHER WORK.....</b>	<b>133</b>
8.1	<i>Introduction.....</i>	133
8.2	<i>Summary of Results.....</i>	133
8.2.1	Morphological Characteristics .....	133
8.2.2	The Sporadic-E Signal Strength .....	134
8.2.3	<i>νftEs</i> Growth Rate Factors affecting the Sporadic-E Signal Strength.....	135
8.2.4	The Correlation of Sporadic-E Observations and E-Region Irregularities .....	137
8.3	<i>Suggestions for Further Work.....</i>	138

**REFERENCES**

# Glossary

Commonly used abbreviations, acronyms and standard constants

<b>A</b>	amperes
<b>AU</b>	Astronomical Unit
<b>B</b>	magnetic flux intensity (teslas)
<i>c</i>	free space speed of electromagnetic waves = $2.998 \times 10^8$
<b>CME</b>	Coronal Mass Ejection
<b>dB</b>	decibels
<b>D</b>	ambipolar diffusion coefficient
<i>e</i>	electron charge = $1.602 \times 10^{-19}$ coulombs
<b>eV</b>	electron volt = $1.602 \times 10^{-19}$ joules
<b>E</b>	electric field (volts/meter)
<i>f</i>	frequency (hertz)
<i>f<sub>o</sub></i>	oblique propagating frequency
<i>f<sub>p</sub></i>	plasma frequency
<i>f<sub>v</sub></i>	vertical propagating frequency
<i>fbEs</i>	sporadic-E blanketing frequency
<i>ffE</i>	E-region junction frequency
<i>ffF</i>	F-region junction frequency
<i>foE</i>	E-region ordinary critical frequency
<i>foEs</i>	sporadic-E ordinary critical frequency
<i>foF</i>	F-region ordinary critical frequency
<i>foF1</i>	F1-region ordinary critical frequency
<i>foF2</i>	F2-region ordinary critical frequency
<i>ftEs</i>	sporadic-E top frequency
<i>ftF</i>	F-region top frequency
<i>fxE</i>	E-region extraordinary critical frequency
<i>fxEs</i>	sporadic-E extraordinary critical frequency
<i>fxF</i>	F-region extraordinary critical frequency
<i>fxF1</i>	F1-region extraordinary critical frequency
<i>fxF2</i>	F2-region extraordinary critical frequency
<b>FAC</b>	Field Aligned Current
<b>g</b>	acceleration due to gravity ( $9.81 \text{ m s}^{-2}$ )
<b>GSE</b>	Geocentric Solar Ecliptic

<i>h'E</i>	E-layer height
<i>h'Es</i>	sporadic-E height
HF	High Frequency (~3 to 30 MHz)
Hz	hertz
I	geomagnetic field inclination angle
ICEPAC	Ionospheric Communication Enhanced Profile Analysis and Circuit prediction program
IMF	Interplanetary Magnetic Field
J	current density (amperes m <sup>-2</sup> )
k	Boltzmann's constant = $1.381 \times 10^{-23}$ joule/kelvin
K	Kelvin
K	3-hour (local) magnetic index
K <sub>p</sub>	3-hour planetary magnetic index
kW	kilowatt
LT	Local Time
m	meter
<i>m<sub>e</sub></i>	electron rest mass = $9.107 \times 10^{-31}$ kg
<i>m<sub>i</sub></i>	ion mass
MHD	MagnetoHydroDynamic
MLT	Magnetic Local Time
MSS	Median Signal Strength
nT	nanotesla
<i>n</i>	complex refractive index = $\mu - i\chi$
<i>N<sub>e</sub></i>	electron number density
<i>N<sub>i</sub></i>	ion number density
<i>P</i>	partial pressure
PF	oblique Probing Frequency
R	sunspot number
R <sub>E</sub>	Earth's radius (6371.03 km)
RSS	Representative Signal Strength
s	second
SABRE	Sweden And Britain Radar- aurora Experiment
SAMNET	Sub-Auroral Magnetometer Network
SS	Signal Strength
STARE	Scandinavian Twin Auroral Radar Experiment
ULF	Ultra Low Frequency (~3 to 300 s)

UT	Universal Time
$v_g$	group speed of electromagnetic waves
$v_p$	phase speed of electromagnetic waves
$v_i, v_e$	ion and electron velocity ( $\text{m s}^{-1}$ )
$\nu_{fE_s}$	equivalent vertical Sporadic-E top frequency
$\mathbf{w}$	neutral wind velocity
VHF	Very High Frequency (~30 to 300 MHz)
VPF	equivalent Vertical Probing Frequency
W	watts
Z, Y, D	orthogonal geomagnetic field coordinates
$\epsilon_0$	permittivity of free space = $8.854 \times 10^{-12}$ farad/meter
$k$	wave number = $2\pi/\lambda$
$k_p, k_H, k_d$	Pedersen, Hall and direct (parallel) mobilities
$\lambda$	wavelength
$\mu$	(phase) refractive index (real) = $c/v_p$
$\mu'$	group refractive index (real) = $c/v_p$
$\mu_0$	permeability of free space = $12.57 \times 10^{-7}$ henry/meter
$\rho$	normalised ion-neutral collision frequency
$\sigma_p, \sigma_H, \sigma_d$	Pedersen, Hall and direct (parallel) conductivities
$\nu_{in}, \nu_{en}$	ion- and electron-neutral collision frequencies ( $\text{s}^{-1}$ )
$\chi$	complex refractive index
$\omega$	angular frequency = $2\pi f$
$\omega_{Hi}, \omega_{He}$	ion and electron gyrofrequencies

Vectors are denoted by bold type throughout this thesis

# If

*If you think you are beaten, you are*

*If you think you dare not, you don't*

*If you'd like to win, but think you can't*

*It's almost certain you won't.*

*If you think you'll lose, you've lost*

*For out of the world we find*

*Success begins with a fellow's will -*

*It's all in the state of mind.*

*If you think you're outclassed, you are*

*You've got to think high to rise*

*You've got to be sure of yourself before*

*You can ever win a prize.*

*Life's battles don't always go*

*To the stronger or faster man*

*But sooner or later the man who wins*

*Is the one who Thinks he can.*

Anonymous

# Chapter 1

## The Solar-Terrestrial Environment

### 1.1 Introduction

Beyond line-of-sight communications may be achieved through the reflection and refraction of High Frequency (HF) radio waves within the ionosphere. This partially ionised region of the Earth's upper atmosphere varies both spatially and temporally, thus determining the characteristics of the propagation circuit. Sporadic-E layers are 'abnormal' plasma enhancements, occurring in thin layers at altitudes  $\sim 110$  km, contributing both beneficially and adversely to the propagation of such waves. The study of these layers is the subject of this thesis.

The ionised nature of the ionosphere is a direct consequence of solar energy coupling processes, by means of radiation, particles and magnetic fields. The following presents an overview of these processes, from their solar origins to the resulting characteristic features of the Earth's solar-terrestrial environment.

### 1.2 The Solar and Geomagnetic Environment

#### 1.2.1 The Sun

The Sun is a typical galactic, Main Sequence star. It is a hot sphere of fully ionised plasma with a core temperature  $\sim 10^7$  K, comprising  $\sim 91\%$  hydrogen and  $\sim 9\%$  helium. This temperature and the atomic composition of the sun, are a direct consequence of the Sun's mass ( $\sim 10^{32}$  kg). Intense gravitational forces are generated, resulting in extreme forces of *contraction*, promoting nuclear fusion at the core, converting hydrogen to helium in the process. The subsequent energy release creates thermal *expansion* forces of sufficient magnitude to overcome the gravitational forces, preventing internal collapse and ultimately giving rise to the solar atmosphere and radiation. This electromagnetic radiation is emitted over a wide spectral range, and takes approximately 8.3 minutes to traverse one Astronomical Unit (AU), the mean Sun-Earth distance ( $\sim 150,000,000$  km).

The visible surface of the Sun, the *photosphere*, approximates to a black body of temperature  $\sim 6000$  K. It defines our view of the Sun, having a radius  $\sim 700,000$  km, approximately 110 times that of the Earth. Above this thin layer is the *chromosphere*, through which the density decreases and the temperature rises steadily. The outermost layer is the *corona*, a hot, rarefied plasma, having typical densities  $\sim 10^8 \text{ m}^{-3}$  and temperatures reaching  $\sim 10^6$  K (e.g. *Priest*, 1995).

The Sun has an active magnetic field which reverses polarity approximately once every 11 years. During a solar cycle, the activity level of the Sun can be monitored by observing the number, and latitudinal extent, of relatively cool spots ( $\sim 4000$  K) within the photosphere. These *sunspots* occur in pairs and having opposite polarity may be joined by closed loops of magnetic flux. Particles trapped in the closed loops can be seen from Earth as *prominences*. Further, sunspots tend to occur in groups and it is this combination of observed groups and pairs that define the sunspot number 'R', utilised as a measure of solar activity. Sunspot lifetimes are highly variable, often lasting many days. They may thus be observed to rotate with the sun, a rotation period approximating to 27 days but which is noted to vary significantly (and increasingly) with latitude. It is interesting to note that while emissions of extreme ultraviolet and X-radiation vary by several factors over the solar cycle, the visible spectrum generally varies by less than 1% during the same period.

### 1.2.2 The Solar Wind and Interplanetary Magnetic Field

The *solar wind* is the expanding corona of the Sun, consisting largely of streaming electrons and protons (e.g. *Parker*, 1961). Details of the particle acceleration are not fully understood but the solar wind is known to become supersonic above a few solar radii. At 1 AU the solar wind has typical velocities between  $300 \text{ km s}^{-1}$  and  $600 \text{ km s}^{-1}$ , translating to transit times  $\sim 4.5$  days. Typical solar wind densities in the near Earth environment are between  $5 \times 10^6 \text{ m}^{-3}$  and  $15 \times 10^6 \text{ m}^{-3}$ . Both these parameters can increase significantly during times of solar flares and Coronal Mass Ejections (CMEs) (*Gosling et al.*, 1976; *King*, 1986).

The Sun has a very complex surface magnetic field created by convective flow of the electrically conducting solar material. The solar wind, being highly conducting and more energised than the solar magnetic field, 'freezes-in' the field, thus drawing it out into space, hence defining the Interplanetary Magnetic Field (IMF). At 1 AU the IMF has a typical magnitude  $\sim 5$  nT. Due to the rotation of the Sun, the solar wind particles and hence the

frozen-in IMF, radiate out from the Sun in the form of an Archimedean spiral, often referred to as the Parker spiral (*Parker, 1958*). At 1 AU, the spiral subtends an angle of approximately  $45^\circ$  to the radial direction (cf. Figure 1.1a).

A current sheet is formed approximately on the ecliptic plane, between the oppositely directed field lines of the northern and southern solar hemispheres, as depicted in Figure 1.1b. The spiral field is thus directed either towards or away from the Sun, depending on whether the current sheet is above or below the plane, hence defining a sector structure in the IMF. Four sectors are represented in Figure 1.1a, but this may vary between two and six between solar minimum and maximum (e.g. *Yeoman et al., 1990a*). The north-south (Z) component of the IMF (GSE coordinates) may typically vary on a time scale  $\sim 1$  hour and is instrumental in determining the degree of coupling between the IMF and the Earth's magnetic field, and hence solar energy influx into the Earth's environment.

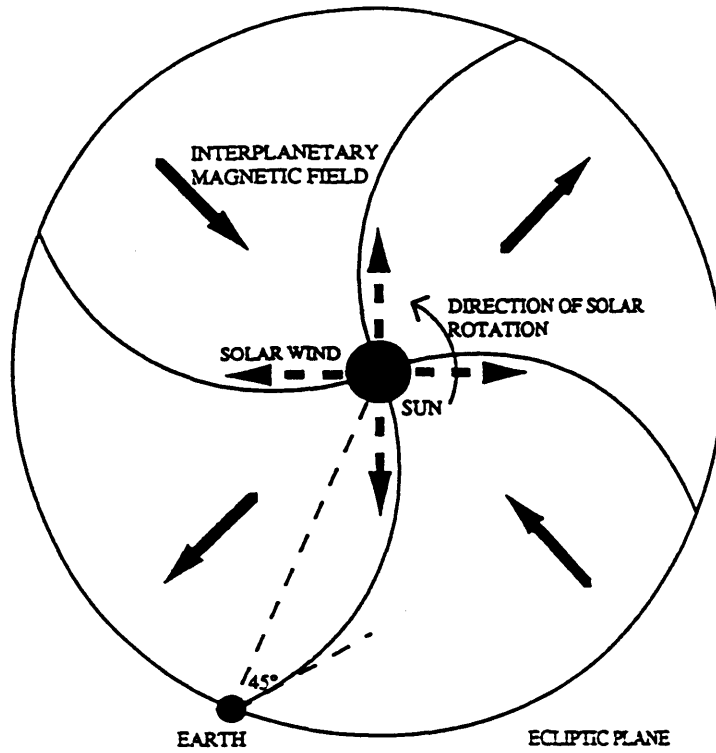
### 1.2.3 The Magnetosphere

The magnetised solar wind impinges upon the geomagnetic field with a speed greatly exceeding that of the Alfvén speed, resulting in the generation of a *bow shock* between about 12 and 15 Earth radii ( $R_E$ ) upstream of the Earth. Due to its high electrical conductivity, the solar wind can not penetrate the Earth's magnetic field lines and is thus swept around, so defining the geomagnetic cavity, termed the *magnetosphere*, depicted in Figures 1.2(a,b). The magnetosphere may be defined as the region of the Earth's atmosphere in which the energy density of the magnetic field, exceeds that of the plasma, i.e.:-

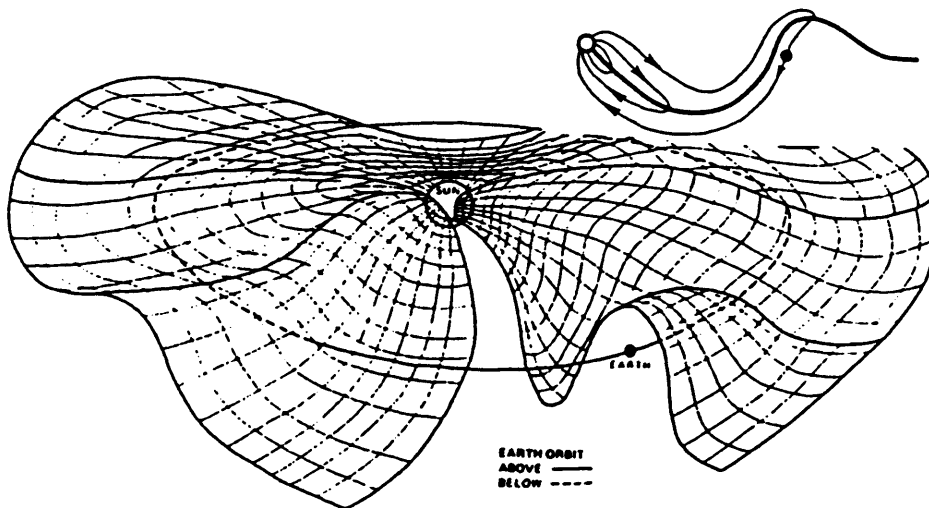
$$\frac{B^2}{2\mu_0} > N_e kT \quad (1.1)$$

where  $B$  is the magnetic flux density,  $\mu_0$  is the permeability of free space,  $N_e$  is the electron density,  $k$  is the Boltzmann constant and  $T$  is the plasma temperature. This definition however also encompasses much of the topside ionosphere, hence an additional constraint defines the magnetosphere to be above about 1000 km altitude (e.g. *Ratcliffe, 1972*).

The magnetosphere is greatly distorted from a simple dipole field, being compressed on the sunward side and stretched out into a roughly cylindrical *magnetotail* on the nightside. The magnetopause is located  $\sim 10 R_E$  sunward of the Earth (*Ness, 1964*), with the tail having been

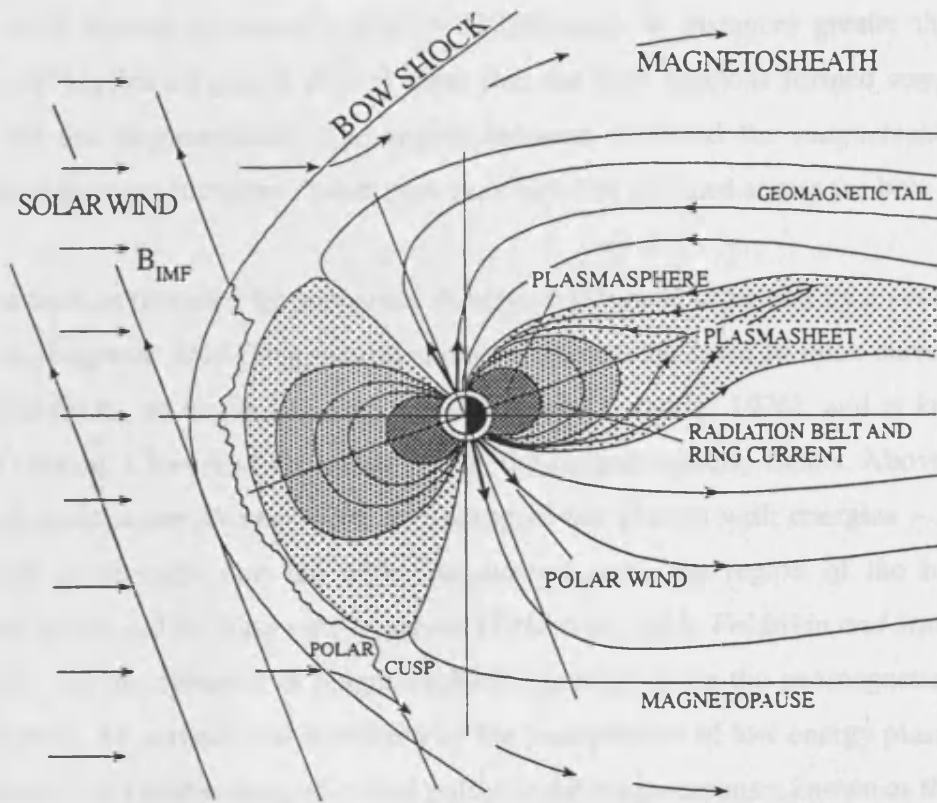


(a)

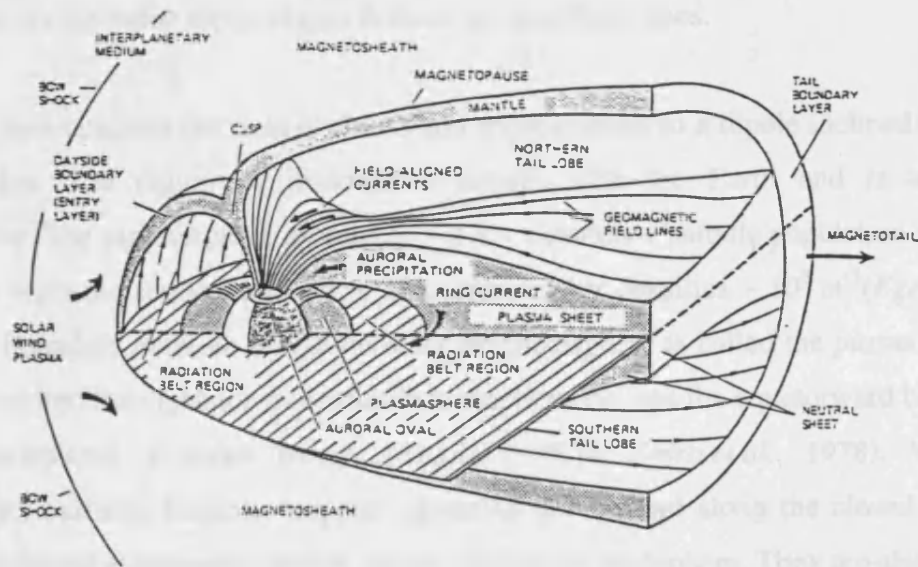


(b)

FIGURES 1.1(a,b) Two-dimensional (a) and three-dimensional (b) schematics of the solar interplanetary magnetic field. The field forms a sector structure of 'toward' and 'away' magnetic field lines, as the Earth's orbit alternately lies above and below the current sheet. ((1.1b) after *S.-I Akasofu*.)



(a)



(b)

FIGURE 1.2 Two-dimensional (a) and three-dimensional (b) schematics of the magnetosphere, interacting with the solar wind.

observed well beyond the moon's orbit ( $\sim 380,000$  km), at distances greater than  $1000 R_E$  (Villante, 1975). From Figure 1.2a it is clear that the bow shock is formed some 2 to  $3 R_E$  upstream of the *magnetopause*. The region between is called the *magnetosheath* and is characterised by more turbulent, hotter plasma, which has diffused across the bow shock.

The magnetotail is threaded by oppositely directed field lines, separated by a *neutral sheet* of nearly zero magnetic field. This neutral sheet carries a total dawn to dusk current, between  $\sim 10 R_E$  and  $60 R_E$ , of about  $10^7$  Amperes (Iijima and Potemra, 1976), and is known as the *cross-tail current*. Closure of the current is via the magnetospheric flanks. Above and below the neutral sheet is the *plasma sheet*, consisting of hot plasma with energies  $\sim 1$  to  $10$  keV. The plasma sheet maps into the nightside *auroral oval*, the region of the high latitude ionosphere where visible aurora are observed (Feldstein, 1963; Feldstein and Starkov, 1967), produced by the precipitation of magnetospheric particles along the geomagnetic field lines. On the dayside, the auroral oval is defined by the precipitation of low energy plasma from the magnetosheath, via neutral magnetic field points at the magnetopause, known as the *cusps*.

Further currents observed in the auroral zones are the *Birkland* currents. These Field Aligned Currents (FACs) flow into and out of the ionosphere and have typical total magnitudes  $\sim 10^6$  to  $10^7$  A, increasing approximately linearly with magnetic activity. Within the confines of the auroral oval lies the *polar cap*, a region defined by open field lines.

At low and mid-latitudes the field is closed and approximates to a dipole inclined at  $\sim 12^\circ$  to the spin axis. The region so enclosed co-rotates with the Earth and is termed the *plasmasphere*. The plasmasphere extends to  $\sim 4 R_E$ , contains a particle population which is in equilibrium with the ionosphere and is characterised by densities  $\sim 10^8 \text{ m}^{-3}$  (Egeland et al., 1973). The boundary between it and the outer magnetosphere is called the *plasmopause* and when mapped into the nightside mid-latitude ionosphere, defines the equatorward boundary of the plasma-depleted, F-region *trough* (Knudsen, 1974; Spiro et al., 1978). Within the plasmasphere, particles become 'trapped', gyrating around and along the closed field lines and being reflected at magnetic 'mirror points' within the ionosphere. They are also subjected to gradient-curvature longitudinal drift, the electrons drifting to the east and the protons to the west, constituting the *ring current* of magnitude  $\sim 10^7$  A. The particle densities peak at  $\sim 2 R_E$  and  $\sim 4 R_E$ , in what are termed the Van Allen radiation belts. These belts define regions of high energy ( $\sim$  MeV) particle populations, and are a major source of energy input into the ionosphere at times of magnetic activity.

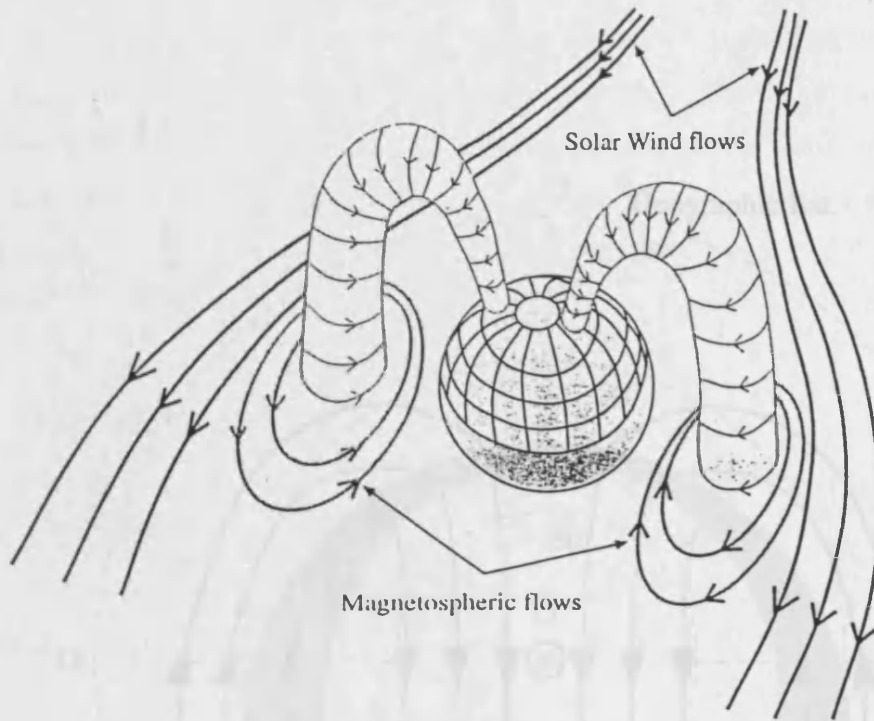
## 1.2.4 Solar Wind and Magnetospheric Coupling

Two models describe the transfer of energy from the solar wind to the magnetosphere. The *closed* or *viscous interaction* model (Axford and Hines, 1961) is depicted in Figure 1.3a. The coupling process is uncertain but may be initiated by Kelvin-Helmholtz instabilities. The open model (Dungey, 1961) is depicted in Figure 1.3b and describes a process of magnetic reconnection. New 'open' field lines are created on the dayside by *magnetic reconnection* between the IMF and previously 'closed' field lines. These field lines are dragged antisunward across the polar cap, transporting frozen-in plasma towards the geomagnetic tail. Under steady state conditions, these open field lines are subsequently closed by further magnetic reconnection, at the distant neutral line, approximately  $100 R_E$  down the magnetotail. Closed magnetic flux and plasma convects back to the dayside at auroral and sub-auroral latitudes. This cyclical motion of the field lines is known as *magnetospheric convection*.

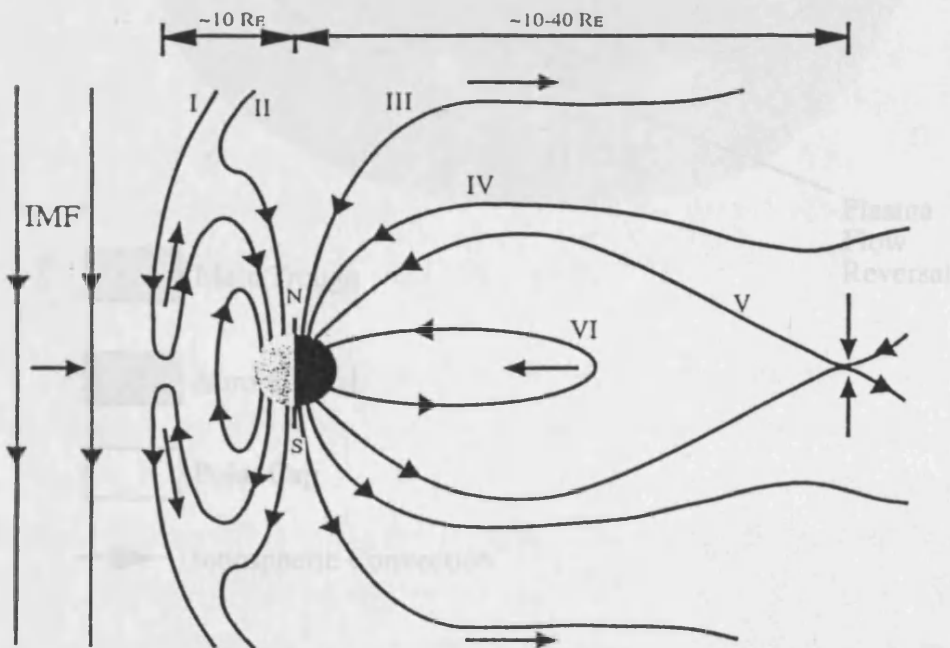
Both the open and closed models predict similar convection patterns though the open model is considered to dominate, particularly at times when the IMF has a southward component (GSE coordinates), i.e. when reconnection is very efficient. When the IMF has a northward component, the convection cell flows may be reversed, with sunward flow dominating. Under such conditions, magnetic reconnection occurs between the IMF and *open* field lines, with viscous flows influencing the final convection cell structure.

The convecting magnetoplasma is noted to move with a velocity,  $v$ , relative to the Earth's magnetic field,  $\mathbf{B}$ , generating magnetospheric electric fields,  $\mathbf{E}$ , given by  $\mathbf{E} = -\mathbf{v} \wedge \mathbf{B}$ . These electric fields map into the polar cap via the highly conducting magnetic field lines, and so define the *cross polar cap potential* (e.g. Cowley, 1984). A schematic of the southward IMF, F-region (cf. §1.3.2) ionospheric twin cell plasma convection pattern, arising from *both* electron and ion 'E cross B' drifts (e.g. Heelis and Hanson, 1976), is depicted in Figure 1.4. The general features are anti-sunward flow across the polar cap, with return flow at lower latitudes. Co-rotation effects and the significant influence of the east-west component of the IMF, will in fact lead to more complex, asymmetric cells, during both southward *and* northward IMF conditions (Burch *et al.*, 1985).

In the high latitude E-region (cf. §1.3.2), the normalised collision frequencies of the electrons and ions (cf. §2.3.2) dictate that the ions are coupled to the neutrals, whereas the electron flow is still defined by 'E cross B' drifts. This differential flow results in E-region Hall currents flowing along largely horizontal lines of equipotential, and approximately mirroring



(a)



(b)

FIGURE 1.3. The two-cell plasma convection pattern, associated with the high-latitude ionosphere. Note the north to southward turning of the electric field. **FIGURES 1.3(a,b)** Schematic illustrations of the *closed* (a) and *open* (b) magnetospheric models (Axford and Hines, 1961; Dungey, 1961, respectively). Both models demonstrate the resulting polar cap plasma flows, the former by *viscous interaction* and the latter by *magnetospheric convection*.

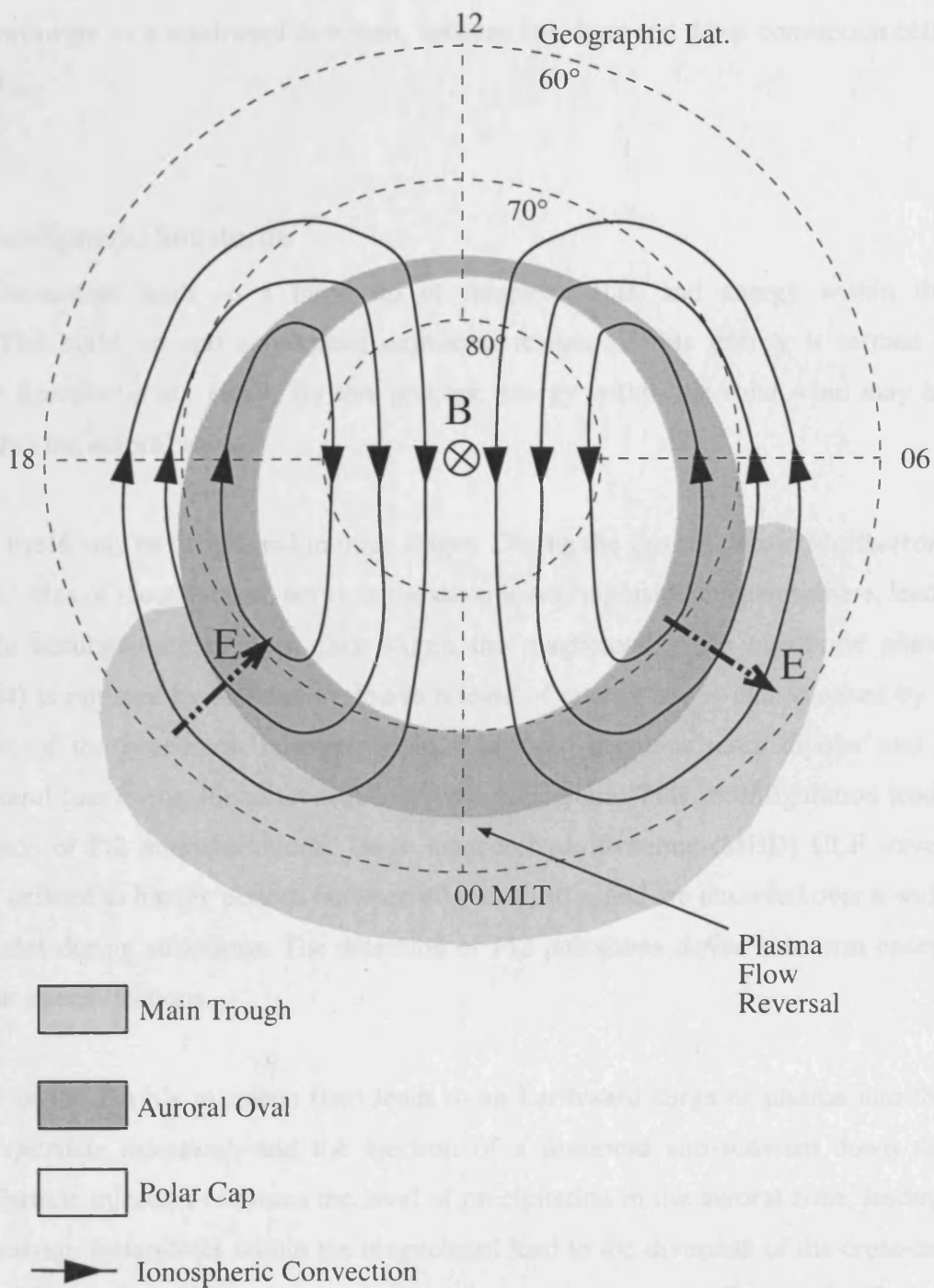


FIGURE 1.4 The twin cell plasma convection pattern, associated with the high-latitude ionosphere. Note the north to southward turning of the electric field, across the plasma flow reversal.

the F-region twin cell pattern. The *electrojets* are enhanced Hall currents, flowing both eastwards and westwards on the dusk and dawn side of the nightside plasma flow reversal respectively (cf. Figure 1.4). It thus follows that the auroral electric fields on the nightside, turn from a northward to a southward direction, between the dusk and dawn convection cells (cf. Figure 1.4).

### 1.2.5 Magnetospheric Substorms

Magnetic reconnection leads to a build up of magnetic flux and energy within the magnetotail. The build up and subsequent explosive release of this energy is termed a *substorm* (e.g. *Rostoker et al.*, 1980). By this process, energy within the solar wind may be dissipated within the auroral zone.

The substorm cycle may be considered in three stages. During the *growth phase* (*McPherron*, 1970), unequal rates of reconnection, between the dayside and nightside magnetosphere, leads to an unstable accumulation of open flux within the magnetotail. The *expansion phase* (*Akasofu*, 1964) is initiated by the said explosive release of energy and is characterised by a reconfiguration of the near-Earth magnetic field. The field becomes more dipolar and a near-Earth neutral line forms, the exact sequence being uncertain. This reconfiguration leads to the generation of Pi2 micropulsations. These magnetohydrodynamic (MHD) ULF waves are nominally defined as having periods between 40 s and 140 s, and are observed over a wide range of latitudes during substorms. The detection of Pi2 pulsations *define* substorm onsets and subsequent intensifications.

Dipolarisation of the Earth's magnetic field leads to an Earthward surge of plasma into the auroral zone (*particle injection*), and the ejection of a plasmoid anti-sunward down the magnetotail. Particle injection enhances the level of precipitation in the auroral zone, leading to *auroral break-up*. Instabilities within the magnetotail lead to the diversion of the cross-tail current, via the highly conducting auroral E-region, as depicted in Figure 1.5. The so generated upward and downward FACs, enhance the westward electrojet, thus defining the *substorm current wedge* (*McPherron et al.*, 1973). An auroral arc brightening is also noted at the foot of the western FAC at substorm onset. The general expansion both westward and poleward of the electrojet and auroral forms, is termed the *westward travelling surge*. The expansion phase is deemed to be over when the westward electrojet and associated FACs begin to diminish. During the *recovery phase* the auroral intensity decreases and the magnetic

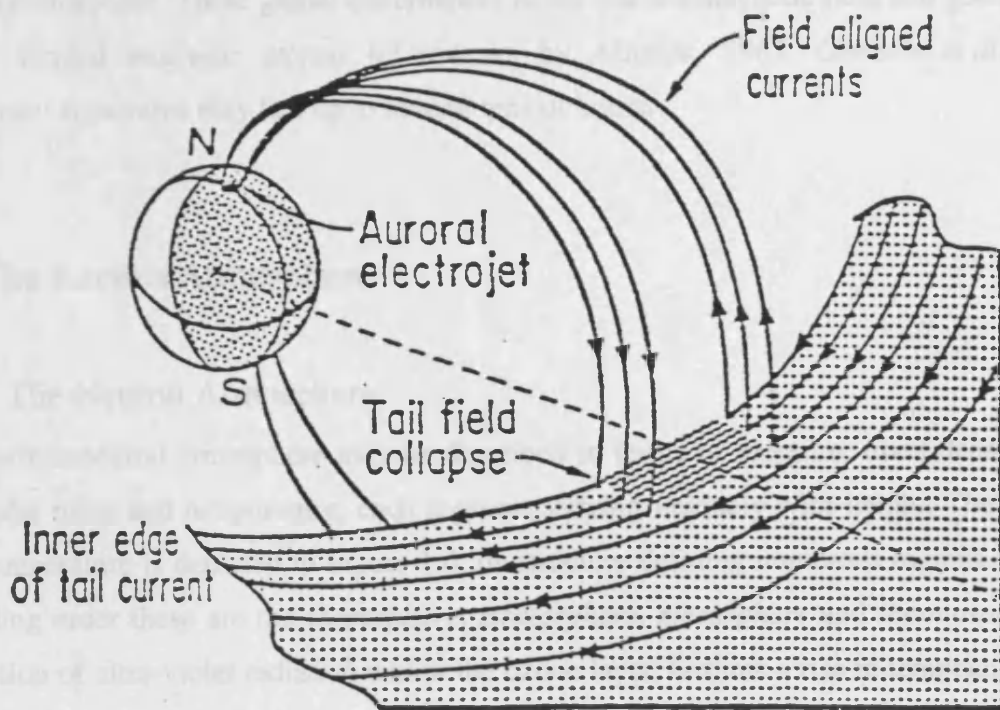


**FIGURE 1.5** The substorm current wedge, arising from the diversion of the cross-tail current. The resulting upward and downward field-aligned-currents, enhance the westward electrojet in the auroral E-region (after McPherron *et al.*, 1973).

field returns to a quiet time configuration. The whole substorm cycle has a typical duration ~ 1 to 3 hours but may be characterised by multiple onsets and surges.

Further disturbances to the geomagnetic environment may arise from shock waves in the solar wind, generated by solar flares or CMEs, or prolonged periods of coupling between the IMF and magnetosphere. These global disturbances to the Earth's magnetic field and geospace, are simply termed *magnetic storms* (cf. reviews by Akasofu, 1963; Gonzalez et al., 1994). Significant signatures may last up to several tens of hours.

## 1.3 The Earth's Atmosphere

### 1.3.1 The Neutral Atmosphere

The Earth's neutral atmosphere may be described in terms of pressure, mass density, mean molecular mass and temperature, each measure varying uniquely with height. The variation with temperature is depicted in Figure 1.6, its structure defining numerous regions. In height ascending order these are the *troposphere*, *stratosphere*, *mesosphere* and *thermosphere*. The absorption of ultra-violet radiation within the ozone layer, ensures a rise in temperature at the *stratopause*. The same radiation is also responsible for the substantial and continuous rise in temperature within the thermosphere.

The atmosphere is primarily heated by solar radiation, but particle precipitation and frictional heating also make varying contributions. Temperature variations give rise to pressure gradients driving prevailing winds, tides and gravity waves. These bulk neutral motions are discussed more fully in Chapter 2. The overwhelming dependence of the temperature on solar and magnetospheric processes, ensures that the temperature profile is highly variable, changing diurnally, seasonally and with solar activity.

The composition of the neutral atmosphere is depicted in Figure 1.7. Within the *turbosphere* or *homosphere* (below ~ 100 km), turbulent mixing ensures that the constituents are essentially homogenous. The major species at sea level are molecular nitrogen (~ 78%) and oxygen (~ 21%) and atomic argon (~ 0.9%), the percentages defining number densities. Other trace constituents are hydrogen, helium, carbon dioxide and water. Above the *turbopause*, the increase in temperature with height produces an atmosphere stable to vertical motion. The

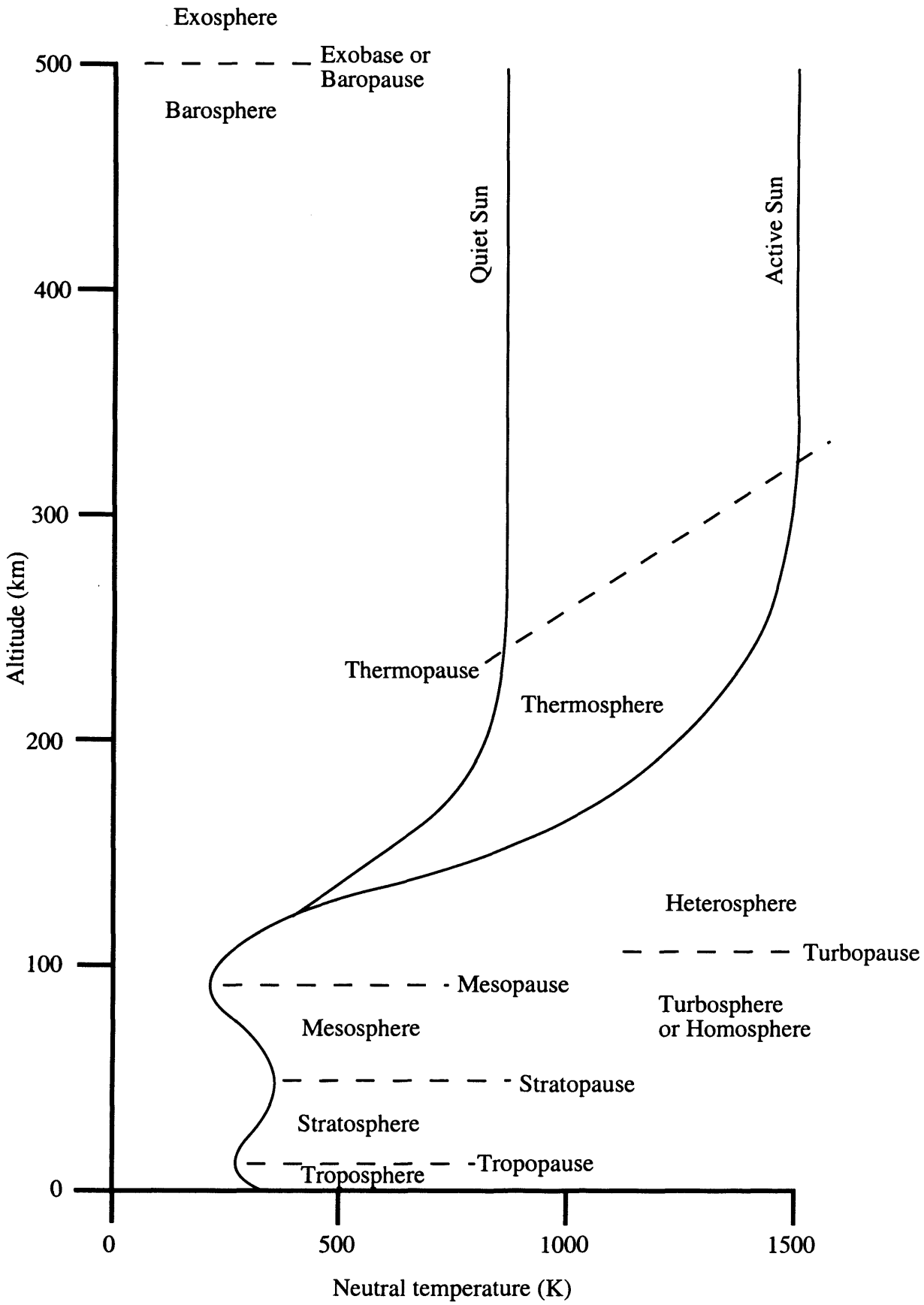


FIGURE 1.6 Temperature profile of the neutral atmosphere with respect to altitude, for high and low solar activity.

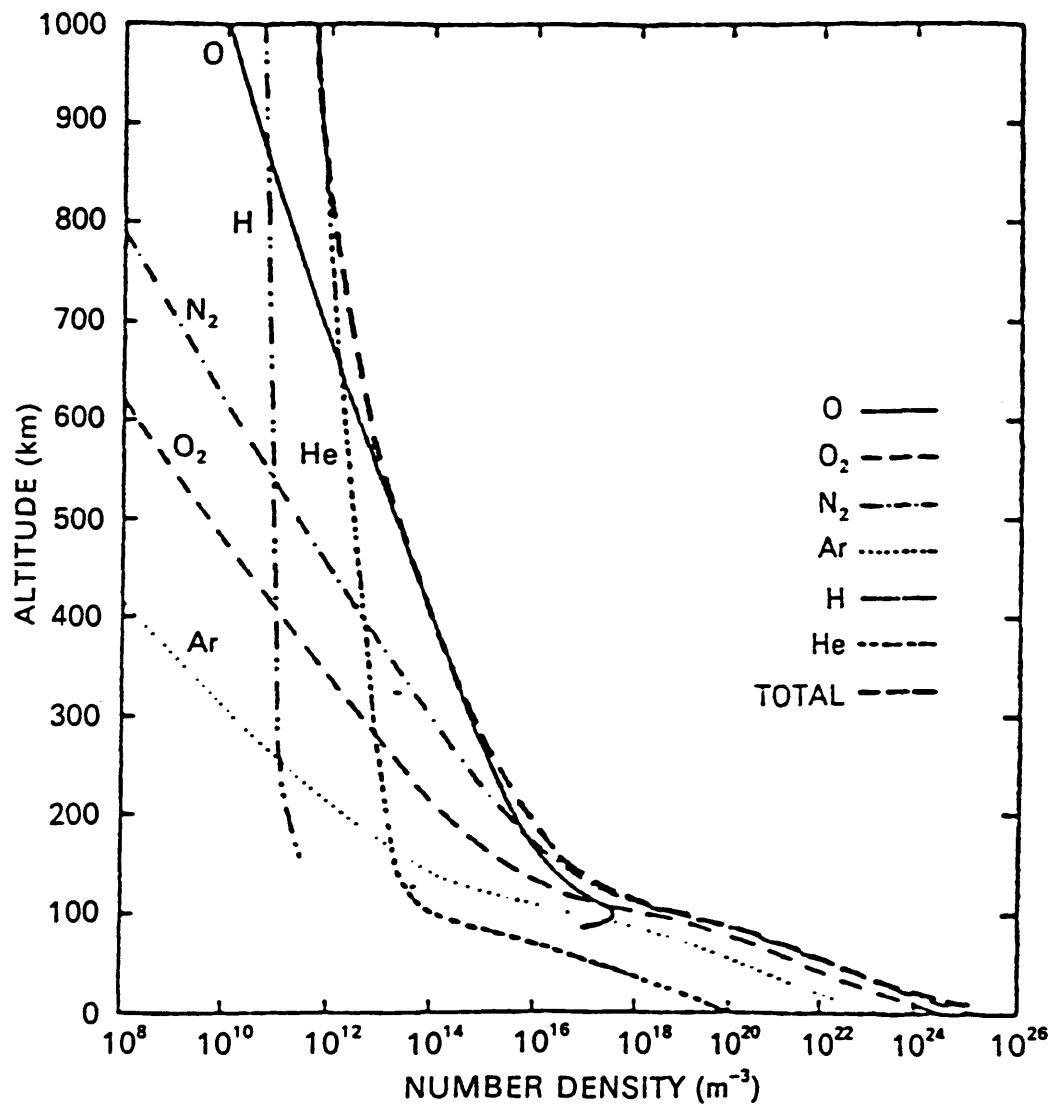


FIGURE 1.7 The typical neutral composition of the near-Earth atmosphere. Note the increasing dominance of the lighter constituents at greater altitudes (reproduced from J. K. *Hargreaves*, 1992)

*heterosphere* is thus defined by diffusive separation under the influence of gravity. Each species takes up individual distributions, characterised by a scale height,  $H_n$ , defined as:-

$$H_n = \frac{kT_n}{m_n g} \quad (1.2)$$

where  $T_n$  and  $M_n$  are the temperature and mass of the neutral species,  $k$  is the Boltzmann constant, and  $g$  is the acceleration due to gravity. The scale height is typically  $\sim 8$  km at sea level but increases to several hundred kilometers in the upper ionosphere. The mean molecular mass thus decreases with height as the lighter elements increasingly dominate the neutral composition. The number density,  $n$ , may be approximated from the equation of state for an ideal gas i.e.:-

$$PV = nkT \quad (1.3)$$

where  $P$ ,  $V$  and  $T$  define the pressure, volume and temperature. At sea level, the neutral number density approximates to  $10^{25} \text{ m}^{-3}$ , falling to about  $10^{19} \text{ m}^{-3}$  at a height of 100 km.

### 1.3.2 The Ionosphere

The ionosphere is an ionised region of the Earth's atmosphere, extending from  $\sim 60$  km to  $\sim 1000$  km. The ratio of ions to neutrals varies with altitude but is generally less than  $10^{-6}$  at all but the upper heights. Nevertheless, the ionosphere may still be defined as that region of the atmosphere where ionisation is present in sufficient quantities to significantly influence the propagation of radio waves.

Photoionisation is the principle process for electron-ion pair creation, i.e.:-



where  $X$  is a neutral atom or molecule. Extreme Ultra Violet (EUV) and X-radiation from the sun are the principle radiation sources. By making various simplifying assumptions, *Chapman* (1931) derived the ion production rate,  $q$ , at a solar zenith angle,  $\chi$ , the formula being expressed in Equation 1.5:-

$$q(z, \chi) = q_0 \exp[1 - z - \sec \chi \exp(-z)] \quad (1.5)$$

where  $z = (h - h_o)/H$ ,  $h$  and  $H$  are the actual and scale heights, and  $q_o$  is the maximum rate of production at height  $h_o$ , when the sun is overhead ( $\chi=0^\circ$ ). Actual ionisation magnitudes are largely determined by competing photoionisation and chemical loss processes. *Radiative recombination* is defined by the reverse reaction in Equation 1.4, and is relatively slow ( $\sim 10^{-12} \text{ cm}^3 \text{ s}^{-1}$  within the lower ionosphere (Rishbeth and Garriott, 1969)). *Dissociative recombination* is a much more rapid process ( $\sim 10^{-7} \text{ cm}^3 \text{ s}^{-1}$ ), common ionospheric examples being given below:-



Equation 1.8 is actually a combination of *charge exchange* followed by dissociative recombination, a process of considerable importance discussed below. The rate of dissociative recombination is determined by the *equal* concentrations of ions and electrons, and is thus proportional to  $N_e^2$ . Under equilibrium conditions where production equals loss, and dissociative recombination is the dominant loss process, it can be shown from Equation 1.5 that:-

$$N_e(\chi) = N_o \cos^n \chi \quad (1.9)$$

where  $N_o$  is the maximum ion density of a Chapman layer, for  $\chi=0^\circ$ , and  $n$  equals 0.5. In practice,  $0.2 < n < 0.9$  (Davies, 1990).

The varying neutral composition of the ionosphere with altitude (cf. Figure 1.7) determines the radiation absorbed at a given height, and the nature of the chemical loss processes. The consequence is a multi-layered ionisation profile as depicted in Figure 1.8. The layers, or ledges, are termed the D-, E- and F-regions, the F-region often being defined by two distinct regions during the day, the F1- and F2-layers, the splitting process known as *bifurcation*. Figure 1.8 depicts typical densities, actual densities varying by up to an order of magnitude between sunspot maximum and minimum.

### *D-Region*

The D-region extends from  $\sim 60 \text{ km}$  to  $\sim 90 \text{ km}$  and has typical daytime electron densities  $\sim 10^9 \text{ m}^{-3}$ . Principle sources of ionisation are X-radiation, and to a lesser extent, Lyman- $\alpha$ ,

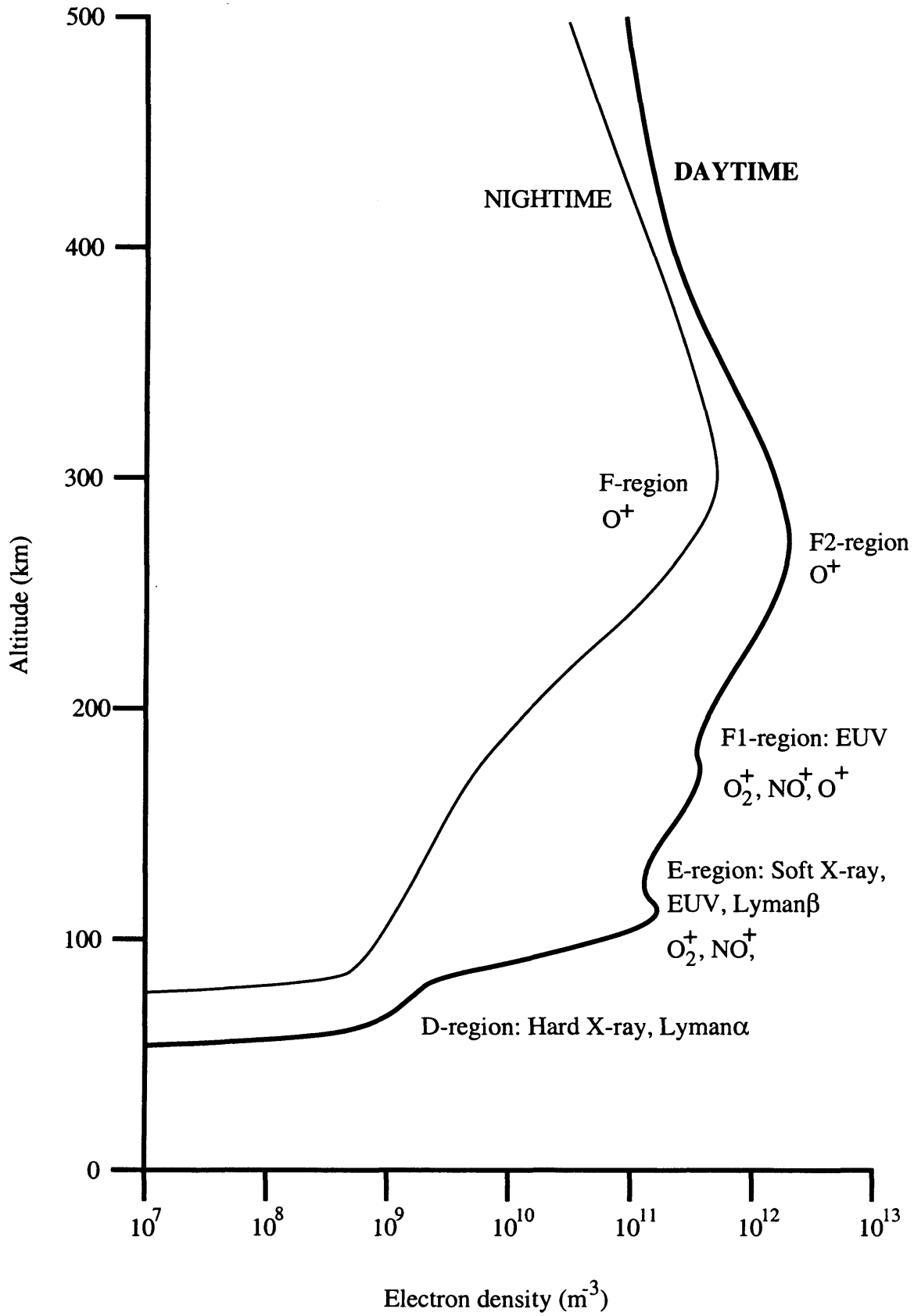


FIGURE 1.8 Typical mid-latitude electron density profiles for moderate solar activity, with principle ion constituents and ionising sources.

EUV and galactic cosmic rays. The D-region defines a ledge of ionisation and completely recombines at night. The primary ions are  $\text{NO}^+$  and  $\text{O}_2^+$ ,  $\text{N}_2^+$  rapidly converting to  $\text{O}_2^+$  by charge exchange. Negative ions are also significant in the D-region, created through *charge attachment*. Non-deviative absorption (cf. §3.2.7) maximises within the D-region.

### *E-Region*

The E-region extends from ~ 90 km to ~ 160 km, typically peaking at ~ 110 km with electron densities  $\sim 10^{11} \text{ m}^{-3}$ . The principle source of ionisation is EUV radiation, with soft X-rays becoming significant at sunspot maximum. The primary ions of production are  $\text{N}_2^+$ ,  $\text{O}_2^+$  and  $\text{O}^+$ , with subsequent reactions (cf. Equation 1.8a) leaving  $\text{NO}^+$  and  $\text{O}_2^+$  as the most abundant. The E-region ionisation profile is characterised by the Chapman formula (cf. Equation 1.5). The E-region is the focus of this thesis, it being the region of sporadic-E occurrence. The mid-latitude generation mechanism of sporadic-E is largely a consequence of the differing ion-neutral and electron-neutral collision rates, in comparison to their respective gyrofrequencies. Ions are coupled to the neutral wind, with electrons largely 'E cross B' drifting. This topic is discussed more fully in Chapter 2.

At high latitudes, the E-region is dominated by the auroral zones, two annuli, positioned over the north and south geomagnetic poles (*Feldstein, 1963*). Electrons and protons from varying magnetospheric origins, precipitate into these zones, and directly and indirectly generate a range of ionisation features. The most striking of these is the visual or *luminous aurora*, resulting primarily from the ionisation of atomic oxygen and molecular nitrogen, generating green, red and violet displays. The statistical location of these displays define the *auroral oval* (*Feldstein and Starkov, 1967*). The oval is eccentric with respect to the dipole pole, the centre being displaced towards the nightside. The magnetic latitude of the statistical maximum is near  $67^\circ$  at local midnight but about  $77^\circ$  at local noon. Increased geomagnetic activity results in oval broadening and an expansion to lower latitudes.

Precipitating particles have a range of energies up to many tens of keV. The average energy dissipated per ion-electron pair produced is 35 eV. The depth of penetration into the ionosphere thus depends on the particle's initial energy. Electrons with energies between ~1 keV and ~ 30 keV produce ionisation in the E-region. Approximately co-located with the luminous aurora is the *radar aurora* (*Chestnut, 1972*). Auroral radars receive echoes associated with both *discrete* and *diffuse* auroral forms, the former being associated with the higher electron energies noted above. The more common, sub-visual diffuse type, constitute lower energy precipitation (0.1 to 10 keV) which originates in the central plasma sheet of the

magnetosphere (*Whalen, 1983*). The hardest electrons in this band are responsible for *auroral E*, the enhancement of the auroral E-region densities (*Robinson and Vondrak, 1985*).

### *F-Region*

The F1-region is a daytime, largely summer-time peak or ledge of ionisation, forming in the lower F-region at an altitude  $\sim 160$  to  $\sim 180$  km. Its presence pertains to the altitude of maximum solar radiation absorption. Its characteristics approximate to a Chapman layer and it is essentially similar to the daytime E-region, though with a larger electron density peak.

The F2-region ( $\sim 200$  to  $\sim 400$  km) does not coincide with a maximum ionisation rate, its rate of production being less than that of the F1-layer. Its electron density peak is determined by loss processes, specifically those defined by Equation 1.8. The dominant ion at these altitudes is the single atomic ion  $O^+$  (cf. Figure 1.7). The ion *loss* process is thus a two-stage reaction, *slow* charge exchange (Equation 1.8a), followed by *rapid* dissociative recombination (Equation 1.8b). As  $N_2$  decreases with altitude, so too does the chemical loss rate, and hence the ion density increases with height above the F1-layer. At greater heights still, decreasing neutral density results in loss by diffusion becoming more important than *both* the production and chemical loss processes. A peak in ion density is thus constituted. The deviation from a solar controlled Chapman type layer results in other F-region anomalies e.g. the electron density often not peaking at midday and densities often being higher in winter than in summer.

## **1.4 Radio Wave Propagation**

### **1.4.1 Ionospheric Influences**

Though the ionospheric plasma is on average neutral, containing equal numbers of positive ions and free electrons, the effect of the electrons is predominant. The electric field of the propagating radio wave excites the charged particles into oscillation, each thus radiating electromagnetic waves of the same frequency. The resulting interference of these ‘wavelets’ define the propagation characteristics of the wave. The amplitude of the oscillations relate directly to the particle mass, and as the positive ions are  $\sim 60000$  times more massive than the free electrons, their effect on the wave’s propagation is relatively negligible.

Attenuation of the radio wave occurs when the oscillating electrons collide with the ambient neutral gas atoms and molecules, the wave's energy rapidly dissipating through the predominantly neutral medium via the subsequent neutral-neutral collisions. The characteristics of radio wave propagation is thus dominated by the relative magnitudes of the ambient electron density, the electron-neutral collision frequency and significantly, the Earth's magnetic field.

Also of considerable importance is the relative magnitude of the *propagating* wave frequency, to that of the '*Plasma Frequency*',  $f_p$ , defined as :-

$$f_p^2 = \frac{N_e e^2}{4\pi^2 \epsilon_0 m_e} \quad (1.10)$$

where  $e$  is the electronic charge,  $\epsilon_0$  is the permittivity of free space and  $m_e$  is electron rest mass. The square of the plasma frequency is thus directly proportional to the electron density of the medium. It is an intrinsic property of an ionised medium and arises from the development of space charge, the small scale, temporary separation of positive and negative charges. The resulting electrostatic forces generate heavily damped oscillations, with time constants of a few milliseconds or less. It is this property of the plasma that determines whether incident radio waves are reflected or refracted. A review of radio wave propagation, as related to this thesis, is presented in Chapter 3.

#### 1.4.2 High Frequency Radio Waves

High Frequency (HF) waves range between 3-30 MHz and are a constituent of the commonly termed *radio wave* band of the electromagnetic spectrum. They are ideal for reliable, low power (few kW or less), low cost transmissions, having an adequate bandwidth, relatively low atmospheric noise, increasingly reduced absorption at the higher frequencies (cf. §3.2.7) and excellent range potential, in particular, beyond-line-of-sight links (e.g. *Maslin*, 1986). With the advent of increasingly cheaper and often more reliable satellite channels and point-to-point microwave links, much HF traffic has switched over to these more 'high technology' means of communication. The HF band however, is still used extensively for both fixed and mobile transmissions, of both voice and data, particularly in the military, maritime and aeronautical sectors.

## 1.5 The Current Investigation

This thesis is primarily engaged in analysing and interpreting oblique ionosonde data, derived from HF 'Chirp' Sounders (Barry, 1971). Data was recorded over three, eleven day periods between 1987 and 1988, at sub-auroral and mid-latitudes, as a means of investigating sporadic-E layers (cf. reviews by Whitehead, 1970; Whitehead, 1989; Matthews, 1998) through oblique sounding techniques. Sporadic-E layers, commonly termed Es-layers or Es, are generally considered to be unpredictable enhancements of the E-region electron density, forming an altitude thin layer (~ 0.5-2 km) at heights near 110 km altitude. A commonly quoted characteristic is their 'top frequency', *ftEs*, the maximum frequency reflected from remote transmissions. A comprehensive review of sporadic-E layers is presented in Chapter 2.

Sporadic-E is influential in specifying reliable communication channels and despite the extensive amounts of research performed in this field, there is still much detail to be determined on the morphology of these layers. Chapter 4 contributes to this end. It also lends itself as a springboard for further data analysis, characterising the nature of the sporadic-E layers pertaining to this study, and by thus establishing the 'typical' nature of the layers, allows generally applicable deductions to be presented in subsequent Chapters.

Chapter 5 and Chapter 6 examine the relative signal strength returns, reflected from mid-latitude sporadic-E layers, with respect to the scanning, 'Probing Frequency' of the ionosonde (cf. §3.3.2). For the data set employed, ionograms are composed every 5 minutes, signal strength measurements therein being recorded at 100 kHz intervals of the frequency modulated transmissions. This high resolution information is utilised to postulate on the internal plasma composition of the layers, allowing deductions to be made on the response of this composition to differing rates of change of the top frequency.

The thesis concludes with a series of case studies, examining how both the morphology and internal plasma structure of sub-auroral sporadic-E, are influenced during times of substorm activity (e.g. Rostoker *et al.*, 1980) and other magnetically disturbed periods. During these intervals, the top frequency of sporadic-E is correlated with plasma irregularity backscatter intensity (e.g. Fejer and Kelly, 1980), as detected by 'SABRE', a VHF coherent backscatter radar (cf. §3.4.1).

# Chapter 2

## A Review of Sporadic-E Observations and Theory

### 2.1 Introduction

Sporadic-E (or Es-layer), is the term used to describe anomalous patches or layers of enhanced ionisation within the E-region (*Kirby and Judson, 1935*). It is an all encompassing term, relating to features noted at all latitudes, often with different morphological characteristics and generation mechanisms. Indeed, the name itself implies unpredictability in occurrence, which is often inappropriate, even on a daily time scale. Originally termed ‘abnormal-E’ (*Ratcliffe and White, 1933*), it is unfortunate that this more accurate description has been usurped. This thesis will however adhere to the widely used and recognised terminology, that of ‘sporadic-E’.

Sporadic-E is generally observed between heights of 95 km and 120 km, with some evidence of ‘preferred’ heights (e.g. *Smith and Mechtly, 1972*). It is mostly observed as thin sheets, ~ 500 m to 2 km, though thicker layers are observed at greater heights (e.g. *Rowe, 1974*). It is this narrowness of extent, first observed employing vertical sounding techniques, that distinctly identifies the layers, the returned echoes being of constant virtual height (cf. §3.2.5). Sporadic-E has been observed extending over many hundreds of kilometers (e.g. *Ovezgel’dyyev, 1972*) with the associated movement of these large scale structures being consistent with the neutral wind in the E-region (e.g. *Tanaka, 1979; Kolawole and Derblom, 1978*). The layers may be completely blanketing, reflecting all incident radio waves, or be totally or partially transparent to the higher frequencies (e.g. *Whitehead, 1972*).

At mid-latitudes, the occurrence of sporadic-E is directly linked to the semidiurnal atmospheric tide, hence determining maximum occurrence peaks pre-noon and late afternoon (*Smith, 1957*). Layers observed at these times are often noted to descend in height at speeds ~ 1-2 m s<sup>-1</sup>, corresponding to the downward phase velocity of the tidal motion (*MacDougal, 1974, 1978; Fomichev and Shved, 1981*). Such layers are termed ‘sequential’ sporadic-E. At other latitudes the tides are less important and the occurrence and intensity of sporadic-E depends on a range of other local factors (cf. reviews by *Whitehead, 1970; Whitehead, 1989; Mathews, 1998*, and references therein).

One of the most important and interesting aspects of sporadic-E is the temporal and spatial variability of its plasma composition. It is these properties that largely define its unpredictability and with which this investigation is primarily engaged. While other latitudes are mentioned in passing, the following discussion and review largely confines itself to sporadic-E observed at mid- and sub-auroral latitudes ( $\sim 10^\circ$  to  $60^\circ$ ), pertaining to the data in this thesis.

## 2.2 Observations of Sporadic-E

### 2.2.1 Scaling Parameters

Sporadic-E is often characterised by its '*top frequency*', or '*ftEs*', the maximum frequency returned from remote transmissions. By its very nature, this parameter does not cluster around a predictable value but often varies considerably over short (< 1 hour) time scales. As a consequence, occurrence statistics are usually quoted as a percent probability that layers will exist with top frequencies *greater than* a given threshold value. The probability of sporadic-E occurrence, '*P*', for top frequencies greater than a given frequency, '*f*', was empirically determined by *Phillips* (1947) as :-

$$\log_{10} P = a + bf \quad (2.1)$$

where '*a*' and '*b*' are customised constants, depending on geographic location, daytime or night-time, etc. The threshold frequency may be selected to highlight unusually intense Es-layers, but is more commonly chosen to be 5MHz, a value high enough to consistently avoid 'contamination' by normal E-region data.

Sporadic-E is also characterised by a '*blanketing frequency*' (*fbEs*). This parameter specifically refers to the frequency below which all *vertically* incident frequencies are totally reflected. Returns from higher ionospheric layers are thus impeded. At *oblique* incidence and in general, it is more applicable to define this parameter in terms of the plasma composition of the layer and this is considered in more detail in §2.4. The blanketing frequency is a manifestation of the historical practice of parametising sporadic-E in relation to features noted on *vertical* ionograms (see §3.3).

## 2.2.2 Geographical Distribution and Morphology

*Smith* (1957) compiled extensive geographic and temporal occurrence statistics for sporadic-E occurrence. Data pertaining to three distinct geographic locations was compiled, namely the equatorial, mid-latitude and auroral zones. The auroral zone ( $\geq 60^\circ$ ) is noted for the night-time occurrence of sporadic-E while conversely, the equatorial zone ( $\leq 10^\circ$ ) and mid-latitudes are characterised by daytime Es-layers. Generation mechanisms within these zones are known to be different and are discussed more fully in §2.3.

The mid-latitude zone (often denoted as the ‘temperate’ zone in early literature) is characterised by summer time and daytime occurrence maxima, though a minor occurrence maximum is often noted in the winter (e.g. *Baggaley*, 1985). Figure 2.1 summarises these observations. It should be emphasised that even within a given zone, local anomalies exist. At mid-latitudes, where sporadic-E occurrence is linked to the horizontal component of the magnetic field (cf. *Heisler and Whitehead*, 1960, and discussions below), occurrences over South Africa are an order of magnitude less than those noted over Japan, despite both being at similar relative magnetic latitudes ( $\sim \pm 35^\circ$ ).

Temporal studies of mid-latitude sporadic-E occurrence again reveal many local influences, but the majority are defined by pre-noon and late afternoon maxima, the former being more prominent (e.g. *Smith*, 1957; *Dyer*, 1972; *Harris and Taur*, 1972). Figure 2.2 presents some typical observations. Note the similarities and differences between the three mid-latitude, yet geographically dispersed, stations.

## 2.2.3 The Effects of Magnetic Activity

Magnetic activity has a markedly different influence on sporadic-E at high-latitudes (e.g. the auroral zone) as compared to mid-latitudes. Within the auroral zone, increased precipitation and electric fields, during storm or substorm activity, can generate auroral-type sporadic-E layers, characterised by an inherent irregularity structure (e.g. *Reddy et al.*, 1969; *Dudeney and Rodger*, 1985). *Weber et al.* (1977) relate sporadic-E occurrence to the enhanced discrete aurora, while *Besprozvannaya et al.* (1980) correlate the general enhancement of sporadic-E occurrence to electron precipitation of energies up to 10 keV.

At mid-latitudes the effect of magnetic activity on sporadic-E occurrence is disputed. *Smith* (1957) and *Dyer* (1972) both indicate a negative correlation while at sub-auroral latitudes, the

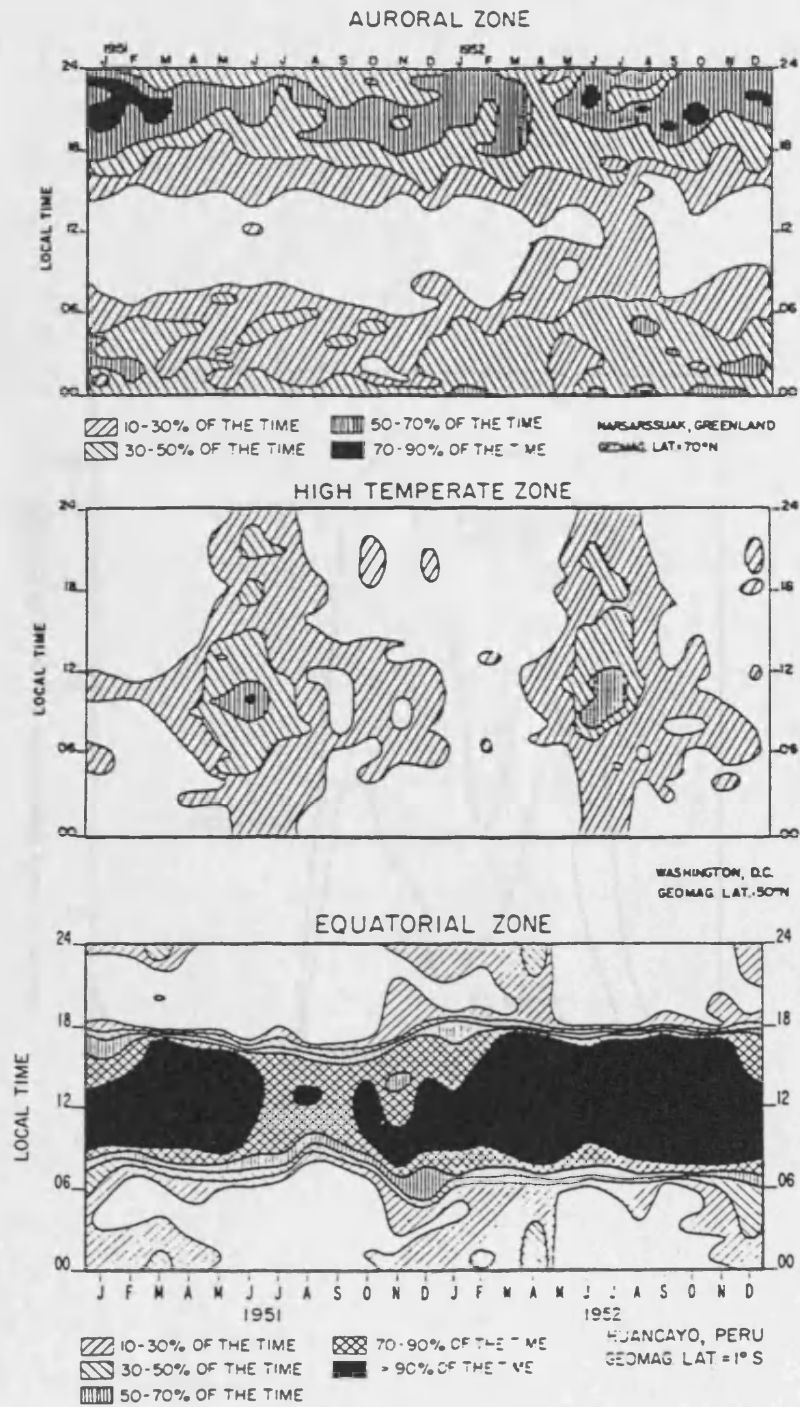


FIGURE 2.1 Diurnal and seasonal occurrence statistics of sporadic-E, for  $fE_s > 5$  MHz (after E. K. Smith, 1957). Three distinct latitudinal zones are presented, the 'high temperate zone' corresponding to the Bodø/Wick propagation path, during magnetically quiet times (cf. Chapter 4).

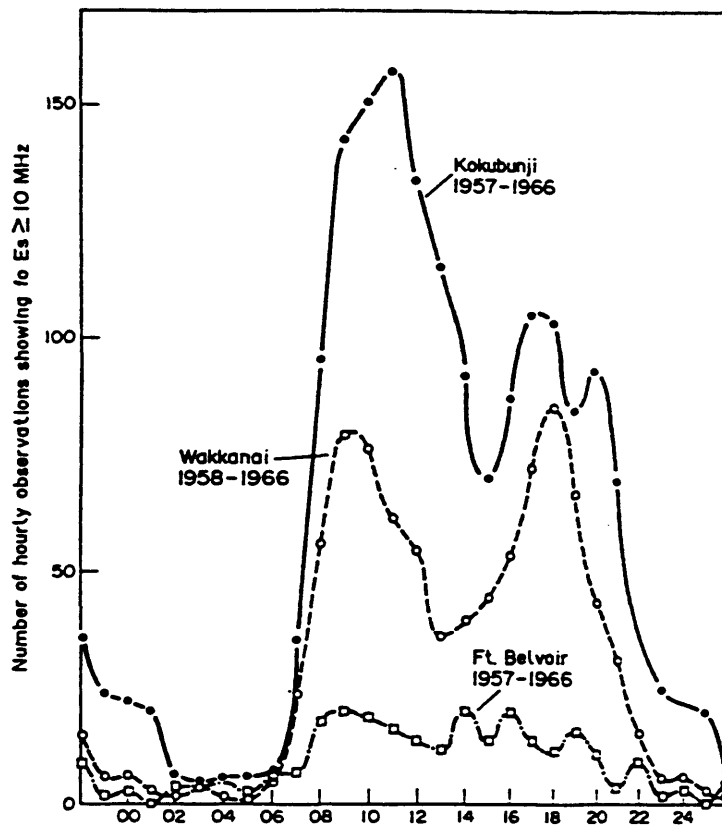


FIGURE 2.2 Temporal occurrence statistics of intense sporadic-E layers ( $ftEs > 10$  MHz), at three mid-latitude, but geographically dispersed ionosonde stations (after *E. K. Smith*, 1968). The pre-midday and early evening occurrence maxima, noted at the Kokubunji and Wakkanai stations, are most typical in the literature.

potential increase in the convection electric fields can both promote layer formation or disperse existing layers (Nygrén *et al.*, 1984a; Bristow and Watkins, 1994). Similar effects may be observed by equatorward propagating gravity waves, generated in a more active auroral zone (Hunsucker, 1982). All these aspects of sporadic-E generation are discussed more fully in §2.3 and §2.4.

## 2.3 The Theory of Sporadic-E Generation

### 2.3.1 Introduction

The almost universally accepted mechanism for the formation of mid-latitude sporadic-E is that encompassed in the Windshear Theory (Whitehead, 1961; Axford, 1963, MacLeod, 1966, and Kato, 1966). In its simplest form, it describes the convergence of ions into thin layers, within the lower E-region, Lorentzian forces driving the ions downward from above and upwards from below, as a consequence of a shear in the zonal neutral wind. There is much direct and indirect evidence to support this theory, the most compelling being the coincident observations of sporadic-E and wind profiles, usually by means of rocket experiments (e.g. Smith, 1970; Kato *et al.*, 1972).

A more generalised form of the theory encompasses meridional wind shears (considered in isolation by Dungey, (1956) and (1959) ) and the E-region electric field (Rees *et al.*, 1976). This General Windshear Theory is considered in detail below. But first, some important and relevant E-region physics is considered.

### 2.3.2 E-region Conductivities, Mobilities and Collision Frequencies

The differential flow of ions and electrons, i.e. the differential plasma drift, defines a current which is summarised by the general version of Ohm's law, i.e.:-

$$\mathbf{J} = \underline{\underline{\sigma}} \cdot \mathbf{E} \quad (2.2)$$

where  $\mathbf{J}$  is the ionospheric current density,  $\underline{\underline{\sigma}}$  is the conductivity tensor and  $\mathbf{E}$  the ambient electric field. Equation 2.2 is more conveniently expressed with respect to the magnetic field,  $\mathbf{B}$ , as:-

$$\mathbf{J} = \sigma_p \mathbf{E}_\perp + \sigma_H \frac{\mathbf{E}_\perp \wedge \mathbf{B}}{B^2} + \sigma_o \mathbf{E}_\parallel \quad (2.3)$$

where  $\mathbf{E}_\perp$  and  $\mathbf{E}_\parallel$  are the electric field components perpendicular and parallel to  $\mathbf{B}$ , and  $\sigma_p$ ,  $\sigma_H$ , and  $\sigma_o$  are the Pedersen, Hall and direct conductivities respectively, defined as (Rees, 1989):-

$$\sigma_p = \sum_i \frac{eN_i}{B} \left( \frac{v_{en} \omega_{He}}{\omega_{He}^2 + v_{en}^2} + \frac{v_{in} \omega_{Hi}}{\omega_{Hi}^2 + v_{in}^2} \right) \quad (2.4a)$$

$$\sigma_H = \sum_i \frac{eN_i}{B} \left( \frac{\omega_{He}^2}{\omega_{He}^2 + v_{en}^2} - \frac{\omega_{Hi}^2}{\omega_{Hi}^2 + v_{in}^2} \right) \quad (2.4b)$$

$$\sigma_o = \frac{e^2 N_e}{m_e (v_{en} + v_{ei})} + \sum_i \frac{e^2 N_i}{m_i v_{in}} \quad (2.4c)$$

where  $N_{e,i}$ ,  $m_{e,i}$ ,  $v_{en,in}$  and  $\omega_{He,Hi}$  are the electron and ion number densities, mass, neutral collision frequencies and gyrofrequencies. The conductivities are depicted in Figure 2.3, for a typical mid-latitude ionosphere. The Hall conductivity maximises at  $\sim 110$  km, thus defining the height of maximum differential plasma drift. The Pedersen conductivity maximises at  $\sim 130$  km though decreases less rapidly with height. The direct or parallel conductivity increases with height as the collision frequencies reduce, and dominates above the F-region.

Ion and electron ‘mobilities’ are closely related to the conductivities, each conductivity being essentially defined by the sum or difference of the respective ion and electron mobilities (Rishbeth and Garriott, 1969).

The height varying conductivities and mobilities are largely a manifestation of the important differences that exist between the electron- and ion-neutral normalised collision frequencies, particularly within the E-region. Normalised collision frequencies decrease with height but at differing rates for the electrons and ions. For electrons, the transitional value of 1 (collision frequency equaling the gyrofrequency) occurs at  $\sim 80$  km; for ions the respective height is  $\sim 120$  km (e.g. Wright and Fedor, 1970). Within the E-region, it is thus important to distinguish between the electron and ion (mobility) terms within Equations 2.4(a,c). Electron motion is largely dominated by the magnetic field, ‘E cross B’ drifting being dominant. Below  $\sim 120$  km, the ion motion is collision dominated. These contrasting forces are instrumental in determining the theory of sporadic-E generation at mid-latitudes, pre-disposing the layers to form between heights  $\sim 95$  km and  $\sim 120$  km (cf. §2.1). Ion motion

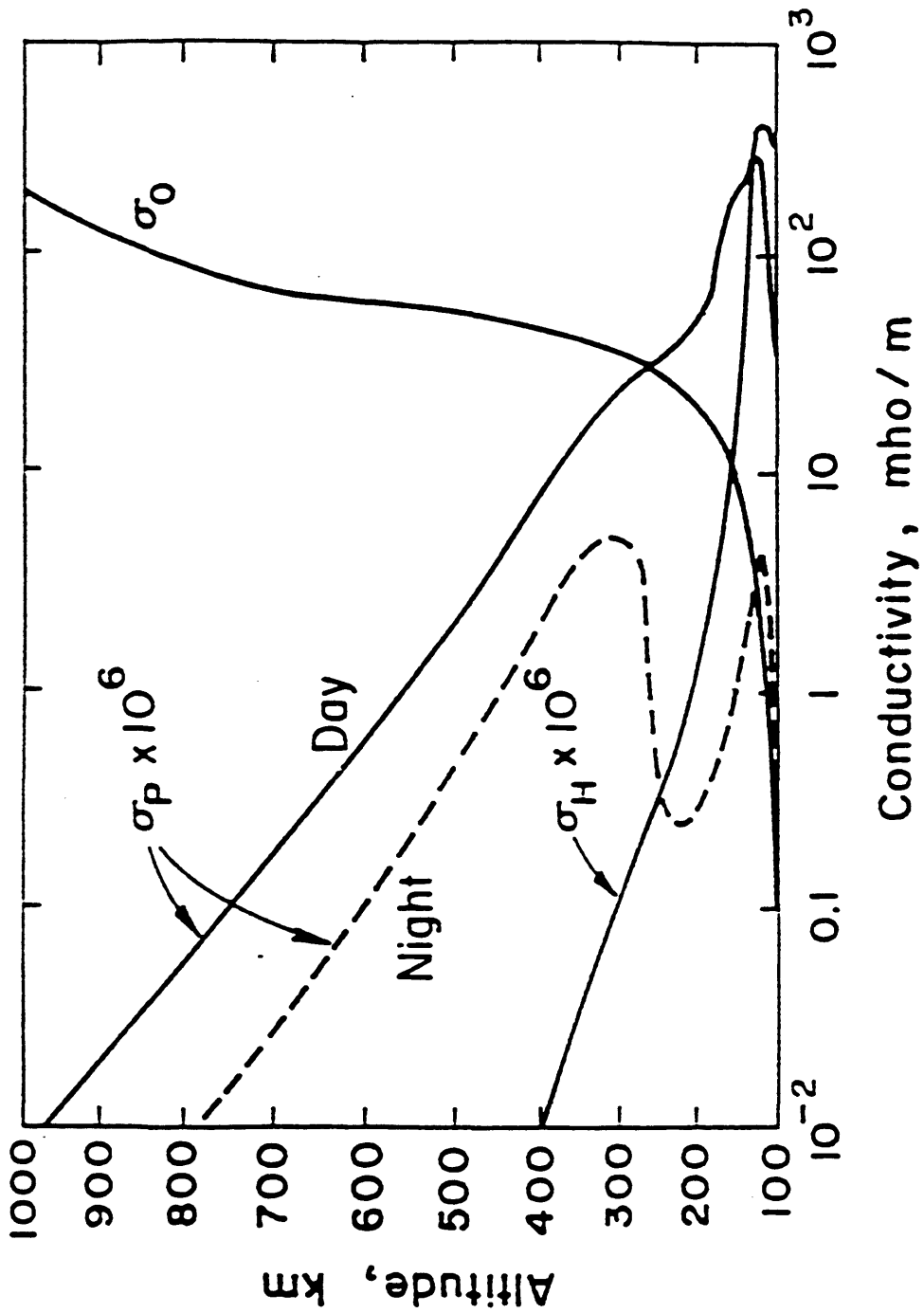


FIGURE 2.3 Typical altitude profiles for the Hall ( $\sigma_H$ ), Pedersen ( $\sigma_P$ ) and direct ( $\sigma_o$ ) conductivities, for the mid-latitude daytime ionosphere (the night-time profile for the Pedersen conductivity is depicted as a dashed curve).

dominates the theory, with the electrons, through high 'direct' mobility, drifting parallel to the magnetic field lines to neutralise the space charge so established. A stable structure is thus maintained.

### 2.3.3 The Windshear Theory

#### *The continuity equation*

The continuity equation for ions in the lower E-region may be expressed in terms of production and loss rates ( $Q$  and  $L$  respectively), a transport term and the diffusion rate, i.e.:-

$$\frac{\partial N_i}{\partial t} = Q - L - \nabla \cdot (N_i \mathbf{v}_i) + \nabla^2 (DN_i) \quad (2.5)$$

where  $N_i$  is the ion number density,  $\mathbf{v}_i$  is the ion velocity and  $D$  is the ambipolar diffusion coefficient. A layer of enhanced ion (plasma) density may thus be produced by either a local *increase* in the ionisation rate, a local *decrease* in the ion loss rate, or a *redistribution* of existing ionisation. The first two possibilities are inappropriate for sporadic-E layers. Increasing the ionisation rate would require an implausibly large localisation of absorption or collision processes in a very thin layer. Moreover, ionisation by impact with charged particles would be accompanied by excitation and hence by the emission of light; this is not generally observed. Enhancement resulting from a local decrease in the ion loss rate can be ruled out because the metal ions, that are known to be the major constituent of thin sporadic-E layers (cf. §2.3.7), already have a very low loss rate at the altitudes in question. These deductions imply a redistribution of existing plasma. Diffusion, by definition, will not enhance the ion density, and horizontal transport of ionisation is again inconsistent with sporadic-E observations, the horizontal scale of ion distribution being so much larger than the vertical scale (cf. §2.1). Vertical transport appears to be the only plausible mechanism.

#### *Equation of Motion*

The general equation of motion for a given ion, may be defined in terms of momentum transfer, Lorentz's Law, gravity and partial pressure gradients (*Miller and Smith, 1976*):-

$$m_i \frac{d\mathbf{v}_i}{dt} = m_i \mathbf{v}_i (\mathbf{w} - \mathbf{v}_i) + e\mathbf{v}_i \wedge \mathbf{B} + e\mathbf{E} + m_i \mathbf{g} - \frac{1}{N_i} \nabla p \quad (2.6)$$

where  $\mathbf{v}_i$  and  $\mathbf{w}$  are the ion and neutral wind velocities and  $p$  is the partial pressure. If steady state conditions are assumed, and both gravity and partial pressure are neglected as relatively insignificant (*MacLeod et al.*, 1975), the equation may be solved for  $\mathbf{v}_i$ , in terms of the normalised ion collision frequency,  $\rho$ , giving:-

$$\mathbf{v}_i = \frac{1}{1+\rho^2} \left[ \rho^2 \mathbf{u} + \rho \mathbf{u} \wedge \hat{\mathbf{B}} + (\mathbf{u} \cdot \hat{\mathbf{B}}) \hat{\mathbf{B}} \right] \quad (2.7a)$$

where:-

$$\mathbf{u} = \mathbf{w} + \frac{\mathbf{E}}{\rho B}; \quad \rho = \frac{v_{in}}{\omega_{Hi}}; \quad \omega_{Hi} = \frac{eB}{m_i} \quad (2.7b,c,d)$$

Equation 2.7 represents the most concise and generalised form of the Windshear theory of sporadic-E generation. The first term gives the ion velocity parallel to the resultant wind velocity and electric field, the second term gives the velocity perpendicular to both the wind velocity/electric field vector and the magnetic field, and the third term gives the velocity parallel to the magnetic field. Different terms will dominate at different heights, according to the value of the normalised collision frequency. The ion motion is more easily interpreted by substituting Equation 2.7b into Equation 2.7a. In doing so, we implicitly assume that the electric field is perpendicular to the magnetic field, the 'direct' conductivity, parallel to the magnetic field, being very large (cf. §2.3.2). Hence (after *Kirkwood and von Zahn*, 1991):-

$$\mathbf{v}_i = \frac{\rho}{1+\rho^2} \left[ \frac{\mathbf{E}}{B} + \frac{\mathbf{w} \wedge \mathbf{B}}{B} \right] + \frac{1}{1+\rho^2} \left[ \frac{\mathbf{E} \wedge \mathbf{B}}{B^2} \right] + \mathbf{w}_\perp \left[ \frac{\rho^2}{1+\rho^2} \right] + \mathbf{w}_\parallel \quad (2.8)$$

where  $\mathbf{w}_\perp$  and  $\mathbf{w}_\parallel$  are the neutral wind components parallel and perpendicular to the magnetic field. Note that Equation 2.8 is general, having only neglected some minor perturbing forces. The first term describes the Pedersen current and Lorentz forcing, the latter driving the ions across the magnetic field lines as a consequence of ion-neutral collisions. This Lorentz forcing defines the Windshear theory, the term dominating at the lower heights under consideration, as can be determined from the value of its coefficient. The second term describes the Hall current and will dominate at the upper heights, again determined by its coefficient value. At these heights ( $\geq 150$  km) both the electrons and ions will 'E cross B' drift, moving largely independent of the neutral wind.

It was stated earlier that sporadic-E layers will be generated from the vertical transport of ions. It is appropriate then, to define the ion velocity in the vertical,  $z$ -direction. The electric and magnetic field are assumed to be constant with height, as is the inclination angle of the magnetic field, ' $I$ '. The variation of the normalised ion collision frequency with height is implicit and instrumental to the Windshear theory. Equation 2.8 thus yields:-

$$v_{iz} = \frac{\rho}{1 + \rho^2} \left[ \frac{E_N}{B} + w_E \right] \cos I \quad (2.9a)$$

$$+ \frac{1}{1 + \rho^2} \left[ \frac{E_E}{B} - w_N \sin I \right] \cos I \quad (2.9b)$$

$$+ \left[ 1 - \frac{\cos^2 I}{1 + \rho^2} \right] w_z \quad (2.9c)$$

where the subscripts ' $N$ ' and ' $E$ ' denote northerly and easterly directions.

At the lower heights, between  $\sim 95$  km and  $\sim 120$  km, Equation 2.9a is in ascendancy and the vertical ion motion is determined by the northward component of the electric field, and the eastward component of the neutral wind. At greater heights, between  $\sim 120$  km and  $\sim 140$  km, Equation 2.9b dominates, the vertical ion motion thus being determined by the eastward component of the electric field, and the northward component of the neutral wind. The vertical component of the neutral wind will have an influence at all heights (Equation 2.9c). At heights below  $\sim 95$  km, sporadic-E layers are rapidly dispersed by turbulence.

Equation 2.9 thus encapsulates all the E-region features that directly impact upon the vertical motion of ions, hence determining whether ion convergence will occur, leading to a layer of enhanced ionisation, a sporadic-E layer.

#### 2.3.4 Mid-Latitude Approximations of the General Windshear Theory

At mid-latitudes the electric field is mostly very small ( $\sim$  a few  $\text{mV m}^{-1}$ ) (Mozer, 1972; Schutz *et al.*, 1973; Harper *et al.*, 1976). It is thus not considered to play an important role in determining the magnitude and sign of the ion convergence term,  $C$ , defined as  $-(dv_{iz} / dz)$ .

It is however often considered to influence the exact *height* of the convergence node (Rees *et al.*, 1976).

The vertical component of the neutral wind is also known to be small (*Manring et al.*, 1961; *Bedinger and Knafllich*, 1966), the neutral wind often considered to reside solely in the horizontal plane, concentric to the Earth's surface (this said, a vertical wind of a few  $\text{m s}^{-1}$  may have the same effect on vertical ion motion as a horizontal wind of a few 10's of  $\text{m s}^{-1}$  (*Wright and Fedor*, 1969) ). Neglecting these two terms and letting  $\omega_{Hi}^2 \ll v_{in}^2$ , as in the lower E-region, Equation 2.9 transforms into the simple zonal Windshear theory (*Whitehead*, 1961) as below:-

$$v_{iz} \approx w_E \cdot \frac{\omega_{Hi}}{v_{in}} \cdot \cos I \quad (2.10)$$

The east-west shear is more efficient than the north-south shear, sporadic-E being much more frequently observed between heights of 95 km to 120 km (cf. §2.1). The motion encapsulated within Equation 2.10 thus defines the familiar zonal wind mechanism for sporadic-E generation, applicable to the majority of layer observations. Note that Equation 2.10 also highlights the dependence of the ion convergence on the horizontal component of the magnetic field (*Heisler and Whitehead*, 1960), a notable factor in the worldwide occurrence statistics of sporadic-E (cf. §2.2.2).

Figure 2.4 depicts the Windshear theory as applicable to Equation 2.10, with the angle of the vertical ion drift being defined by the ratio of the Pedersen,  $k_1$ , and Hall,  $k_2$ , mobilities (*Rishbeth and Garriott*, 1969), i.e.:-

$$\tan \theta = \frac{k_2}{k_1} = \frac{\omega_{Hi}}{v_{in}} \quad (2.11)$$

### 2.3.5 High-Latitude Approximations of the General Windshear Theory

As the magnetic inclination angle decreases with increasing latitude, the Windshear mechanism becomes less efficient (cf. Equation 2.10). The electric field however may increase by well over an order of magnitude, with values of 50-100  $\text{mV m}^{-1}$  being common within the auroral zone (*Horowitz et al.*, 1978), particularly during active periods (*Steen et al.*, 1988). For a typical high latitude magnetic flux density of 50,000 nT (cf. *IGRF model*), and an electric field component of just 5  $\text{mV m}^{-1}$ , the electric field terms in Equations 2.9(a,b) are equivalent to neutral wind speeds of  $100\text{ms}^{-1}$ . Indeed, electric fields larger than  $\sim 3 \text{mV m}^{-1}$  have been noted to disrupt the Es-layering process (*Morton and Mathews*, 1993). The electric field will thus have a dominating influence within this zone.

neglecting the neutral wind, Equation 2.9 simplifies to (after Nygrén et al., 1984):

$$v = \frac{E \sin \alpha}{\mu_0 \cos \alpha} \left( \frac{1}{\cos \alpha} - \sin \alpha \right) \quad (2.17)$$

where  $\alpha$  is the angle between the electric field and magnetic north, in a plane perpendicular to the magnetic field.  $\alpha$  is positive from north to west. The vertical component of the ion velocity will then equal zero where  $\mu = \tan \alpha$ .

Figure 2.5b demonstrates the nature of the ion velocity profile for differing orientations of the electric field vector. The case where  $\alpha = 0$  is shown when the magnetic field vector points in the north-south quadrant. The angle  $\theta$  is the angle between the ion velocity vector and the neutral wind vector. The angle  $\theta$  will maximize in the upward direction for a southward electric field (Figure 2.4b), will minimize in the downward direction for a northward electric field (Figure 2.4a), and will be zero for a zero electric field (Figure 2.4c).

Observations and measurements of the electric field and ion velocity profile indicate a positive and negative ionospheric electric field. The electric field vector points in the post-sunset quadrant (Figure 2.4b). The ion velocity profile is shown in Figure 2.4b. The ion velocity vector is shown at an angle  $\theta$  to the neutral wind vector.

Figure 2.4a shows the ion velocity profile for a northward electric field. The ion velocity vector is shown at an angle  $\theta$  to the neutral wind vector. The ion velocity profile is shown in Figure 2.4a. The ion velocity vector is shown at an angle  $\theta$  to the neutral wind vector.

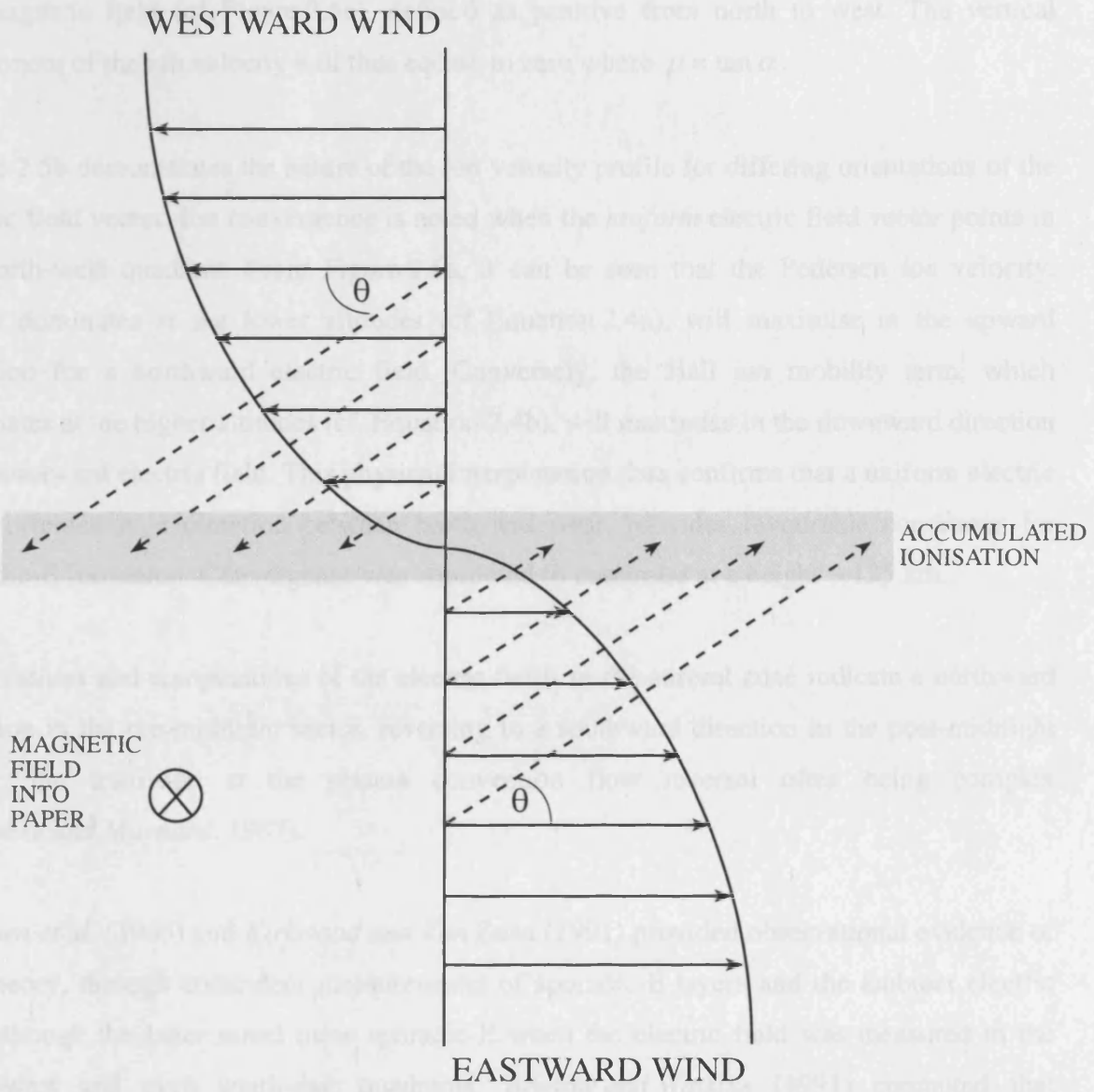


FIGURE 2.4 Schematic representation of the Windshear Theory, depicting a zonal windshear, Lorentz forces driving the ions at an angle  $\theta$  to the horizontal neutral wind.

Neglecting the neutral wind, Equation 2.9 transforms to (after *Nygrén et al.*, 1984a):-

$$v_{iz} = \frac{E/B}{1 + \rho^2} [\rho \cos \alpha - \sin \alpha] \cos I \quad (2.12)$$

where  $\alpha$  is the angle between the electric field and magnetic north, in a plane perpendicular to the magnetic field (cf. Figure 2.5a), defined as positive from north to west. The vertical component of the ion velocity will thus equate to zero where  $\rho = \tan \alpha$ .

Figure 2.5b demonstrates the nature of the ion velocity profile for differing orientations of the electric field vector. Ion convergence is noted when the *uniform* electric field vector points in the north-west quadrant. From Figure 2.5a, it can be seen that the Pedersen *ion* velocity, which dominates at the lower altitudes (cf. Equation 2.4a), will maximise in the upward direction for a northward electric field. Conversely, the Hall *ion* mobility term, which dominates at the higher altitudes (cf. Equation 2.4b), will maximise in the downward direction for a westward electric field. This physical interpretation thus confirms that a uniform electric field, oriented in a direction between north and west, provides favourable conditions for sporadic-E formation. Convergence was computed to maximise at a height  $\sim 125$  km.

Observations and computations of the electric fields in the auroral zone indicate a northward direction in the pre-midnight sector, reversing to a southward direction in the post-midnight sector, the transition at the plasma convection flow reversal often being complex (*Heppner and Maynard*, 1987).

*Turunen et al.* (1985) and *Kirkwood and Von Zahn* (1991) provided observational evidence of this theory, through coincident measurements of sporadic-E layers and the ambient electric field, though the latter noted more sporadic-E when the electric field was measured in the south-west and even south-east quadrants. *Bristow and Watkins* (1991) computed that sporadic-E could still form with the electric field within these quadrants, as the downward ion velocity would decrease with height. The subsequent height of formation ( $\sim 110$ - $115$  km) was also noted to be more favourable. Indeed, *Nygrén et al.* (1984a) also noted that sporadic-E *could* form as a result of suitably oriented *uniform* neutral winds (cf. also *Rowe and Gieraltowski*, (1974) ).



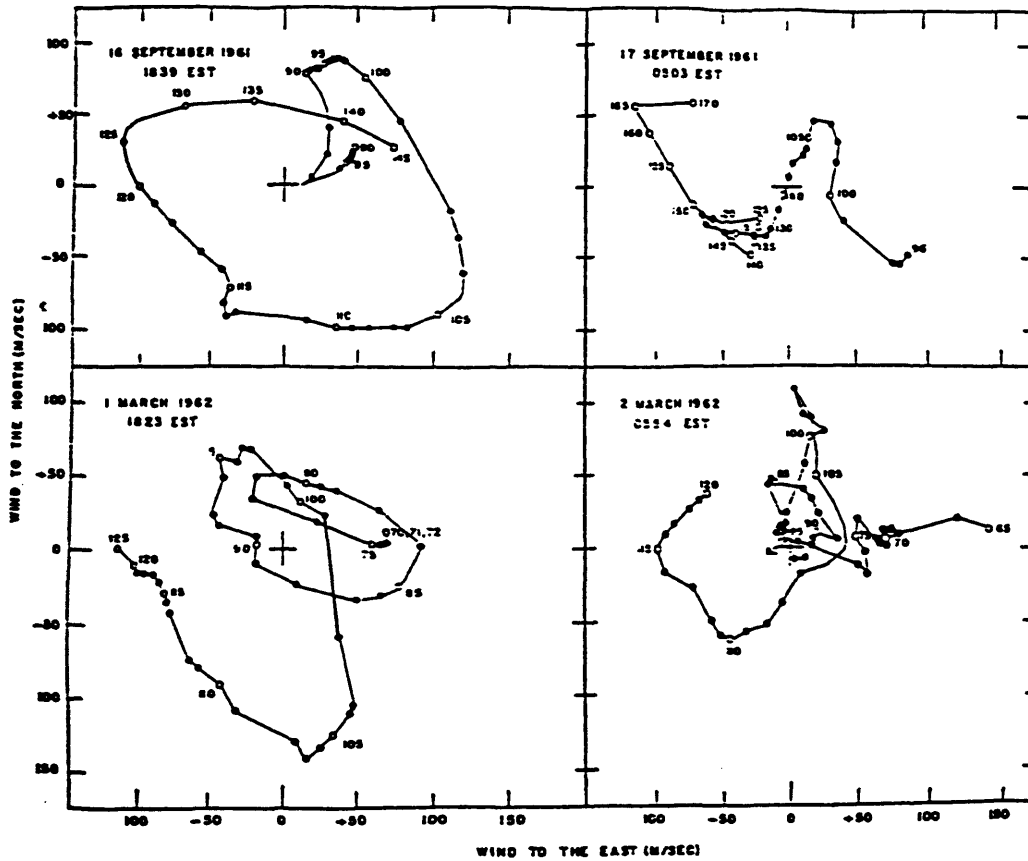
### 2.3.6 E-Region Tides and Gravity Waves

Implicit to the Windshear theory is the presence of suitably oriented shears in the neutral wind. Apart from the prevailing winds, the E-region is dominated by atmospheric solar tides and gravity waves (*Greenhow and Neufeld, 1961; Kochanski, 1964*). The solar tides have many temporal components with the semi-diurnal (*Fujitaka and Tohmatsu, 1973; Williams and Virdi, 1989*) and to a lesser extent, the diurnal (*Mathews et al., 1993*) components being dominant and being most strongly associated with sporadic-E. They have downward phase velocities of a few meters per second and vertical wavelengths of up to several tens of kilometers (*Viridi et al., 1986*).

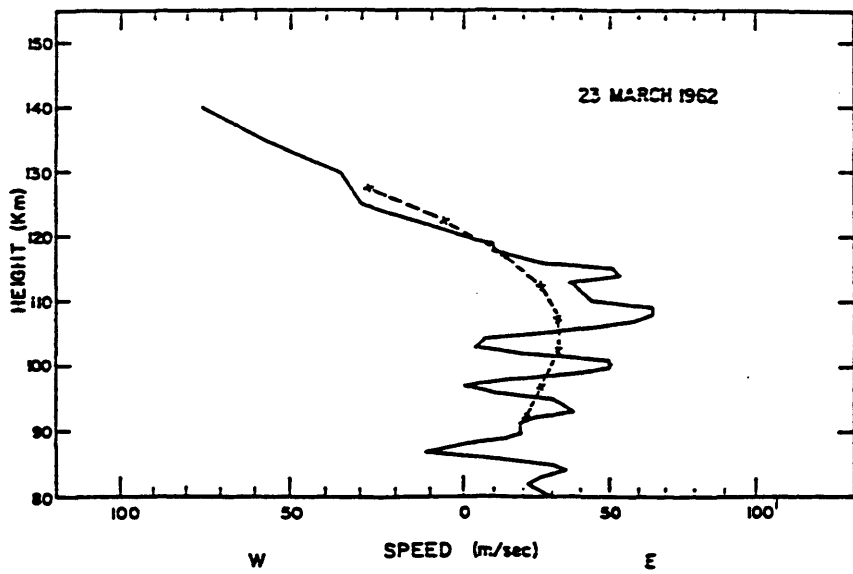
Atmospheric gravity waves (*Hines, 1960*) are similar in many respects to the atmospheric tides, but their fundamental period is shorter. The lower limit of the period is  $\sim 5$  minutes at E-region heights, it being determined by the Brunt-Väisälä period. Gravity wave sources are also more diverse. They may originate at low altitudes e.g. due to thunderstorms and jet streams, or at ionospheric heights, particularly in the upper E-region auroral zone, due to Lorentz forces or particle or joule heating. They can also be produced in the upper atmosphere by the break down of tidal motions. Their signature in the ionosphere is the Travelling Ionospheric Disturbance (TID) (*Williams et al., 1988*).

The tidal winds, to a first order approximation, have a spiral profile, the wind vector having a strong tendency to rotate in a clockwise direction with increasing height (*Bedinger et al., 1968*). However, the non-linear character of the wind system and the contribution from gravity waves and turbulence, results in more complex profiles, with sharp 'corners'. These 'corners' represent abrupt changes in direction of the horizontal wind gradient, and with typical wind speeds between  $50 \text{ m s}^{-1}$  and  $100 \text{ m s}^{-1}$ , the resulting wind shears are sufficiently large to promote ion convergence (*Kirkwood and von Zahn, 1993*). Further, the 'corners' are most frequently observed between heights of 85km and 120km and are noted to be stable and persistent features, with lifetimes of several hours. Typical 'hodographs' and windshears are depicted in Figures 2.6(a,b) (after *Bedinger et al., 1968*).

The stratified structure of the E-region wind system is thus ideally suited for sporadic-E generation, via the Windshear mechanism. Layers will tend to form at or near convergent nodes in the wind profile, and will then descend with the downward phase velocity at a rate of a few meters per second. Such layers are known as 'sequential' and were first described by *Axford (1961)* in his 'corkscrew' theory. At heights below  $\sim 95 \text{ km}$ , the ion-neutral collision



(a)



(b)

FIGURE 2.6a Typical mid-latitude hodographs, demonstrating the helical nature of the neutral wind altitude profile, though often with numerous sharp 'corners'. The heights are marked in kilometers, at either 5 km (open circles) or 1 km (dots) intervals.

FIGURE 2.6b Typical mid-latitude zonal wind structure (solid line), with the broken line representing a smoothing over 25 km. (both Figures from *Bedinger et al.*, 1968)

frequency is sufficiently large to impede further descent, the layers being effectively ‘dumped’ at this lower height (*Chimonas and Axford, 1968*).

The interference between tidal and gravity waves, and *between* gravity waves, can however significantly perturb this ideal, though often observed, sporadic-E motion. *Whitehead (1971)* has suggested that gravity waves may enhance or diminish a tidal convergence profile. Modulations in Es-layer intensity and/or height have been noted in the presence of gravity waves, (e.g. *van Eyken, 1982; Lanchester et al., 1989*). Layers have also been noted to *ascend* in height (e.g. *Turunen et al., 1988; Nygrén et al., 1990*), consistent with the vertical phase velocity of an upward propagating gravity wave. This upward motion may arise from the gravity wave’s low altitude generating source, or be the result of upward reflection, or ducting between two reflection levels (*Pittaway and Hines, 1965*). Further consequences of the interference between tidal and gravity waves, relating to the structure of Es-layers, are considered in §2.4.

### 2.3.7 Ion Composition of Sporadic-E Layers

The majority ion constituents in the E-region are  $\text{NO}^+$  and  $\text{O}_2^+$ . Recombination rates for these ion species are however  $\sim 10$  seconds, and a sporadic-E layer consisting primarily of these ions would be unstable. Sporadic-E has instead been shown to consist of metallic ions (e.g. *Kopp, 1997*) of meteoric origin, with lifetimes  $\sim 10^6$  seconds (*Istomin, 1963; Narcisi and Bailey, 1965*). Within the D- and E-regions they exist in densities between  $10^8$  and  $10^9 \text{ m}^{-3}$  (*Johannesen, 1974*), having been ionised by charge-exchange processes with the molecular ions, e.g. from *Brown (1973)*:-



where  $k_1$  and  $k_2$  are the reaction rates. The metallic ion densities are thus determined by molecular ion densities.

*Huuskonen et al. (1988)* noted relative abundances of  $\text{Fe}^+$  within sporadic-E layers, of between 30-80%, with  $\text{Mg}^+$  being less significant and  $\text{Na}^+$ ,  $\text{Al}^+$  and  $\text{Si}^+$  also being present in measurable quantities. *Smith and Miller (1980)* have actually noted that the concentration of

molecular ions *reduces* within Es-layers, as the general increase in ion densities promote their rapid dissociative recombination, as compared to the slow radiative recombination processes associated with the metallic ions. Loss rates in sporadic-E layers are thus dominated by dynamic, not chemical processes.

The existence of *neutral* metal layers coincident with sporadic-E layers, has been investigated by various authors, (e.g. *von Zahn and Hansen*, 1988; *Kirkwood and von Zahn*, 1993). It is clear that a correspondence exists but that idiosyncratic features of both types of layers influence the degree of the occurrence correlation.

### 2.3.8 Sporadic-E layers in the Equatorial and Polar Regions

For completeness, the generation of sporadic-E within the equatorial and polar regions will be briefly considered, the Windshear mechanism being unable to operate in either of these zones.

At the equator, the magnetic field has no vertical component and hence the space charge established by the ion displacement, can not be neutralised by the electrons. However, 'abnormal' E-layers are generated by the two-stream and gradient drift instabilities, in the presence of the equatorial electrojet (*Cohen*, 1967). These layers are termed 'equatorial' sporadic-E and are a regular and fairly predictable feature.

Sporadic-E in the polar regions is generated by electric fields redistributing the plasma, as in the high latitude mechanism described previously. Polar Es is heavily dependent on the IMF, being most prevalent when the z-component of the IMF is northward (*Besprozvannaya et al.*, 1980).

## 2.4 Sporadic-E Profiles and Internal Plasma Structure and Composition

### 2.4.1 Sporadic-E Profiles

With reference to the E-region Continuity Equation, defined by Equation 2.5, it is possible, with some simple assumptions, to derive a first order approximation for a sporadic-E density profile. Within an existing sporadic-E layer, the production and loss rates of the metallic ions will be negligible with respect to the transport and diffusion terms. Presuming a steady state,

with significant loss terms only operative in the vertical z-direction, Equation 2.5 may be simplified, giving:-

$$\frac{d}{dz}(N_i w_z) = \frac{d}{dz}\left(D \frac{dN_i}{dz}\right) \quad (2.13)$$

If a horizontally stratified wind profile is now assumed, varying linearly with height and having zero velocity at a height  $z_o$ , i.e.  $w_z = a(z_o - z)$ , then the layer profile is defined by:-

$$N_i = N_{io} \cdot \exp\left[-\frac{a(z_o - z)^2}{2D}\right] \quad (2.14)$$

where 'a' is a constant and  $N_{io}$  is the maximum ion density at the convergent node,  $z_o$ .

Equation 2.14 defines a diffusion-limited sporadic-E layer, whose ion profile is described by a simple gaussian shape. This is often a very good approximation and indeed approximations to the gaussian profile are often observed (*Smith and Miller, 1980*). However, from Figures 2.6(a,b), it is clear that the vertical variance of the wind profiles may be very non-linear and *Smith and Miller (1980)*, evaluated some diffusion limited density profiles for a range of theoretical wind shears, their results being depicted in Figure 2.7.

Further complexities may arise in the sporadic-E profiles due to their metallic ion composition. *Nygrén et al. (1984b)* computed double peaked profiles, relating separately to iron and magnesium constituents, the complex profiles observed by *Smith and Mechtly (1972)* being possible manifestations. Sequential sporadic-E layers are observed to get thinner with descent (e.g. *Smith, 1970; Lanchester et al., 1989*) as a consequence of the more efficient zonal, as opposed to meridional, wind shears at lower altitudes. It has also been noted that layers formed by *uniform* winds or electric fields will by definition not be symmetrical, the effective driving forces from above and below being different.

#### 2.4.2 Inhomogeneities Within Sporadic-E layers

The internal structure of sporadic-E is very complex and varied, even when solely considering the mid-latitude region. Inhomogeneities of differing scale sizes are common, and are nominally categorised as 'cloud' structure or 'irregularities'. Both give rise to *transparency*

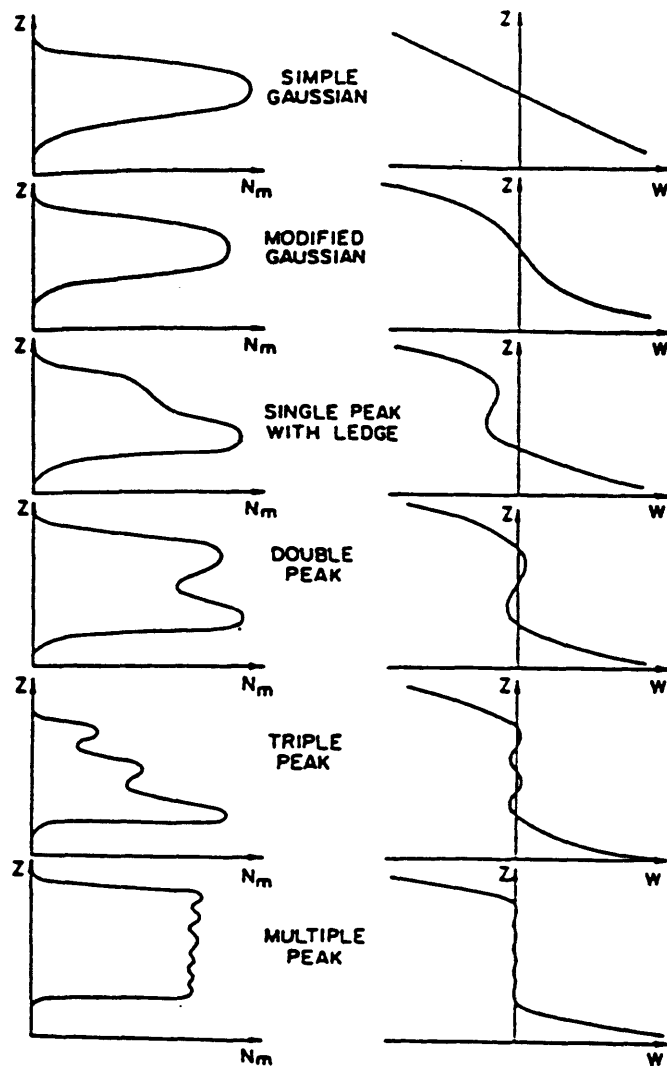


FIGURE 2.7 Modelled sporadic-E electron density profiles (left-hand plots), arising from a variety of neutral wind shears (right-hand plots) (after *Smith and Miller*, 1980). The simple gaussian profile, arising from a linear wind shear, is defined by Equation 2.14.

ranges, as discussed below. The literature is often very inconsistent when referring to an observed structure, particularly as there is no definitive distinction between the scale sizes of the two categories. If anything, the generation mechanism and reflection characteristics define the terminology adopted. Note that the two classifications of structure are *not* mutually exclusive and this can make signal strength interpretations difficult. For the purpose of this study, the term ‘irregularity’ is reserved for field aligned structure arising from plasma instabilities. Cloud structure refers to any other spatially varying plasma inhomogeneities.

#### 2.4.2.1 *The Cloud Model of Sporadic-E*

The ‘cloud model’ of sporadic-E defines an inhomogeneous plasma structure, characterised by scale sizes of ~ kilometers. It may be visualised as either a ‘corrugated’ plasma profile, or more usually as isolated ‘blobs’ of enhanced plasma density, embedded within the background Es-layer. This structure was first inferred from observations of *partial transparency*, the transmission of radio waves *through* sporadic-E layers between the blanketing frequency, *fbEs*, and the top frequency, *ftEs* (e.g. *Whitehead*, 1972). For a homogenous layer and at vertical incidence, *fbEs* and *ftEs* should define the critical frequencies of the ordinary and extraordinary modes, differing by half the gyrofrequency, ~ 0.8MHz (cf. §3.2.3). However, *ftEs* – *fbEs* is often noted to extend over several megahertz (e.g. *Reddy and Mukunda Rao*, 1968). The cloud model proposes that *fbEs* equates to the maximum *ambient* density within the Es-layer, while *ftEs* corresponds to the maximum plasma density of the cloud population.

The cloud population may in principle, extend over any range of densities and scale sizes. However, clouds contributing to partial transparency conditions must by definition, have scale sizes less than the first Fresnel zone. Scale sizes up to ~ 40 km have been noted (*From*, 1983; *From and Whitehead*, 1978) using HF radars, though the most compelling observations were made employing incoherent scatter techniques (*Miller and Smith*, 1975; *Miller and Smith*, 1978). Scale sizes of a few kilometers were noted, Figure 2.8 presenting some typical observations. The clouds will typically occupy only ~ 1% of the layer’s total area (*Rawer*, 1962) but this is generally sufficient for radio wave *refraction* to ensue.

Various cloud generation mechanisms have been suggested. *Chimonas* (1971) proposed a horizontal convergence of plasma, driven by an interference of gravity waves and tides (essentially a horizontally varying windshear). *Nygrén et al.* (1990) suggested a non-linear interaction between an F-region gravity wave and the semidiurnal tide, to account for a

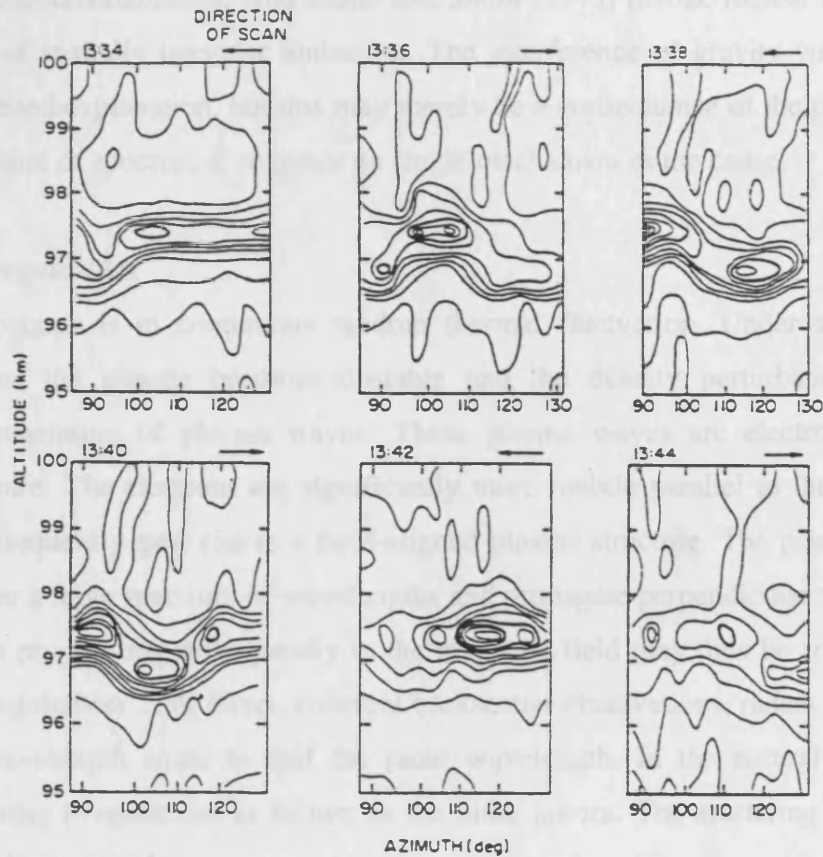


FIGURE 2.8 Incoherent scatter (Arecibo) observations of sporadic-E electron density 'cloud' structure. The plots represent a series of azimuthal scans, depicting electron density contours at intervals of  $1 \times 10^{10} \text{ m}^{-3}$  (contours at  $1 \times 10^{11} \text{ m}^{-3}$  having been darkened). The horizontal dimension of each region is approximately 20 km (after *Miller and Smith, 1978*).

spectrum of E-region gravity waves, and hence sporadic-E cloud scale sizes. Similarly, *Fritts et al.* (1988) discuss instabilities generated within large amplitude gravity waves.

Horizontal shears in the neutral wind have also been proposed by *From* (1984) and *From and Whitehead* (1978). *Mathews* (1998) suggests that the complex structure of sporadic-E may be explained by a corresponding E-field structure, arising from F/E-region coupling and associated instabilities. And *Miller and Smith* (1978) invoke meteor ablation as a possible source of spatially irregular ionisation. The interference of gravity waves is the most readily suggested explanation, but this may merely be a consequence of the observation techniques. The nature of sporadic-E suggests no single mechanism as the cause.

#### 2.4.2.2 Plasma Irregularities

The ionospheric plasma is in continuous random thermal fluctuation. Under appropriate ambient conditions, the plasma becomes unstable and the density perturbations grow, resulting in the generation of plasma waves. These plasma waves are electrostatic and longitudinal in nature. The electrons are significantly more mobile parallel to the magnetic field lines and consequently give rise to a field-aligned plasma structure. The plasma waves may be excited over a large spectrum of wavelengths and propagate perpendicular to the field lines. Radar waves propagating orthogonally to the magnetic field may thus be *scattered* by these so called ‘irregularities’. For direct, coherent backscatter observations, radars will detect irregularities of wavelength equal to half the radar wavelength. In the auroral zone, the signature of scattering irregularities is known as the radar aurora. The scattering process is considered more fully in §3.4.1.

Important plasma instability mechanisms are the ‘two-stream’ (e.g. *Kelly*, 1989) and ‘gradient-drift’ (e.g. *Ossakow and Chaturvedi*, 1979). The two-stream instability may be excited when the relative ion-electron flow exceeds the ion-acoustic velocity ( $\sim 300\text{--}400 \text{ m s}^{-1}$ ). Gradient-drift irregularities may be excited at much lower plasma drift velocities ( $V_D$ ). The conditions for generation require plasma drift perpendicular to a density gradient, given sufficient magnitudes of both.

From linear theory (*Farley*, 1963; *Buneman*, 1963), the dispersion relationship for the real angular frequency,  $\omega$ , of all the irregularity waves, is given by:-

$$\omega = \frac{\mathbf{k} \cdot \mathbf{V}_D}{(1 + \Psi)} \quad (2.15)$$

where  $\mathbf{k}$  is the irregularity wave vector and  $\Psi$  is a small perturbing term dependent on the ion and electron collision and gyro-frequencies and the magnetic aspect angle of  $\mathbf{k}$ . The growth rate of the instability,  $\gamma$ , is defined as:-

$$\gamma = \frac{\Psi}{1 + \Psi} \left( \frac{\omega^2 - k^2 C_s^2}{v_i} + \frac{\omega \Omega_e}{k L v_e} \right) \quad (2.16)$$

where  $C_s$  is the ion-acoustic speed and  $L (= N_e / (dN_e/dx))$  is the electron density gradient scale length along the ambient electric field, other terms having their usual definitions. The two terms in Equation 2.16 define the two-stream and gradient-drift instabilities respectively. At the larger wavelengths ( $\geq 10$  m), ‘primary’ (linear theory) gradient drift irregularities are more easily excited, the excitation wavelength being inversely proportional to the plasma drift velocity (*Farley, 1963*). At smaller wavelengths, two-stream irregularities dominate the linear instability mechanisms, though ‘secondary’ (non-linear) gradient-drift irregularities may ‘cascade’ from larger wavelength irregularities, through a non-linear mechanism (*Sudan et al., 1973*).

Gradient-drift instabilities are prevalent at all latitudes: Two-stream (Farley-Buneman) instabilities may be generated at mid-latitudes (*Haldoupis and Schlegel, 1993*) but are much more common at equatorial, auroral and sub-auroral latitudes, due to the potential for larger plasma drift velocities. In depth reviews of these two instability mechanisms are given in *Fejer and Kelly (1980)* and *Haldoupis (1989)*.

#### 2.4.2.3 Irregularities and Sporadic-E

At mid-latitudes, sporadic-E layers may possess density gradients of sufficient magnitudes to excite the generation of gradient-drift irregularities within the layer itself. They will develop either on the lower or upper side of the layer depending on the orientation of the vertical component of the ambient electric field, with respect to the vertical density gradient (*Ecklund et al., 1981*). Orientations may be more favourable if the layer structure is distorted by gravity waves (*Woodman et al., 1991*). The greater ionic mass within sporadic-E layers, due to the prevalence of metallic ions, also reduces critical drift velocities required to excite gradient-drift irregularities, increasing further the potential for excitation (*Tanaka and Venkateswaren, 1982a*). This reduction in critical drift velocities may account for the generation of Type III irregularities, they being interpreted as two-stream instabilities (Type I) excited at drift velocities below the ion-acoustic velocity (*Haldoupis et al., 1992*).

Scale sizes have been observed or interpreted to range from ~ meters to ~ kilometers (e.g. *Haldoupis and Schlegel*, 1993; *Keys and Andrews*, 1984; *Riggin et al.*, 1986; *Tanaka and Venkateswaren*, 1982a,b,c), though direct observations are pre-determined by the radar wavelength. As such, scale sizes between 3 and 6 meters dominate observations. Returns from irregularity scattering will tend to be considerably weaker (~ 10's dB) than those arising from refraction alone (*Miya and Sasaki*, 1966; *Booker*, 1959), with a scattering cross-section proportional to approximately the third power of the irregularity wavelength (*Farley et al.*, 1981; *Oksman et al.*, 1979). Note then that the scattered signal strength is independent of the intrinsic plasma density, and that scattered returns from sporadic-E layers, are highly aspect angle sensitive. Scattered power reduces by ~ 10 dB per degree deviation from orthogonality (*Fejer and Kelly*, 1980).

A further characteristic of irregularities and sporadic-E, is ionogram *range spreading*, the diffuse appearance of sporadic-E with respect to range or height. This is most notable within so called auroral-Es (Es-a), which like equatorial-Es, is solely an irregularity structure, both gradient-drift and two-stream, and is formed independent of any windshear or electric field compression mechanisms (*Nath et al.*, 1980; *Turunen*, 1977). This type of sporadic-E is closely associated with substorm activity and low energy (~ 1 – 10 keV) electron precipitation (*Besprozvannaya et al.*, 1980; *Turunen*, 1977; *Weber et al.*, 1977).

## 2.5 Summary

Within the mid-latitude E-region, sporadic-E generation is dominated by the windshear mechanism. Conditions for generation are more favourable below altitudes ~ 125 km, where zonal windshears operate efficiently. Above ~ 125 km, meridional winds are more important. Electric fields also influence the formation of Es-layers and are instrumental at high latitudes, where the fields are much stronger and the windshear mechanism is inefficient. Few sporadic-E layers however, form into homogenous plasma sheets. Partial transparency is indicative of a complex plasma structure, consisting of enhanced plasma clouds and field aligned plasma irregularities. Both are influential in defining reflection and scatter characteristics and hence effective propagation circuits.

# Chapter 3

## Experimental and Analysis Techniques

### 3.1 Introduction

This thesis is primarily engaged in analysing and interpreting oblique ionosonde data, derived from High Frequency ‘Chirp’ Sounders. To further understanding of the received data, the basic concepts of High Frequency (HF) propagation are discussed below, with particular emphasis being given to the interpretation and understanding of ionograms. A description of ionosondes then follows, together with a full account of the ‘Chirp’ sounder. Where applicable, the oblique ionograms were scaled with respect to the extensive set of scaling rules and procedures devised and written for *vertical* ionograms (cf. *Piggott and Rawer, 1961*). Adopted procedures, together with more idiosyncratic interpretations are described below.

In addition to the oblique ionosonde radars, data was utilised from the Wick receiver of SABRE (Sweden and Britain Radar-aurora Experiment) and from the SAMNET (Sub-Auroral Magnetometer Network) facility. SABRE is a VHF backscatter radar, operating at ~ 150 MHz and sensitive to E-region plasma instability waves. In Chapter 7, this data is employed to study coincident observations of sporadic-E layers and plasma irregularities. Data from SAMNET is utilised throughout this thesis as a guide to local prevailing geomagnetic activity. Descriptions of both are presented below.

### 3.2 Propagation Theory

#### 3.2.1 In the beginning . . .

The existence of a conducting layer in the Earth’s atmosphere was first speculated upon by C. F. Gauss in 1839, to explain the small, daily variations in the Earth’s magnetic field. But serious consideration of such a feature only began in 1901, after, it is believed, G. Marconi succeeded in transmitting a short wave radio signal from Cornwall, England, to Newfoundland, Canada. Such a propagation distance could not be explained by known diffraction effects, and independently, both *Heaviside (1902)* and *Kennelly (1902)* suggested

that free electrons in the atmosphere were responsible for the reflection of the radio waves. Confirmation came from experiments conducted by *Appleton and Barnett* (1925a,b) and *Breit and Tuve* (1925,1926), leading to estimates of the height of such layers. Further studies on the effects of the Earth's magnetic field, upon propagating electromagnetic waves in ionised gases (*Appleton*, 1925; *Nichols and Schelleng*, 1925), finally led to the development of the magneto-ionic theory (*Appleton and Builder* 1932) and the now commonly called Appleton formula.

### 3.2.2 The Appleton-formula

The electric field,  $E$ , of an electromagnetic plane wave, in a homogenous medium, propagates according to the ubiquitous Wave Equation, described by:-

$$\nabla^2 E = \frac{1}{v_p^2} \frac{\partial^2 E}{\partial t^2} \quad (3.1)$$

The phase velocity,  $v_p$ , is related to the refractive index,  $n$ , of the medium through which it is propagating, by:-

$$v_p = \frac{c}{n} \quad (3.2)$$

where  $c$  is the free space velocity. The refractive index is thus fundamental to the wave's propagating characteristics.

The propagation of a radio wave through an ionised medium will modify the electron and ion concentrations, the electric field causing the space charge to oscillate with the frequency of the wave. But the displacement of the ions, relative to the electrons, is negligible, it being directly proportional to the relative masses of the particles. The effective particles in the plasma are thus the electrons.

In a homogeneously ionised medium, with an ambient magnetic flux density,  $B$ , an electron-neutral collision frequency,  $\nu_{e,n}$ , the refractive index of a plane wave, propagating at an angle  $\phi$  to the uniform magnetic field, is defined by the Appleton formula:-

$$n^2 = (\mu - i\chi)^2 = 1 - \frac{X}{1 - iZ - \frac{Y_T^2}{2(1 - X - iZ)} \pm \left[ \frac{Y_T^4}{4(1 - X - iZ)^2} + Y_L^2 \right]^{1/2}} \quad (3.3a)$$

where 'n' is the complex refractive index, 'μ' and 'χ' its real and imaginary parts,  $Y_T$  and  $Y_L$  the transverse ( $Y \sin \phi$ ) and longitudinal ( $Y \cos \phi$ ) components of  $Y$ , with respect to the magnetic field, and:-

$$X = \frac{\omega_p^2}{\omega^2}; \quad Y = \frac{\omega_H}{\omega}; \quad Z = \frac{\nu_{e,n}}{\omega} \quad (3.3b,c,d)$$

where:-

$\omega = 2\pi f$  = the angular propagating radio frequency

$\omega_p = 2\pi f_p$  = angular plasma frequency (cf. Equation 1.10)

$\omega_H = 2\pi f_H = \frac{eB}{m_e}$  = angular electron gyrofrequency

$m_e$  = the electron rest mass

The refractive index is thus complex in nature, resulting from the attenuation of the wave via electron-neutral collisions (cf. the 'Z' term). It is also noted to be birefractive due to the dominating effect of the (Earth's) magnetic field (cf. the 'Y' term). In an anisotropic medium, two independent modes of propagation thus exist (cf. the  $\pm$  sign), termed the 'ordinary' (+ve sign) and 'extraordinary' (-ve sign) characteristic modes.

Both the strength and the orientation of the geomagnetic field, with respect to the propagating wave normal, determine the differing polarisations of the ordinary and extraordinary modes (termed O-mode and X-mode respectively). The two modes propagate along physically different paths, varying by up to several tens of kilometers in the F-region. They also exhibit different absorption characteristics, the X-mode being more readily absorbed.

### 3.2.3 Approximate Solutions of the Appleton Formula

For radio waves pertinent to the HF band, and collision frequency values,  $\nu_{e,n}$ , typical to the E- and F- ionospheric regions (Schunk and Nagy, 1980), the 'Z' term is very small and may be neglected. If the magnetic field is also considered to be negligible i.e.  $Y \ll 1$  then the refractive index reduces to a real expression:-

$$\mu^2 = 1 - X = 1 - \left( \frac{f_p}{f} \right)^2 \quad (3.4)$$

For a wave with an angle of incidence upon the ionosphere of  $\theta_o$ , Snell's law defines the degree of refraction,  $\theta$ , with respect to the changing refractive index,  $\mu$ , by the relationship:-

$$\mu \sin \theta = \mu_o \sin \theta_o \quad (3.5)$$

For vertical incidence ( $\theta_o = 0^\circ$ ), reflection occurs when  $\mu = 0$ , i.e. when  $X = 1$ . For a propagating wave of frequency  $f$ , the refractive index,  $\mu$ , thus reduces with increasing plasma frequency, from a value of  $\mu_o = 1$ , in free space, to a value of zero at reflection, when the propagating frequency,  $f$ , is equal to the plasma frequency,  $f_p$ . This is the ordinary mode. Clearly, if  $f$  exceeds the maximum plasma frequency, the propagating wave penetrates the ionosphere.

For oblique incidence, reflection occurs when  $\theta = \pi/2$ , i.e.:-

$$\mu = \sin \theta_o \quad (3.6)$$

It follows that a relationship exists between a vertically and obliquely propagating frequency,  $f_v$  and  $f_o$ , which both reflect from the same real height (and plasma frequency). Combining Equations 3.4 and 3.6, where  $f_p = f_v$ , gives:-

$$f_o = k.f_v.\sec \theta_o \quad (3.7)$$

where, for sporadic-E reflection at a height  $h$ ,  $\theta_o$  is defined by:-

$$\tan \theta_o = \frac{\sin(\varphi/2)}{1 + h/R_E - \cos(\varphi/2)} \quad (3.8)$$

for a curved Earth of radius  $R_E$  and an angle  $\varphi$  subtended by the path at the centre of the Earth. This relationship is referred to as the Secant Law and is fundamental to studies employing oblique propagation techniques.  $\sec \theta_o$  is termed the 'secant factor'.  $k$  is a factor to correct for the curvature of the ionosphere, due to modifications in Snell's law. It varies between 1.0 and

1.2, increasing with ground range (Davies, 1990). For the sporadic-E propagation circuits utilised in this thesis, its value is taken as 1.0 (Davies, 1990). It is clear from Equation 3.7 that the ionosphere supports the propagation of higher oblique frequencies than vertically incident frequencies, and that the difference increases with the secant factor i.e. with reduced elevation angles. The Secant Law is discussed later, with respect to scaled ionogram data.

If the magnetic field term,  $Y$ , in Equation 3.3, is not neglected, and vertical propagation is again considered, solutions to the Appleton Formula at reflection are  $X = 1$  and  $X = 1 \pm Y$ . The latter solution defines the (two) extraordinary waves. The  $X = 1 + Y$  solution defines what is often denoted the  $Z$ -mode and is rarely observed when the propagating frequency exceeds the gyrofrequency. Combining solutions  $X = 1$  and  $X = 1 - Y$ , defines a relationship between the  $O$ -mode and  $X$ -mode at reflection, i.e.:-

$$f_{O-MODE} = \left( f_x^2 - f_x f_H \right)^{1/2} \approx f_x - \frac{1}{2} f_H \quad (3.9)$$

where  $f_x$  is the extraordinary propagating frequency. Thus, at a given propagating frequency, the  $O$ -mode reflects at a greater height than the  $X$ -mode, but for a given height, the  $O$ -mode reflects at a lower frequency than the  $X$ -mode, the difference being equivalent to half the gyrofrequency.

### 3.2.4 Phase and Group Velocity

Assuming the wave normal to be in the  $z$  direction, a solution of Equation 3.1 is:-

$$E = \exp\{i(\omega t - kz)\} \quad (3.10)$$

where the phase velocity,  $v_p$ , is defined as  $\omega/k$ , in the direction of the wave normal. In reality, it is impossible to generate a pure, single frequency, investigative probing of the ionosphere being achieved through the generation and transmission of pulses. From Fourier analysis, the pulse will thus be defined by a spectrum of characteristic frequencies. And as the ionosphere is a dispersive medium, that is, one in which the component frequencies of the pulse all have individual phase speeds, the concept of a wave packet arises.

The wave packet is analogous to the *envelope* of two interfering waves, as depicted in Figure 3.1a, and characterises the direction and velocity of the energy flow of the pulse. The

velocity is termed the group velocity or wave packet velocity, and for a homogeneous, isotropic, collisionless medium, is defined, in the direction of the wave normal, as:-

$$v_g = \frac{d\omega}{dk} \quad (3.11)$$

By analyzing the phase refractive index (cf. Equation 3.2), the group refractive index,  $n_g$ , is defined, in the direction of the wave normal, as:-

$$n_g = n + \omega \frac{dn}{d\omega} \quad (3.12)$$

the latter is termed the group refractive index, and is defined in Equation 3.4. In the general case of an anisotropic, uniaxial crystal, the situation is depicted in Figure 3.1b where the wave normal,  $\underline{k}$ , is not coincident with the direction of the ray,  $\underline{S}$ , the direction of energy flow, the two vectors subtending an angle  $\alpha$ .

This divergence of the vectors arises from the anisotropic medium distorting the operation of the wave front (cf. Figure 3.1c). The anisotropy results in the refraction of the ray. The phase and group velocities are aligned with the wave normal  $\underline{k}$ , and the wave packet velocity,  $\underline{u}$ , with the ray direction,  $\underline{S}$ .

It follows from the above that the ray path,  $\underline{S}$ , is the direction of energy flow (Figure 3.1d) that:-

$$\underline{S} = \frac{d\underline{r}}{dt} = \frac{d}{dt} \left( \frac{d\underline{r}}{ds} \right) ds = \frac{d\underline{r}}{ds} \frac{ds}{dt} = \underline{u} \quad (3.13)$$

Noncircular wave fronts are formed constantly varying over a given propagation circuit. The exact nature of the surface depending on the characteristics of the medium.

### 3.2.3 Phase and Group Paths

Information systems and receive radio wave pulses via ionospheric reflection, is a means to determine the propagation time (cf. 3.1.3). To this end, only the time of flight of the pulse,  $T$ , is of interest.

**FIGURES 3.1(a,d)** Concepts of phase, group and packet velocities,  $v_p$ ,  $v_g$  and  $u$  respectively, defined in the direction of the wave normal  $\underline{k}$ , and inclined at an angle  $\alpha$  to the ray vector,  $\underline{S}$ , in an anisotropic, inhomogeneous medium. Figure 3.1a demonstrates the relationship between the group velocity of the wave envelope, and the phase velocity of the waveform within the envelope. Figure 3.1b depicts the varying divergence of the normal to the phase front,  $\underline{k}$ , and the wave packet direction,  $\underline{S}$ , arising from a distortion of the wave front (Figure 3.1c), due to the anisotropic, inhomogeneous medium, the relationship being defined by Figure 3.1d and Equation 3.13 (after Davies, 1990).

$\underline{S}$ , and the group refractive index, in the direction of the wave normal,  $\underline{k}$ , as:-

velocity is termed the group velocity or wave packet velocity, and for a homogenous, isotropic, collisionless medium, is defined, in the direction of the wave normal, as :-

$$v_g = \frac{d\omega}{dk} \quad (3.11)$$

By analogy to the phase refractive index (cf. Equation 3.2), the group refractive index,  $n'$ , is defined, also in the direction of the wave normal, as:-

$$\mu' = \frac{c}{v_g} = c \frac{dk}{d\omega} = \frac{d(\omega n)}{d\omega} = \frac{1}{\mu} \quad (3.12)$$

the latter part of the derivation being based on the value of ' $\mu$ ' defined in Equation 3.4. In the general case of an inhomogeneous, anisotropic medium, the situation as depicted in Figure 3.1b exists, i.e. the wave normal, as defined by the vector  $\mathbf{k}$ , is not coincident with the direction of the ray,  $S$ , (the direction of energy flow), the two vectors subtending an angle ' $\alpha$ '. This divergence of the vectors arises from the anisotropic medium distorting the orientation of the wave front (cf. Figure 3.1c). The inhomogeneity results in the refraction of the ray. The phase and group velocities are aligned with the wave normal,  $\mathbf{k}$ , and the wave packet velocity,  $\mathbf{u}$ , with the ray direction i.e. tangential to the ray path. It thus follows from Figure 3.1d that :-

$$u = v_g \cdot \sec \alpha = \frac{c}{\mu'} \cdot \sec \alpha \quad (3.13)$$

The phase and group velocities are hence constantly varying over a given propagation circuit, the exact nature of this variance depending on the characteristics of the medium.

### 3.2.5 Phase and Group Paths

Ionosondes transmit and receive radio wave pulses via ionospheric reflection, as a means to determine ionospheric densities (cf. §3.3). To this end, only the time of flight of the pulse,  $T_g$  (or *group delay*), is measured directly and it is this that defines the concept of a phase path,  $P$ , and in particular a group path,  $P'$ , they being defined by assuming a constant propagation velocity, equal to that in free space. Phase and group velocities can only be inferred thereafter. The group path is thus defined with respect to the group velocity, in the direction of the ray,  $S$ , and the group refractive index, in the direction of the wave normal,  $\mathbf{k}$ , as:-

$$P' = cT_g = c \int_S^E \frac{ds}{u} = \int_S^E \mu' \cos \alpha ds \quad (3.14)$$

where 'S' and 'E' are defined as in Figure 3.1b.

Given the usual approximations of an isotropic, collisionless medium, and a flat Earth and ionosphere, Breit and Tuve's theorem (*Breit and Tuve, 1925,1926*) equates the group path to the length of the '*equivalent triangle*'. For relatively short propagation paths, for example the Bodø/Wick oblique path (cf. Chapter 4), the curved Earth approximates to a flat Earth, and the aforementioned theorem is thus applicable. Figure 3.2 depicts the *equivalent triangle*, TAR, for a curved Earth of radius  $R_E$ , where the Ground Path Length,  $D$ , subtends an angle  $\varphi$  at the centre of the Earth. The angle of incidence of the ray on the ionosphere,  $\theta_o$ , is defined by Equation 3.8 in terms of  $\varphi$ , presuming sporadic-E reflection i.e. negligible ray refraction. Breit and Tuve's theorem is important for oblique ionogram scaling, as the recorded *group delay* can be equated to a *virtual height* of reflection,  $h'$  (cf. Figure 3.2), which for sporadic-E reflection, approximates to the 'Real' height of reflection,  $h_r$ , the shaded area in Figure 3.2 being negligible.

It should be noted that neither the group nor phase paths represent 'Real' paths, both being defined assuming a constant free space velocity, allowing for a simple translation of ionosonde signals. The 'Real' path,  $S$ , is defined with respect to Figure 3.1b as:-

$$S = \int_S^E ds \quad (3.15)$$

### 3.2.6 Practical Oblique Propagation

Figure 3.3a is a simple representation of the different ionospheric paths that are permitted for a given single frequency, transmitted over a range of elevation angles. The height of reflection and propagation distance are noted to vary in a non-linear manner, a feature of which is the 'skip zone', where no transmitted signals may be received. At a critical elevation angle, pertinent to the propagation frequency and the ionospheric conditions (i.e. the plasma frequency profile), penetration of the ionosphere takes place.

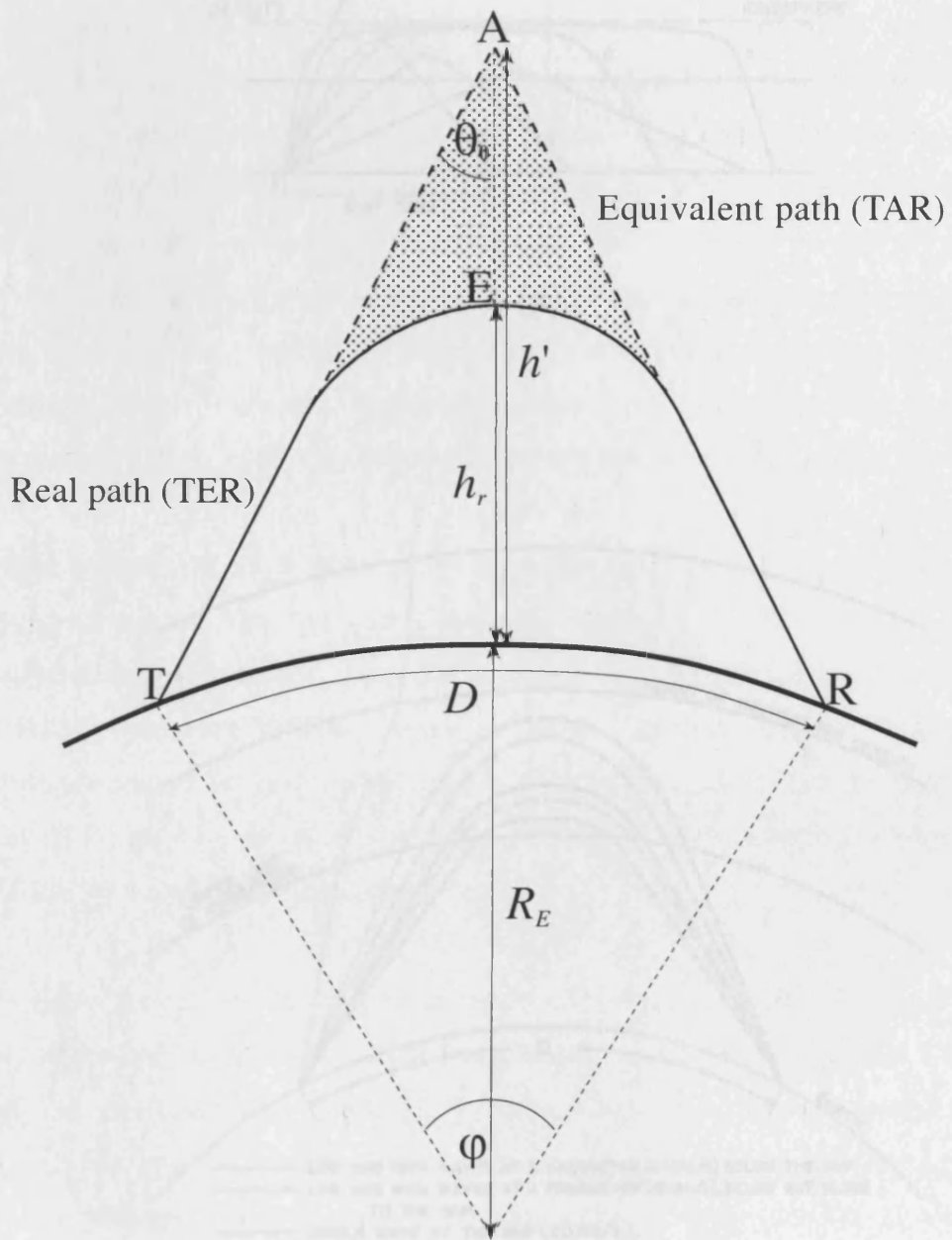
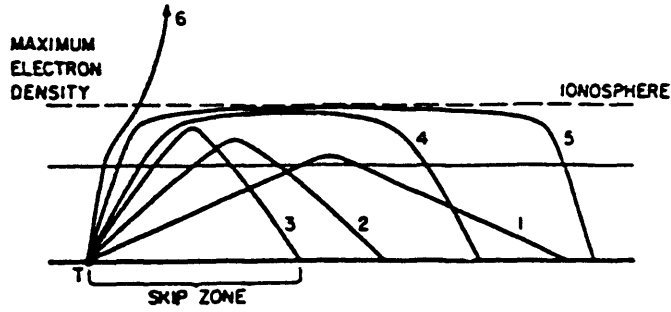
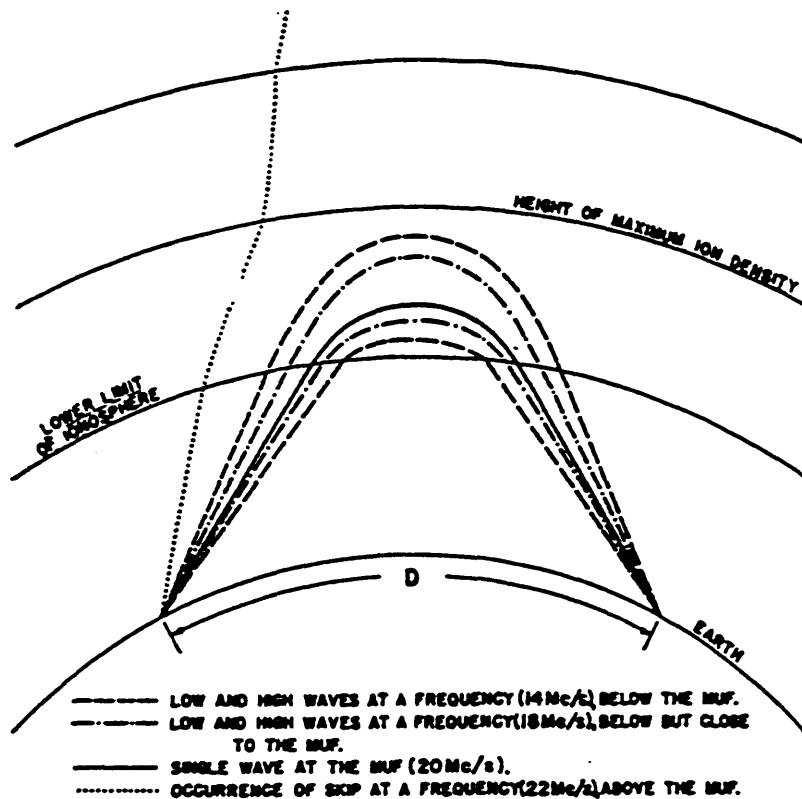


FIGURE 3.2 Schematic representation of the 'Real' (TER) and 'Equivalent' (TAR) paths of propagation, together with the associated true and virtual (group) heights,  $h_r$  and  $h'$  respectively, for a ground propagation distance,  $D$ . The relationship between  $\theta_0$  and  $\phi$  is defined by Equation 3.8, presuming that the shaded area is negligible, a good approximation for sporadic-E reflection.



(a)



(b)

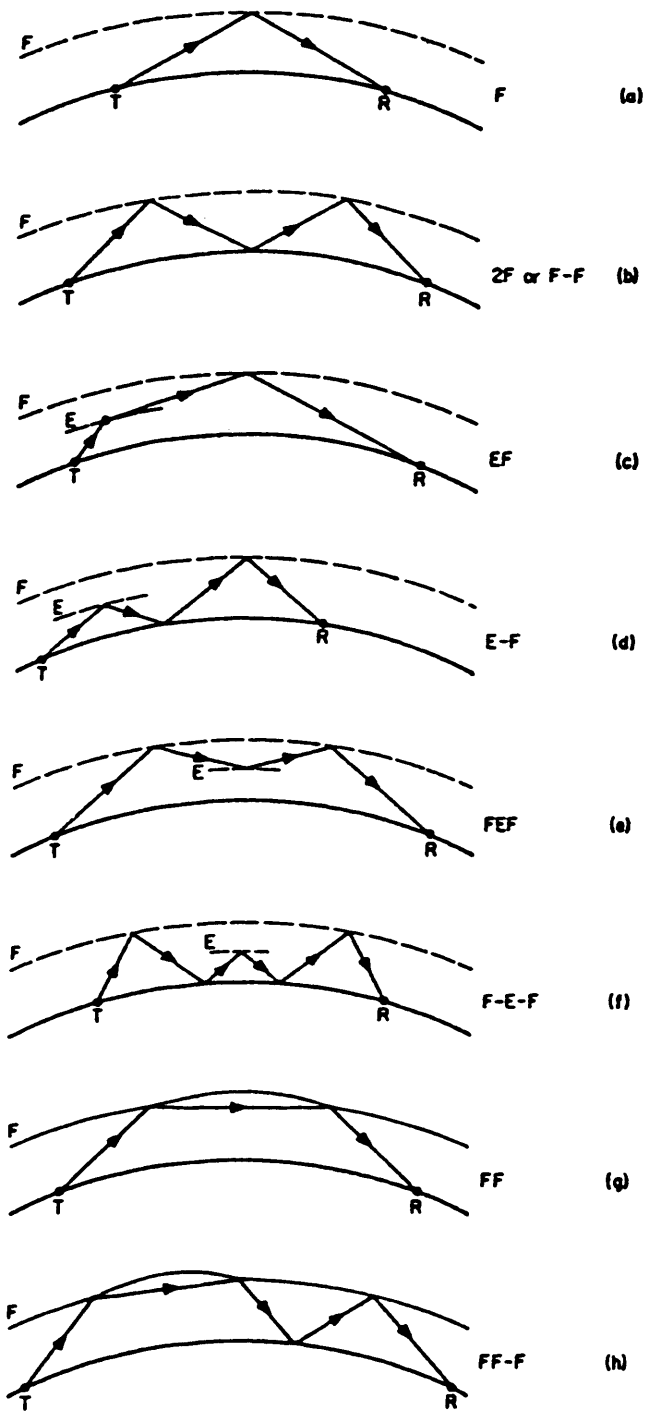
FIGURES 3.3(a,b) Examination of the ray paths associated with oblique High Frequency, ionospheric propagation. Figure 3.3a depicts the propagation path of a fixed frequency ray at increasing elevation angles. Note the coincident reception of rays 1 (low-angle) and 5 (high-angle), and the skip zone arising from ionospheric penetration (ray 6) above a critical elevation angle. Figure 3.3b depicts high- (Pedersen) and low-angle rays, for increasing frequencies up to the junction frequency (after Davies, 1965).

In Figure 3.3a, it can also be seen that a transmitted frequency may be received via two distinct ray paths. This is further examined in Figure 3.3b. For a given frequency, propagating via a single ionospheric layer, e.g. the E-layer, the two distinct ray paths are a characteristic feature of oblique ionograms. Figure 3.3b demonstrates the situation for several different frequencies. The two ray paths are termed the *low-* and *high-angle* (or Pedersen) rays. The difference in reflection heights reduces as the propagating frequency increases, until the '*junction frequency*' is reached, the maximum oblique frequency that may be reflected from the layer, by ionospheric refraction alone. At the junction frequency, the two ray paths merge into one and focussing takes place so as to enhance the signal strength of the received ray. It should be noted that the junction frequency does not reflect from the height of maximum plasma density. The 'Maximum Usable Frequency' (MUF) is defined as the maximum junction frequency for a given ionosphere, and usually equals that for the F- or F2-layer.

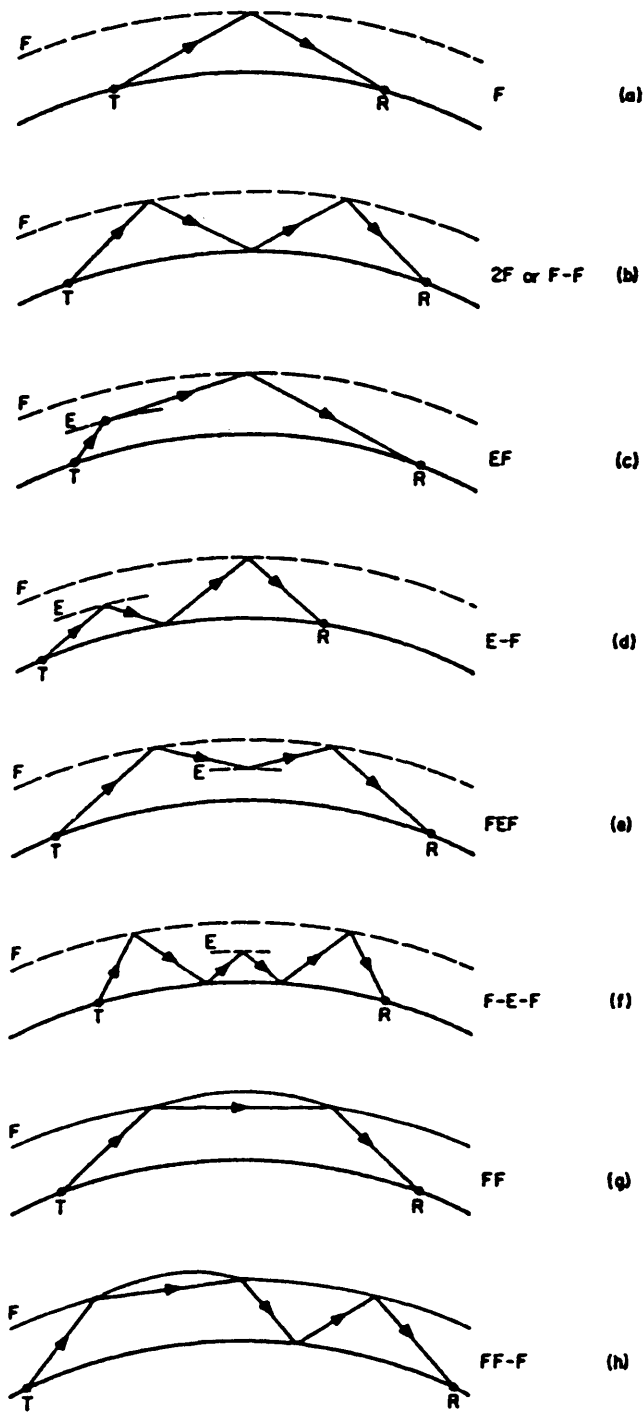
Two further useful terms, are widely used to define the snapshot of the ionosphere as captured by an oblique ionogram. The 'Maximum Observed Frequency' (MOF) is self explanatory and may be independent of propagation path or reflection characteristics. It is often equivalent to the maximum frequency reflected from an intense sporadic-E layer, particularly for propagation distances beyond ~1000km (cf. the Secant Law). The 'Lowest Observed Frequency' (LOF) is the converse of the MOF, and may be affected by ionospheric absorption (cf. §3.2.7) or by antenna gain parameters.

Figures 3.4(a,h) further demonstrate the diversity of oblique propagation paths. Propagation paths are not confined to reflections from a single ionospheric point (cf. Figure 3.4a) but may propagate in a multi-hop mode (e.g. Figure 3.4b), via other ionospheric layers (e.g. Figure 3.4c), or by a combination of both (e.g. Figures 3.4d-h). The propagation path may also be influenced by scattering from field-aligned irregularities (cf. §3.4.1), or other plasma perturbations.

Figures 3.4(a,h) demonstrate the constructive and destructive effects of sporadic-E layers on propagation circuits. Multi-traverses of the absorbing D-region may be desirably reduced via an M-mode propagation path (e.g. Figure 3.4e), or conversely, the receiver may be skipped over by the very same mode. Further, the sporadic-E layer may 'screen' the propagating ray from a more optimal F-region propagation mode. The ability to predict the occurrence and intensity of sporadic-E layers is thus essential for sustainable communication links.



FIGURES 3.4(a,h) Multi-hop and multi-mode oblique propagation paths, via sporadic-E layers and the F-region. The presence of sporadic-E may enable or disable the desired propagation circuit (after *Davies, 1990*).



FIGURES 3.4(a,h) Multi-hop and multi-mode oblique propagation paths, via sporadic-E layers and the F-region. The presence of sporadic-E may enable or disable the desired propagation circuit (after *Davies, 1990*).

### 3.2.7 Attenuation of Radio Waves

It can be demonstrated from the Appleton Formula (Equation 3.3) that, for no magnetic field ( $Y=0$ ), but significant collisions, the attenuation of a wave,  $L$  (dB), due to electron-neutral collisions, is given by:-

$$L = 8.86 \int K ds \quad (3.16)$$

i.e. the integration of  $K$  ( $\text{Np m}^{-1}$ ) along the propagation path, where  $K$  is the absorption coefficient, defined as:-

$$K = \frac{e^2}{2\epsilon_0 c m_e} \frac{1}{\mu} \frac{N_e \nu}{\omega^2 + \nu^2} \quad (3.17)$$

This equation defines two distinct manifestations of absorption, namely '*deviative*' and '*non-deviative*'.

#### *Non-Deviative Absorption*

In the D- and lower E-region, while the electron density,  $N_e$ , is of low enough magnitude for  $\mu \approx 1$ , the product of the electron density and electron-neutral collision frequency,  $N_e \nu_{e,n}$ , is observed to maximise. The absorption coefficient,  $K$ , thus also maximises. The resulting absorption is termed '*non-deviative*' and for  $\omega^2 \gg \nu^2$ , Equation 3.17 reduces to:-

$$K \approx \frac{e^2}{8\pi^2 \epsilon_0 c m_e} \frac{N_e \nu}{f^2} \quad (3.18)$$

The attenuation of a radio wave propagating through the said regions is thus proportional to the electron density and inversely proportional to the square of the propagating frequency.

#### *Deviative Absorption*

In §3.2.3 it was determined that, for vertical propagation, the refractive index,  $\mu$ , tends to zero as the propagating frequency approaches reflection. The absorption coefficient defined in Equation 3.17 will thus become very large (Appleton and Piggott, 1954). This is termed '*deviative*' absorption due to refraction of the ray at reflection, and arises from an enhanced radio wave electric field, resulting in an increased interaction between the oscillating electrons and the neutrals.

The higher frequencies at which oblique modes operate, results in much reduced non-deviative absorption, allowing for signal returns from, for example, less intense sporadic-E layers, than would be possible at vertical incidence. Further, deviative absorption is much less significant for oblique propagation. From Equation 3.6, the value of  $\mu$  at reflection depends on the degree of obliqueness and for paths studied in this thesis,  $\mu \sim 1$  at reflection.

### 3.3 Ionosondes and Ionograms

An ionosonde is a sweep-frequency pulsed radar, providing a relatively cheap and reliable means to probe the ionosphere (*Villard, 1976*). They operate in the HF band, and hence receive signals reflected and scattered from a range of ionospheric layers and features (cf. §1.3.2). Two basic types are employed, namely ‘vertical’ and ‘oblique’, their descriptions being indicative of the initial angle of propagation of the transmitted pulse, relative to the Earth’s surface.

Ionosondes are most often used for either direct propagation mode prediction, for systematic morphological studies of ionospheric features, or in conjunction with other probing techniques e.g. incoherent and coherent radars, as a means of calibration. The frequency sweep time may range from a few seconds to several minutes, depending on the ionosonde type and/or the information required: the mode of operation is often a compromise between temporal and frequency resolution. Many ionosondes (mainly the vertical type) are deployed permanently, worldwide, for systematic, ionospheric morphological studies. Oblique ionosondes are less often deployed on a permanent basis and are generally more appropriately used for propagation mode studies.

#### 3.3.1 Vertical Ionosondes

For vertical ionosondes, the time of flight of the propagating pulse,  $T_g$ , is recorded and translated into a virtual height,  $h'$ , the relationship being derived from Equation 3.14, where, for vertical propagation,  $\alpha = 0$ , such that:-

$$h' = \frac{1}{2} c T_g = c \int_0^{h_r} \frac{dh}{v_g} = \int_0^{h_r} \mu' dh \quad (3.19)$$

where  $h_r$  is the true height of reflection. Virtual height versus sweep frequency may be depicted in an 'ionogram', which is then 'reduced' or 'scaled' to determine more quantitative results. Electron density versus true height profiles may be generated using the Appleton Formula (Equation 3.3), Plasma Frequency definition (Equation 1.10) and associated theory, together with an iterative model profile approach, though interpretations may be ambiguous during non-quietest times (e.g. *Titheridge, 1985*).

A typical mid-latitude, vertical ionogram, recorded during the early evening, is presented in Figure 3.5. The ordinate and abscissa represent virtual height and transmitted ionosonde frequency. Note the presence of both O-mode and X-mode traces pertinent to the E- and F-regions, and also a 2-hop F mode trace. A non-blanketing sporadic-E trace (cf. §2.2.1) is observed with a critical frequency of approximately 3.6 MHz. At critical frequencies, the virtual heights are observed to increase significantly, as the group velocity tends to zero (cf. Equation 3.19). Note that at vertical incidence, the critical frequencies are indicative of the maximum plasma density of the respective layer (cf. Equation 1.10), in contrast to the junction frequency at oblique incidence (cf. §3.2.6).

### 3.3.2 Oblique Ionosondes and the Chirp Sounder

Oblique ionosondes are essential for propagation mode studies and are often indispensable for probing specific ionospheric regions, e.g. in conjunction with other radars, which may prove inaccessible to vertical ionosondes. One such scenario, pertinent to this thesis, is the subject of Chapter 7, in which coincident studies of sporadic-E layers are undertaken, by means of an HF sounder and SABRE, a VHF coherent backscatter radar, described below (cf. §3.4.1).

#### *HF 'Chirp' Sounder*

The oblique HF 'Chirp' Sounder (or simply Barry Sounder) (*Barry, 1971*) was utilised extensively for the purpose of the current investigations, its ionograms being the prime source of analysed data. Whereas most oblique sounders are pulse-amplitude modulated, the Chirp sounder is pulse-frequency modulated or more specifically, *Continuous Wave Frequency Modulated* (CWFM). The frequency of the transmitted signal varies linearly with time as depicted in Figure 3.6a. The transmitter frequency thus changes by  $\Delta f$  in a time  $\Delta t$  such that (cf. Figure 3.6b) :-

$$\Delta f = \frac{df}{dt} \cdot \Delta t \quad (3.20)$$

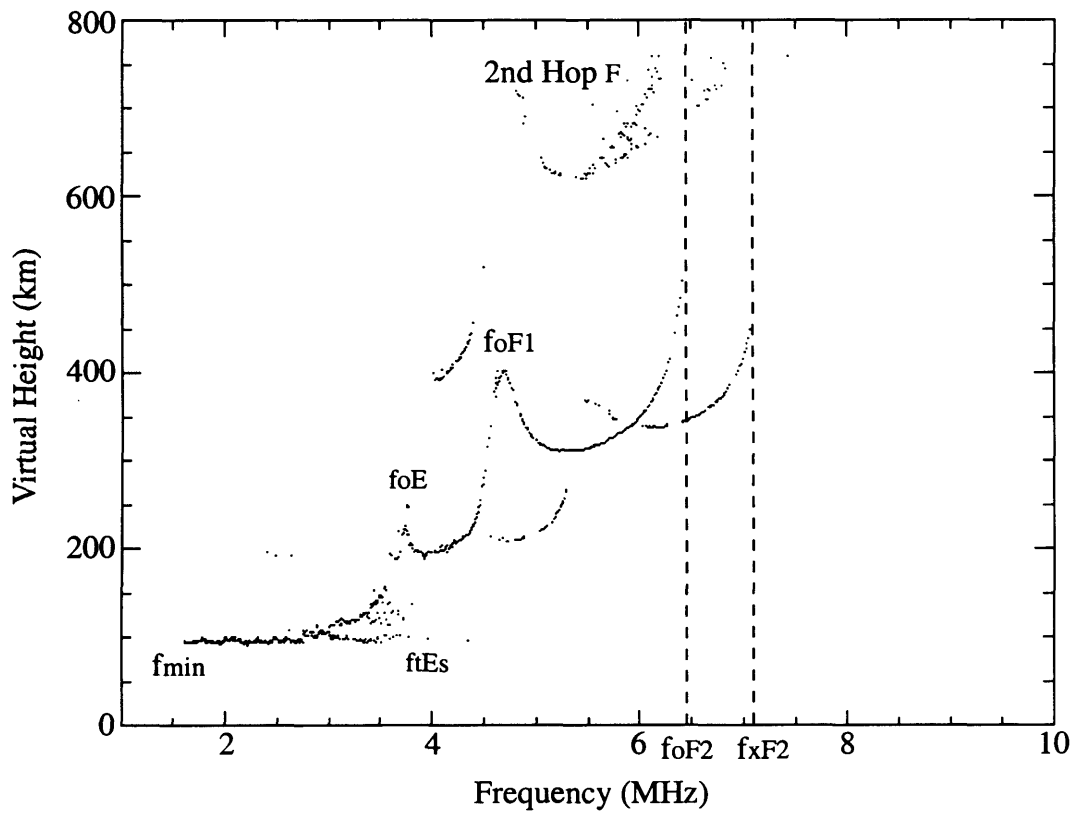
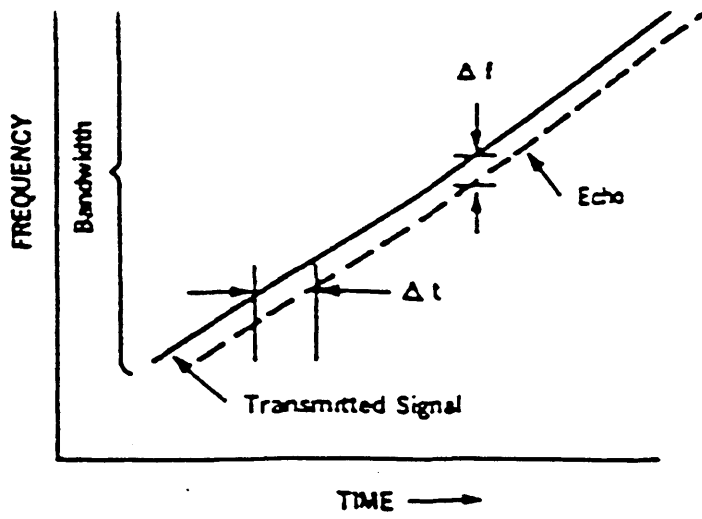
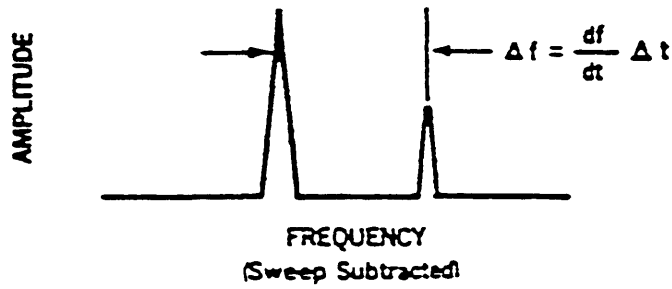


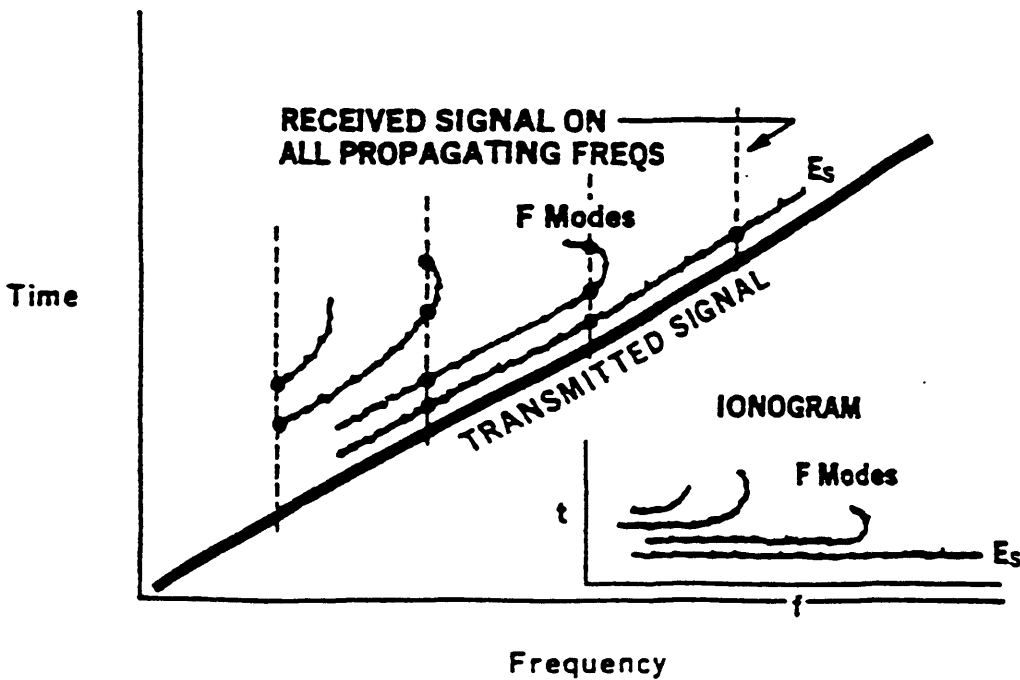
FIGURE 3.5 A typical example of an early evening vertical ionogram. Note the O- and X-mode critical frequencies of the E- and F-regions, but the difficulty in distinguishing these modes for the sporadic-E layer. The ionogram was recorded at Bear Lake, USA on 14/08/93, at 19:00:16 to 19:00:20.



(a)



(b)



(c)

FIGURES 3.6(a,c) Principles of the oblique HF 'Chirp' (Barry) sounder. The sounder transmits a frequency modulated signal, varying linearly with time (Figure 3.6a), such that the frequency difference,  $\Delta f$ , between the transmitted and received signals, defines the propagation time of flight,  $\Delta t$  (Figures 3.6(a,b)). The oblique ionogram may thus be compiled (Figure 3.6c) (after Barry, 1971 and the RCS-5 Operating and Service Manual).

By frequency analysing all received signals, the receiver can thus determine the time-of-flight,  $\Delta t$ , of any given echo, transmitted at a frequency  $f$ . By this means (cf. Figure 3.6c), the ionogram is compiled (Poole, 1985; Poole and Evans, 1985). This technique ensures good signal-to-noise at low transmitted powers (100 W) as a result of the Fourier analysis of the received signals: spiky noise is flat in the frequency spectrum whereas the transmitted signals will be sharp.

The RCS-5 receiver employed was configured to frequency scan at a rate of 100 kHz per second, over a frequency range of 2.1 MHz - 29.9 MHz. Each ionogram thus takes 279 seconds to compile, the maximum recording rate of ionograms being one every five minutes. Spectrum analysis calculations are performed once per second and hence the frequency resolution is 100 kHz. Each discrete frequency may conveniently be referred to as the '*Probing Frequency*', a term that will be utilised throughout this thesis.

Each associated TCS-4 transmitter begins transmitting the Chirp signal at a fixed pre-set time offset within a given 5 minute period. This is programmed into the RCS-5 receiver which simultaneously begins frequency scanning. The receiver will lock onto the Chirp signal if both the TCS-4 and RCS-5 are synchronised to within 1 second. Note however that the recorded time delay is only relative for each ionogram. The receiver adjusts its group delay ordinate, on a per-ionogram basis, so as to centre the most strongly received signal.

The group delay resolution is 25  $\mu$ s, corresponding to a group path of 7.5 km. The recorded signal strength is an *absolute* measure, covering the range from -62 dBm to -122 dBm, i.e. a range of 60 decibels. Each measurement is computed from the total signal strength received on a given spectrum analysed frequency (Probing Frequency). The value is hence the sum of signal strengths received from *all* traces at that Probing Frequency: signal strengths received from individual traces can not be determined, unless of course they are received in isolation. This feature was predominant in characterising the analysis methods pertaining to Chapter 5 and Chapter 6. A summary of the RCS-5 chirp receiver specifications, are presented in Table 3.1, with full details to be found in the RCS-5 Operating and Service Manual.

#### *Characteristic Features of Chirp Sounder Ionograms, Pertinent to Sporadic-E Layers*

The previous Section highlights some important sporadic-E scaling considerations. The signal strength of a sporadic-E trace may only be determined, at a given Probing Frequency, if the trace is observed in isolation. This introduces the concept of a cut-off frequency, below which, sporadic-E signal strengths are indeterminable. Due to the nature of oblique

<b>TCS-4 or RCS-5 Specification</b>	<b>Specification Details</b>
Peak Transmitted Power	100 Watts
Frequency Range	2.1 MHz – 29.9 MHz
Input Waveform	Linear FM/CW
Sweep Rate	100 kHz s <sup>-1</sup>
Sweep Duration	279 seconds
Group Delay Range	5 milliseconds
Group Delay Resolution	25 microseconds
Signal Strength Range	-62 dB to -122 dB
Minimum Detectable Chirp Signal	-135 dBm
Noise Figure	16 dB
Input Signal Level Required to Lock	-125 dBm
Auto Sync	Automatic search and lock on to the chirp signal when receiver is started within ±1 second of the transmitter
Auto Sync Sensitivity	Auto sync will automatically search, acquire and lock onto a Chirp signal within 30 seconds (90% probability) for signals within amplitude of -125 dBm and +6dB signal-to-noise ratio (500 Hz bandwidth)

**Table 3.1**

Summary of the TCS-4 transmitter and RCS-5 chirp sounder receiver technical specifications, as applicable to the 'December', 'March' and 'August' campaigns

ionograms, with oblique junction frequencies being determined as much by the geometry of the propagation path, as by the intrinsic plasma density (cf. the Secant Law (Equation 3.7)), the cut-off frequency may arise from either F-region or 'normal' E-region traces. The minimum Probing Frequency from which sporadic-E signal strength determinations may be measured, is henceforth termed the '*E/F-region cut-off frequency*', and is an important parameter in the signal strength deliberations of Chapter 5 and Chapter 6.

The Chirp sounder receiver is designed to determine the optimum propagation path mode between two sites. On compiling the ionogram, the receiver's gain control is thus adjusted to *display* only the strongest signals, within a dynamic range. As a consequence, weaker signals, though detected, may not be displayed. At Probing Frequencies where strong F-region traces are detected, the weaker sporadic-E trace may consequently be omitted from the ionogram. This effect has been termed '*F-region shielding*' within this thesis. It has no major impact on subsequent analysis other than occurrence statistics (cf. Chapter 4), which may be disregarding low top frequency sporadic-E layers, which are not observed at Probing Frequencies greater than the 'top' F-region frequencies (*ftF*).

#### *The Secant Law and Equivalent Vertical Frequencies*

For oblique propagation, the group delay scales directly to a group path (cf. Equation 3.14) but *not* to a virtual (or group) height, as defined in Equation 3.19. The virtual height may however be determined by application of Breit and Tuve's theorem (cf. §3.2.5), presuming that the propagation path is symmetrical about a reflection point, and that the whole path follows a '*great circle path*'. This idealised reflection point is then termed the '*nominal reflection point*' and may justifiably be used at mid-latitudes, where significant perturbing ionospheric tilts and horizontal density gradients are unusual. The '*nominal reflection point*' is widely used in this thesis.

Unlike vertical ionograms, the scaled data from oblique ionograms is very idiosyncratic to the specific oblique propagation path geometry. To compare scaled data pertaining to different oblique paths, a common transformation reference is required. The Secant Law, defined by Equation 3.7, is used extensively for this purpose, transposing an oblique junction frequency into an '*equivalent vertical frequency*', the vertically incident frequency that would be reflected at the same height. The equivalent vertical frequency not only provides a common reference frequency, but by definition, may be directly translated into the plasma density (cf. Equation 1.10).

Application of the Secant Law presumes a symmetrical oblique path defined by the nominal reflection midpoint, as described above. Further, the angle of incidence of the propagating ray on the ionosphere needs to be evaluated. This can prove very difficult and involves electron density modelling, when the ray penetrates the ionosphere substantially. For sporadic-E reflection this is conveniently not the case, and the angle of incidence,  $\theta_o$ , defined in Figure 3.2 and by Equation 3.8, may be easily determined, knowing the sporadic-E virtual height and propagation group path. The virtual height is determined from the equivalent propagation triangle, TAR, (cf. §3.2.5), which itself may be calculated from the predicted group delay of the sporadic-E propagation path, determined from ICEPAC, the empirical propagation-mode prediction program (Tascione *et al.*, 1987, 1988). ICEPAC assumes a typical sporadic-E height of 110 km (e.g. Smith and Mechtly, 1972), which for sporadic-E reflections, approximates to the virtual height (cf. Figure 3.2). By these means, equivalent vertical sporadic-E top frequencies (*vftEs*) are determined throughout this thesis, allowing for universal direct comparisons with related studies.

#### *Oblique Ionogram Scaling Considerations*

Oblique ionograms are distinctively different from their vertical counterparts. A typical example, composed by the Chirp sounder receiver from the Bodø/Wick propagation path, is presented in Figure 3.7. The main panel depicts the actual ionogram, scaled by relative group delay (ms) versus ionosonde frequency (MHz). The *relative* nature of the group delay makes translation to a virtual height impossible. The upper panel represents the *absolute* signal strength recorded by each Probing Frequency, in decibels.

The ionogram was recorded near midday (13:16 UT) and hence both the O- and X-mode, F1- and F2-layers are identifiable. Respective X-mode junction frequencies are 12.7 MHz and 11.4 MHz. Two-hop F-layer modes are also noted, with X-mode junction frequencies of 9.2 MHz and 8.5 MHz. The prominent, constant group delay trace, is a sporadic-E layer. Sporadic-E is characterised by an altitude confined E-region plasma layer. The high- and low-angle rays are hence approximately coincident and reflection may be considered to be from the maximum plasma density of the layer (cf. §3.2.6).

However, the same narrow-layer characteristic makes the O- and X-modes extremely difficult to distinguish, on either vertical or oblique ionograms. Many rules are defined to deduce the magneto-ionic components of the '*top frequency*', depending on the time of day and characteristics of the other ionogram traces (Piggott and Rawer, 1961). These rules are however largely inappropriate to oblique ionograms and the distinction between the O- and

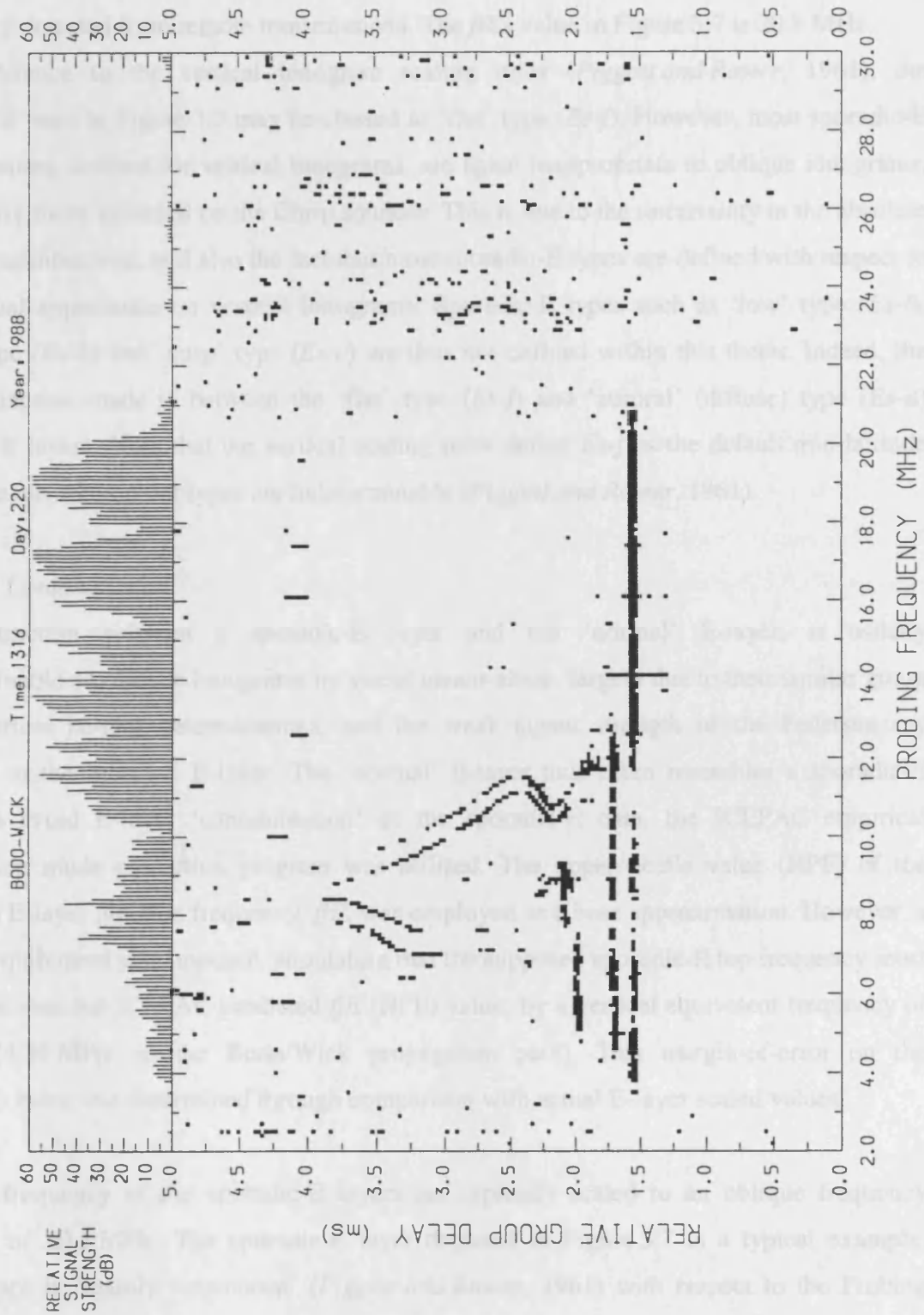


FIGURE 3.7 A typical midday oblique ionogram recorded over the Bodø/Wick propagation path (cf. Table 4.3), utilising an oblique 'Chirp' sounder. The upper panel depicts the relative signal strength with respect to frequency. Note the presence of O- and X-mode F-region traces (F1 and F2 layers), but the difficulty in distinguishing such modes in the prominent sporadic-E trace. Note also the difficulty in identifying the E-region junction frequency. The ionogram was recorded between approximately 13:16 and 13:20, on day 220, 1988.

X-mode components is uncertain at best. It is hence more appropriate to simply refer generically to the *top frequency* ( $f_i E_s$ ) of a sporadic-E layer, defined as the maximum Probing Frequency detected from remote transmissions. The  $f_i E_s$  value in Figure 3.7 is 20.8 MHz.

With reference to the vertical ionogram scaling rules (*Piggott and Rawer, 1961*), the sporadic-E trace in Figure 3.7 may be classed as ‘flat’ type ( $E_s-f$ ). However, most sporadic-E classifications, defined for vertical ionograms, are again inappropriate to oblique ionograms, particularly those recorded on the Chirp sounder. This is due to the uncertainty in the absolute height determinations, and also the fact that most sporadic-E types are defined with respect to their visual appearance on vertical ionograms. Sporadic-E types such as ‘low’ type ( $E_s-l$ ), ‘high’ type ( $E_s-h$ ) and ‘cusp’ type ( $E_s-c$ ) are thus not defined within this thesis. Indeed, the only distinction made is between the ‘flat’ type ( $E_s-f$ ) and ‘auroral’ (diffuse) type ( $E_s-a$ ) sporadic-E layers. Note that the vertical scaling rules define  $E_s-f$  as the default mid-latitude type Es-layer, when other types are indeterminable (*Piggott and Rawer, 1961*).

#### *E-Layer ‘Contamination’*

The distinction between a sporadic-E layer and the ‘normal’ E-layer, is usually indeterminable on oblique ionograms by visual means alone, largely due to their similar group delay (virtual height) determinations, and the weak signal strength of the Pedersen ray pertinent to the ‘normal’ E-layer. The ‘normal’ E-layer thus often resembles a sporadic-E trace. To avoid E-layer ‘contamination’ of the sporadic-E data, the ICEPAC empirical propagation mode prediction program was utilised. The upper decile value (HPF) of the predicted E-layer junction frequency,  $f_j E$ , was employed as a base approximation. However, a further requirement was imposed, stipulating that the supposed sporadic-E top frequency must be greater than the ICEPAC predicted  $f_j E$  (HPF) value, by a vertical equivalent frequency of 1 MHz (4.59 MHz on the Bodø/Wick propagation path). This margin-of-error on the  $f_j E$  (HPF) value was determined through comparison with actual E-layer scaled values.

The top frequency of the sporadic-E layers are typically scaled to an oblique frequency accuracy of  $\pm 0.1$  MHz. The sporadic-E layer depicted in Figure 3.7 is a typical example, whose trace is ‘mainly continuous’ (*Piggott and Rawer, 1961*) with respect to the Probing Frequency. Occasionally this is not the case, and the top frequency is determined by a subjective judgement, based on the signal strength. The top frequency may also be poorly defined, due to, for example, E-region scatter. Again the error in the scaled top frequency value may be increased. These scaling uncertainties however constitute a small minority of recordings and do not significantly influence the statistical analysis presented in later Chapters.

Figure 3.8 highlights some of the scaled data aspects considered above. The Figure presents a single day's summary of sporadic-E observations, the main panel being equivalent vertical Probing Frequency versus Universal Time. The vertical lines each represent the range of Probing Frequencies for which *sole* sporadic-E signal strengths may be determined. The upper limit of the vertical lines is thus either the  $fE_s$  value of each scaled Es-layer, or the maximum ionosonde Probing Frequency, while the base of each line indicates the *E/F-region cut-off frequency*. It is noted that the *cut-off frequency* is determined by the maximum value of either the ICEPAC  $fjE$  (HPF), or the scaled F-region top frequency ( $f_tF$ ), i.e. the 'normal' F-layer or F-region scatter. The former is substituted by actual scaled  $fjE$  values when they have been determined.

The upper panel in Figure 3.8 presents the 'Representative Signal Strength' (RSS) of each sporadic-E layer, i.e. in this case, the median signal strength of each sporadic-E layer, with respect to the *range* of Probing Frequencies defined by the vertical lines in Figure 3.8. This measure allows a signal strength determination to be made for each observable Es-layer, and is useful in this context alone. However, to avoid differing absorption characteristics of the Probing Frequency (cf. §3.2.7), sporadic-E signal strength determinations within this thesis, are usually determined at a *single, common* Probing Frequency (cf. Chapter 5 and Chapter 6), though a modified RSS is briefly employed in Chapter 6.

The *E/F-region cut-off frequency* is dominated by E-layer values during the daytime and F-region values during the night. The difficulty in scaling E-layer junction frequencies is highlighted by the relatively few measurements plotted in Figure 3.8. Note however that most scaled  $fjE$  values are similar to the ICEPAC  $fjE$  values, though some are observed to be greater.

## 3.4 Further Ionospheric Diagnostic Equipment

### 3.4.1 The SABRE Radar

The Sweden And Britain Radar-aurora Experiment (SABRE) is a bistatic, VHF coherent backscatter radar, sensitive to field-aligned plasma instability waves within the auroral E-region (*Greenwald et al.*, 1978). However, during 1987 and 1988, the radar was operated in a monostatic mode, with the transmitter and receiver being co-located at Wick, Scotland. The radar operates continuously, transmitting 50 kW peak pulses, at a frequency of 153.2 MHz,

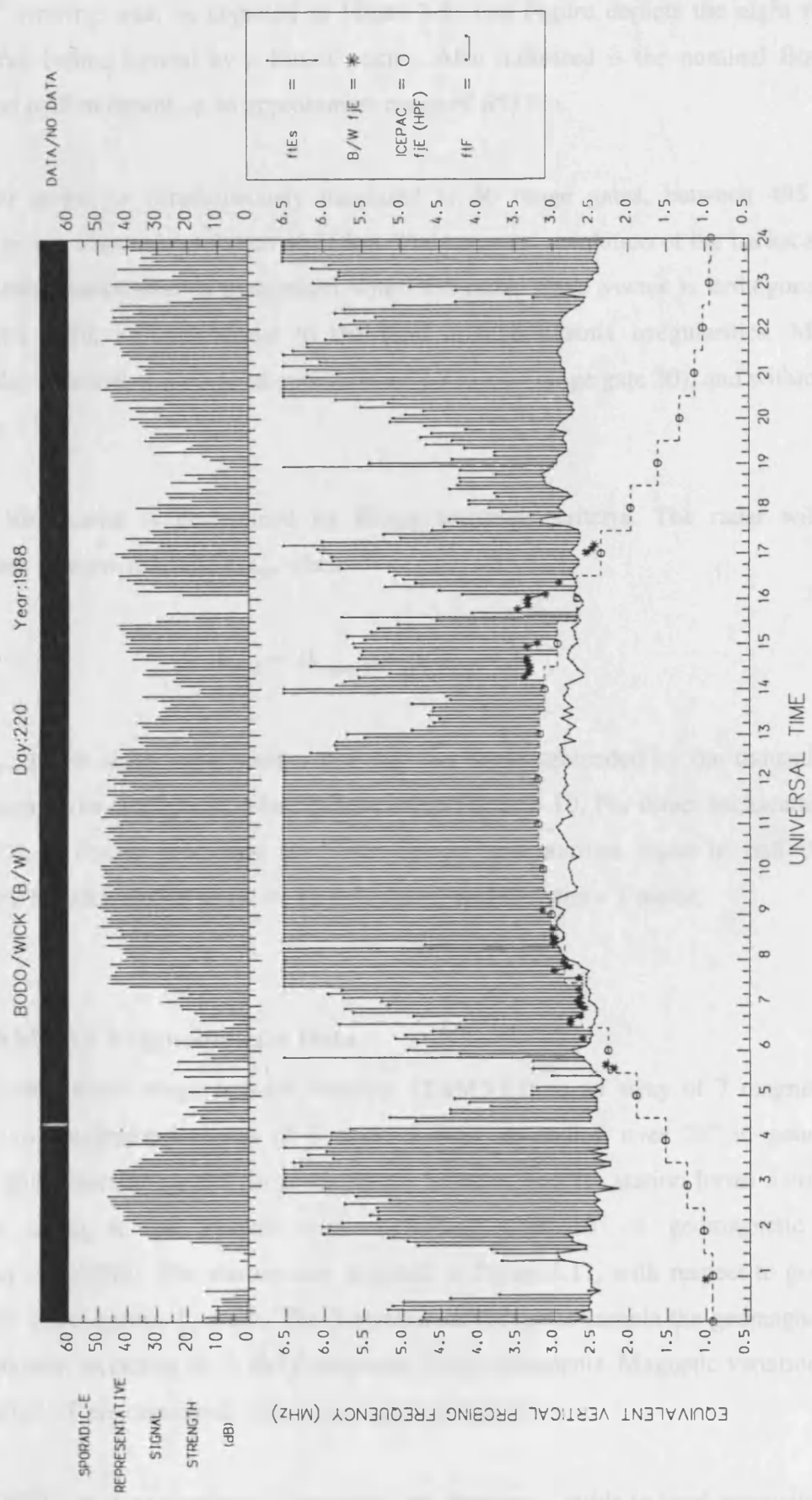


FIGURE 3.8 Summarised scaled, oblique ionogram data, pertaining to the Bodø/Wick propagation path (cf. Table 4.3), on day 220, 1988. The vertical lines within the main panel, indicate the range of frequencies over which sole sporadic-E signal strengths may be measured, the top of the lines defining the sporadic-E *top frequency*.

into a 30° viewing area, as depicted in Figure 3.9. The Figure depicts the eight receiving phased array beams formed by a Butler matrix. Also indicated is the nominal Bodø/Wick propagation path midpoint, at an approximate range of 655 km.

Backscatter power is simultaneously measured at 50 range gates, between 495 km and 1230 km, giving a spatial resolution of 15 km. The temporal resolution of the backscatter data is 20 seconds. Backscatter is maximised when the radar wave vector is orthogonal to the geomagnetic field, i.e. orthogonal to the field aligned plasma irregularities. Maximum orthogonality is noted at a range of approximately 930 km (range gate 30), and within beam 5 (cf. Figure 3.9).

Coherent backscatter is determined by Bragg scattering criteria. The radar will detect irregularities of wave number,  $k_{irreg}$ , when:-

$$k_{irreg} = 2k_{radar} \cos(\alpha/2) \quad (3.21)$$

where  $k_{radar}$  is the radar wave number and  $\alpha$  is the angle subtended by the transmitted and received signal, the configuration being depicted in Figure 3.10. For direct backscatter, i.e. as for SABRE,  $\alpha$  equals zero, and the radar detects irregularities equal to half the radar wavelength. SABRE is thus sensitive to irregularity wavelengths  $\sim 1$  meter.

### 3.4.2 SAMNET Magnetometer Data

The UK Sub-Auroral Magnetometer Network (SAMNET) is an array of 7 magnetometers forming two longitudinal chains of 3 stations each, extending over 28° in geomagnetic longitude and separated by 6.5° in geomagnetic latitude. The 7th station forms a connecting meridional chain at the western edge, extending over 10° of geomagnetic latitude (Yeoman *et al.*, 1990b). The stations are depicted in Figure 3.11, with respect to geographic coordinates and magnetic L-shells. The 3-component fluxgates sample the geomagnetic field every 5 seconds, recording H, D and Z magnetic field components. Magnetic variations over a range of  $\pm 512$  nT are measured, with a resolution of 0.25 nT.

The SAMNET data was employed throughout this thesis as a guide to local magnetic activity conditions, specifically, near the nominal Bodø/Wick propagation path midpoint. To this end, pseudo K-indices were compiled. For each of the H, D and Z magnetic field components, the

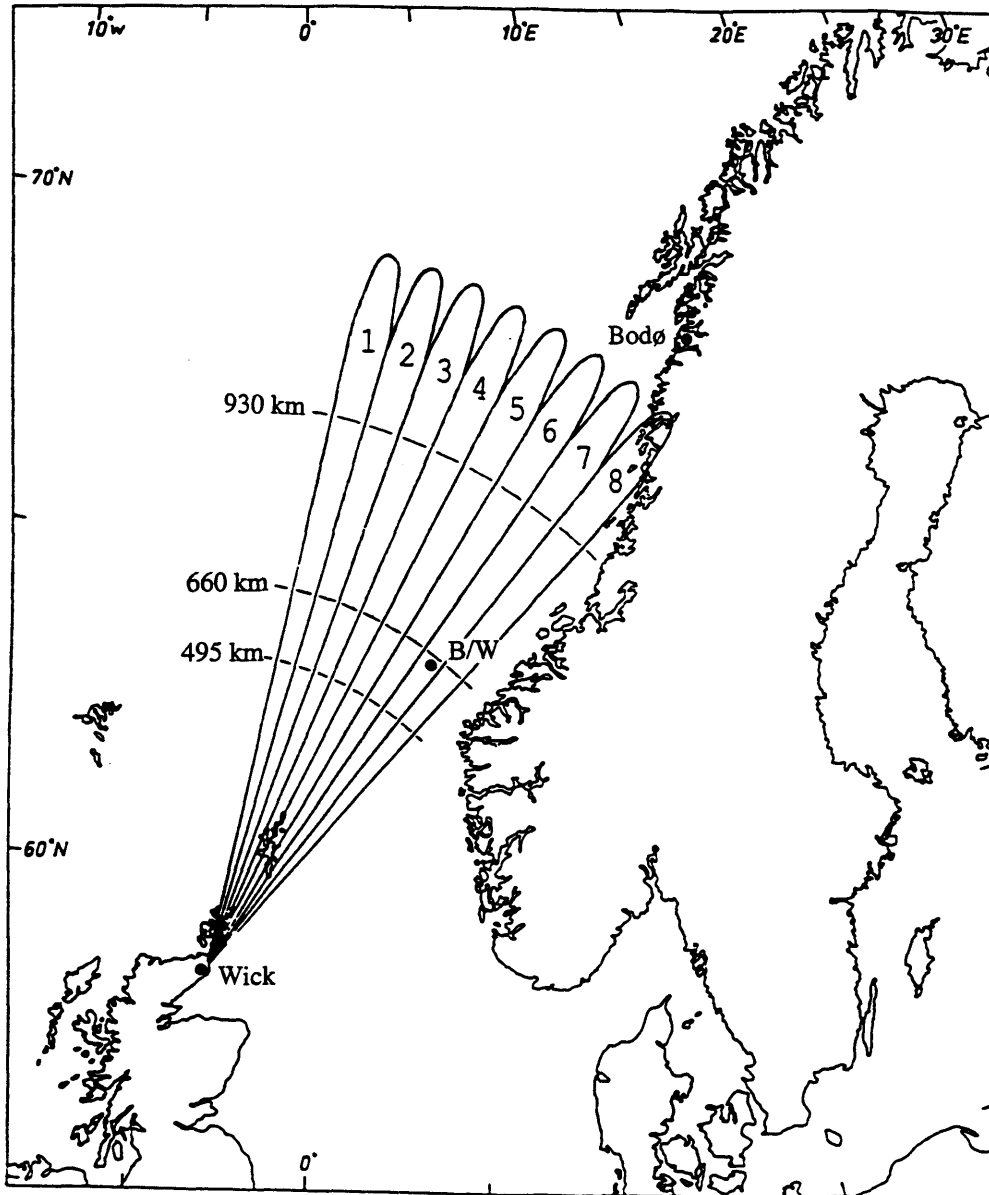


FIGURE 3.9 Map indicating the 8 beams of the SABRE coherent backscatter radar, as defined from the Wick site. Bodø, the prime transmitting site for the oblique 'Chirp' sounder, is also indicated, as are range gates 1 (495 km), 12 (660 km) and 30 (930 km). These correspond approximately to the nearest range of irregularity detection by SABRE, the Bodø/Wick (B/W) nominal propagation path midpoint, aligned with the SABRE beam 7, and the range gate of maximum orthogonality between the SABRE radar vector and the geomagnetic field, respectively.

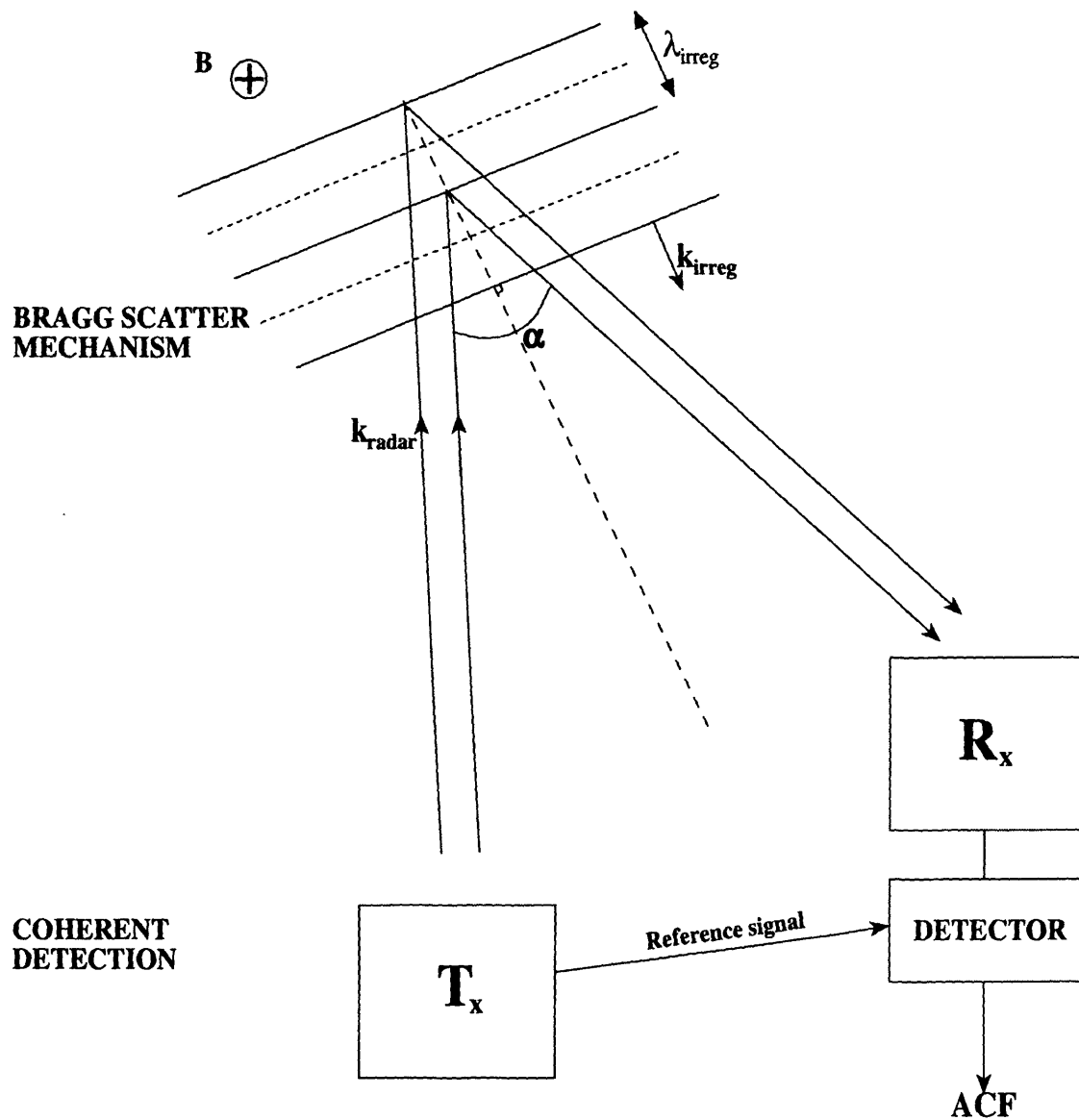


FIGURE 3.10 The Bragg scatter mechanism as applicable to coherent backscatter radars. By this means, SABRE detects irregularities of wavelengths approximating to 1 meter (cf. Equation 3.21) (after Eglitis, 1994).

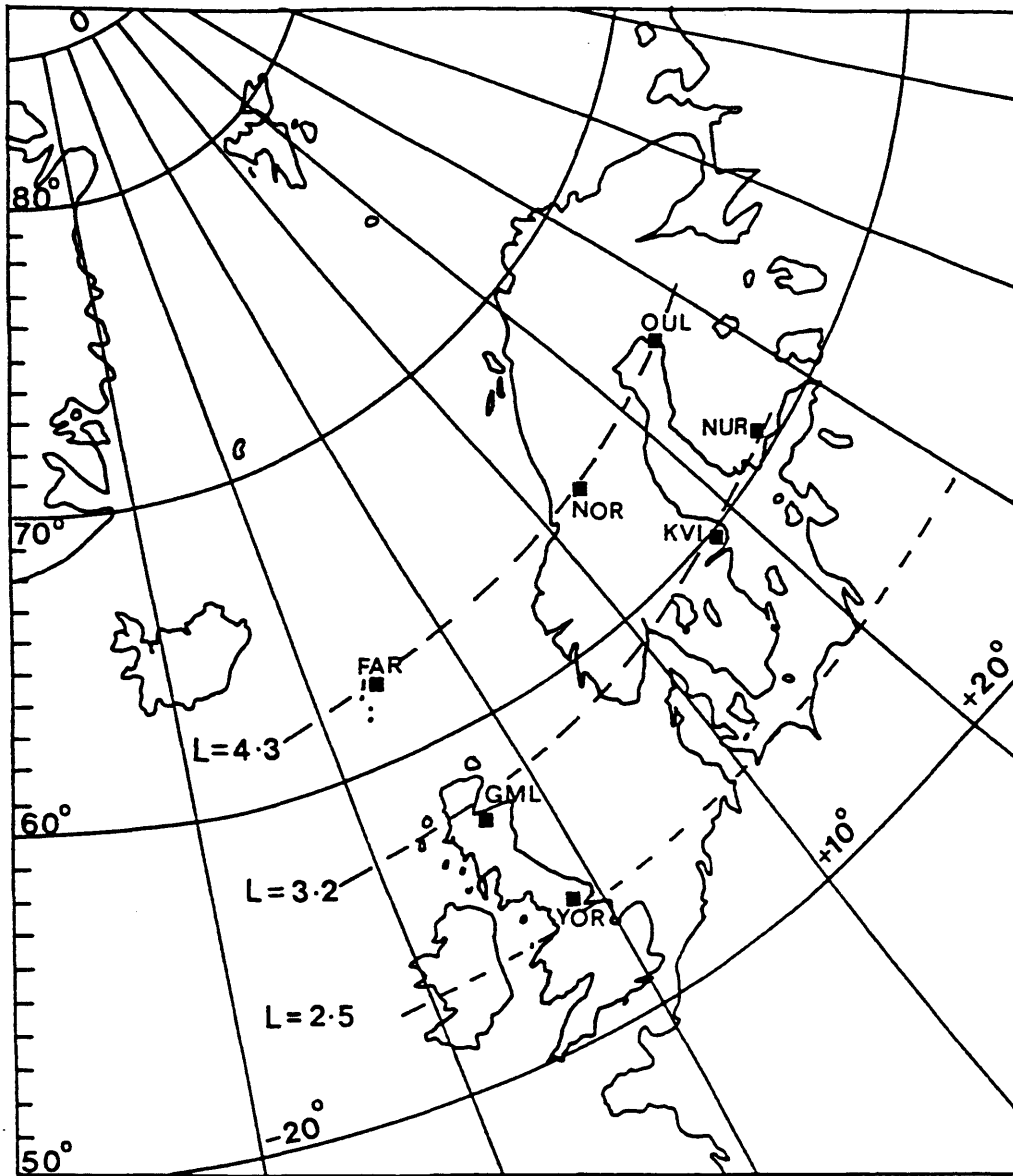


FIGURE 3.11 Map indicating the 7 SAMNET stations. Faroes (FAR), Nordli (NOR) and Oulu (OUL) are located approximately on magnetic L-shell 4.3. Glenmore (GML), Kvistaberg (KVI) and Nordli (NOR) are located on a lower L-shell (~ 3.2), with York (YOR) alone being located on L-shell 2.5.

maximum variation (nT), within each of eight, 3-hour time periods, defines the pseudo K-index range. A fourth index was calculated, as the square root of the sum of the squares, of the H- and D-components, it being considered a more representative guide to magnetic activity. This definition of the pseudo K-index closely matches that of 'standard' local K-indices, though the definition presented here expresses the index in terms of a linear, nT scale, rather than a customised logarithmic scale (cf. *Mayaud*, 1980). The advantage however is to provide more localised magnetic field information than would be available from K-indices calculated for Lerwick, the site of the nearest 'standard' K-index station. 'Raw' SAMNET data was also employed in Chapter 7 to study substorm activity.

### **3.5 Summary**

This Chapter has presented a brief review of High Frequency propagation theory within the ionosphere, and in particular, that applicable to ionosondes. The oblique Chirp sounder is the prime source of data for this thesis and hence the fundamentals of this radar are reviewed. The accurate and consistent interpretation of ionograms is essential. The applicability of the conventional vertical ionosonde scaling rules (*Piggott and Rawer*, 1961) are thus discussed and adapted where appropriate. The important use of the Secant Law to determine equivalent vertical sporadic-E top frequencies ( $v_{fEs}$ ) is also explained. Finally, the SABRE backscatter radar and SAMNET magnetometer network are considered, each providing a significant contribution to the current studies.

# Chapter 4

## An Introduction to the Bodø/Wick Oblique Propagation Circuit and Associated Sporadic-E Recordings

### 4.1 Introduction

The intention of this thesis is to further the understanding of the plasma structure of sporadic-E layers. In pursuit of this goal, oblique ionograms were recorded over three 11 day 'campaigns', during 1987 and 1988, namely December, March and August. In each case, an oblique High Frequency 'Chirp' sounder (cf. §3.3.2) was deployed, transmitting between Bodø, Norway and Wick, Scotland. The ionograms were subsequently collated, scaled and analysed.

For logistical reasons, the most significant data set pertains to the August campaign. Analysis undertaken for Chapter 5 and Chapter 6, solely considers *this* Bodø/Wick oblique propagation circuit. As the aforementioned analysis is of a statistical nature, it is important to assess how representative the data is, with respect to typically observed mid-latitude sporadic-E characteristics. To this end, the morphological aspects of the sporadic-E data, recorded over the said Bodø/Wick propagation path, are described and analysed below. Comparisons are then made with both the literature, and further soundings undertaken during the August campaign, to validate the representative nature of the Bodø/Wick sporadic-E recordings.

In Chapter 7, sporadic-E data pertaining to the December and March campaigns are analysed with respect to substorm activity, on a case by case basis. Due to the nature of that analysis, and the general sparsity of sporadic-E observations observed and recorded during these two campaigns, a similar validation process, with respect to mid-latitude sporadic-E, is considered to be inappropriate and unnecessary. *This* Chapter thus concentrates on the morphological aspects of the August campaign data. The logistical and technical details of all three campaigns are however initially considered below, together with details of further radar deployments.

## 4.2 Campaign Details

### 4.2.1 Radar Deployments

Table 4.1 presents details of the December, March and August campaigns. During the December and March campaigns, the SABRE backscatter radar (cf. §3.4.1) was also operational and utilised in subsequent studies. This radar was unavailable during the August campaign, but five additional oblique sounding paths were constituted, with transmitters in Bodø, Oslo and Reykjavik, and receivers in Wick and Blakehill. For each radar, the availability, as a percentage of the 11 day campaign period, is also presented. The maximum rate of ionogram recordings, together with an associated hourly schedule, is presented in Table 4.2, for each of the six oblique sounders (cf. §3.3.2). It is noted that the Bodø/Wick sounder may *potentially* record 12 ionograms per hour (during all three campaigns) but that the maximum ionogram recording rate for four of the six sounders is only 2 ionograms per hour.

Details of the oblique ionosonde locations, with respect to both geographic and geomagnetic coordinates, are presented in Table 4.3, with the geographic details being presented in Figure 4.1. Additional propagation path and sporadic-E related data is also included in Table 4.3. The geomagnetic coordinates were derived from the IGRF 1985 model, utilising extrapolated epoch coefficients for years 1987 and 1988. It was noted that there is no significant difference between the calculated geomagnetic coordinates for 1987 and 1988, and as such, the Bodø/Wick entries apply equally to all three campaigns. The Ground Path Length between transmitter and receiver ('D' in Figure 3.2), was calculated using spherical geometry, assuming great circle paths and a perfectly spherical Earth, with an actual mean radius of 6371.03 km. The nominal geographic propagation path midpoints were calculated likewise.

The data in Table 4.3 relating to sporadic-E (and specifically the Bodø/Wick propagation path), is utilised as a *guide* throughout this thesis. Sporadic-E layers are noted most commonly at altitudes between 100 km and 120 km, with the altitude of 110 km being commonly taken as a reference (*Smith and Mechtly, 1972*). By applying this reference height to Breit and Tuve's theorem (cf. §3.2.5), nominal elevation angles and group delays (cf. §3.2.5), for HF reflections from sporadic-E layers, may be easily calculated. The errors relate to calculated reflections from sporadic-E layers, at heights ranging between 100 km and 120 km, and are noted to vary with propagation path. The greatest error has been quoted. Note

Campaign	Dates (days, year)	Radars	Availability of Radar (as a % of defined campaign time)
December	335 - 345, 1987	Bodø - Wick Oblique HF Ionosonde	30.1
		SABRE VHF Coherent Radar	84.0
March	074 - 084, 1988	Bodø - Wick Oblique HF Ionosonde	79.6
		SABRE VHF Coherent Radar	92.7
August	216 - 226, 1988	Bodø - Wick Oblique HF Ionosonde	95.9
		Oslo - Wick Oblique HF Ionosonde	58.5
		Reykjavik - Wick Oblique HF Ionosonde	14.3
		Bodø - Blakehill Oblique HF Ionosonde	15.2
		Oslo - Blakehill Oblique HF Ionosonde	15.6
		Reykjavik - Blakehill Oblique HF Ionosonde	15.6

Table 4.1

Radar deployments and timings during the December, March and August Campaigns

Oblique Ionosonde Path (Tx - Rx)	Ionogram Recordings												5 Minute Offset (s)
	(with respect to 5 Minute Blocks Past the Hour)												
	0	5	10	15	20	25	30	35	40	45	50	55	
Bodø - Wick	X	X	X	X	X	X	X	X	X	X	X	X	1:04
Oslo - Wick		X	X	X	X			X	X	X	X		1:55
Reykjavik - Wick	X						X						0:11
Bodø - Blakehill					X						X		1:04
Oslo - Blakehill			X					X					1:55
Reykjavik - Blakehill	X						X						0:11

Table 4.2

Oblique ionogram recording schedule, during the August Campaign

Oblique Ionosonde Paths (Tx - Rx)	Tx Geographic Coordinates	Rx Geographic Coordinates	Tx Geomagnetic Coordinates	Rx Geomagnetic Coordinates	Path Length (km)	Midpoint Geographic Coordinates	Midpoint Geomagnetic Coordinates	Tx/Rx Azimuth Angles (°)	Tx/Rx Elevation Angle (°) ( $\pm < 1.0$ )	1-hop Es TD (ms) ( $\pm < 0.02$ )	2-hop Es TD (ms) ( $\pm < 0.02$ )
Bodø - Wick	67.27N	58.56N	64.21N	56.48N	1309.0	63.19N	60.78N	230.89	6.51	4.46	
	14.39E	3.28W	98.30E	79.16E		4.23E	87.64E	35.08		4.64	
Oslo - Wick	59.56N	58.56N	56.34N	56.48N	788.9	59.24N	56.55N	267.83	13.68	2.75	
	10.41E	3.28W	90.36E	79.16E		3.46E	84.74E	76.07		3.03	
Reyjavik - Wick	63.95N	58.56N	65.19N	56.48N	1192.8	61.60N	60.99N	111.17	7.67	4.07	
	22.72W	3.28W	67.03E	79.16E		12.16W	74.01E	308.27		4.27	
Bodø - Blakehill	67.27N	51.62N	64.21N	48.38N	1954.2	59.68N	56.95N	215.19	1.96	6.61	
	14.39E	1.89W	98.30E	77.11E		4.34E	85.66E	21.02		6.73	
Oslo - Blakehill	59.56N	51.62N	56.34N	48.38N	1169.5	55.74N	52.62N	226.42	7.93	4.00	
	10.41E	1.89W	90.36E	77.11E		3.63E	83.18E	36.24		4.20	
Reykjavik - Blakehill	63.95N	51.62N	65.19N	48.38N	1827.8	58.20N	57.00N	128.73	2.68	6.19	
	22.72W	1.89W	67.03E	77.11E		10.50W	73.38E	326.51		6.32	

Table 4.3

Geographic, geomagnetic and propagation data relating to the oblique ionosonde paths

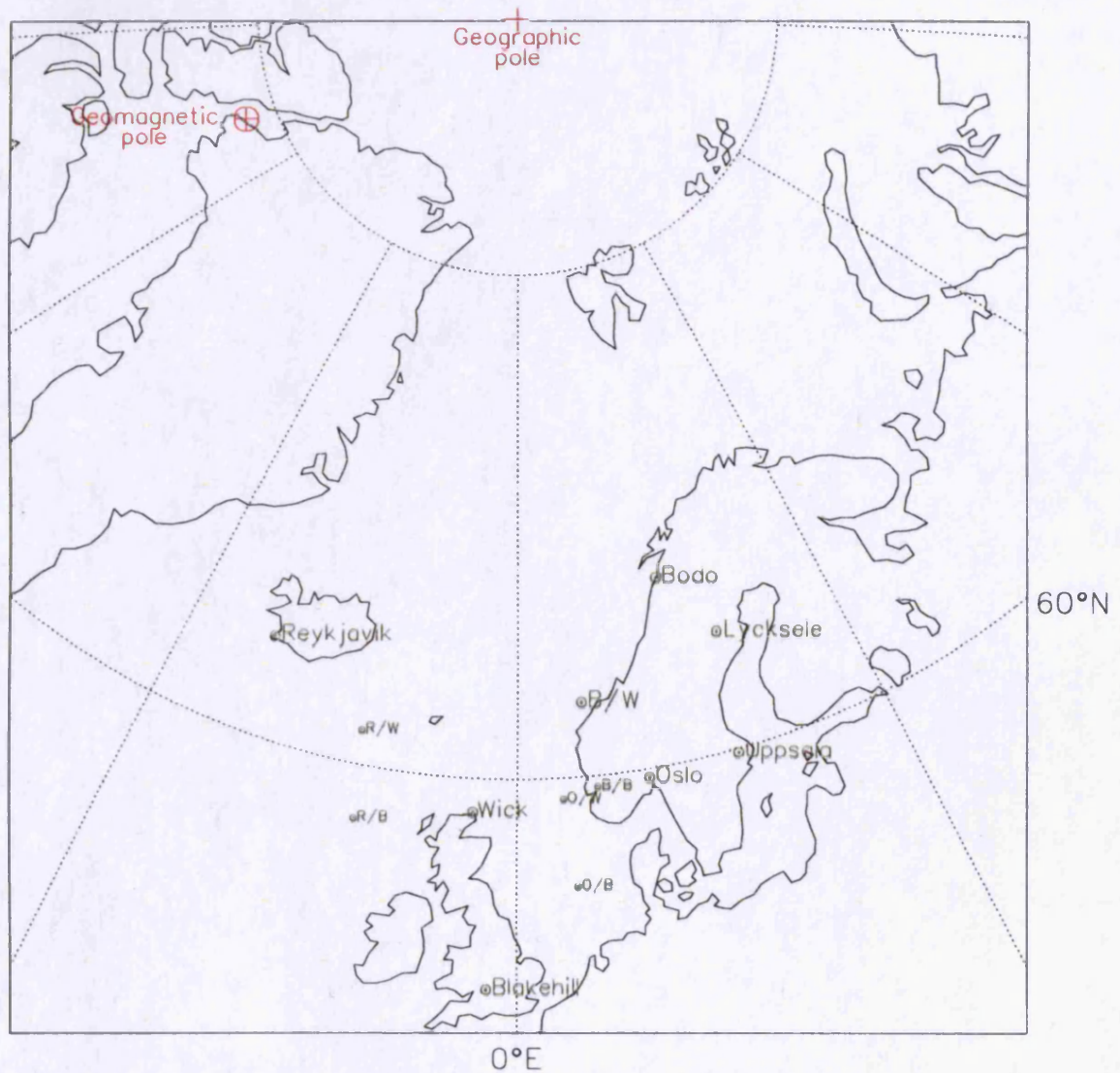


FIGURE 4.1 Oblique ionosonde transmitter (Bodø, Oslo and Reykjavik) and receiver (Wick and Blakehill) locations, utilised during the August campaign (cf. Table 3.1), together with the respective nominal propagation path midpoints (B/W, B/B, O/W, O/B, R/W and R/B). The vertical ionosonde sites of Lycksele and Uppsala are also indicated. Note that the Bodø/Wick (B/W) propagation path was also utilised during the December and March campaigns (cf. Table 3.1).

that the geomagnetic coordinates described above, are *also* based on a geodetic altitude of 110 km, but with no discernible variation noted for heights between 100 km and 120 km.

Finally, it was noted above that only the Bodø/Wick sounder is even *potentially* configured to record ionograms continuously, with most of the sounding circuits, deployed during the August campaign, being limited to relatively infrequent recordings (cf. Table 4.2). As a consequence, their data was of limited benefit to subsequent studies undertaken in this thesis. Analysis of data pertaining to these additional five oblique paths is thus largely confined to the morphological investigations presented herein.

#### 4.2.2 Radar Antennas

The transmitting antennas at Bodø, Oslo and Reykjavik were of the Log-Periodic design, enabling each to give approximately similar gain responses, with respect to the range of sounding frequencies (2 - 30 MHz). Model gain evaluations were obtained from the ICEPAC prediction tool (cf. §3.3.2), applying estimated dimension and ground condition parameters. The results are depicted in Figure 4.2a, for a 10 m tall antenna. The frequency-gain relationship is presented for a range of elevation angles between 2° and 14°, spanning the range of angles pertinent to the propagation paths defined in Table 4.3. The uniformity of these frequency-gain relationships is to be noted, for any given elevation angle, as is the small variation *between* elevation angles, considering the uncertainty in the exact magnitudes of these angles, as attested to above. Note that details pertaining to the Bodø/Wick propagation circuit, as usual, apply equally to each of the three campaigns.

The receiving antennas employed were of the Sloping Vee type, designed to provide wide-angle coverage (> 90°). Figure 4.2b depicts the ICEPAC-modelled, frequency-gain relationship for the Bodø/Wick receiving antenna, the height and arm dimensions being 10 m and 45 m respectively. It is clear that the Sloping-Vee design does not generate uniform frequency-gain relationships at any of the elevation angles pertinent to the sounder paths described in Table 4.3. However, the nominal elevation angle for sporadic-E reflections on the most important and significant, Bodø/Wick sounding path, is  $6.51^\circ \pm 1.0^\circ$ , as noted in Table 4.3. And the gain depicted in Figure 4.2b at the most comparable elevation angle of 6°, only increases by approximately 2 dB between frequencies ~ 15 MHz and ~ 20 MHz. Further, for frequencies greater than ~ 20 MHz, gain uniformity *is* a notable feature at this elevation angle. These almost uniform frequency-gain characteristics, for elevation angles pertinent to

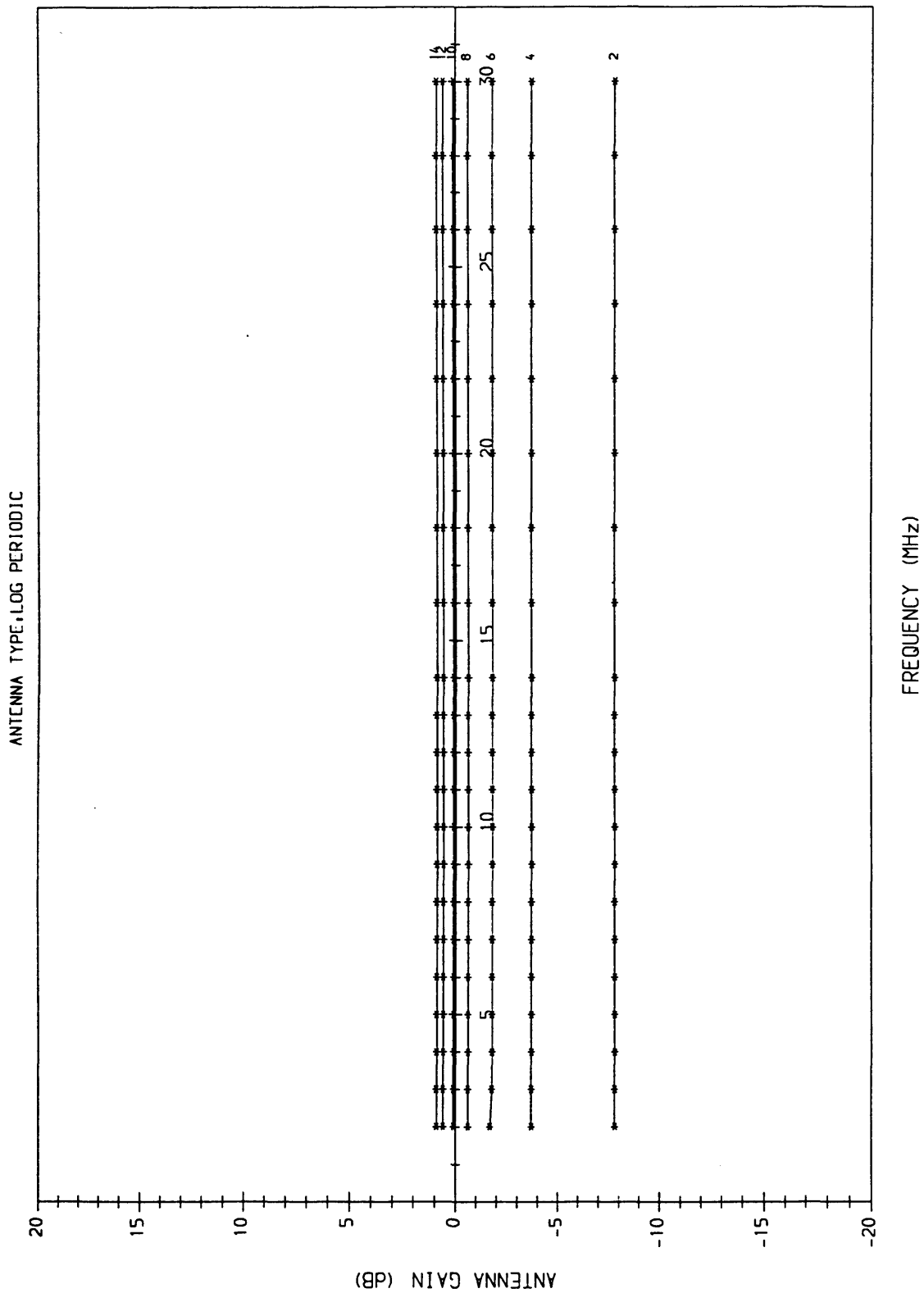


FIGURE 4.2a Model gain-frequency response for a 10 meter tall 'log-periodic' transmitting antenna, derived from the ICEPAC propagation mode prediction program (Tascoine et al., 1987). Note the uniform gain characteristics with respect to HF propagation frequency, for a given transmission elevation angle.

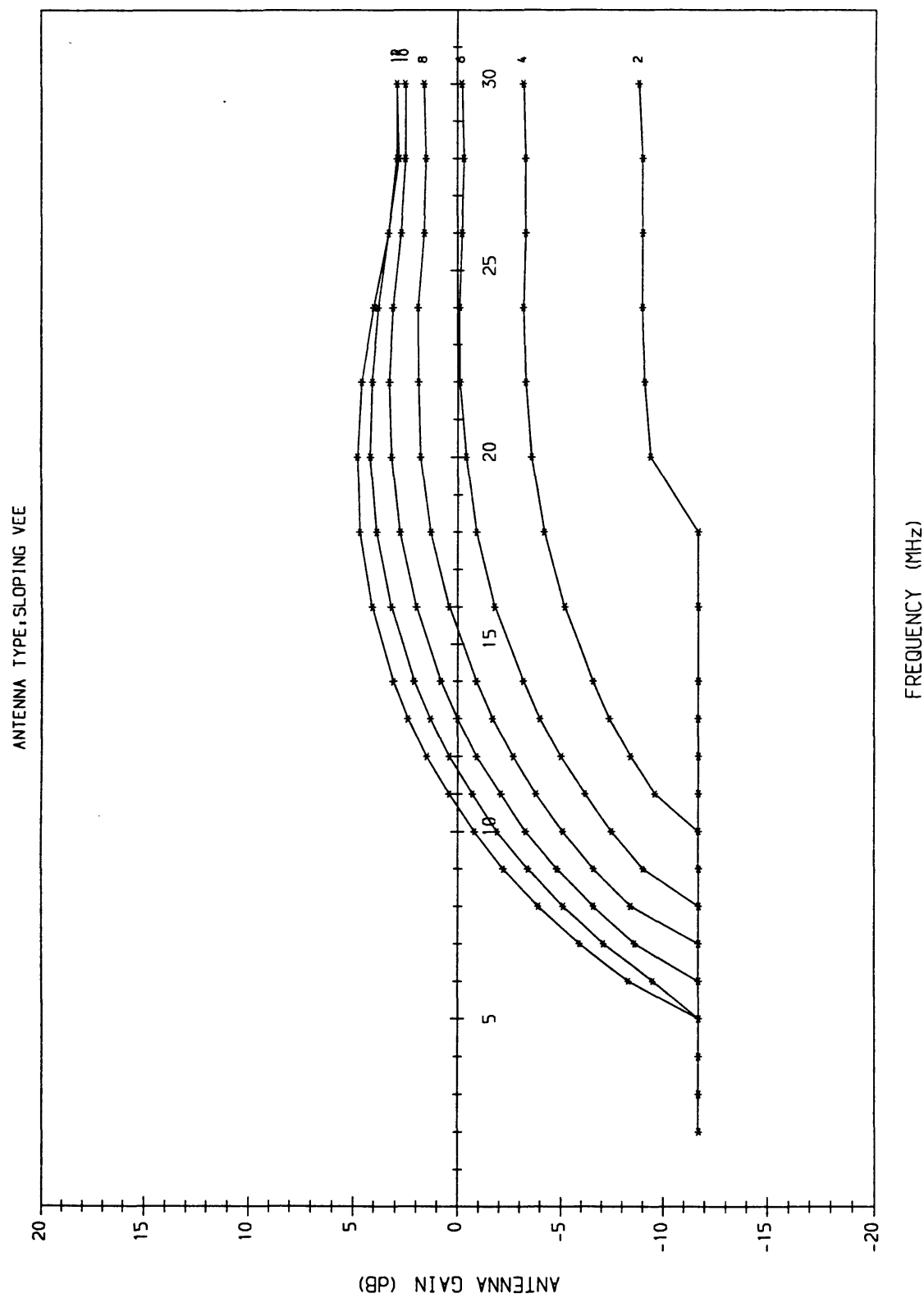


FIGURE 4.2b Model gain-frequency response for a 10 meter tall, 45 meter arm, 'sloping-vee' receiving antenna, derived from the ICEPAC propagation mode prediction program (Tascoine *et al.*, 1987). The gain is noted to vary with both frequency and elevation angle. However, for the Bodø/Wick propagation path, with a nominal elevation angle of  $6.51^\circ$  (cf. Table 4.3), the gain only differs by approximately 2 dB, between Probing Frequencies of 15.0 MHz and 30.0 MHz.

the Bodø/Wick propagation path, and for Probing Frequencies  $\geq 15$  MHz, are important considerations in later Chapters, when signal strength analysis is undertaken.

### 4.3 Morphological Studies of Sporadic-E Layers, Observed on the Bodø/Wick Propagation Path, during the August Campaign

#### 4.3.1 Phillips' Rule

Figure 4.3 summarises the occurrence characteristics of sporadic-E at vertical incidence, recorded over the Bodø/Wick propagation path, during the August campaign. The plot is a representation of Phillips' Rule, which is described by Equation 2.1 and is repeated here for convenience.

$$\log_{10} P = a + bf \quad (4.1)$$

Phillips' Rule describes a logarithmic relationship between a given threshold frequency,  $f$ , and the probability,  $P$ , of the sporadic-E top frequency being greater than that threshold frequency, 'a' and 'b' being customised constants. It is generally applicable to typical mid-latitude sporadic-E observations (*Smith, 1957*). The ordinates in Figure 4.3 thus represent the logarithmic probability and the equivalent linear fractional percentage. The abscissa depicts the equivalent vertical threshold frequency (cf. the Secant Law (Equation 3.2.3)). The vertical dotted lines indicate the ionosonde's scanning range of equivalent vertical frequencies, as applicable to the Bodø/Wick propagation path.

The actual probability of sporadic-E occurrence is represented by the red dotted line, with the green line being a linear regression fit to the probability gradient, described by Phillips' Rule. The near constant probability of occurrence, for  $\nu f E_s$  values  $\leq 3$  MHz, is a manifestation of the effect of F-region shielding (cf. §3.3.2), and also of the scaling restrictions arising from potential 'normal' E-layer contamination of the result set (cf. §3.3.2). Both restrict observations of sporadic-E to  $\nu f E_s$  values  $\geq 3$  MHz. The total probability of occurrence (67.8%) may thus be a slight underestimate of the true value, but this is not considered to be significant. Neither does it influence the applicability of the results to Phillips' Rule, which is gradient driven.

The probability gradient ('b') is noted as  $-0.198 \pm 0.007$ , with an intercept ('a') of  $0.606 \pm 0.038$ . This value of 'b' is typical for mid-latitude sporadic-E layers (*Smith, 1957*). The

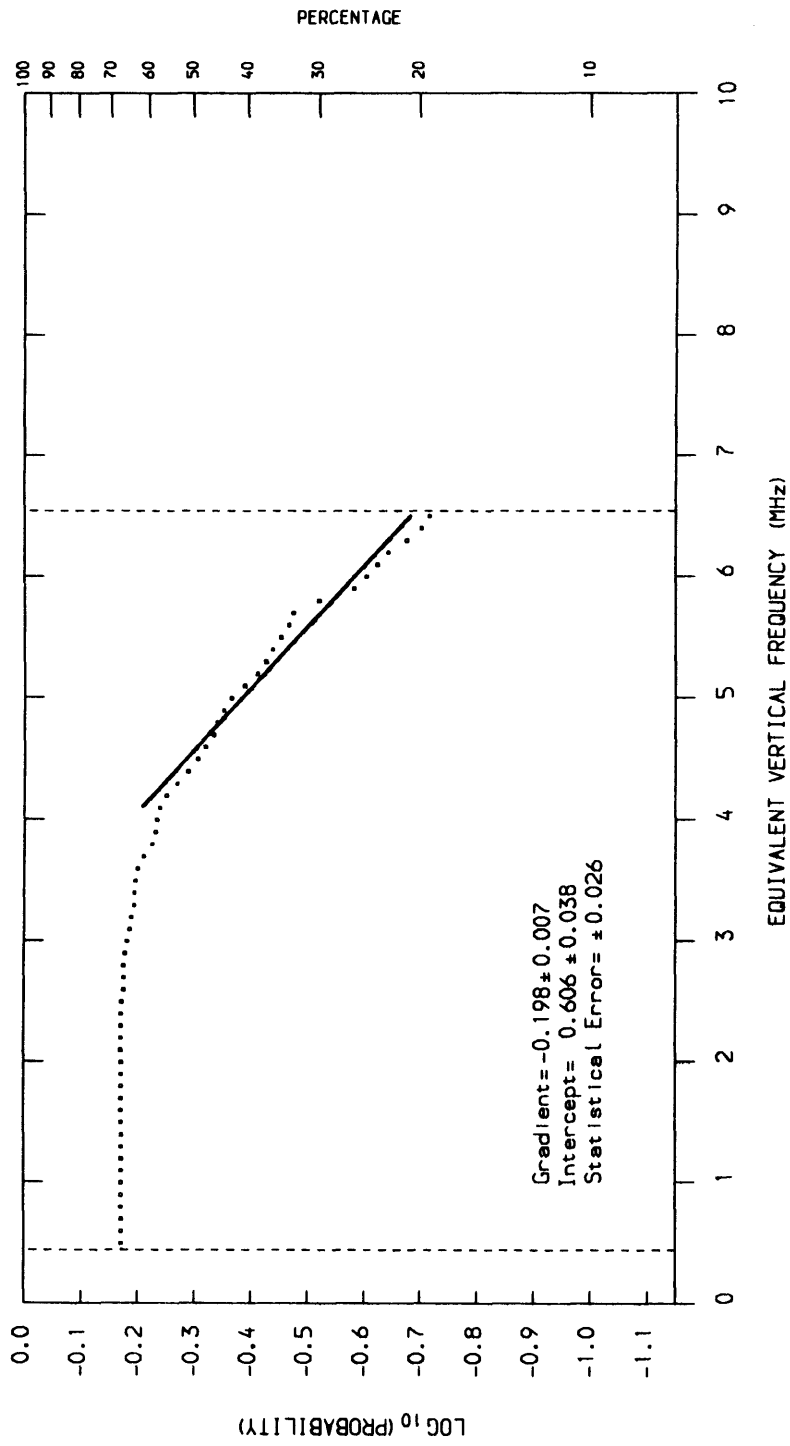


FIGURE 4.3 Phillips' Rule as applied to the Bodø/Wick propagation path, for the August campaign sporadic-E data.

statistical error is of a significantly small magnitude (0.026) to validate the straight line gradient and hence confirm the adherence of the August Campaign Bodø/Wick propagation data to Phillips' Rule. It should also be noted that the intercept constant 'a' from Equation 4.1, is generally non-zero (Smith, 1957).

### 4.3.2 The Diurnal Occurrence of Sporadic-E Layers

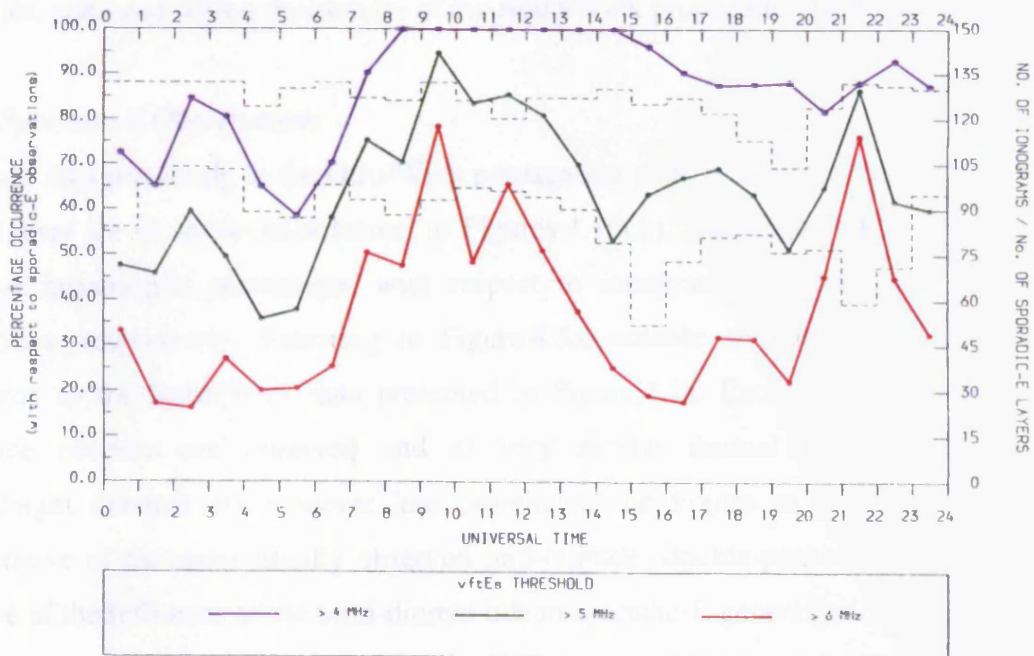
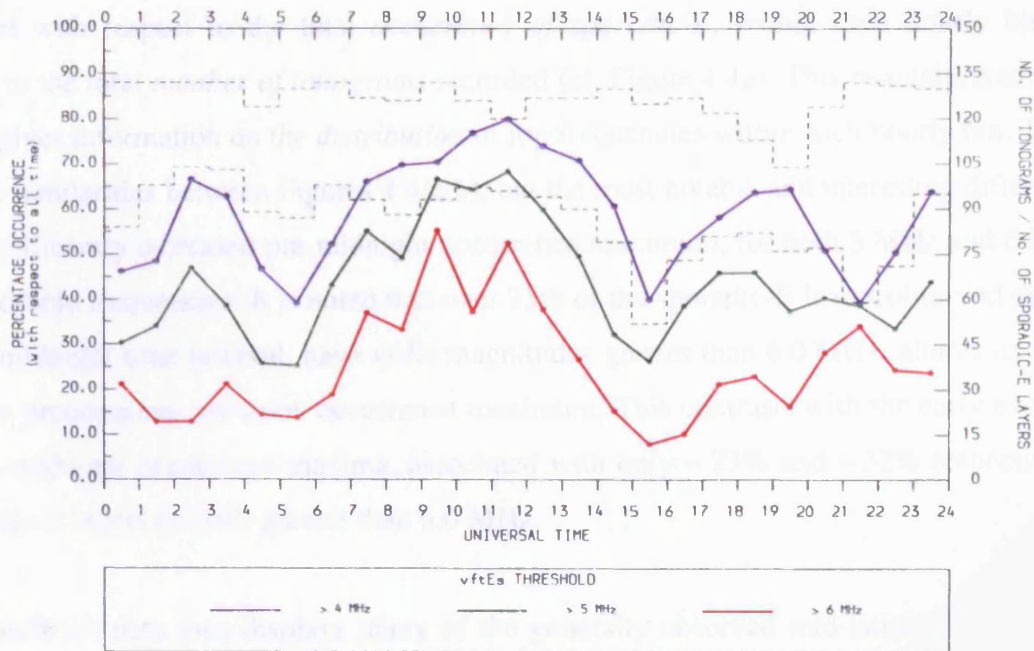
#### *The Occurrence of Sporadic-E as recorded over the Bodø/Wick Propagation Path*

Figure 4.4a presents sporadic-E occurrence details pertaining to the Bodø/Wick propagation path during the August campaign. Three plots are presented, each being the hourly percentage occurrence of sporadic-E, for equivalent vertical incidence top frequencies,  $\nu_{fEs}$ , greater than a given threshold magnitude, i.e. 4.0 MHz, 5.0 MHz and 6.0 MHz. The common abscissa is Universal Time (UT). The number of ionograms recorded per hour, during the 11 day campaign, and the number of sporadic-E layers similarly observed, are also presented in Figure 4.4a as dotted lines. Approximately two-thirds (67.8%) of ionograms recorded a measurable sporadic-E trace.

The most significant observation is the broad, pre-midday occurrence maximum, between 10:00 UT and 12:00 UT, noted for each of the  $\nu_{fEs}$  threshold plots. This occurrence signature is commonly observed during the summer months at mid-latitudes (e.g. Dyer, 1972; Harris and Taur, 1972). Less clearly defined, is an early evening, secondary occurrence maximum, between 18:00 UT and 20:00 UT. This maximum is most easily observed for  $\nu_{fEs}$  magnitudes greater than 4.0 MHz., but is still distinct at the 5.0 MHz and 6.0 MHz  $\nu_{fEs}$  threshold magnitudes. Again, observations of this early evening maximum are widely noted in the literature (e.g. Smith, 1957; Baggaley, 1988).

The early evening maximum is less clearly defined due to the presence of a pre-midnight peak in occurrence, between 21:00 UT and 22:00 UT. This maximum is most notably observed, for  $\nu_{fEs}$  magnitudes greater than 6 MHz, and is not observed at all at the 4 MHz  $\nu_{fEs}$  threshold level. Of equal note is the post-midnight sporadic-E occurrence maximum, between 02:00 UT and 04:00 UT. This maximum is noted in each of the three  $\nu_{fEs}$  threshold plots, though of decreasing prominence for increasing  $\nu_{fEs}$  threshold frequencies.

A different perspective on these observations, is provided in Figure 4.4b. The data is of identical format to that depicted in Figure 4.4a, except that the percentage occurrence data is



FIGURES 4.4(a,b) Sporadic-E occurrence statistics, as observed over the Bodø/Wick oblique propagation path, for the duration of the August Campaign (cf. Table 4.1). The percentage occurrence is plotted with respect to all time (a) and with respect to all measurable sporadic-E observations (b). Within each Figure, the occurrence statistics are calculated for equivalent vertical top frequencies ( $vftE_s$ ) greater than three threshold magnitudes i.e. 4 MHz, 5 MHz and 6 MHz.

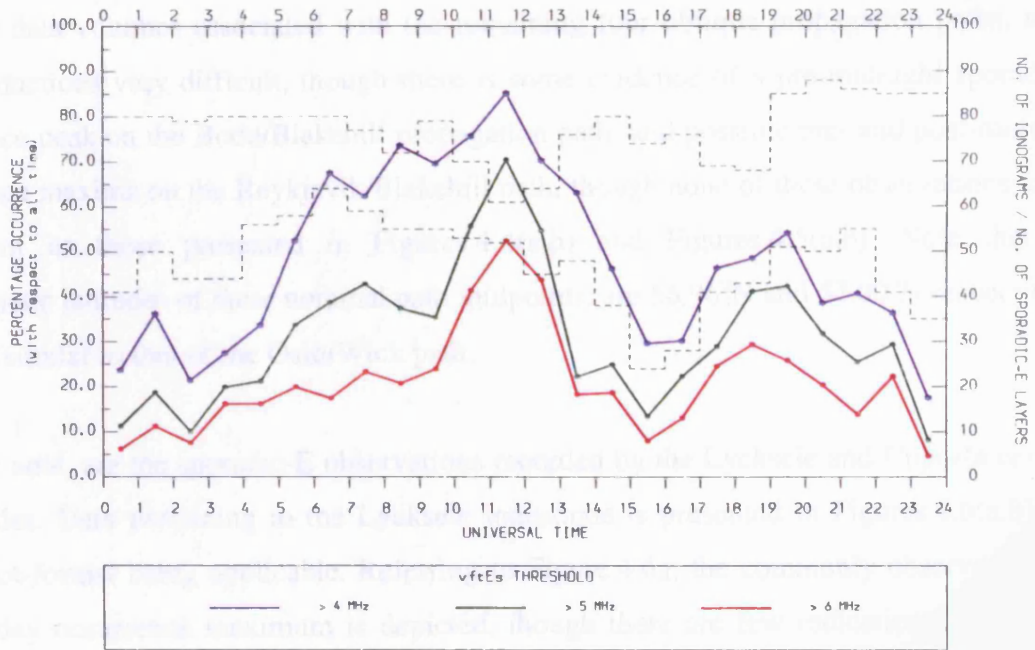
calculated with respect to the total *occurrence of sporadic-E*, within each hourly bin, as opposed to the total *number of ionograms* recorded (cf. Figure 4.4a). This re-interpretation of the data gives information on the *distribution* of top frequencies within each hourly bin. There are many similarities between Figures 4.4(a,b), but the most notable and interesting difference is the significantly increased pre-midnight occurrence maximum, for both 5 MHz and 6 MHz *ν<sub>f</sub>Es* threshold frequencies. It is noted that over 75% of the sporadic-E layers observed during this pre-midnight time interval, have *ν<sub>f</sub>Es* magnitudes greater than 6.0 MHz, almost as great as for the predominant pre-noon occurrence maximum. This contrasts with the early evening and post-midnight occurrence maxima, associated with only ~ 27% and ~ 32% respectively, of sporadic-E layers of *ν<sub>f</sub>Es* greater than 6.0 MHz.

The Bodø/Wick data thus displays many of the generally observed mid-latitude sporadic-E occurrence characteristics associated with the summer months. In addition however, minor pre- and post-midnight occurrence maxima are also noted, with the former being dominated by high *ν<sub>f</sub>Es* values. The following Section briefly compares these observations with data recorded over a further five oblique sounding paths, deployed during the August campaign, as specified in Table 4.1. The observations are also compared to data derived from vertical ionosondes, stationed within the vicinity of the Bodø/Wick propagation path (cf. Figure 4.1).

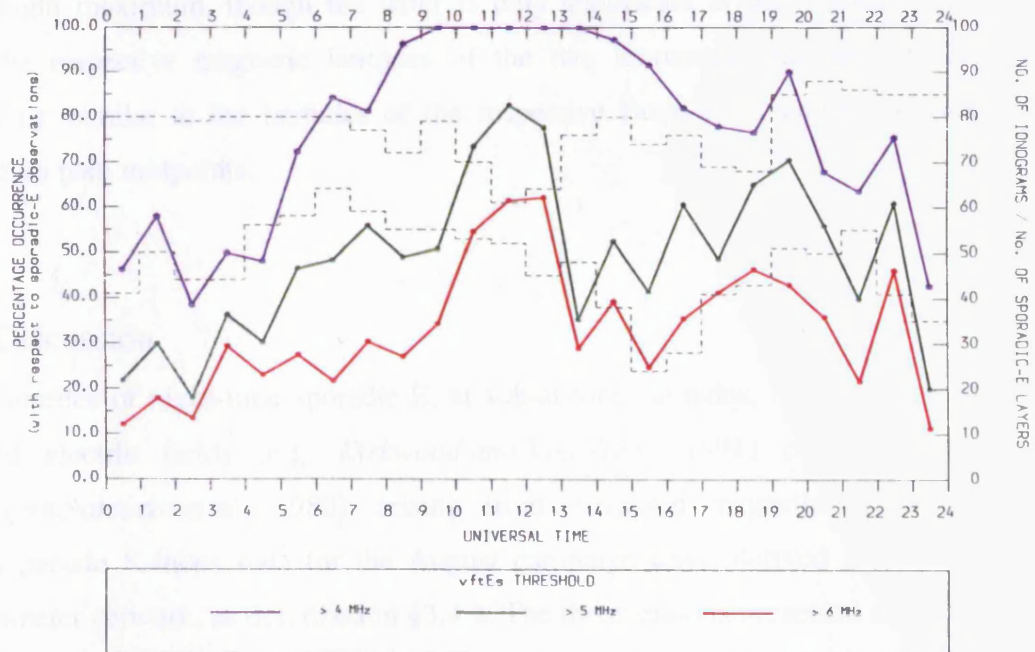
#### *Further Sporadic-E Observations*

Sporadic-E data pertaining to the Oslo/Wick propagation path, is depicted in Figures 4.5(a,b). These Figures are of an identical format to Figures 4.4(a,b), with Figures 4.5(a,b) presenting sporadic-E occurrence percentages with respect to ionogram recordings and sporadic-E observations, respectively. Referring to Figure 4.5a, notable similarities are observed in comparison to the Bodø/Wick data presented in Figure 4.4a. Each of the four sporadic-E occurrence maxima are observed and at very similar diurnal times. The pre- and post-midnight maxima are however less prominent, the Figure as a whole being more representative of the more usually observed mid-latitude ‘double-peaked’ occurrence plots, indicative of the influence of the semi-diurnal tide in sporadic-E generation (cf. §2.3.6).

However, referring to Figure 4.5b, a similar, if not so prominent characteristic, is noted for the pre-midnight occurrence maxima, as compared to Figure 4.4b, i.e. the maxima is proportionately more dominated by higher *ν<sub>f</sub>Es* layers, than seemingly is the case for other hourly bins. Note that the difference in magnetic latitude between the nominal Bodø/Wick and Oslo/Wick propagation path midpoints, is more than 4°, i.e. 60.78°N versus 56.55°N respectively (cf. Table 4.3). This latter aspect is discussed later.



(a)



(b)

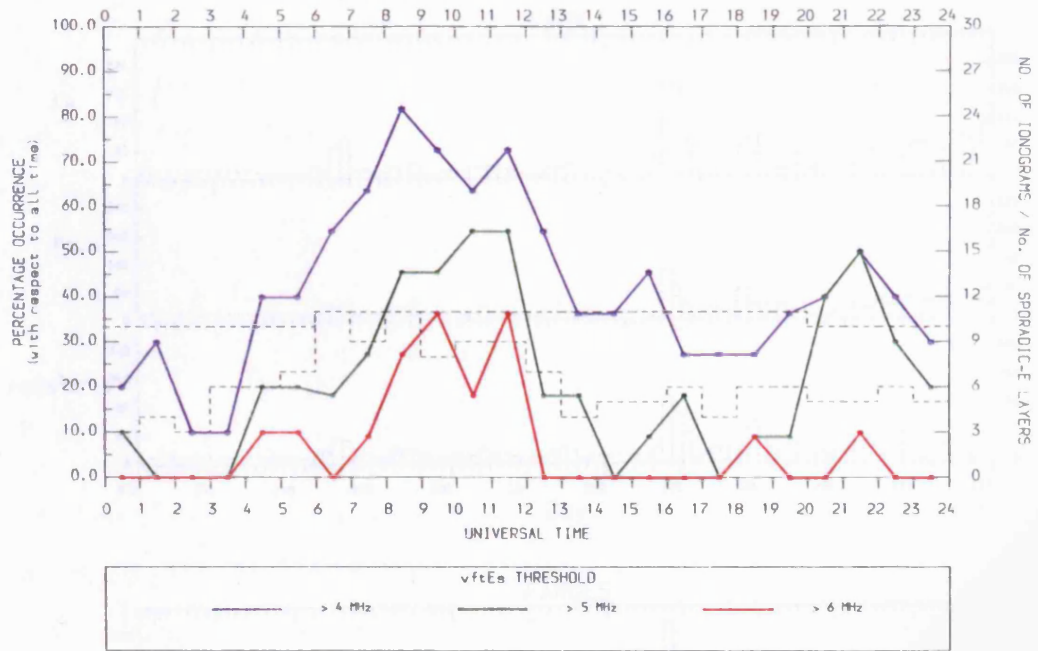
FIGURES 4.5(a,b) As for Figures 4.4(a,b) but plotted for the Oslo/Wick oblique propagation path.

The low data volumes associated with the remaining four oblique propagation paths, make valid deductions very difficult, though there is some evidence of a pre-midnight sporadic-E occurrence peak on the Bodø/Blakehill propagation path, and possible pre- and post-midnight occurrence maxima on the Reykjavik/Blakehill path, though none of these observations are as significant as those presented in Figures 4.4(a,b) and Figures 4.5(a,b). Note that the geomagnetic latitudes of *these* nominal path midpoints, are  $56.96^{\circ}\text{N}$  and  $57.00^{\circ}\text{N}$  respectively, i.e. very similar to that of the Oslo/Wick path.

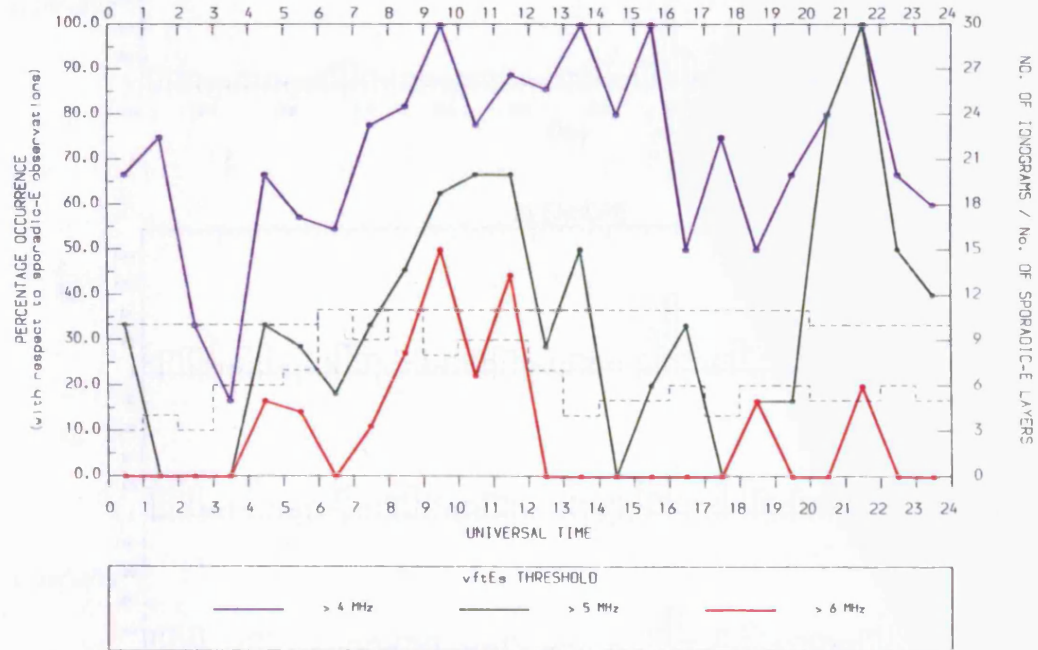
Of more note, are the sporadic-E observations recorded by the Lycksele and Uppsala *vertical* ionosondes. Data pertaining to the Lycksele ionosonde is presented in Figures 4.6(a,b), the usual plot format being applicable. Referring to Figure 4.6a, the commonly observed, broad pre-midday occurrence maximum is depicted, though there are few indications of an early evening occurrence maximum. The pre-midnight occurrence maximum is however very prominent, albeit at the 5 MHz threshold level, the percentage occurrence greater than 6 MHz being much reduced. These observations are replicated in Figure 4.6b. In both Figures, the presence of a post-midnight occurrence maxima is largely indeterminable. The Uppsala data is less noteworthy but an early evening occurrence maximum is observed alongside a pre-midnight maximum, though the latter is only significant at the 4 MHz *vftEs* threshold level. The respective magnetic latitudes of the two ionosonde stations are  $61.17^{\circ}\text{N}$  and  $56.15^{\circ}\text{N}$  i.e. similar to the latitudes of the respective Bodø/Wick and Oslo/Wick nominal propagation path midpoints.

### 4.3.3 Discussion

The occurrence of night-time sporadic-E, at sub-auroral latitudes, is primarily explained by enhanced electric fields (e.g. *Kirkwood and Von Zahn*, 1991) or precipitation events (e.g. *Besprozvannaya et al.*, 1980), arising from increased magnetic activity. Figure 4.7 presents pseudo K-index data for the August campaign days, derived from the SAMNET magnetometer network, as described in §3.4.2. The three stations presented are Nordli, Faroes and Glenmore i.e. the stations surrounding the nominal Bodø/Wick propagation path midpoint. By employing these K-indices, it is possible to determine the magnetic activity at a more localised level. The pseudo indices are calculated for each 3-hour period of the 11 day campaign, and for the H, D and root-sum-square value of the H and D geomagnetic field components. Stared data points indicate omitted K-indices due to uncertainty in the raw geomagnetic field data.



(a)



(b)

FIGURES 4.6(a,b) As for Figures 4.4(a,b) but plotted for the Lycksele vertical ionosonde.

DAY:216 TO DAY:226 YEAR:1988

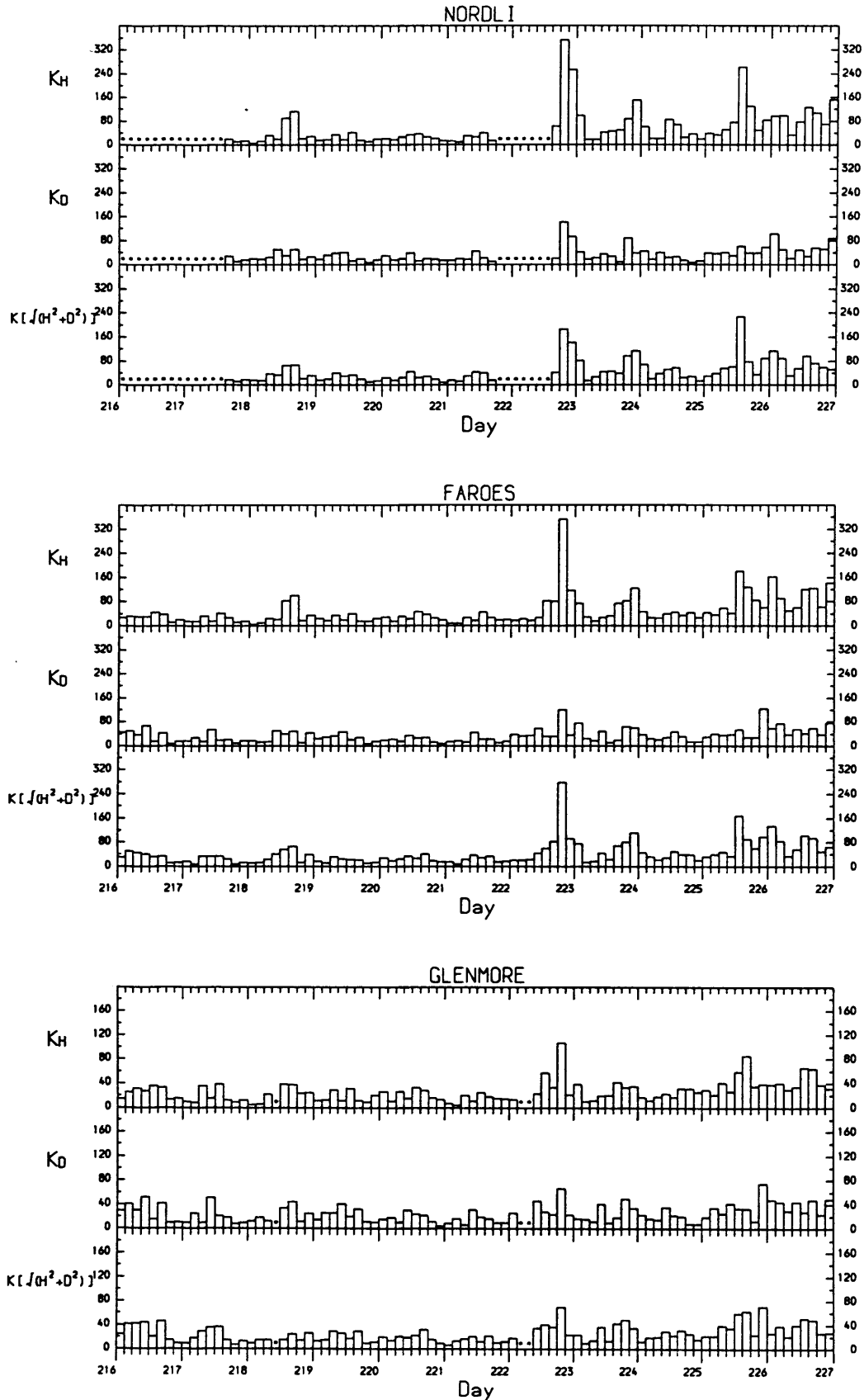


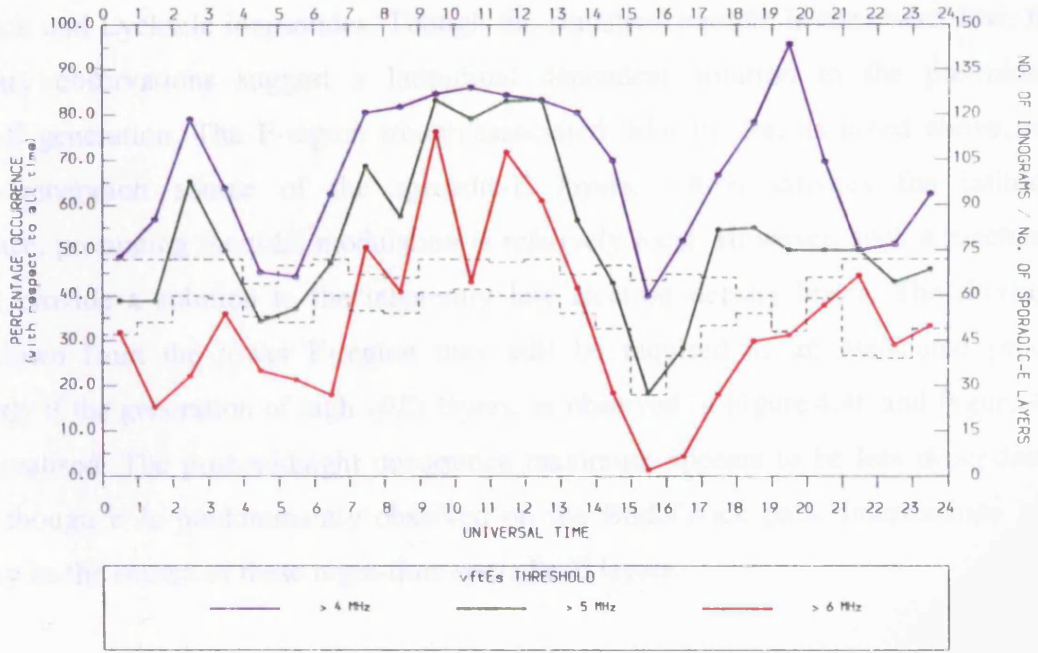
FIGURE 4.7 Pseudo K-index values, compiled from the SAMNET magnetometer network, for the three stations of closest proximity to the nominal Bodø/Wick propagation path midpoint, for the days of the August Campaign (cf. Table 4.1). The magnetic activity is generally 'quiet', or 'moderately disturbed', with 'disturbed' activity noted during the pre-midnight hours of days 222 and 225.

The August campaign is clearly characterised by a magnetically quiet period, up to the evening of day 222. A substorm event is noted during the night of day 222, followed by a few days of mildly disturbed conditions. Only the evening/nights of days 222 and 225 experience true magnetically disturbed conditions. Planetary  $K_p$ -indices correspond with these observations, with more than 85% of all indices being less than 3 $\sigma$ , and the maximum disturbance of 4 $\sigma$  being recorded for only three index values, on days 222 and 225. The campaign as a whole may thus be termed 'predominantly magnetically quiet'.

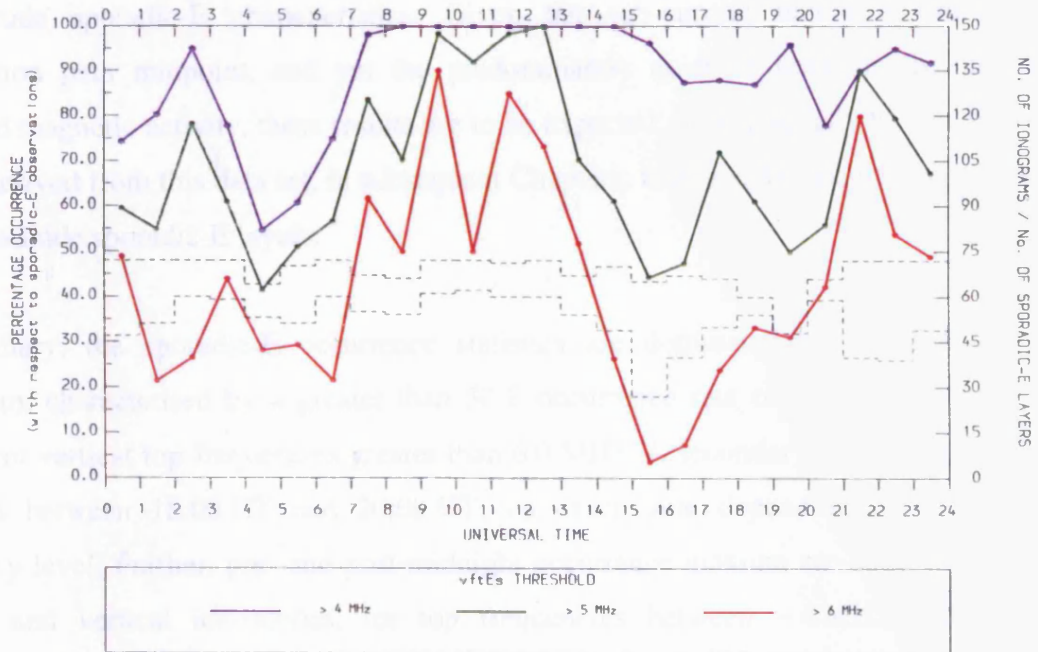
The pre- and post-midnight sporadic-E occurrence maxima, cannot therefore be explained by the aforementioned auroral zone influences. This assertion is fully justified by re-plotting Figures 4.4(a,b) for days 216-221 i.e. the most magnetically quiet days of the campaign. The ensuing results, presented in Figures 4.8(a,b), are largely identical to those observed in Figures 4.4(a,b), given some expected statistical variance.

The difficulty with the generation of night-time sporadic-E layers at mid-latitudes or sub-auroral, or even auroral latitudes, during quiet magnetic times, is the absence of sufficient ionisation within the E-region, with densities reducing to as low as  $5 \times 10^{-9} \text{ m}^{-3}$  (Turunen *et al.*, 1993) (cf. Figure 1.8). However, night-time sporadic-E has been explained in terms of ionisation being driven down from the F-region, by northward neutral winds (Rowe, 1974), forming initially so called 'intermediate' layers (e.g. Mathews *et al.*, 1997). Alternatively, the presence of multiple tidal modes arising from the passage of the F-region trough, has been cited as a possible explanation of pre-midnight, high latitude sporadic-E layers observed during times of extremely quiet magnetic activity (Turunen *et al.*, 1993). Rodger *et al.* (1983) also associate sporadic-E observations with the F-region trough, for a range of magnetic activity conditions. The night-time generation of gradient-drift irregularities within the high electron density gradients of sporadic-E layers (Tanaka and Venkateswaren, 1982a) may explain high critical frequency magnitudes, if not the existence of the layer in the first instance. However, such sporadic-E related, irregularity observations are considered rare (Haldoupis and Schlegel, 1993) due to the very specific conditions necessary for their generation (Woodman *et al.*, 1991), and hence are unlikely to explain the relatively extensive night-time occurrence characteristics of sporadic-E, observed over the Bodø/Wick propagation path.

With reference to the observations determined from Figures 4.4(a,b) to 4.6(a,b), a latitudinal effect was clearly noted, particularly with respect to the pre-midnight occurrence maximum, the most pronounced examples of this maximum being observed at the higher latitudes, by the



(a)



(b)

FIGURES 4.8(a,b) As for Figures 4.4(a,b) but plotted for the magnetically quiet days of 216 to 221.

Bodø/Wick and Lycksele ionosondes. Though the statistical sample is somewhat low, these preliminary observations suggest a latitudinal dependent solution to the pre-midnight sporadic-E generation. The F-region trough-associated tidal modes, as noted above, are a possible generation source of the sporadic-E layers, which satisfies the latitudinal dependence, presuming the tidal modulation is relatively local. However, such a mechanism does not provide a solution to the inherently low electron density levels. The driving of plasma down from the lower F-region may still be required as an associated process, particularly if the generation of high *vftEs* layers, as observed in Figure 4.4b and Figure 4.6b, is to be realised. The post-midnight occurrence maximum appears to be less dependant on latitude, though it is predominantly observed on the Bodø/Wick path. Intermediate layers alone may be the source of these night-time sporadic-E layers.

#### 4.4 Summary

The results presented herein demonstrate that the sporadic-E occurrence data, as recorded over the Bodø/Wick propagation path, during the August campaign, is defined primarily by mid-latitude sporadic-E characteristics. Given the sub-auroral nature of the nominal propagation path midpoint, and yet the predominantly quiet or occasionally moderately disturbed magnetic activity, these results are to be expected. It may equally be concluded that results derived from this data set, in subsequent Chapters, may also be taken as representative of mid-latitude sporadic-E layers.

In summary, the sporadic-E occurrence statistics are dominated by a broad, pre-noon maximum, characterised by a greater than 50% occurrence rate of sporadic-E layers, with equivalent vertical top frequencies greater than 6.0 MHz. A secondary occurrence maximum is noted between 18:00 UT and 20:00 UT, its exact time depending on the threshold frequency level. Further, pre- and post-midnight occurrence maxima are observed with both oblique and vertical ionosondes, for top frequencies between ~4 MHz and ~6 MHz, depending on the propagation path. Intermediate layers and tidal components may be responsible for the generation of these latter night-time sporadic-E layers, the majority of which are observed during relatively quiet magnetic activity.

Finally, it is emphasised that the nature and definition of sporadic-E at mid-latitudes, is of a height-confined layer of plasma intensification, with respect to the ambient plasma density, and that this intensification arises from the vertical compression of plasma by neutral winds

(cf. §2.3.3). The plasma *structure* characteristics of these sporadic-E layers, observed over *any* diurnal time, may consequently be expected to be similar to each other, and this is equally applicable to sporadic-E observations made over the Bodø/Wick propagation path, during the August campaign when magnetic activity was predominantly quiet.

# Chapter 5

## The Sporadic-E Signal Strength Profile

### 5.1 Introduction

In Chapter 2 (§2.2.2) the general morphology of sporadic-E was considered. This information, though important, is insufficient to fully predict and utilise an oblique sporadic-E propagation circuit. To accurately forecast the reception quality of such a circuit, an understanding of the signal strength versus Probing Frequency profile is essential.

The signal strength-frequency profile of mid-latitude sporadic-E layers is significantly different from that of the Chapman-like ‘normal’ E-layer (cf. §1.3.2). In the latter case, *total* reflection from an incident Probing Frequency might be expected, for increasing frequencies up to  $f_oE$ , the critical frequency of the layer. For greater Probing Frequencies, total penetration of the layer will be observed. Reflection characteristics from sporadic-E layers are considerably more complex.

Mid-latitude sporadic-E layers are largely generated from transport processes, specifically, neutral wind generated Lorentzian forces acting on the neutrally coupled ions. With suitable neutral wind profiles, *existing* ionisation is compressed into a layer with narrow height range, but large horizontal extent, as described by the Windshear theory (cf. §2.3.3). However, the plasma density within the sporadic-E layer may not be uniform, but may instead be impregnated with ‘clouds’ of plasma density *enhancements*. Few sporadic-E layers may thus be considered as having a homogenous plasma structure.

The ‘cloud’ theory of sporadic-E (e.g. *Miller and Smith, 1978*) accounts for these plasma inhomogeneities, though no single formation mechanism is considered to prevail under all circumstances. Most impose a horizontal, as well as vertical, structure on the neutral wind, arising from interference between the dominant semi-diurnal tidal mode and gravity waves (e.g. *Chimonas, 1971; Nygrén et al., 1990*). The compressional Lorentzian forces are thus non-uniform in the horizontal plane, and so account for ‘clouds’ of differing plasma densities.

The ‘cloud’ theory of sporadic-E may thus be considered an enhancement to the Windshear theory, which only considers uniform horizontal winds. A more comprehensive discussion of the plasma structure of sporadic-E layers is to be found in §2.4.2.1.

The presence of ‘clouds’ of enhanced plasma density, embedded within an otherwise near homogenous plasma density layer, leads to the observation of a ‘blanketing frequency’,  $fbEs$  (cf. §2.2.1) and a ‘partial transparency’ range of Probing Frequencies, between  $fbEs$  and the top frequency of the sporadic-E layer,  $ftEs$  (cf. §2.4.2). The blanketing frequency represents the plasma frequency (cf. §1.4.1) of the homogenous ambient plasma density of the Es-layer. The ‘partial transparency’ range of frequencies arises from the plasma ‘cloud’ structure within the layer.

It thus follows that a near uniform reflection coefficient  $\sim 1$ , may be expected, for Probing Frequencies *up to* the blanketing frequency, with the coefficient reducing for increasing Probing Frequencies between  $fbEs$  and  $ftEs$ . By definition, the reflection coefficient is zero at  $ftEs$ . The nature of the decrease in reflection coefficient, within this ‘partial transparency’ range of frequencies, depends on the number distribution of clouds with respect to their inherent plasma density. This ‘cloud population’, with respect to plasma density, is investigated within this Chapter.

The signal strength received from sporadic-E layers, at a fixed Probing Frequency, exhibits great temporal variability, even at high temporal resolutions  $\sim$  seconds (*Chessell et al.*, 1973). To investigate the signal strength profile and hence the plasma structure of sporadic-E layers, a statistical approach is thus required. In this Chapter, the ‘partial transparency’ frequency region is studied by noting the signal strength received from a variety of sporadic-E layers, with a wide distribution of  $ftEs$  magnitudes. The Probing Frequency (PF) is generally fixed and in effect, the signal strength is being noted over a range of *normalised* Probing Frequencies i.e.  $(PF/ftEs)$ . The study of the plasma structure of sporadic-E with respect to *normalised* signal strength profiles, is considered more valid than considering signal strength variation with respect to *absolute* differences in  $ftEs$ , and is discussed in more detail later.

The Chapter begins however, by demonstrating the fundamental nature of the ‘partial

transparency' region of sporadic-E layers, i.e. that the signal strength (dB) received at a given *fixed* Probing Frequency, statistically increases, for increasing *ftEs* magnitudes, for Probing Frequencies greater than the blanketing frequency, *fbEs*. For Probing Frequencies less than *fbEs*, an approximate signal strength threshold is observed. Subsequent investigations enable the extent of the 'partial transparency' frequency range to be estimated, *as a relative proportion* of the sporadic-E top frequency. The validity of the data set is verified by comparison with a frequently quoted signal strength model (*Miya and Sasaki, 1966; Miya, Shimizu and Kojima, 1978*), differences being explained in terms of the pertinent reflection characteristics. Finally, with consideration for *other* sporadic-E reflection mechanisms, a gaussian 'cloud population' model is demonstrated to significantly predict the *normalised* sporadic-E signal strength profile.

As acknowledged in Chapter 4, the most significant data set available for study is that from the Bodø/Wick oblique propagation path, recorded during August, 1988. Investigations will concentrate therein. During this observation period, magnetic activity is predominately quiet, with an occasional disturbed event (cf. Figure 4.7). In consideration of this, and the morphological characteristics of the said propagation circuit (cf. §4.3), the internal plasma structure of the sporadic-E layers, recorded during this period, may be taken as generally typical for quiescent mid-latitude conditions.

The exact details of the transmitter and receiver gains and loss factors are unknown, and hence although the signal strength measurements are absolute (cf. §3.3.2), attenuation details are not available. While this prevents calculation of absolute reflection coefficients, it is of little consequence to the following investigations. The statistical variation of observed signal strength, at a largely fixed Probing frequency, is considered adequate to study the sporadic-E signal strength characteristics within the 'partial transparency' frequency range, and consequently enable deductions to be made about the associated plasma (cloud) structure.

## **5.2 Analysis Procedure**

The oblique ionosonde records group delay and signal strength, for ionospherically reflected signals, at oblique Probing Frequencies (PF) that scan between 2.1 MHz and 29.9 MHz (cf. §3.3.2). For each ionogram, the signal strength recorded at any given PF, is a summation

over all traces received at that PF, as described in §3.3.2. Only Probing Frequencies above the *E/F-region cut-off frequency*, of each ionogram, are defined to be exclusively from the sporadic-E trace (cf. §3.3.2). In the proceeding analysis, only these signal strengths and Probing Frequencies are considered.

The influence of the *E/F-region cut-off frequency* will vary throughout the day (cf. §1.3.2), and on the Bodø/Wick path, effectively restricts (oblique) observations of sporadic-E to *ftEs* values greater than ~15 MHz, particularly, but not exclusively, during the daytime. The ionosonde imposes further constraints. As the maximum Probing Frequency transmitted is 29.9 MHz, sporadic-E traces recorded with a finite signal strength at this PF, are omitted from the data set, their *ftEs* in effect being undefined.

Despite the constraints above, the ensuing data set is still considerable, amounting to over 1200 individual observations of sporadic-E, over the 11 campaign days, the resolution of ionogram recordings being 5 minutes. Comparison of the signal strength returns from the range of sporadic-E layers, is achieved by noting the value determined at a nominated Probing Frequency. By utilising a fixed Probing Frequency in this way, frequency dependent, signal strength fluctuations, due to systematic hardware features or ambient ionospheric characteristics (e.g. absorption (cf. §3.2.7)) are avoided. The few results compiled from a composite of Probing Frequencies, are analysed with due regard to the aforementioned features. The error associated with each signal strength measurement is  $\pm 1.5$  dB (*RCS-5 Operating and Service Manual*) and it is assumed that a linear and stable relationship exists between the receiver signal strength input and output, over the whole 60 dB recording range (cf. §3.3.2).

The PF is selected to maximise the data set and to give representative results. Too low a value will be affected by the diurnally varying *E/F-region cut-off frequency*, while higher values will unduly restrict the data set, noting that in addition, the PF must obviously be less than the *ftEs*. Note also that values of PF above ~20 MHz will begin to introduce temporal biasing, higher *ftEs* values being observed at particular times of the day (cf. Chapter 4). A Probing Frequency between 16 MHz and 20 MHz was considered optimum, with a value of 17.0 MHz being generally employed throughout this Chapter.

## 5.3 Introductory Observations

### 5.3.1 The General Signal Strength versus $ftEs$ Relationship

Figure 5.1 exemplifies the general relationship between the sporadic-E top frequency,  $ftEs$ , and the signal strength observed at a designated Probing Frequency, equal to 17.0 MHz in this study. The Figure pertains to all indicated sporadic-E recordings made during the August, 1988 campaign. Top frequency values are partitioned in 0.5 MHz bins, and the median signal strength (MSS) calculated. Signal strength quartiles and data bin counts are also plotted.

It is clear that a proportional relationship exists between the probed sporadic-E signal strength (dB) and  $ftEs$ , for the greater part of the Es-layer top frequencies. For  $ftEs$  values greater than about 27 MHz, proportionality breaks down, with the signal strength tending to a threshold magnitude  $\sim 42$  dB. Statistically, the PF value of 17.0 MHz manifestly falls within the ‘partial transparency’ range of frequencies, for sporadic-E layers with  $ftEs$  magnitudes less than  $\sim 27$  MHz. The *relative* magnitude of the PF is noted, by definition, to decrease with increasing  $ftEs$ , tending increasingly towards the statistical blanketing frequency of the higher  $ftEs$  layers. For sporadic-E layers with top frequencies greater than  $\sim 27$  MHz, the PF is considered *less than* the statistical blanketing frequency of these Es-layers, the signal strength now being approximately constant with respect to the *relative* Probing Frequency.

If the PF is varied, so too will the upper *range* of  $ftEs$  magnitudes corresponding to the signal strength threshold: the greater the PF, the smaller the range. For Probing Frequencies greater than  $\sim 20$  MHz, no signal strength threshold is observed, the difference between the PF and the maximum  $ftEs$  values being smaller than the associated ‘partial transparency’ frequency range. The choice of Probing Frequency thus not only refines the magnitude of the data set, but also the ensuing signal strength characteristics observed.

Each individual sporadic-E observation may be characterised by its own idiosyncratic relationship between  $fbEs$  and  $ftEs$ . The preliminary results presented above however, demonstrate a *statistical* relationship between the median signal strength (MSS), observed at a fixed Probing Frequency, and  $ftEs$ , within the ‘partial transparency’ range of frequencies. No significant temporal variations of the MSS- $ftEs$  relationship were noted e.g. diurnally, between daytime and night-time, or between different campaign days, though this part of the analysis was susceptible to the effects of statistical fluctuations, due to the limited data set. Finally, attention is brought to the distribution of signal strengths at the higher  $ftEs$  values, the

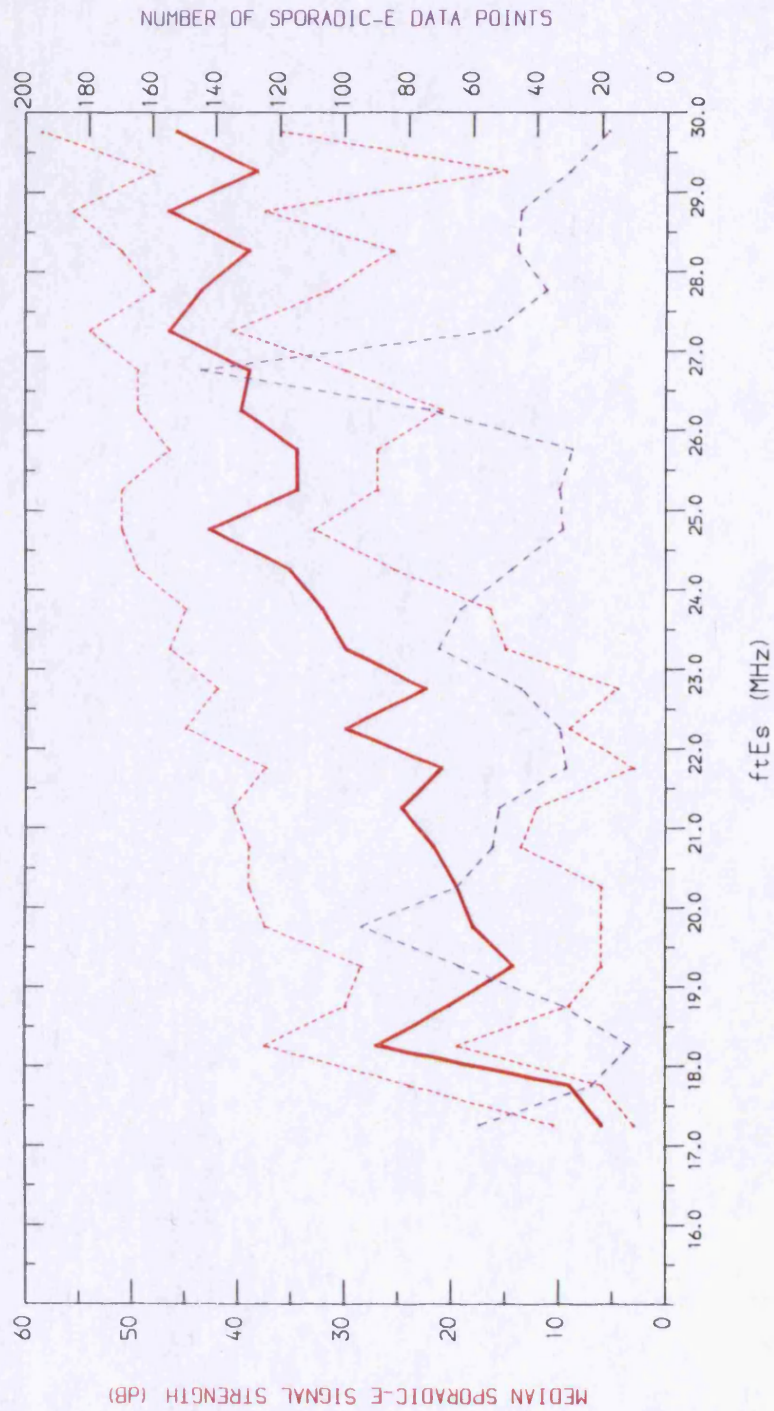


FIGURE 5.1 The relationship between  $ftEs$  and the median signal strength (continuous red plot), determined at a Probing Frequency of 17.0 MHz. The quartile signal strengths (broken red plots) and the data bin count (broken blue plot) are also indicated. The data set pertains to all sporadic-E recorded and scaled over the Bodø/Wick propagation circuit, during August, 1988.

upper and lower quartiles being evenly spread about the median signal strength. There is thus no evidence of a systematic *equipment* signal strength threshold being approached. The results are instead a genuine manifestation of sporadic-E layer characteristics.

### 5.3.2 Diurnal Observations of Sporadic-E Signal Strength and *ftEs*

Having confirmed the statistical relationship between the top frequency of sporadic-E and its signal strength at a given Probing Frequency, it is instructive to discuss examples of the temporal evolution of the two parameters. Figures 5.2(a,b) plot the median *ftEs* and signal strength against Universal Time (UT), the data being binned on an *hourly* basis. The data count per bin is also indicated. In Figure 5.2a the whole campaign day range is considered, as in Figure 5.1. Figure 5.2b, presents data from day 219 alone. The maximum data count per bin is limited by the maximum ionogram recording rate of 12 per hour. In both plots, the signal strength is determined at a Probing Frequency of 17.0 MHz, as in Figure 5.1. For the majority of sporadic-E layers, this Probing Frequency is a constituent of the ‘partial transparency’ range of frequencies.

Considering Figure 5.2a, the zero-time-lag correlation coefficient between the *ftEs* and MSS plots, is 0.67, the results being significant at the 1% level. Thus even on an hourly basis, the *ftEs*-MSS relationship is very notable. It is also worthy of note that the correlation shows no hourly bias. Correlations at other Probing Frequencies within the 16-20 MHz band, give equally significant correlation coefficients between 0.61 and 0.82. The results presented here may justifiably be termed typical.

The results presented in Figure 5.2b are even more striking, they being recorded on a *single* day. A correlation was similarly calculated between the *ftEs* and MSS data, but in this case restricted to the first 15 hourly bins, so as not to be contaminated by hourly bins with no data. A correlation coefficient of 0.81 was determined, again at the 1% significance level. Putting *these* results in context, a correlation coefficient of 0.33 (greater than the 25% significance level) was calculated for a PF of 16.0 MHz, but for other PFs in the nominated band, coefficients between 0.66 and 0.81 were determined, and all at the 1% significance level. Some days display poor correlations, but this was largely due to the hourly range of continuous data being too small for meaningful calculations. Typical values of correlation coefficient are thus difficult to present. But day 219 is not unusual and the data pertaining to days 217, 220 and 223 give comparable and equally compelling results. In conclusion, the

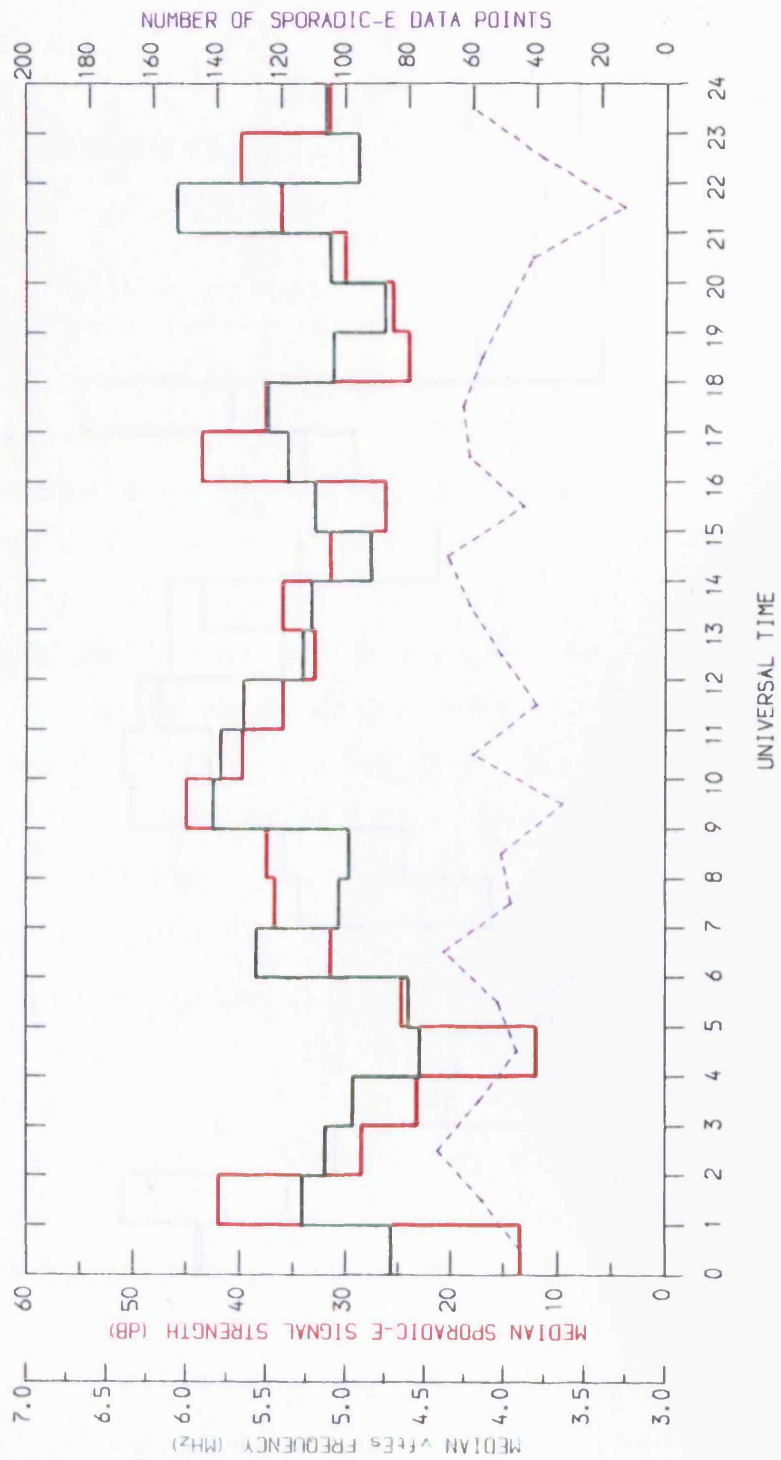


FIGURE 5.2a Plot to highlight the diurnal correlation of median  $fEs$  values with sporadic-E median signal strength (MSS), for the Bodø/Wick propagation circuit, during August, 1988. The plot is compiled for all the August campaign days, and for a Probing Frequency equal to 17.0 MHz.



relationship between  $f_iE_s$  and the signal strength is statistical but is observable over relatively small timescales.

## 5.4 The Partial Transparency Region of Sporadic-E

### 5.4.1 Introduction

The following analysis is to determine a statistical relationship between the sporadic-E blanketing frequency,  $f_bE_s$ , and the top frequency,  $f_iE_s$ , thus defining the 'partial transparency' range of Probing Frequencies, applicable to the *full range* of sporadic-E layers in this study. For vertical ionogram sounding, the blanketing frequency is determined relatively easily from its strict definition: no ionogram traces are observed at Probing Frequencies less than the blanketing frequency (*Piggot and Rawer, 1961*). From a plasma density viewpoint,  $f_bE_s$  may be determined by incoherent radar techniques, through the excitation of the plasma line (*Gordon and Carlson, 1976*). At oblique incidence, individual ionograms do not readily reveal details of the blanketing frequency. However, by appropriate superposition of the signal strength profiles, a signal strength threshold is clearly defined, from which the *relative* blanketing frequency, with respect to  $f_iE_s$ , may be determined. This method was employed herein and is described more fully below.

### 5.4.2 Data Definition

The signal strength of each sporadic-E ionogram trace, may be determined at all Probing Frequencies between the *E/F-region cut-off frequency* and  $f_iE_s$ . Thus at each Probing Frequency, (one discrete value for every 100 kHz scanned by the Chirp sounder (cf. §3.3.2)) a normalised Probing Frequency may be defined as  $(PF/f_iE_s)$ . In this study, all the signal strength measurements were binned with respect to the normalised Probing Frequency, each sporadic-E trace thus contributing many discrete observations to the complete data set. In effect, all the sporadic-E signal strength profiles are superposed with respect to the normalised Probing Frequency. In contrast it is noted that Figure 5.1 was compiled at a single Probing Frequency of 17.0 MHz, each sporadic-E trace contributing only a single signal strength measurement to the data set.

Figures 5.3(a,b) represent nominal daytime (0600-1800) and night-time (1800-0600) data, for the Bodø/Wick path. The median signal strength, plus quartiles, is plotted against the

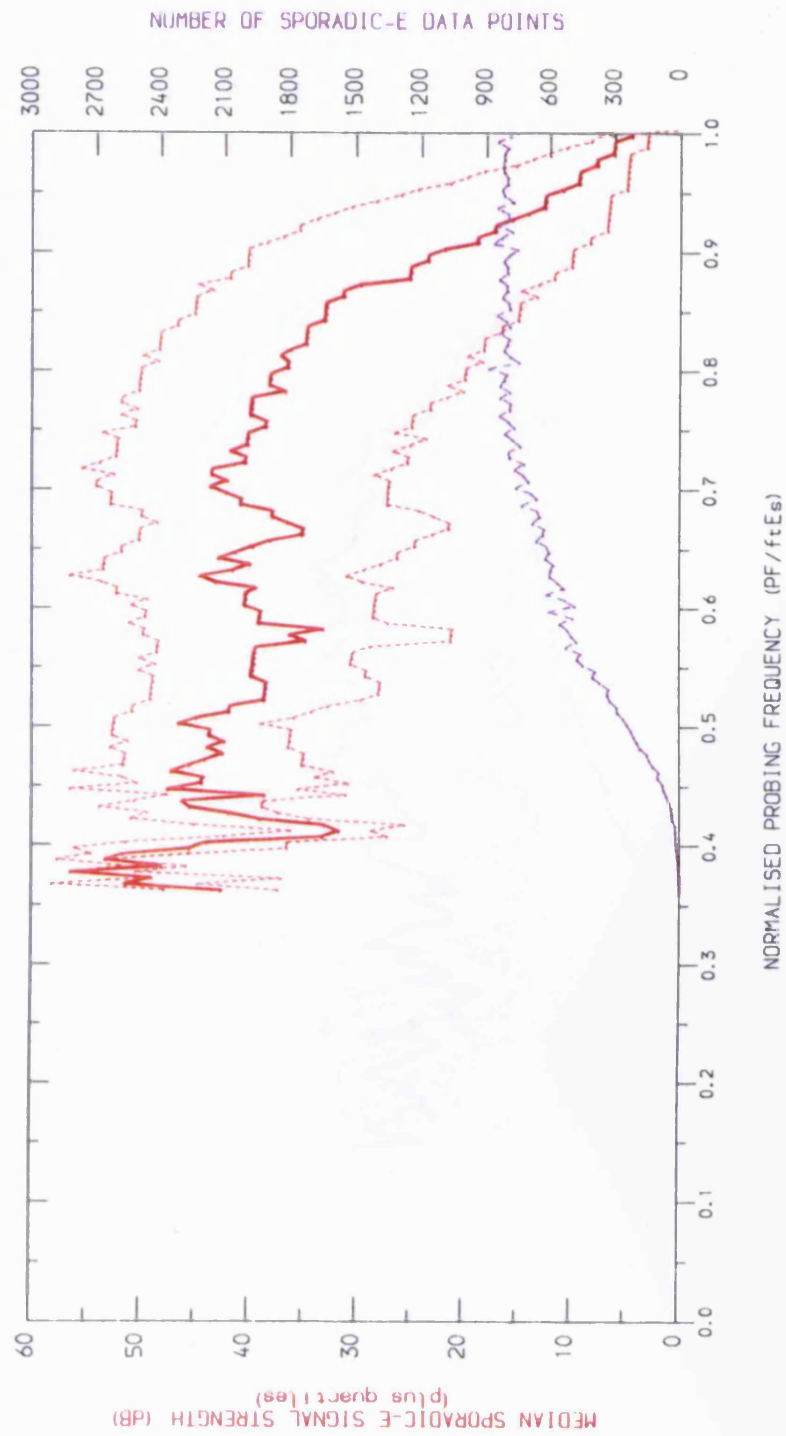


FIGURE 5.3a Superposition plot of the Bodø/Wick sporadic-E signal strength profiles recorded during daytime hours (06:00 – 18:00). Median signal strength (MSS) versus normalised Probing Frequency is presented. The nominal blanketing frequency may be deduced from the signal strength threshold magnitude.

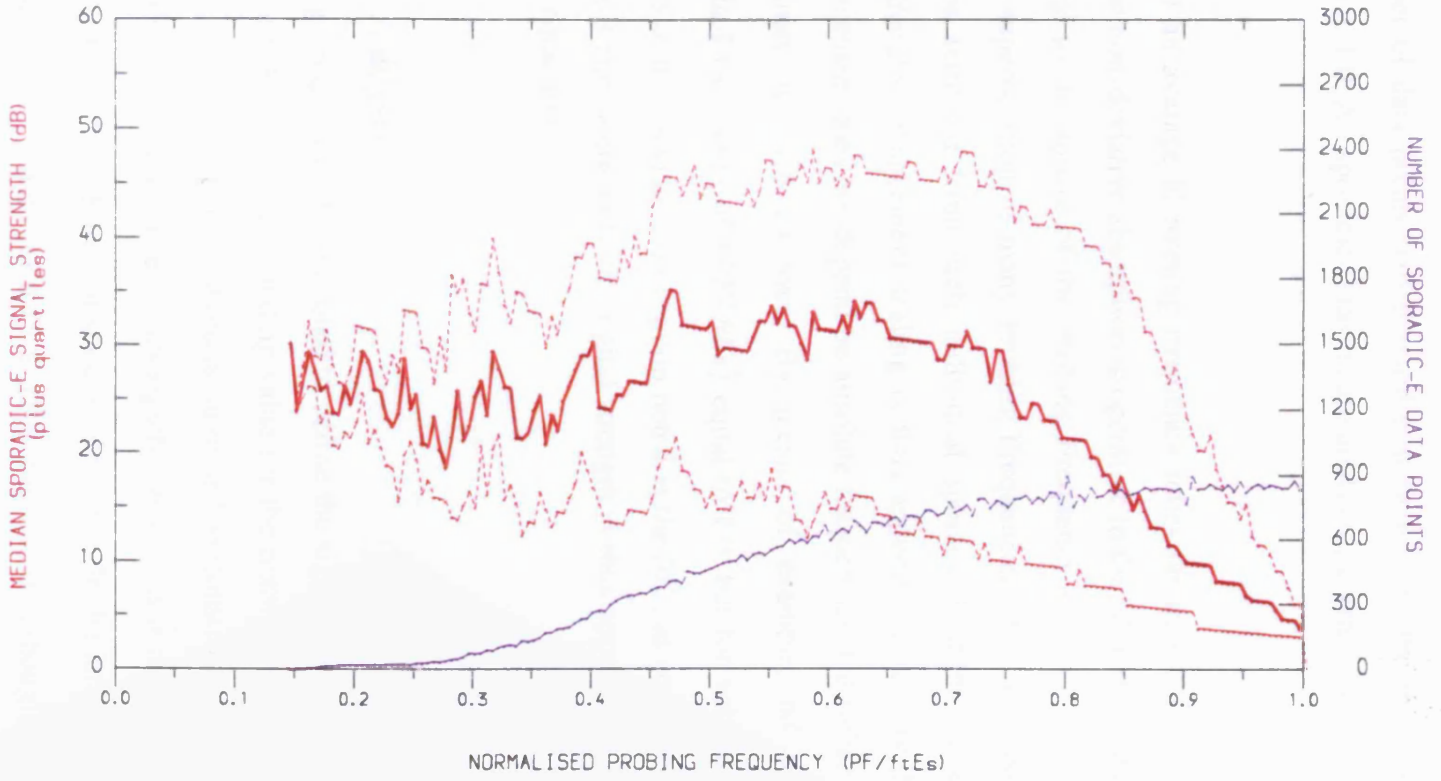


FIGURE 5.3b As for Figure 5.3a but for night-time hours (18:00 – 06:00).

normalised Probing Frequency ( $PF/ftEs$ ), with the data count per bin also being noted. By definition, the number of data points will maximise at or near to the maximum permitted value of ( $PF/ftEs$ ) i.e. 1.0. All sporadic-E layers are analysed, given the constraints imposed in §5.2.

The determination of an average blanketing frequency relies on an accurate signal strength *profile*. It is noted that non-deviative absorption is operative in the HF radio wave band, and is inversely proportional to the square of the Probing Frequency (cf. §3.2.7). As the data in Figures 5.3(a,b) is a superposition of many Probing Frequencies, it is required that *relative* absorption effects be removed from each individual sporadic-E layer, prior to abscissa binning. A signal strength enhancement scaling is thus applied accordingly. Note that the signal strength enhancement does not depend on absolute frequencies, but rather on the values of ( $PF/ftEs$ ) pertinent to each  $Es$ -layer. By means of example, no signal strength enhancement is applied for values of ( $PF/ftEs$ ) equal to 1.0; but for values of ( $PF/ftEs$ ) equal to 0.5, the ratio of non-deviative absorption noted at the  $ftEs$ , as compared to the PF, is  $(0.5)^2$  i.e. 0.25. A 6 dB enhancement to the signal strength is thus appropriate for normalised Probing Frequencies equal to 0.5.

### 5.4.3 Results and Analysis

A *normalised* Probing Frequency  $\sim 0.7$  is noted to define the signal strength threshold for the daytime plot in Figure 5.3a. The corresponding value for the night-time plot (Figure 5.3b) is  $\sim 0.6$ . The night-time signal strength threshold is more or less constant for decreasing values of ( $PF/ftEs$ ) down to  $\sim 0.45$  but then decreases significantly. This is not noted in Figure 5.3a though values of ( $PF/ftEs$ )  $\leq 0.45$  are statistically unreliable. In the latter Figure, there may also be a small rise in signal strength for  $0.45 \leq (PF/ftEs) \leq 0.7$ , though this is difficult to determine, the upper and lower quartiles presenting conflicting trends.

Figure 5.1 was compiled for both daytime *and* night-time data, and for the single Probing Frequency of 17.0 MHz. From *this* plot, a signal strength threshold value may be determined at a  $ftEs$  value  $\sim 27$  MHz, which corresponds to a normalised Probing Frequency  $\sim 0.63$ . This latter value is noted to be between the daytime and night-time normalised Probing Frequencies observed at the signal strength thresholds in Figures 5.3(a,b). Considering the temporal composition of Figures 5.1 as compared to Figures 5.3(a,b), the 17.0 MHz Probing

Frequency thus appears to give representative results, with respect to *all* Probing Frequencies and at all times.

As noted previously, the night-time plot in Figure 5.3b, is observed to extend to significantly lower values of  $(PF/ftEs)$ . This is determined by lower *E/F-region cut-off frequencies* (cf. §5.2) during the night and is largely incidental. Of more note is the decrease in median signal strength below the threshold signal strength value, at normalised Probing Frequencies below  $\sim 0.45$ . As non-deviative absorption has already been accounted for, antenna gain characteristics are deemed responsible (cf. §4.2.2). For all propagation elevation angles, the log-periodic transmitting antenna is characterised by a uniform frequency-gain response (cf. Figure 4.2a). However, the gain characteristics of the sloping-vee receiving antenna *are* frequency dependent (cf. Figure 4.2b) and are thus investigated further.

The nominal propagation elevation angle for the Bodø/Wick path is  $\sim 6.5^\circ \pm 1.0$  (cf. Table 4.3). At this elevation angle, and for received frequencies between  $\sim 20$  MHz and  $\sim 30$  MHz, the sloping-vee antenna gain is approximately uniform (cf. Figure 4.2b). However, for decreasing frequencies below  $\sim 15$  MHz, the gain is noted to decrease by  $\sim 9$  dB. This is comparable with the observed decrease in the MSS value in Figure 5.3b, for normalised Probing Frequencies below  $\sim 0.45$ . And as the sporadic-E layers with the lowest values of  $(PF/ftEs)$ , must generally be the layers with the highest values of  $ftEs$  ( $\sim 30$  MHz), the normalised Probing Frequency value of  $\sim 0.45$  will typically represent an *actual* Probing Frequency of  $\sim 15$  MHz. The decreasing receiver antenna gain with decreasing Probing Frequency, may thus explain the sudden decrease in the MSS below normalised Probing Frequencies of  $\sim 0.45$ .

#### 5.4.4 Discussion

The results from Figures 5.3(a,b) suggest approximate ‘partial transparency’ ranges  $\sim 30\%$  of the top frequency value, during the daytime, and  $\sim 40\%$  during the night-time. The above analysis was repeated for restricted ranges of  $ftEs$ , to consider if there is any *absolute* relationship between the top frequency and the ‘partial transparency’ range of frequencies. For the daytime, a range of percentages was determined, varying between  $\sim 40\%$  and  $\sim 20\%$ , but no systematic relationship with  $ftEs$  was noted. Further, *Jalonen et al.* (1982) noted a qualitative increase in the ‘partial transparency’ range with  $foEs$ , at vertical incidence.

Interpreting the results according to a *proportional*, as opposed to absolute, relationship between *ftEs* and the ‘partial transparency’ range of frequencies, thus appears justified.

One of the most substantial and authoritative data sets comparing the plasma frequency,  $f_p$ , with *fbEs* and *ftEs*, was compiled by *Reddy and Mukunda Rao* (1968) using vertical ionosondes and in-situ rocket measurements. Considering the results with respect to the temporal definitions adopted herein, gives average values of  $f_p/ftEs$ , during the nominal daytime and night-time, of 0.69 and 0.35 respectively. The daytime results are effectively equal to those deduced from Figure 5.3a, though the difference between daytime and night-time is more significant. Further, *Miller and Smith* (1978), employing incoherent radar techniques, determined a value for the said ratio approximating to 0.7, during local times between 1100 and 1430, similar to the results presented herein and to those compiled by *Reddy and Mukunda Rao* (1968).

It is unclear why the night-time ‘partial transparency’ region should be greater than that observed in the daytime, whether by a large or small degree. Invoking the plasma ‘cloud’ model of sporadic-E to explain the ‘partial transparency’ region, and presuming gravity waves as the source of the ‘cloud’ structure (cf. §2.4.2.1), may provide an answer. The auroral zone is a source of gravity waves, especially at night, arising from ion-frictional and particle heating (cf. §2.3.6). The waves subsequently propagate equatorward (*Hunsucker*, 1982), and may thus influence the night-time structure of the sub-auroral Bodø/Wick sporadic-E layers. Further investigations of the ‘cloud’ structure of sporadic-E layers follow in the next Section.

### *Conclusion*

In conclusion, the *normalised* superposition of signal strength profiles appears to be a valid means of determining average ‘partial transparency’ frequency ranges at oblique incidence, and also provides a visual interpretation of the signal strength characteristics of sporadic-E layers. ‘Partial transparency’ ranges ~ 30% and ~ 40% of the top frequency value, were noted during the daytime and night-time respectively. As a means of comparison, it is instructive to convert the transparency frequency ratio, to an equivalent vertical frequency range. For a typical top frequency of 22.5 MHz, application of the Secant Law (Equation 3.7) gives ‘partial transparency’ ranges for daytime and night-time of 1.47 MHz and 1.96 MHz. These compare with ~ 0.8 MHz (half the gyrofrequency) as determined by refractive processes from homogeneous, *non-cloudy* layers, the latter value being intrinsic to O- and X-mode propagation characteristics (cf. §3.2.3). For a typical sporadic-E layer, the daytime ‘partial transparency’ range of frequencies thus extends to nearly twice the range expected from

homogenous plasma layer characteristics alone. And at night-time the difference is even greater.

## 5.5 A Comparison with Model Signal Strength Profiles

### 5.5.1 Introduction and Data Definition

In the previous Section, a relationship between the sporadic-E signal strength (SS) and the *normalised* Probing Frequency,  $(PF/ftEs)$ , was confirmed. It will be demonstrated that such signal strength profile characteristics may be explained by a gaussian ‘cloud population’ density distribution, presuming identical plasma ‘cloud’ scale sizes and an incoherent scatter mechanism. However, before deriving a plasma structure it is instructive to compare the signal strength results presented herein, with a frequently quoted empirical model, derived by *Miya and Sasaki* (1966) and summarised as:-

$$SS \propto \left( \frac{ftEs}{PF} \right)^n \quad (5.1)$$

for which ‘ $n$ ’ is an integer. Whilst *Miya and Sasaki* (1966) and *Miya et al.* (1978) do not specifically consider the value or nature of ‘ $n$ ’, other authors (*Bramley*, 1972; *From*, 1984, *Whitehead*, 1970) present results for *constant* values of ‘ $n$ ’ ranging up to a value of 50. It is clear from Figures 5.3(a,b) that ‘ $n$ ’ is not, and can not be a constant. For Probing Frequencies less than the blanketing frequency, the value of ‘ $n$ ’ approximates to zero, though this is evidently not the situation for Probing Frequencies within the ‘partial transparency’ range of frequencies, where a finite value persists. A more detailed comparison between the Bodø/Wick propagation data and the *Miya and Sasaki* model is considered appropriate, in order to validate the Bodø/Wick signal strength results and hence derive a plasma (cloud) model from them.

The values of ‘ $n$ ’ as defined by Equation 5.1, are easily determined through logarithmic plotting. Noting that the signal strength recordings are already expressed in decibels, a plot of median signal strength (dB) versus  $10\log_{10}(PF/ftEs)$  will give a gradient of magnitude ‘ $-n$ ’. Figure 5.4 was so compiled, employing a Probing Frequency of 17.0 MHz, as in Figure 5.1 and Figures 5.2(a,b). As discussed previously, employing a single Probing Frequency for signal strength determinations, avoids potential misinterpretations arising from uncertain

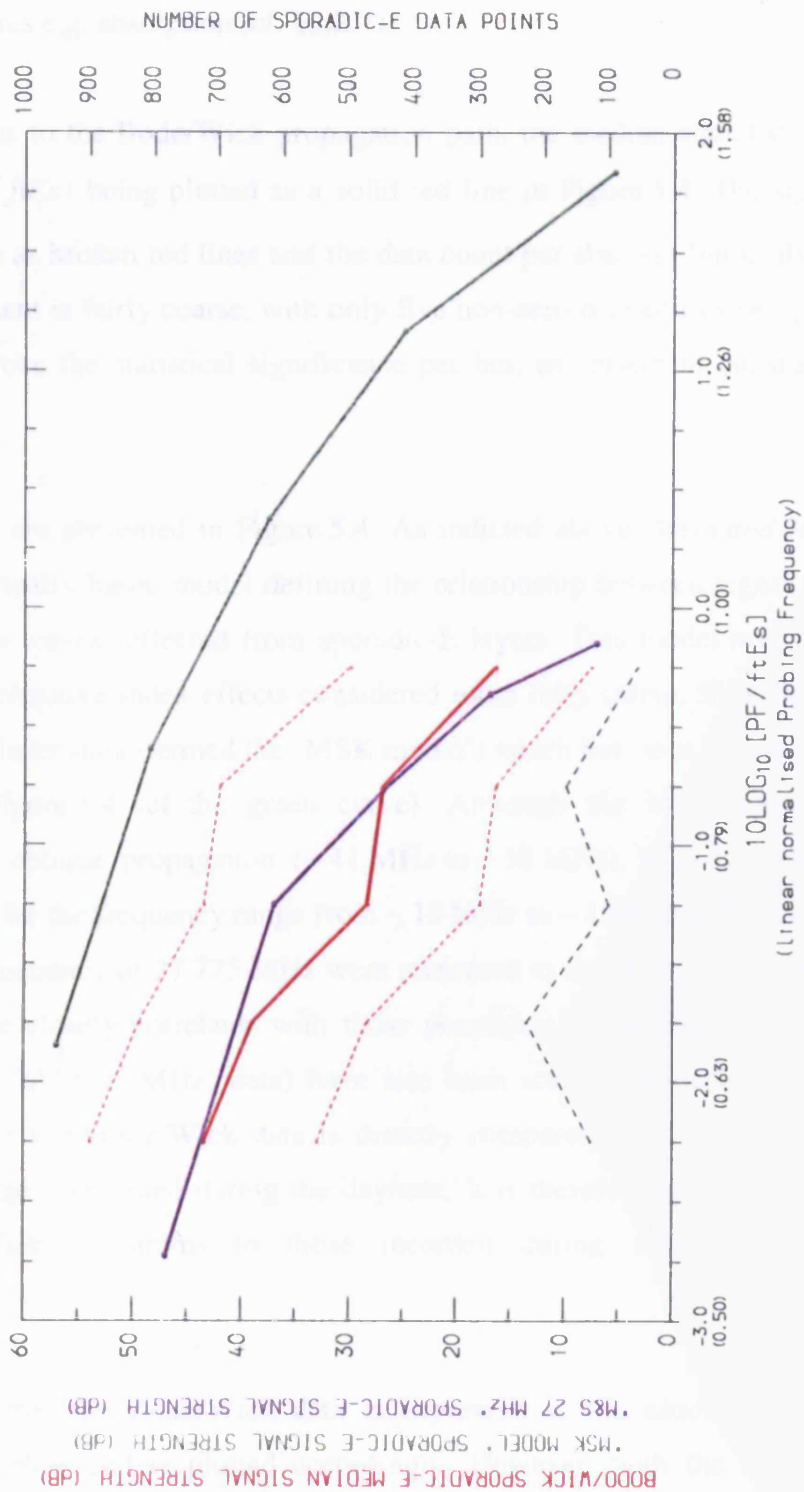


**FIGURE 5.4** Plot to determine the 'n' factor, as defined by Equation 5.1. The signal strength (dB) versus  $10 \log_{10}(PF/ftEs)$  relationship is represented for three distinct data sets. Firstly, the daytime (06:00-18:00) Bodø/Wick data (median and quartiles), derived from a Probing Frequency of 17.0 MHz; secondly, an HF/VHF signal strength model (MSK model) (Miya *et al.*, 1978); and thirdly, HF (27.775 MHz) propagation data (M&S 27 MHz) relating to both the MSK model and the Bodø/Wick propagation circuit. The 'n' factor is determined from the gradient of the plots.

frequency dependent factors, e.g. transmitter and receiver gain and loss factors, and ionospheric influences e.g. absorption (cf. §3.2.7).

The data set pertains to the Bodø/Wick propagation path, the median signal strength (MSS) versus  $10\log_{10}(PF/ftEs)$  being plotted as a solid red line in Figure 5.4. The signal strength quartiles are plotted as broken red lines and the data count per abscissa bin is also presented. The bin apportionment is fairly coarse, with only five non-zero data counts being noted. This does however improve the statistical significance per bin, an important consideration on a log-log plot.

Two further curves are presented in Figure 5.4. As indicted above, *Miya and Sasaki* (1966) developed an empirically based model defining the relationship between signal strength and *ftEs*, for VHF radio waves reflected from sporadic-E layers. This model was later refined, with atmospheric refractive index effects considered more fully (*Miya, Shimizu and Kojima*, 1978) and it is this latter data (termed the ‘MSK model’) which has been appropriately scaled and included in Figure 5.4 (cf. the green curve). Although the MSK model was based primarily on VHF oblique propagation (~ 41 MHz to ~ 58 MHz), it is considered, by the authors, to be valid for the frequency range from ~ 10 MHz to ~ 150 MHz. In addition, results for a propagating frequency of 27.775 MHz were presented in isolation in the 1966 paper. As this frequency more closely correlates with those pertaining to the Bodø/Wick path, these results (termed the ‘M&S 27 MHz’ data) have also been scaled and depicted in Figure 5.4 (cf. the blue curve). The Bodø/Wick data is directly compared to the MSK model, whose source data was largely recorded during the daytime. It is therefore appropriate to limit the range of Bodø/Wick ionograms to those recorded during nominal daytime hours (0600 to 1800).

It is worth noting that the Bodø/Wick data is expressed as the *absolute* signal strength recorded at the receiver and is plotted accordingly. However, both the MSK Model and M&S 27 MHz data sets, were originally expressed in terms of attenuation. *Absolute* comparisons between the two data types are thus difficult though also unnecessary for the purpose of this study. As only the *rate of decrease* of signal strength with respect to *ftEs* is being measured, the positioning of the latter data sets, with respect to the ordinate, is arbitrary, the depicted position being selected solely to aid visual comparisons. Only a *relative* correlation thus exists between the signal strength ordinate and these latter plots. But this has no consequence with regards to calculations of the values of ‘*n*’, which are based solely on *gradient* determinations.

## 5.5.2 Results and Analysis

The first notable observation is the confirmation that 'n' is not constant but rather increases with normalised Probing Frequency ( $PF/ftEs$ ). With regard to the Bodø/Wick data, values of 'n'  $\sim 9.3$ ,  $\sim 12.1$  (interpolated) and  $\sim 20.1$  may be calculated, for values of  $10\log_{10}(PF/ftEs)$   $\sim -2.0$ ,  $\sim -1.25$  (interpolated) and  $\sim -0.5$ . The interpolated (or average) gradient, defined for  $10\log_{10}(PF/ftEs) \sim -1.25$ , enables a comparison to be made with the MSK model at the same abscissa value, as considered below. Magnitudes of 'n' for the MSK model, range from  $\sim 6.8$  to  $\sim 27.6$  and for the M&S 27 MHz data, from  $\sim 6.7$  to  $\sim 43.5$ . These gradient calculations do not however pertain to coincident normalised Probing Frequencies, a problem addressed below.

The sparsity of binned MSS data points, and the varying abscissa ranges over which the three data plots apply, make gradient comparisons difficult. The Bodø/Wick data may be approximately compared to the MSK model data, for values of  $10\log_{10}(PF/ftEs)$  between  $-1.5$  and  $0.0$ . The respective values of 'n' are  $\sim 12.1$  and  $\sim 20.1$  for the former data set, and  $\sim 6.8$  and  $\sim 10.8$  for the MSK model. The Bodø/Wick data is thus giving values of 'n' approximately twice the magnitude of those from the MSK model.

Comparisons may be made between the Bodø/Wick data and the M&S 27 MHz data, for values of  $10\log_{10}(PF/ftEs)$  between  $-2.0$  and  $-0.5$ , giving respective values of 'n'  $\sim 9.3$  and  $\sim 20.1$  for the former data set, and  $\sim 6.7$  and  $\sim 21.3$  for the latter. For higher values of 'n', the comparison with the Bodø/Wick data is extremely favourable (20.1 versus 21.3), though significant differences ( $\sim 50\%$ ) exist between the lower values of 'n' (9.3 versus 6.7). A summary of the respective values of 'n', versus normalised Probing Frequency, is presented in Table 5.1, together with errors which are considered below.

To effectively compare these gradient determinations, it is necessary to consider all potential sources of error associated with the gradient calculations pertaining to the three plots in Figure 5.4. Scaling considerations, as well as the consistency of the MSK model itself, are assessed. From such considerations, the validity of the Bodø/Wick median signal strength profile can be assessed.

### *Sources of Error*

The Bodø/Wick data is based on median values, and associated abscissa data bins. With the number of independent signal strength measurements per bin varying between  $\sim 100$  to  $\sim 200$ ,

Normalised Probing Frequency $10 \log_{10}(PF/ftEs)$	Approximate value of the Gradient 'n'		
	Bodø/Wick data	MSK Model data	M&S 27 MHz data
-2.00	9.3		6.7 (~±4%)
-1.25	12.1*	6.8 (~±30%)	
-0.50	20.1	10.8 (~±30%)	21.3 (~±21%)

\* = interpolated gradient

Table 5.1

Summary of the approximate values of 'n', as related to Equation 5.1, for the Bodø/Wick, MSK model and M&S 27 MHz data sets, as derived from Figure 5.4.

the statistical error in the median determination is comparatively small. The error in the gradient measurement is thus largely determined by the accuracy of the *ftEs* scalings of the source ionograms (cf. §3.3.2), and the subsequent partitioning of data between abscissa bins. The vast majority of oblique *ftEs* scalings are considered accurate to within 0.1 MHz. The sum of both these error sources is thus considered negligible, particularly compared to other errors considered below.

Errors relating to the M&S 27 MHz data, arise from scaling the data depicted in Figure 7 of *Miya and Sasaki* (1966). Presuming that *these* errors are more significant than the unknown empirical errors associated with the actual data recordings, errors in '*n*' vary between ~ 4%, for the lower values, and ~ 21% for the higher values.

The MSK model data is defined for a continuous range of propagation distances and values of (*PF/ftEs*), and as for the M&S 27 MHz data, errors arise from manual scalings, in this case, from a graphical representation of the model (Figure 12, *Miya et al.*, 1978). Further intrinsic errors may arise, emanating from the extensive degree of interpolation and extrapolation involved in the graphical depiction of the model. The MSK model was thus tested for self-consistency, predicted sporadic-E loss factors being noted for a range of (*PF/ftEs*) values, at propagation distances similar to the Bodø/Wick propagation distance (~ 1300±100 km). As a result of the derivation method of the model (discussed in more detail below), comparisons between predicted loss factors, at different propagation distances, can be made by application of the Secant Law (cf. §3.2.3). All sporadic-E loss factors at coincident normalised Probing Frequencies should then be equal. This was generally found not to be the case. For fixed normalised Probing Frequencies, '*n*' was noted to vary by up to ~ ±30%. It was concluded that values of '*n*' determined from the MSK model, should be considered no more accurate than ±30%, this being a combination of scaling and self-consistency errors.

Errors associated with the M&S 27 MHz data and the MSK model are thus significantly greater than those applicable to the Bodø/Wick data, with the greatest errors being noted for the MSK model (up to ±30%). However, even these large errors do not account for the differences noted between the values of '*n*' calculated for both the Bodø/Wick data and the MSK model (cf. Table 5.1). Comparisons between values of '*n*' calculated for the Bodø/Wick data and the M&S 27 MHz data are however more favourable, particularly for the higher values of '*n*' (cf. Table 5.1). The estimated error in *these* values of '*n*' (~ 21% for the M&S 27 MHz data) fully accounts for the small differences observed between the two data

sets. Unaccounted for differences still however persist between the lower values of 'n', pertinent to the Bodø/Wick and M&S 27 MHz data (cf. Table 5.1).

### 5.5.3 Discussion

From Figure 5.4 and the results discussed above, it is of significant note that the values of 'n' determined from the Bodø/Wick data, are in much greater agreement with those derived from the M&S 27 MHz data, than with those values of 'n' calculated from the MSK model. It is therefore worth reiterating that the M&S 27 MHz data pertains to a ground propagation path length of 1243 km, similar to the corresponding Bodø/Wick distance of 1309 km (cf. Table 4.3). Further, the propagation frequency of the M&S 27 MHz data, coincides with the HF Probing Frequency band transmitted by the 'Chirp' oblique sounder employed at Bodø. Significant similarities between the two data sets thus exist.

In contrast, values of 'n' determined for the MSK model, are approximately half the magnitude of those calculated for the Bodø/Wick data, with known errors ( $\sim \pm 30\%$ ) failing to account for the discrepancies. Unlike the M&S 27 MHz data however, the MSK model is compiled from a fundamentally different range of Probing Frequencies, specifically, frequencies between  $\sim 41$  MHz and  $\sim 58$  MHz, i.e. the VHF frequency band, and then extended to the HF band. As a consequence, the model is derived from a significant proportion of what may be termed 'underdense reflections' i.e. the scattering of equivalent vertical frequencies (cf. the Secant Law, §3.2.3) greater than the plasma frequency of the scattering region (cf. Equation 1.10), a fact confirmed by *Miya et al.* (1978).

Initial indications thus suggest that the Bodø/Wick results *are* representative of HF propagation characteristics, and that the VHF MSK model is invalid within the HF band. The following discussion substantiates this assertion and thus vindicates the subsequent derivation of a sporadic-E plasma ('cloud') structure based on the Bodø/Wick results.

#### *Es Scatter*

Scattering from mid-latitude sporadic-E layers is largely due to embedded gradient drift irregularities within the layer (e.g. *Ecklund et al.*, 1981; *Haldoupis and Schlegel*, 1993). Signal strength intensity aside, the detection of irregularity scatter is determined by the relationship between the radar and plasma wave instability wavelengths (cf. §3.4.1), and thus does not depend directly on intrinsic plasma densities (*Reddy and Mukunda Rao*, 1968).

'Underdense reflections' are thus a characteristic feature of Es scatter (cf. §2.4.2.3).

The MSK model, determined by *Miya et al. (1978)*, is specifically based on *both* Es reflection and Es scatter data, initial distinctions being identified by fading characteristics and absolute attenuation levels. This is clearly apparent from Figure 5.4, where a substantial proportion of the MSK model 'curve' is plotted for  $(PF/fEs) > 1.0$ , by definition a normalised Probing Frequency region associated with 'underdense reflections'. The MSK model data thus appears to have been biased by Es scatter data, even for normalised Probing Frequencies  $< 1.0$ , as a result of the merging and interpolation of all the empirical data, over the range of Probing Frequencies (~ 41 MHz to ~ 58 MHz) and ground propagation distances (~ 900 km to ~ 2510 km) pertinent to the MSK model data set.

Evidence for this assertion is implicit to the MSK model and M&S 27 MHz data sets depicted in Figure 5.4. The MSK model data plotted in Figure 5.4, is for a ground propagation distance of ~ 1300 km. The said distance pertinent to the M&S 27 MHz data is 1243 km i.e. very similar. The latter is thus a fundamental *constituent* of the MSK model data at ~ 1300 km, and yet the two curves are patently different. So while the M&S 27 MHz data is most likely dominated by Es reflection data, and exhibits good agreement with the Bodø/Wick data, it appears that the MSK model data is biased by Es scatter data, arising from its associated higher Probing Frequencies.

The influence of 'underdense reflections' is however likely to decrease with decreasing normalised Probing Frequency, for  $(PF/fEs) < 1.0$ . It is notable from Figure 5.4, that for the lower values of  $10\log_{10}(PF/fEs)$ , i.e. ~ -1.5, there *is* good agreement between the MSK model and the M&S 27 MHz data, with respect to mutual gradients, the correspondingly higher values of signal strength being less likely the result of Es scatter (*Booker, 1959; Bowles and Cohen, 1957; Spizzichino and Giraud, 1966*).

The extension of the MSK model to the HF propagation band is thus questionable. But before concluding, it is prudent to first eliminate other possible factors that may give rise to the discrepancies in the value of 'n' calculated for the Bodø/Wick and the MSK model data. The procedures employed to derive the signal strength 'curves' depicted in Figure 5.4 are initially discussed, followed by a justification for the Secant Law scaling employed on the MSK model data.

### *Derivation of the signal strength curves*

The Bodø/Wick data set is self contained. Both the  $f_i E_s$  values and the signal strength at the Probing Frequency, are scaled within each incorporated ionogram. By definition, no abscissa values are defined for values of  $(PF/f_i E_s)$  greater than 1.0. The signal strengths are subsequently binned with respect to  $(PF/f_i E_s)$ , for a fixed  $PF = 17.0$ , and median values calculated. In contrast, *Miya et al. (1978)* and *Miya and Sasaki (1966)* used a method of equal probabilities of observing a given signal strength and  $f_o E_s$  (vertical incidence) morphology. It was demonstrated in preliminary analysis by this author, that these two methods are equivalent and are not responsible for the discrepancies in 'n'. Hence the simpler, former, analysis approach was adopted for the Bodø/Wick data.

### *Scaling Considerations*

The signal strength curves attributed to *Miya et al. (1978)* and *Miya and Sasaki (1966)* were derived from two independent sources. Signal strength magnitudes were recorded for varying, obliquely propagating Probing Frequencies, while the sporadic-E *critical frequency*,  $f_o E_s$ , was determined by a *vertical* sounder, positioned near to the nominal propagation path midpoint. The signal strength of sporadic-E reflected transmissions, are thus expressed with respect to  $(PF/f_o E_s)$ . To compare with the Bodø/Wick data, the sporadic-E critical frequency from the MSK model, needs to be expressed as an equivalent *oblique* frequency, and this is achieved through use of the Secant Law (cf. §3.2.3).

The Secant Law, as defined by Equation 3.7, is expressed in 'modified' form, with a 'correction' factor 'k', i.e.  $f_o = k \cdot f_v \cdot \sec \theta_o$ . This correction factor arises from the flat ionosphere approximation, made in the derivation of the law, and may be shown to vary between 1.0 and ~ 1.2 for typical realistic ionospheres (*Davies, 1990*), increasing with propagation distance. In Figure 5.4, the MSK model, and indeed the M&S 27 MHz data, were both scaled with a 'k' factor of 1.0.

Higher 'k' factors effectively shift the MSK model data, in Figure 5.4, to lower abscissa values. Applying a 'k' factor of 1.2 to the model data, results in values of 'n' between ~ 6.8 to ~ 18.2, measured at the values of  $10 \log_{10}(PF/f_i E_s)$  applicable to the Bodø/Wick data (i.e. ~ -2.0 to -0.5). These shifted 'n' values are significantly closer to the Bodø/Wick 'n' values and in particular, to the M&S 27 MHz results. However, transmission curves for typical ionospheres give 'k' factors near to unity, for propagation distances ~ 1300 km (*Davies,*

1990), though higher effective values have been noted (e.g. *Kerblay et al.*, 1976). Further, however, near unity '*k*' factors are generally applicable for *all* reflections from typical sporadic-E heights (~ 110 km), even at the largest propagation distances (*Davies*, 1990).

### *Density Gradients*

The most compelling justification for employing a unity '*k*' factor however, arises from the study of density gradients within sporadic-E layers, and their effect on propagation characteristics. Density gradients within sporadic-E, particularly at its edges, have been proposed and observed as a source of 'underdense' partial reflections (e.g. *Budden and Cooper*, 1962; *Reddy*, 1968; *Chessel et al.*, 1973). However, theoretical studies, employing full wave analysis techniques, at vertical (*Miller and Smith*, 1977) and oblique incidence (*Barnes*, 1994) suggest that 'typical' sporadic-E gradients have a very limited influence on reflection conditions. Specifically, *Barnes* (1994) noted no significant 'underdense' reflections for Es-layers with thicknesses  $\geq 1$  km and with gaussian-type density profiles (cf. §2.4.1). For such 'typical' characteristics, it was confirmed that the 'standard' Secant Law ( $k = 1.0$ ) is obeyed, even over relatively long propagation paths. The '*k*' factor may thus be taken as equal to 1.0, for all sporadic-E reflection resulting from refractive processes (including refraction arising from a plasma 'cloud' structure (cf. §2.4.2.1)). These results are in agreement with the transmission curves discussed above, which did not specifically apply to sporadic-E layer reflections. Confirmation of a unity '*k*' factor, with respect to 'typical' sporadic-E plasma gradients, is determined in §5.6.2.

### 5.5.4 Summary

Differences in the values of '*n*' calculated for the Bodø/Wick and MSK model data, appear therefore not to be explainable by differences in analysis procedures, nor a feature of the necessity to scale the MSK model results by means of the 'standard' Secant Law ('*k*' = 1.0). Observations of effective '*k*' factors significantly greater than 1.0, are not consistent with theory nor most observations, in relation to sporadic-E. The incorporation of Es scatter data into the MSK model is instead deemed to be the dominant factor in evaluating the source of the '*n*' value discrepancy between the Bodø/Wick and MSK model data. The merging of Es reflection and scatter data within the same signal strength model, does not appear to be appropriate. Indeed, intuitively, modelling of Es scatter, arising from embedded irregularities, should be considered in its own right.

Considering the general agreement with the M&S 27 MHz data, it may be concluded that the Bodø/Wick data has demonstrated more representative values of 'n', as applicable to HF, *overdense* sporadic-E reflection. Values of 'n' decrease with decreasing normalised Probing Frequency ( $PF/foEs$ ), from values ~ 20 for ( $PF/foEs$ ) equal to 1.0, to a threshold magnitude approaching zero, for normalised Probing Frequencies pertinent to the sporadic-E blanketing range of frequencies.

Finally, it is interesting to note that *Bramley* (1972), quotes a mean value of 'n' of 18, derived from VHF propagation over path lengths between ~ 1500 km to ~ 2000 km. From Secant Law scaling considerations, his results appear to be almost exclusively Es scatter. Further, *Booker* (1959) defines a general relationship for ionospheric irregularity scatter, not too dissimilar in form to Equation 5.1, i.e.:-

$$\sigma \propto \left( \frac{\lambda}{\sin(\theta/2)} \right)^n \quad (5.2)$$

where  $\sigma$  is the scattering cross-section,  $\lambda$  the scattered wavelength and  $\theta$  the scattering angle. Values of 'n' between ~ 4.5 and ~ 6.0 were derived in general, for a Probing Frequency range between 30 MHz and 100 MHz and coincidentally, a ground propagation path ~ 1300 km, i.e. similar to that for the Bodø/Wick path. However, application of the theory and empirical results to sporadic-E observations, determined a value of 'n' equal to 18. A value approximating to 18 thus appropriately agrees with the upper value of 'n' derived for the Bodø/Wick data (~ 20), at the transition between over- and underdense 'reflections'. These corroborating results add extra weight to the validity of the Bodø/Wick signal strength profile, from which a plasma structure will now be determined.

## 5.6 Examining the Cause of the Sporadic-E Signal Strength Profile

### 5.6.1 The Influence of the Sporadic-E Cloud Structure

#### *Introduction*

The 'cloud model' of sporadic-E was discussed earlier, in §5.1, with a more complete account presented in Chapter 2 (§2.4.2.1). It may be summarised as the presence of enhanced plasma 'clouds', embedded within a homogenous plasma layer. Both the plasma and number density of the clouds may vary, giving rise to different reflection characteristics (e.g. *Barnes*, 1992;

*Barnes, 1995; Whitehead, 1972*). The blanketing frequency,  $fbEs$ , defines the ambient density of the Es-layer, while  $ftEs$  defines the maximum plasma density of those clouds giving rise to detectable signal returns.

In Figure 5.4, the decline of signal strength with decreasing  $ftEs$ , at a fixed Probing Frequency, is defined by Equation 5.1. A significant frequency range of partial transparency is thus observed. If the cloud model of sporadic-E is invoked to interpret this ‘curve’, then by definition, the maximum scale size of the pertinent clouds is limited by the first Fresnel zone. Presuming a flat Earth and ionosphere, and a symmetric propagation path, the first Fresnel zone,  $F$ , at oblique incidence and in the transmitter-receiver line-of-sight, may be approximated by:-

$$F = \left( \frac{\lambda R}{2 \cos^2(\theta/2)} \right)^{\frac{1}{2}} \quad (5.3)$$

where  $\lambda$  is any propagating wavelength,  $R$  is the propagation distance from the ground to the Es-layer, and  $\theta$  is the angle subtended by the incident and reflected rays at the layer (*Davies, 1990*). For a ground distance  $\sim 1300$  km, the first Fresnel zone, in the transmitter-receiver direction, approximates to  $\sim 20$  km to  $\sim 25$  km for HF waves pertinent to this study (i.e.  $\sim 15$  MHz to  $\sim 30$  MHz). Under transparency conditions, cloud sizes *up to* this scale length are thus inferred.

The characteristics of the returned signal strength are extremely complex and intricately determined by the specific details of the cloud model, e.g. the *number* density of clouds, their scale sizes, their *plasma* densities, and crucially their quasi-independence (e.g. *Spencer, 1991*). Presuming scale sizes less than the Fresnel zone, both coherent and incoherent theory may be applied to determine the returned signal power, dependent on the number of clouds per Fresnel zone, the number of zones reflecting power to the receiver, and the independence of the reflecting clouds. ‘Coupled’ clouds within a single Fresnel zone, will contribute coherently to the received signal power. ‘Independent’ clouds, extending over several Fresnel zones, will contribute incoherently. To interpret the Bodø/Wick signal strength curve in Figure 5.4, a simplified interpretation of this theory was derived. In the first instance, ‘independent’ clouds, a more realistic scenario, are presumed and thus incoherent scatter theory is applied.

### *Plasma Cloud Population Distribution Models*

Two *cloud population* (number) distributions, as a function of plasma density, will be discussed below, with the intention of modelling the Bodø/Wick signal strength curve in Figure 5.4. The two plasma cloud distributions are a simplified gaussian and a linear model. In these models, many clouds are assumed to populate the sporadic-E layers, each being of an *identical size*, but varying in plasma density. The minimum plasma density is taken to be equal to the ambient, homogenous sporadic-E layer density, as defined by  $fbEs$ . Considering the suggested gravity wave cloud generation mechanism (cf. §2.4.2), this is a reasonable assumption. The cloud population at any given plasma density is determined by the respective distribution model. It thus follows that only a proportion of the total cloud population will be of sufficient plasma density to support the refraction of incident Probing Frequencies, and that the proportion decreases, according to the specific cloud population distribution, with increasing Probing Frequency. The signal strength received is then set proportional to the total number of (equal size) clouds of plasma density greater than the equivalent Probing Frequency plasma density (cf. *Barnes, 1995; Spencer, 1991*), i.e. those plasma clouds that will support ionospheric refraction. Such a presumption is based on incoherent scatter principles, i.e. when signals are received incoherently, the received power is proportional to the 'reflecting' (or scattering) area (or volume).

### *The Gaussian Probability Distribution*

The general gaussian probability distribution,  $P$ , with respect to a variable,  $x$ , is defined as:-

$$P(x, \mu, \sigma) = \frac{1}{\sigma\sqrt{2\pi}} \exp\left[-\frac{(x-\mu)^2}{2\sigma^2}\right] \quad (5.4a)$$

where  $\mu$  is the mean of the distribution and  $\sigma$  is the standard deviation. The exact form of the gaussian is incidental in relation to the cloud distribution to be 'fitted' to the Bodø/Wick signal strength curve in Figure 5.4. The mean,  $\mu$ , may thus be set to zero, and the standard deviation,  $\sigma$ , set to 1. The so defined 'normalised' gaussian may thus be expressed as:-

$$P(x) = \frac{1}{\sqrt{2\pi}} \exp\left[-\frac{x^2}{2}\right] \quad (5.4b)$$

The integral of Equation 5.4b between  $\pm \infty$  is equal to 1 i.e. the normalised probability. The probability of  $x$  being greater than a given positive value e.g.  $z$ , is the integral of

Equation 5.4b between  $z$  and  $+\infty$ . Such integrals are not so readily determined, however integrals between 0 and  $z$ , where  $z$  is a multiple or semi-multiple of the standard deviation, i.e.  $\sigma$ , or  $\sigma/2$ , are readily available in tabulated form. The integral of the ‘tail’ region of a gaussian distribution is thus easily determined by evaluating  $\int_0^{\infty} P dx - \int_0^z P dx$ , where  $\int_0^{\infty} P dx$  is equal to a  $1/2$  and  $P$  is the normalised gaussian function. These principles are employed to calculate plasma cloud populations, defined by a gaussian distribution, with plasma densities greater than a given threshold, e.g.  $z$  (and by implication, up to infinity).

### *The Gaussian Plasma Cloud Population Distribution*

The *proportion* of plasma clouds contributing to the received signal strength, at a given Probing Frequency, is determined through appropriate integration of the respective cloud population distribution, between limits effectively defined by the Probing Frequency and the maximum extent of the distribution (infinity for a gaussian). In the case of the gaussian distribution it should also be noted that only the upper half of the standard distribution is of relevance i.e. the cloud population maximises at plasma densities approximating to the ambient, homogenous plasma density of the sporadic-E layer. At higher cloud plasma densities, the cloud population decreases. The cloud population never increases with increasing plasma density.

In §5.5.4, it was observed that the Bodø/Wick signal strength curve was tending to a zero gradient at the lower values of  $(PF/fE_s)$ , and thus a maximum, threshold signal strength. Such a trend is to be expected, considering the definition of  $fbE_s$ , and the results depicted in Figures 5.1 and 5.3(a,b). For the purpose of the cloud population model distributions, a 50 dB signal strength threshold ( $SS_{THRESHOLD}$ ) is assumed, applicable to the signal strength returned from the entire cloud population, and hence also by the ambient plasma density. Probing Frequencies at or below  $fbE_s$  are thus constrained to reflect this maximum signal strength, with higher Probing Frequencies, within the partial transparency region, reflecting reduced signal strengths as described above.

It follows from the above discussions, that the signal strength received from a given Probing Frequency ( $SS_{PF}$ ) may be expressed as a fraction of the specified signal strength threshold, ( $SS_{THRESHOLD}$ ), where the fraction, ‘ $F$ ’ represents the *proportion* of clouds, within the ‘tail’ of the upper half of the gaussian distribution. The ‘tail’ is defined between a lower limit of ‘ $z$ ’ and infinity, where for the purposes of this study, ‘ $z$ ’ is a multiple of  $\sigma/2$ . Hence:-

$$SS_{PF} = F \times SS_{THRESHOLD} \quad (5.5)$$

where:-

$$F = \frac{\int_0^{\infty} P dx - \int_0^z P dx}{\int_0^{\infty} P dx}; \quad z = 0, \sigma/2, \sigma, 3\sigma/2, 2\sigma, \dots, 4\sigma$$

and  $P$  is the normalised gaussian distribution defined by Equation 5.4b.

A similar, if simpler, procedure was employed to evaluate the signal strengths pertaining to a *linear* cloud population distribution, ' $F$ ' being simply defined as a linear fractional reduction. The signal strengths derived from both the gaussian and linear distributions, are appropriately scaled with respect to the *normalised* Probing Frequency, and the results presented in Figure 5.5.

### *Results and Analysis*

Figure 5.5 is dimensioned identically to Figure 5.4. Indeed, the Bodø/Wick (red) and M&S 27 MHz (blue) signal strength curves are similarly depicted. The MSK model data and the quartiles have been removed. The two additional plots represent the signal strengths predicted from the suitably constrained gaussian (green curve) and linear (yellow curve) *cloud population* distribution models described above, the distributions defining the number density of plasma 'clouds' as a function of plasma density.

The gaussian 'fit' to the Bodø/Wick (and M&S 27 MHz) data in Figure 5.5, is clearly very favourable. In comparison, the results pertaining to the linear distribution are significantly less good. To an extent, the gaussian cloud distribution model is constrained to 'fit', but it is not felt that any assumptions made are unwarranted. The unvarying, single cloud scale size is probably a simplification, but equally, a continuous spectrum of sizes is unlikely. Presuming a gravity wave generation mechanism, scale sizes indicative of discrete harmonic wavelengths (cf. Nygrén, 1990) is potentially a more realistic cloud distribution.

The assumption that the received power is proportional to the cloud population, is valid for either incoherent (Barnes, 1995) or coherent (Spencer, 1991) models, providing the scale sizes are significantly less than the Fresnel zone size. Miller and Smith (1978) directly observed cloud structures ~ a few km in size (cf. §2.4.2.1) and From and Whitehead (1978) and Barnes (1992) deduced scale sizes of ~ 5 km and  $\leq 3$  km respectively. These sizes are indeed significantly less than the first Fresnel zone diameter calculated above.

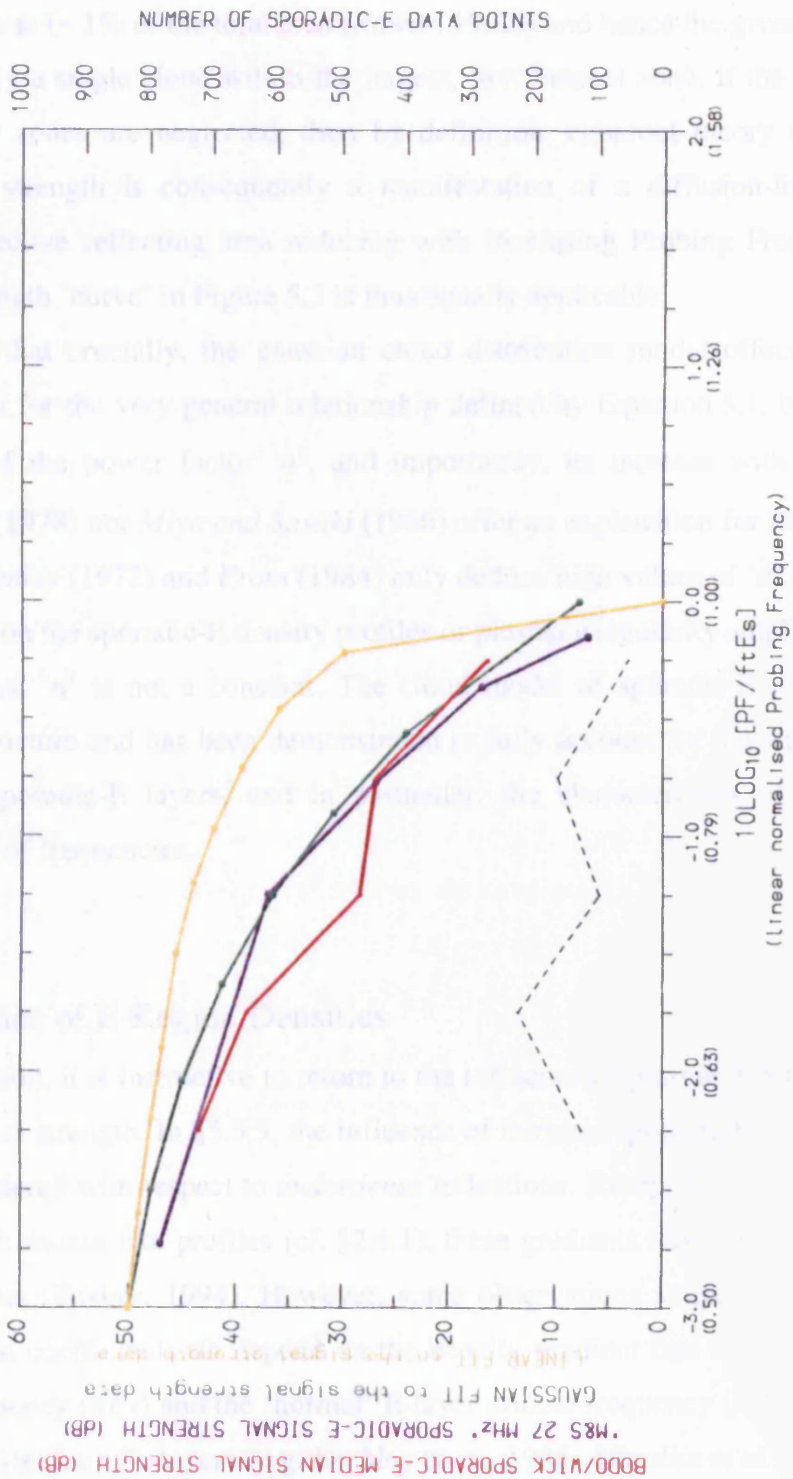


FIGURE 5.5 Comparison of the Bodø/Wick and M&S 27 MHz signal strength data, as defined in Figure 5.4, with the predicted signal strength curves deduced from both a gaussian and a linear sporadic-E cloud distribution model.

From rocket measurements (e.g. *Reddy and Mukunda Rao*, 1968), the cloud population is considered to be sparse (~ 1% of the total area (*Rawer*, 1962)) and hence the given cloud sizes suggest possibly only a single cloud within the largest, first Fresnel zone. If the contribution from other, smaller zones are neglected, then by definition, coherent theory applies. The decrease in signal strength is consequently a manifestation of a diffusion-limited cloud (cf. §2.4.1), the effective reflecting area reducing with increasing Probing Frequency. The observed signal strength ‘curve’ in Figure 5.5 is thus equally applicable.

It should be noted that crucially, the gaussian cloud distribution model offers a potential physical explanation for the very general relationship defined by Equation 5.1, both in terms of the magnitude of the power factor ‘*n*’, and importantly, its increase with  $(PF/ftEs)$ . Neither *Miya et al.* (1978) nor *Miya and Sasaki* (1966) offer an explanation for the magnitude of ‘*n*’, and both *Bramley* (1972) and *From* (1984) only deduce high values of ‘*n*’ by imposing extreme constraints on the sporadic-E density profiles or plasma irregularity amplitudes. None consider the fact that ‘*n*’ is not a constant. The cloud model of sporadic-E is a generally accepted plasma structure and has been demonstrated to fully account for the signal strength characteristics of sporadic-E layers, and in particular, the characteristics of the ‘partial transparency’ range of frequencies.

### 5.6.2 The Influence of E-Region Densities

As a final investigation, it is instructive to return to the influence of plasma density gradients, on the received signal strength. In §5.5.3, the influence of intrinsic sporadic-E plasma density gradients was considered with respect to *underdense* reflections. Except for unusually narrow layers or layers with square-like profiles (cf. §2.4.1), these gradients have little effect on the reflection coefficients (*Barnes*, 1994). However, some observations suggest that *overdense* sporadic-E reflection coefficients *do* depend on the density gradient that exists between the sporadic-E top frequency (*ftEs*) and the ‘normal’ E-layer critical frequency (*foE*), particularly for low altitude (< 100 km) Es-layers (e.g. *Kerblay et al.*, 1986; *Minullin et al.*, 1988). Such observations appear to depend solely on *ftEs* and *foE*, i.e. independent of the Es-layer thickness or profile. Considering the relationship between plasma frequencies and electron densities i.e.  $N \propto f^2$  (cf. Equation 1.10), this gradient dependence may be expressed as:-

$$SS \propto (ftEs^2 - foE^2) \quad (5.6)$$

The density gradient described by Equation 5.6 may exist independent of the relationship between the sporadic-E and E-layer critical frequency heights ( $h'Es$  and  $h'E$  respectively). Larger gradients are however more likely when  $h'Es$  is less than  $h'E$ , with the gradient being inversely proportional to  $h'Es$  under quiescent ionospheric conditions (cf. Figure 1.8). Hence the bias towards low altitude sporadic-E (Kerblay *et al.*, 1986). The applicability of Equation 5.6 to the Bodø/Wick data set is considered below. Further, it is important to be able to conclusively dismiss the possibility of a significant proportion of 'non-typical' sporadic-E profiles, with plasma gradients that may indeed give rise to non unity values of the Secant factor 'k', as discussed in §5.5.3.

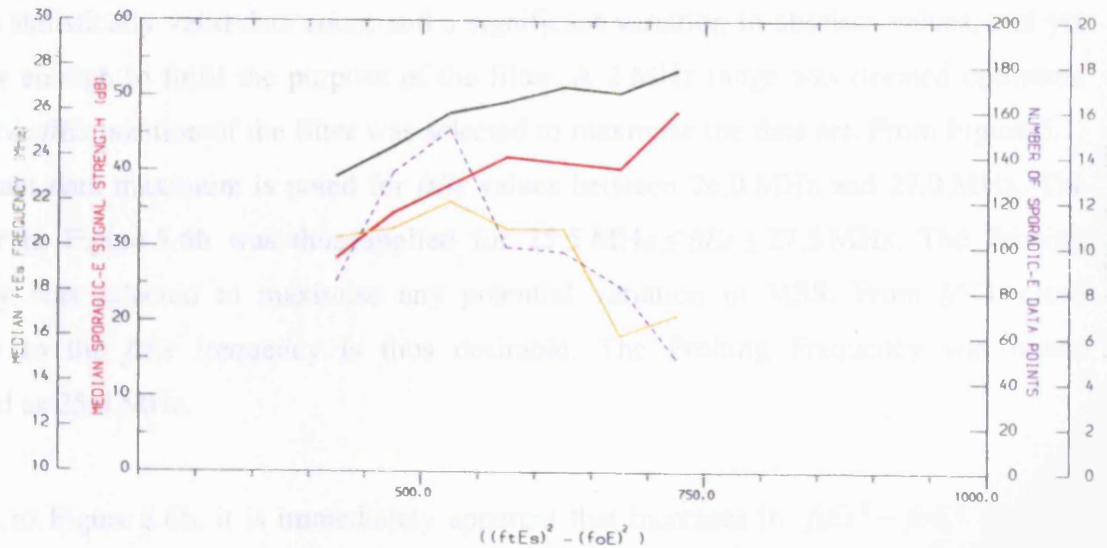
#### *Figure 5.6a – Unfiltered Data*

Two plots have been compiled to investigate the influence of  $foE$ . Figure 5.6a is compiled from the complete Bodø/Wick data set i.e. all valid sporadic-E observations (cf. §5.2) from all days and times of the August campaign. The Probing Frequency is a constant 17.0 MHz as in previous Figures. Figure 5.6a essentially takes the format of Figure 5.1 with respect to the ordinates, but with the data being binned according to the relationship expressed in Equation 5.6. In addition to the associated median signal strength (red line), median  $ftEs$  (green line) and data count (blue line) being plotted, the median  $foE$  is also depicted (yellow line). When the E-layer can be distinguished from the sporadic-E layer,  $foE$  values are scaled directly from the oblique ionograms. The majority are however accurate ICEPAC predictions, as described in §3.3.2. To aid comparison, the range of abscissa values for which data is plotted, is constrained to match those applicable to Figure 5.6b. Quartiles have also been omitted for clarity.

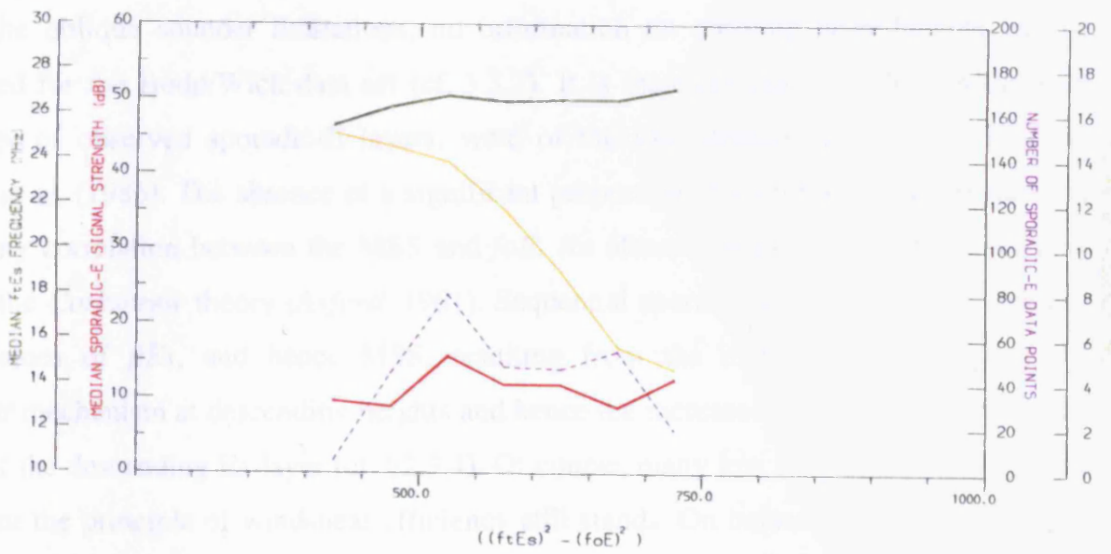
Referring to Figure 5.6a, increasing values of  $ftEs^2 - foE^2$  unsurprisingly leads to increases in  $ftEs$  and decreases in  $foE$ . The median signal strength (MSS) is also noted to increase with increasing abscissa values. It is unclear however whether the apparent relationship between the MSS and  $ftEs^2 - foE^2$  is genuine, or merely a manifestation of the general relationship between the MSS and  $ftEs$ , as determined in previous Sections. To separate these inter-relationships, Figure 5.6b was compiled.

#### *Figure 5.6b – Filtered Data*

The general format of Figure 5.6b is similar to Figure 5.6a, but in order to reduce the influence of the  $ftEs$  value on determining the MSS value, the  $ftEs$  has been constrained within a narrow 'permitted' range. The width of this range needs to be wide enough to



(a)



(b)

**FIGURES 5.6(a,b)** Plots to examine the relationship between median signal strength and the E-layer/Es-layer density gradient, defined by the abscissa. The median signal strength (MSS),  $f_t E_s$  and  $f_o E$  are all plotted, together with the data bin count. Figure 5.6a utilises the complete range of  $f_t E_s$  values, probing at 17.0 MHz, whilst Figure 5.6b restricts the  $f_t E_s$  to between 25.5 MHz and 27.5 MHz, probing at 25.0 MHz. From the latter it is clear that the signal strength reflected from the sporadic-E layers, is independent of the said density gradient.

provide a statistically valid data count and a significant variation in abscissa values, and yet be narrow enough to fulfil the purpose of the filter. A 2 MHz range was deemed optimum. The relative  $ftEs$  position of the filter was selected to maximise the data set. From Figure 5.1, a significant data maximum is noted for  $ftEs$  values between 26.0 MHz and 27.0 MHz. The  $ftEs$  filter in Figure 5.6b was thus applied for  $25.5 \text{ MHz} \leq ftEs \leq 27.5 \text{ MHz}$ . The Probing Frequency was selected to maximise any potential variation in MSS. From §5.3, close proximity to the  $ftEs$  frequency is thus desirable. The Probing Frequency was hence nominated as 25.0 MHz.

Referring to Figure 5.6b, it is immediately apparent that increases in  $ftEs^2 - foE^2$  are now determined by decreases in  $foE$ ,  $ftEs$  values being approximately constant. And significantly, the MSS is *also* noted to be approximately constant, in contrast to its behaviour in Figure 5.6a. Clearly it may be deduced that the signal strength of HF waves reflected from sporadic-E layers, pertaining to this study at least, are independent of  $foE$  and  $ftEs^2 - foE^2$ , and by implication, any plasma density gradients, and are instead dependent solely on  $ftEs$ .

#### *Data Interpretation*

Due to the oblique sounder limitations, no information on absolute layer heights can be determined for the Bodø/Wick data set (cf. 3.3.2). It is therefore not possible to state what percentage of observed sporadic-E layers, were of the low altitude type, as specified by *Kerblay et al.* (1986). The absence of a significant proportion of such layers may explain the lack of any correlation between the MSS and  $foE$ . An alternative explanation however may relate to the *Corkscrew* theory (*Axford*, 1961). Sequential sporadic-E (cf. §2.3.6) will tend to higher values of  $ftEs$ , and hence MSS, resulting from the increased efficiency of the windshear mechanism at descending heights and hence the increased compression and plasma density of the descending Es-layer (cf. §2.3.4). Of course, many low altitude layers may form in-situ, but the principle of windshear efficiency still stands. On balance then, there is a bias towards higher  $ftEs$  values at the lower altitudes, and this fact alone will result in associated increases in returned signal strength, independent of any E-layer/Es-layer density gradients.

At altitudes much below 100 km however, windshear efficiency rapidly reduces due to increased turbulence (cf. §2.3.3). Further, *Turunen* (1977) observed the dominating presence of *weak*, low altitude, sporadic-E returns which he attributed to ‘steep density gradients’, presumably between the sporadic-E layers and the normal E-layer. This conclusion is in direct contrast to the increasingly *stronger* signals espoused by *Kerblay et al.* (1986), but agrees

with the results presented herein: Es-layer/E-layer density gradients contribute at most only *weakly* to the total returned signal strength, higher returns being the consequence of the inherent *ftEs* magnitude. In conclusion, it is interesting to note that Equation 5.6 is a modified form of Equation 5.1, for a constant PF and a value of '*n*' equal to 2. This value of '*n*' is considerably lower than is generally observed over the Bodø/Wick propagation path (cf. §5.5.2).

## 5.7 Summary

The relationship between *ftEs* and signal strength has been firmly established, for *overdense* sporadic-E reflections, by means of High Frequency radio wave propagation. Equation 5.1 describes this relationship, for values of '*n*' between zero, for the 'blanketing' frequency range, up to ~ 20 at the sporadic-E layer top frequency. Differing values of '*n*' are observed when *underdense*, Es scatter is considered (e.g. *Bramley*, 1972; *Miya and Sasaki*, 1966; *Miya et al.*, 1978), particularly for VHF propagation circuits.

These signal strength profile characteristics, with emphasis on the 'partial transparency' range of *normalised* Probing Frequencies, may be modelled by invoking a plasma cloud structure (e.g. *Whitehead*, 1972), with a gaussian population distribution. The received signal strength may then be interpreted in terms of incoherent or coherent scatter theories. These characteristics are pertinent to strong, *overdense*, sporadic-E HF reflections, via refractive processes alone, as opposed to weaker Es scatter, determined by *underdense* plasma irregularities (e.g. *Booker*, 1959). 'Normal' E-layer densities are considered to generally have little or no impact on sporadic-E reflection coefficients.

Partial transparency ranges ~ 30% and ~ 40% of the top frequency value, were noted during the daytime and night-time respectively. The daytime value agrees closely with observations made by *Miller and Smith* (1978) and *Reddy and Mukunda Rao* (1968).

# Chapter 6

## An Investigation into the Effect of $\nu ftEs$ Growth Rates on the Sporadic-E Signal Strength Profile

### 6.1 Introduction

In Chapter 5, an empirical statistical relationship was derived, demonstrating that for High Frequency, ‘overdense’ sporadic-E reflections, the received signal strength (SS) is proportional to  $(ftEs/PF)^n$ . The value of ‘ $n$ ’ was observed to systematically vary between 0 and 20, such that for Probing Frequencies less than the blanketing frequency,  $fbEs$ , ‘ $n$ ’ approximates to zero, whilst for Probing Frequencies equal to  $ftEs$ , ‘ $n$ ’ approximates to  $\sim 20$  (cf. §5.5). The relationship is simply summarised in Figure 5.1 for a fixed Probing Frequency pertinent to the ‘partial transparency’ range of frequencies. For such a Probing Frequency, the received signal strength is noted to increase with increasing sporadic-E top frequency. This fundamental observation was however determined independent of top frequency *growth rate* considerations. This omission is rectified within this Chapter.

This Chapter will demonstrate that the top frequency growth rate of sporadic-E layers does indeed influence the signal strength relationship described above, but only when the said growth rate exceeds an empirically determined threshold magnitude. That magnitude, expressed in terms of an equivalent vertical frequency, is  $\sim 0.6$  MHz per 5 minutes (cf. §6.4). For larger top frequency growth rates, the signal strength measured for a typical sporadic-E layer, increasingly falls short of the magnitude predicted by the *growth rate independent* signal strength relationship established in Chapter 5. Further, for top frequency growth rates  $\geq 1.2$  MHz per 5 minutes, the signal strength received at a given Probing Frequency is *independent of* the sporadic-E top frequency. This contrasts sharply with the signal strength relationship evaluated in Chapter 5 and summarised above.

These observations are interpreted in terms of the sporadic-E plasma ‘cloud’ structure (cf. §2.4.2.1), with merit also being given to other possible influences e.g. field-aligned plasma irregularities and off great circle path propagation modes. It is emphasised however,

that only ~ 25% of equivalent vertical top frequency growth rates are greater than 0.6 MHz per 5 minutes. The majority of (smaller) growth rates thus have no influence on the relationship between signal strength and top frequency, as determined in Chapter 5. The analysis herein does not therefore fundamentally undermine this relationship, but rather establishes the need for the top frequency growth rate to be factored in to the said relationship.

## 6.2 Data Description

As in Chapter 5, the following investigation concentrates on the Bodø/Wick ionogram data set, recorded during August, 1988. The resolution of ionogram recordings is hence one every five minutes (cf. Table 4.2). The growth rate of the sporadic-E top frequency is investigated by comparing scaled top frequency magnitudes from a *pair* of *consecutively* recorded ionograms. All top frequencies are measured in equivalent *vertical* frequencies (*vftEs*) to allow for universal comparisons with different data sets. The top frequency growth rate is thus expressed as a change in *vftEs* per 5 minute time interval. For a set of 'x' ionograms, a maximum of 'x-1' *pairs* of sporadic-E traces may be considered, each Es-layer being potentially paired with both its temporal neighbours. A distribution of *vftEs* growth rates may thus be compiled.

For each recorded *vftEs* growth rate, between a pair of sporadic-E ionogram traces, the signal strength of *both* of the layers is determined, at a given Probing Frequency. In this way, the characteristic signal strength of a sporadic-E layer may be expressed as a function of *vftEs* growth rate, and comparisons made with the *growth rate independent* relationship, between signal strength and sporadic-E top frequency, established in Chapter 5.

The data set is subject to the same scaling constraints as applied in Chapter 5 (§5.2), with the additional proviso that the constraints be applied to *both* consecutively recorded sporadic-E layers within any defined pair. In particular, for each *pair* of sporadic-E layers, the designated Probing Frequency must be greater than the *E/F-region cut-off frequency* but less than the *vftEs* of *both* Es-layers. Further, *both* sporadic-E layers must have a measurable oblique top frequency less than 29.9 MHz. The enforcement of these constraints on *both* sporadic-E layers within each defined pair, slightly reduces the data set as compared to that used in Chapter 5.

It should be noted that throughout much of the analysis and discussion in this Chapter, the term ‘growth rate’ is used generically i.e. is equally applicable to both positive and negative rates of *vftEs* growth. The terms ‘decay rate’ and ‘negative growth rate’ are synonymous and are used when a specific distinction with ‘positive growth rate’ is deemed prudent.

## 6.3 Introductory Observations of *vftEs* Growth Rates

### 6.3.1 Typical Daily Variations of *vftEs*

Figure 6.1 presents typical observations of sporadic-E layers, for the Bodø/Wick propagation path, during the August Campaign (cf. Table 4.1). The format of the plot ideally summarises the sporadic-E scaling procedures adopted throughout this thesis, and was discussed in detail in §3.3.2. The Figure represents a whole day’s ionogram recordings (day 223), 288 ionograms thus being summarised and depicted. The scaled data, in the main panel is presented in terms of equivalent vertical Probing Frequency versus Universal Time (UT).

Each of the prominent vertical lines in the main panel indicates the recording of a sporadic-E layer, the line itself representing the Probing Frequency range for which sporadic-E signal strength measurements may be recorded. The higher frequency end of the lines is thus the sporadic-E top frequency, while the lower frequency end is the *E/F-region cut-off frequency* (cf. §3.3.2). The upper panel in Figure 6.1 presents the median signal strength of each sporadic-E trace, derived from the range of Probing Frequency measurements as described above.

The important information to note in Figure 6.1, is the variation in sporadic-E top frequency between consecutive ionograms, i.e. the change in top frequency per 5 minute time interval. It appears that the majority of top frequency growths (and decays) are less than 1.0 MHz per 5 minutes. To quantify these observations in detail, the histogram in Figure 6.2 was compiled, for *all days* of the August campaign.

### 6.3.2 *vftEs* Growth rate Distribution

Figure 6.2 presents top frequency, growth rate distribution data, in the form of a histogram. The data is binned at *vftEs* growth rate intervals of 0.2 MHz per 5 minutes. The histogram

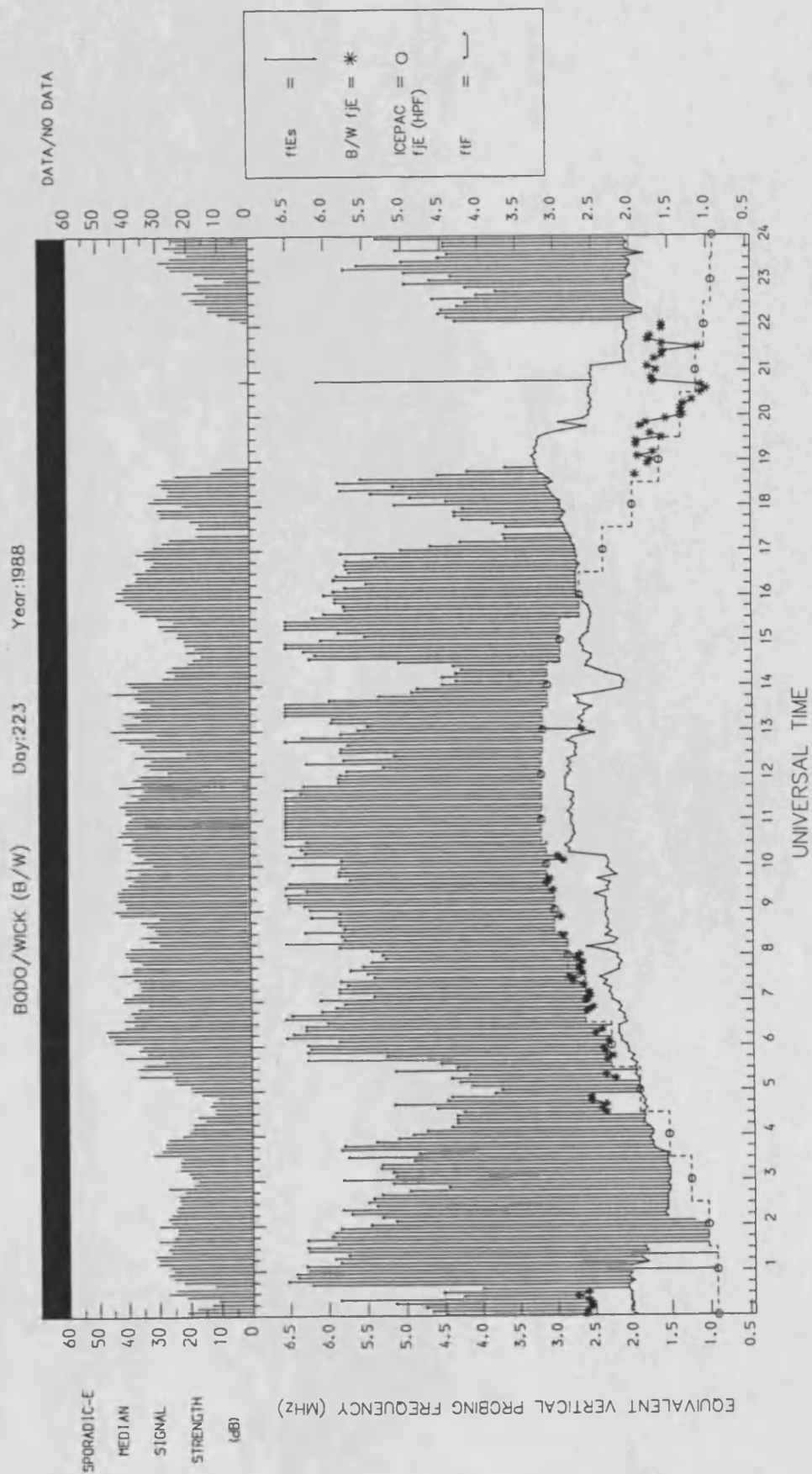


FIGURE 6.1 Summary scaled oblique ionosonde data pertaining to the Bodø/Wick propagation path, for day 223, 1988. The main panel depicts the range of ionosonde Probing Frequencies for which sporadic-E signal strengths may be determined, for each of the 288 ionograms recorded. The upper panel gives the median signal strength for each sporadic-E ionogram trace.

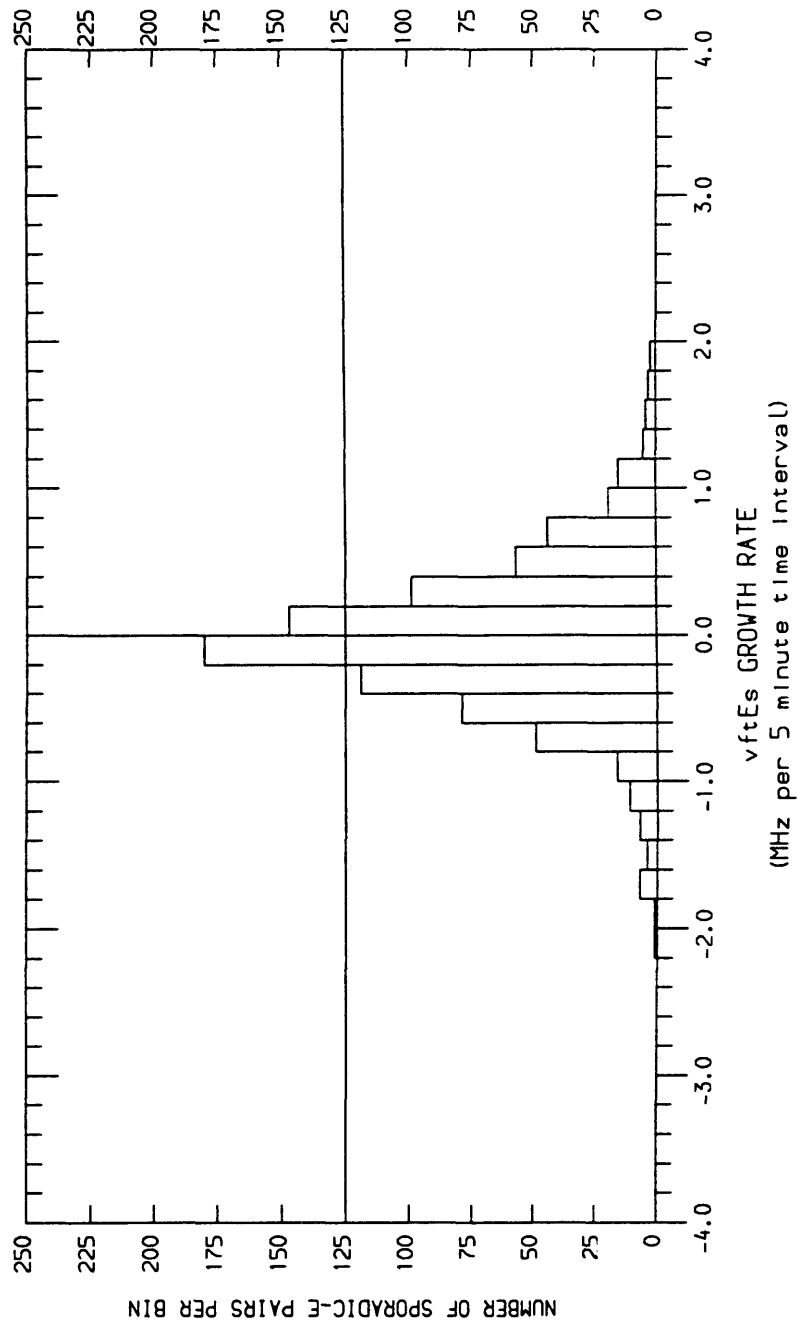


FIGURE 6.2 The growth rate distribution of the equivalent vertical top frequency of sporadic-E, *vftEs*, as recorded on the Bodø/Wick propagation path during the August, 1988 campaign. Note that the term 'growth' is generic, applying equally to both positive and negative changes in the top frequency.

depicts the number of *pairs* of consecutive sporadic-E layers per growth rate bin. It is noted that 35.9% of all *vftEs* growth rates are less than 0.2 MHz per 5 minute time interval, and that 88.7% are less than 1.0 MHz per 5 minutes. Practically no growth rates exceed 2.0 MHz per 5 minute interval. These observations, though not directly comparable, are similar to those determined by *Goodwin and Summers* (1970).

It was noted in §6.1, and will be demonstrated in the analysis below, that the relationship between signal strength and normalised Probing Frequency, established in Chapter 5, is only applicable for *vftEs* growth rates  $\leq 0.6$  MHz per 5 minute time interval. For higher *vftEs* growth rates the relationship breaks down. It is therefore of particular interest, that from Figure 6.2, a significant majority ( $\sim 75\%$ ) of all *vftEs* growth rates are  $\leq 0.6$  MHz per 5 minute time interval. Conversely however,  $\sim 25\%$  of all growth rates *are*  $\geq 0.6$  MHz per 5 minutes and this provides a large enough data sample to analyse the influence that these larger *vftEs* growth rates have on the *growth rate independent* signal strength relationship depicted in Figure 5.1. This influence is analysed below.

## **6.4 The Relationship between Sporadic-E Signal Strengths and Top Frequency Growth Rates**

### **6.4.1 Introduction**

This Section will clearly demonstrate that the signal strength characteristics of sporadic-E are not only determined by the top frequency and Probing Frequency parameters, as established in Chapter 5 and summarised by Equation 5.1, but that the sporadic-E top frequency *growth rate*, is also a significant factor.

This conclusion is determined by statistically comparing the sporadic-E signal strength, for given Probing Frequencies, as a function of both top frequency and top frequency growth rate. For the higher rates of *vftEs* growth ( $\geq 0.6$  MHz per 5 minutes), the signal strength-frequency profiles are demonstrated to fundamentally differ from the *growth rate independent*, statistical profiles depicted in Figures 5.3(a,b). The relationship between signal strength and *vftEs* growth rate, and the associated signal strength-frequency profiles, are primarily explained in terms of the plasma ‘cloud’ model of sporadic-E (cf. §2.4.2.1).

## 6.4.2 Analysis Procedure

The terminology adopted within this Section, is defined in Figure 6.3. For simplicity, the signal strength-frequency profiles depicted in this Figure, take the form of the *growth rate independent* profiles derived in Chapter 5 and presented in Figures 5.3(a,b). From the above discussions, it will be shown that these profiles adopt an increasingly modified form, for increasing *vftEs* growth rates.

Growth rates of *vftEs* are studied by comparing the change of *vftEs* between consecutive ionograms, at the maximum temporal resolution of the data set, i.e. 5 minutes, as described in §6.2. The constituents of these *pairs* of sporadic-E layers are simply termed the '*higher-ftEs*' and '*lower-ftEs*' layers. It follows that for *positive* top frequency growth, the '*lower-ftEs*' layer chronologically precedes the '*higher-ftEs*' layer, whilst the converse is true for *vftEs* decay.

Figure 6.3 also defines two Probing Frequency ranges for each sporadic-E pair, namely the '*common*' and '*growth*' ranges. Note that the generically termed '*growth*' range is by definition, applicable only to the *higher-ftEs* layer. The '*common*' frequency range defines the range of Probing Frequencies for which signal strength measurements may be determined from *both* sporadic-E layers within a given pair. The following data analysis is primarily associated with signal strength characteristics within this '*common*' frequency range.

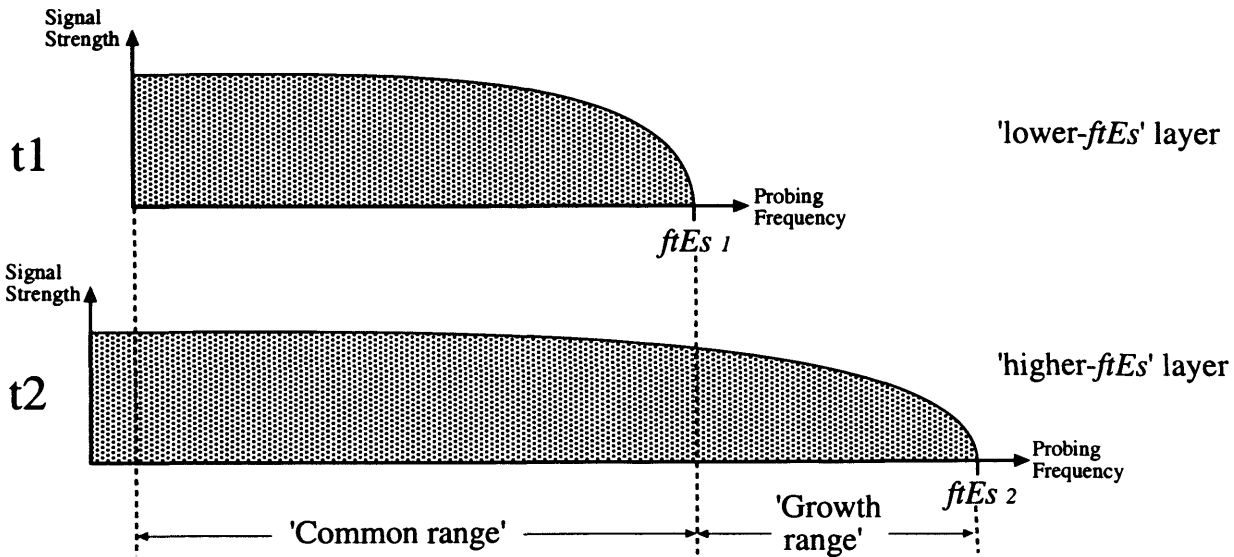
Signal strength features associated with the '*growth*' frequency range are however equally important in consideration of the signal strength-Probing Frequency relationship determined for increasing rates of *vftEs* growth. These characteristics are considered towards the end of this Section.

## 6.4.3 Signal Strength Observations of the Sporadic-E '*Common*' Region

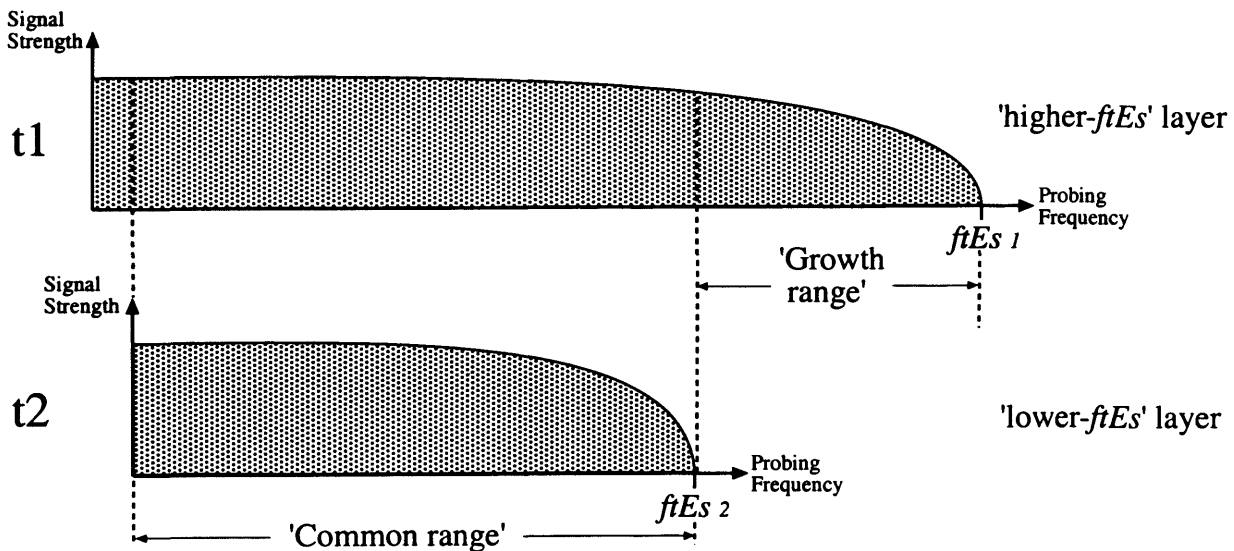
### *Data Description*

Figure 6.4 presents data based on the '*higher-ftEs*' sporadic-E layers, within each pair of layers defined in the preceding Section and depicted in Figure 6.3. The signal strength characteristics of each sporadic-E layer, are determined at a single Probing Frequency equal to 19 MHz, for these particular observations. This frequency was selected as best typifying

# Sporadic-E *ftEs* Growth Terminology



(a)  
Positive *ftEs* Growth



(b)  
Negative *ftEs* Growth

FIGURE 6.3 Schematics of a pair of consecutively recorded sporadic-E layers exhibiting both positive (a) and negative (b) *ftEs* growth. Within each pair, each layer is identified as either the 'higher-*ftEs*' layer or the 'lower-*ftEs*' layer, zero growths being largely ignored. In each case,  $t_1 < t_2$  and the difference between  $t_1$  and  $t_2$  is always 5 minutes, the interval between ionogram recordings.

Note that the minimum observed frequency for each of the 'higher-' and 'lower-*ftEs*' layers, may not be coincident due to ionospheric variability. The 'Common range' is coincident with both the 'higher-' and 'lower-*ftEs*' layers, whereas the 'Growth range' is unique to the 'higher-*ftEs*' layer.

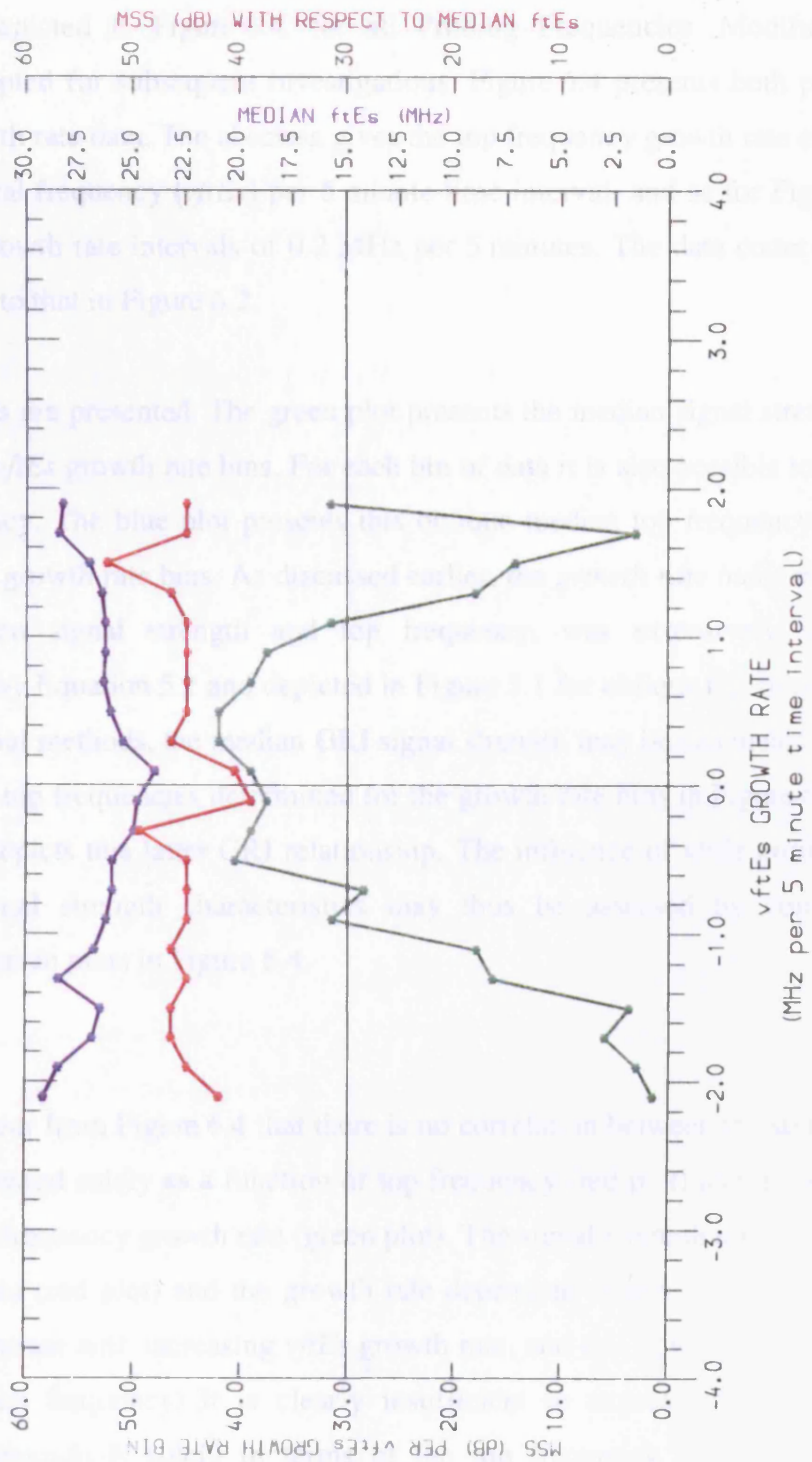


FIGURE 6.4 Median signal strength (MSS) of sporadic-E layers, plotted with respect to the  $vftEs$  (independent of  $vftEs$  growth rate) and with respect to the  $vftEs$  growth rate, as defined by the abscissa bins. The median  $ftEs$  is also plotted as a function of  $vftEs$  growth rate, all data being recorded during the August, 1988 campaign. All the data pertains to the 'higher- $ftEs$ ' sporadic-E layers, with the distribution of data being identical to that depicted in Figure 6.2.

the observations depicted in Figure 6.4, for all Probing Frequencies. Modified analysis approaches are adopted for subsequent investigations. Figure 6.4 presents both positive and negative  $\nu ftEs$  growth rate data. The abscissa gives the top frequency growth rate expressed as an equivalent vertical frequency ( $\nu ftEs$ ) per 5 minute time interval, and as for Figure 6.2, the data is binned at growth rate intervals of 0.2 MHz per 5 minutes. The data count per growth rate bin is identical to that in Figure 6.2.

Three data ordinates are presented. The green plot presents the median signal strength (MSS) with respect to the  $\nu ftEs$  growth rate bins. For each bin of data it is also possible to calculate a median top frequency. The blue plot presents this oblique median top frequency,  $ftEs$ , with respect to the  $\nu ftEs$  growth rate bins. As discussed earlier, the *growth rate independent* (GRI) relationship between signal strength and top frequency, was extensively analysed in Chapter 5, defined by Equation 5.1 and depicted in Figure 5.1 for oblique top frequencies. By similar computational methods, the median GRI signal strength may be calculated for each of the median oblique top frequencies determined for the growth rate bins in Figure 6.4. The red plot in Figure 6.4 depicts this latter GRI relationship. The influence of  $\nu ftEs$  growth rates on the sporadic-E signal strength characteristics may thus be assessed by comparing the respective red and green plots in Figure 6.4.

#### *Data Observations*

It is immediately clear from Figure 6.4 that there is no correlation between the signal strength characteristics expressed solely as a function of top frequency (red plot) and those expressed as a function of top frequency growth rate (green plot). The signal strength *difference* between the GRI observations (red plot) and the growth rate dependent observations (green plot), is instead noted to increase with increasing  $\nu ftEs$  growth rate, and this is for binned data with a common median top frequency. It is clearly insufficient to express the signal strength characteristics of sporadic-E solely in terms of the top frequency (for a fixed Probing Frequency). The qualitative influence of the  $\nu ftEs$  growth rate on signal strength characteristics is thus clearly demonstrated. It is possible however to deduce from Figure 6.4, that the aforementioned signal strength difference is small for  $\nu ftEs$  growth rates  $\leq 0.6$  MHz per 5 minutes. The significance of this apparent threshold growth rate is demonstrated below.

#### 6.4.4 'Common' Signal Strength Differences Between Consecutive Sporadic-E Layers

##### *Data Definition*

Figures 6.5a and 6.5b depict median signal strength *differences* observed between pairs of consecutively observed sporadic-E layers, as described in §6.2, the results being binned with respect to  $\nu ftEs$  growth rate, as in Figure 6.4. The ordinate is thus the median signal strength (MSS) *difference* between the 'higher- $ftEs$ ' and 'lower- $ftEs$ ' Es-layers (cf. Figure 6.3). The two Figures relate respectively to negative and positive  $\nu ftEs$  growth rates, with the MSS difference being defined in a chronological sense. Negative  $\nu ftEs$  growth rates will thus result in negative MSS differences, while positive  $\nu ftEs$  growth rates will generate positive MSS differences.

The signal strength data in Figures 6.5(a,b) was compiled from a *range* of Probing Frequencies, the range being arbitrarily defined in terms of *oblique* incidence frequencies. The range of Probing Frequencies was defined to be within 3 MHz of the  $ftEs$  values of each of the probed Es-layers, the range being small enough to exhibit distinct signal strength *difference* characteristics and yet still give statistically valid results. For an  $ftEs$  value of, for example, 25.0 MHz, the pertinent sporadic-E layer is probed at *all* frequencies between 22.0 MHz and 25.0 MHz, presuming of course that this range is 'common' to both the 'higher-' and 'lower- $ftEs$ ' layers (cf. Figure 6.3). Note that the Probing Frequencies are deliberately selected to be close to the  $ftEs$  value, so as to maximise the potential signal strength difference for a given  $\nu ftEs$  growth rate i.e. to be far removed from the blanketing frequency range. Note also that as all pairs of sporadic-E layers are probed over a *range* of frequencies, then even given the above constraints, each plot in Figures 6.5(a,b) represents over 1000 data points.

The range of Probing Frequencies must be selected for only one of the constituent  $ftEs$  values within each sporadic-E pair. It is clear from Figure 6.3 that by definition, this must be the 'lower- $ftEs$ ' layer for both positive and negative  $\nu ftEs$  growth rates, given that the Probing Frequency must intersect both the 'higher-' and 'lower- $ftEs$ ' Es-layers, within the 'common' frequency range.

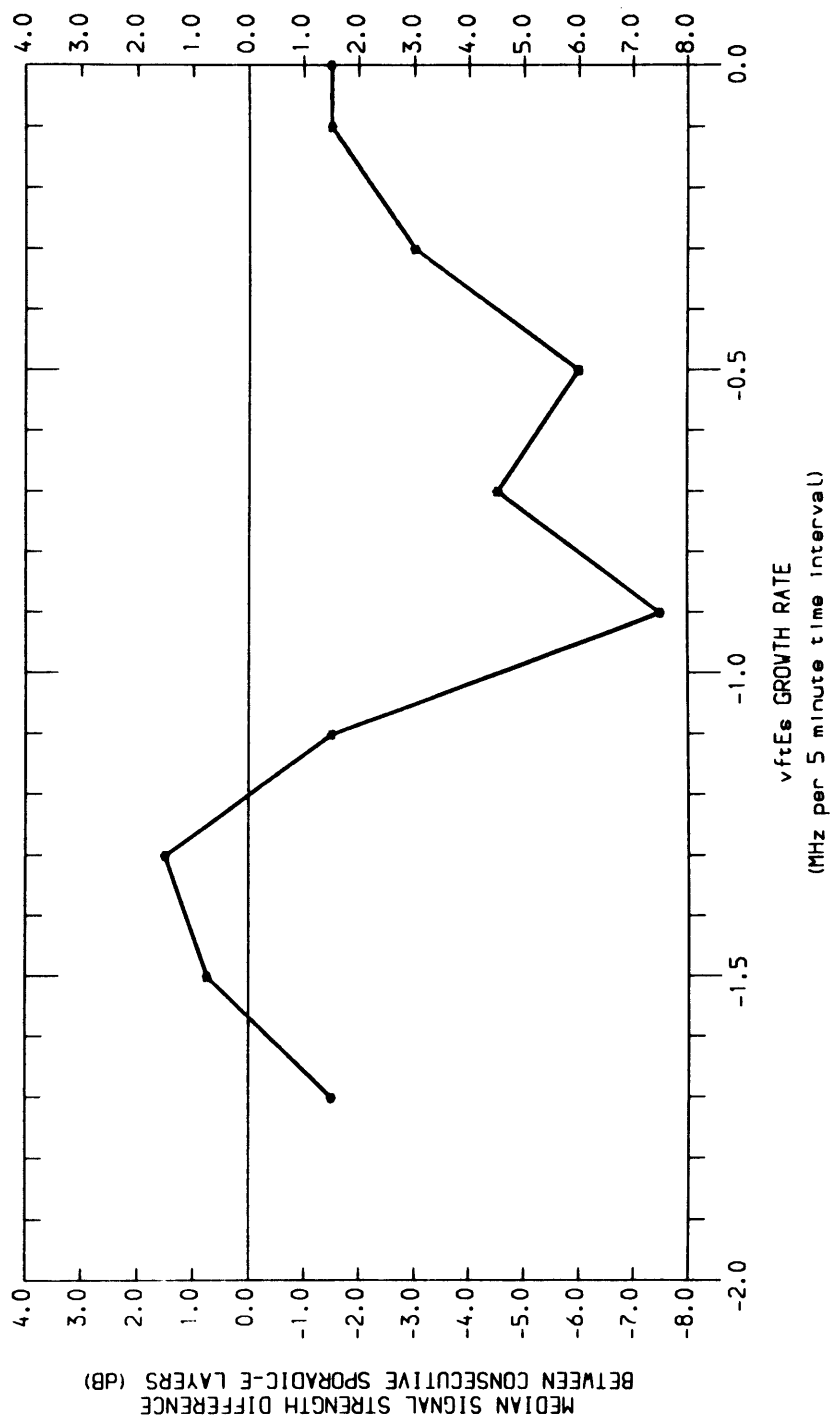


FIGURE 6.5a Median signal strength *difference* (dB) with respect to *negative*  $v f_{Es}$  growth rates (MHz per 5 minutes), between consecutively observed sporadic-E layers. The plot is compiled from signal strengths pertaining to Probing Frequencies within a 3 MHz range of the oblique sporadic-E top frequencies. Note the initially increasing signal strength difference with increasing negative  $v f_{Es}$  growth, followed by a period of transition, and finally a decrease in the difference to zero, at the largest  $v f_{Es}$  growth rates ( $\sim -1.2$  MHz per 5 minutes). All data was recorded over the Bodø/Wick propagation path during the August campaign.

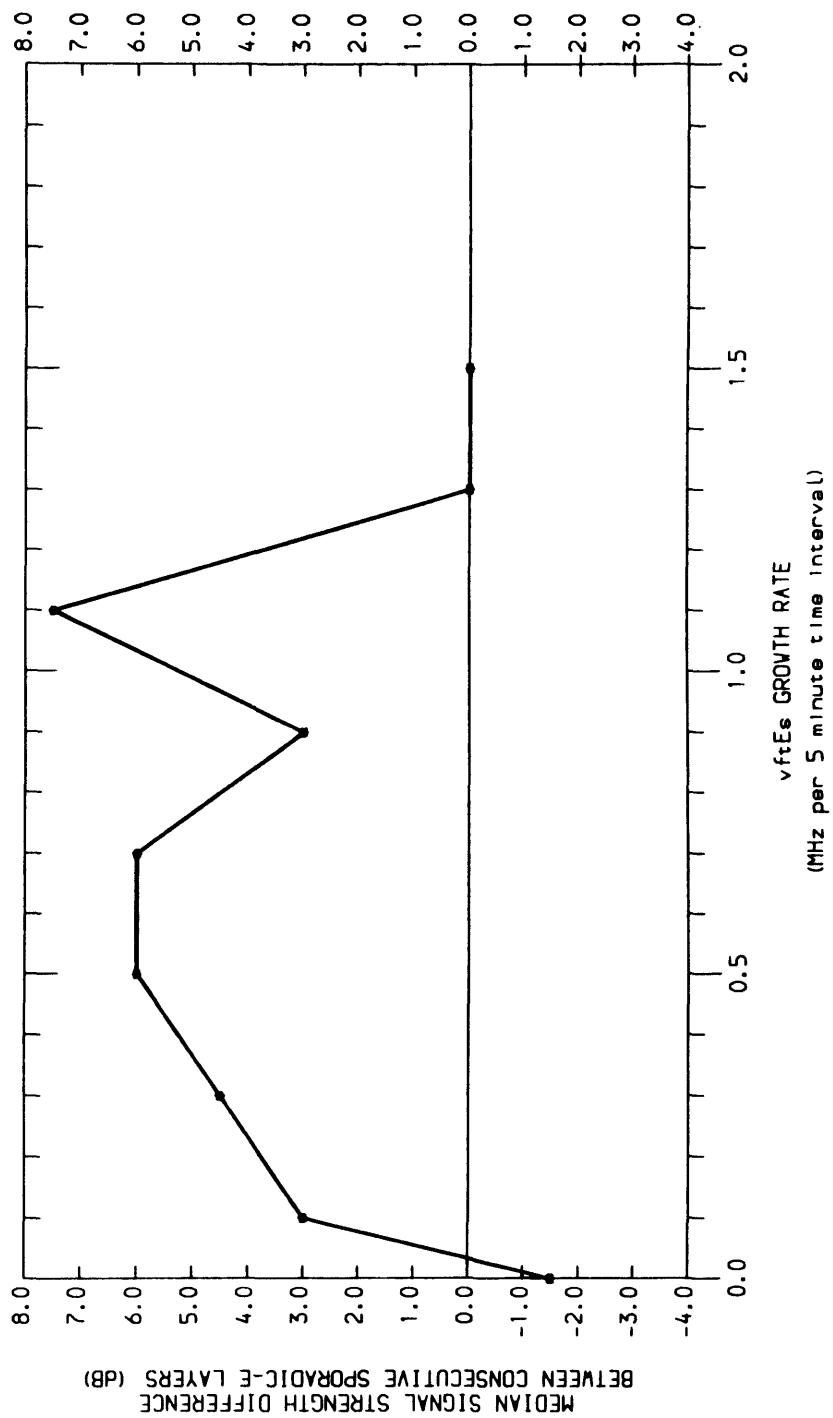


FIGURE 6.5b As for Figure 6.5a but for *positive*  $v_{ftEs}$  growth rates (MHz per 5 minutes). Note the similar variation of the signal strength difference between the consecutively observed sporadic-E layers, noting however that the difference is positive for positive  $v_{ftEs}$  growth.

### *Data Description and Analysis*

Figures 6.5(a,b) clearly demonstrate that the measured median signal strength *difference*, between two consecutively recorded sporadic-E layers, is a non-linear function of  $\nu ftEs$  growth rate. From Figure 6.5a, it is noted that the MSS difference between the ‘higher-’ and ‘lower- $ftEs$ ’ Es-layers, increases with the (negative)  $\nu ftEs$  growth rate. From a magnitude of -1.5dB for zero  $\nu ftEs$  growth rate, the MSS difference *increases* to  $\sim -6.0$  dB for a  $\nu ftEs$  growth rate  $\sim -0.5$  MHz per 5 minutes and then, intermittently, increases to  $\sim -7.5$  dB, for a  $\nu ftEs$  growth rate  $\sim -0.9$  MHz per 5 minutes. These observations are similar to what might be predicted from the *growth rate independent* signal strength- $ftEs$  relationship depicted in Figure 5.1 and analysed in Chapter 5.

However, for (negative) growth rates greater than  $\sim -0.9$  MHz per 5 minutes, the MSS difference is observed to *decrease* in value, tending to zero dB for  $\nu ftEs$  growth rates greater than  $\sim -1.2$  MHz per 5 minutes. This trend directly contradicts the signal strength- $ftEs$  relationship analysed in Chapter 5. The signal strength difference between a pair of sporadic-E layers, should only tend to zero if the Probing Frequency approximates to or is less than the blanketing frequency. If this were the case, a zero MSS difference would be observed for *all* the  $\nu ftEs$  growth rates. This is clearly not the situation in Figure 6.5a.

A small or zero MSS difference, indicates that the signal strength characteristics of the ‘higher- $ftEs$ ’ Es-layer, are similar to those of the ‘lower- $ftEs$ ’ Es-layer, within the ‘common’ frequency range (cf. Figure 6.3), for two consecutively observed sporadic-E layers. However, when the magnitudes of the respective  $ftEs$  values are significantly different, as is the case for the large  $\nu ftEs$  growth rates, it is also predicted from Figure 5.1, that the signal strength *difference* is comparatively large, and certainly not equal to zero dB. This anomaly confirms the preliminary observations noted with regard to Figure 6.4, i.e. that the  $\nu ftEs$  growth rate has a significant impact on the signal strength-top frequency relationship summarised by Equation 5.1.

Very similar characteristic features are noted in Figure 6.5b, for *positive*  $\nu ftEs$  growth rates. From a MSS difference of  $-1.5$  dB, for a zero  $\nu ftEs$  growth rate (cf. Figure 6.5a), the MSS difference increases with  $\nu ftEs$  growth rate, approaching a *threshold* value of  $\sim +6.0$  dB for  $\nu ftEs$  growth rates between  $\sim +0.5$  and  $\sim 1.1$  MHz per 5 minutes. The MSS difference then decreases to  $\sim$  zero for a  $\nu ftEs$  growth rate  $\sim 1.3$  MHz per 5 minutes. Note that a threshold MSS difference may also be applicable to the negative  $\nu ftEs$  growth rates in Figure 6.5a, for

*vftEs* growth rates between  $\sim 0.5$  and  $0.9$  MHz per 5 minutes. Note also that the finite MSS difference for zero *vftEs* growth rate is most likely a statistical feature of the result set.

It might be surmised from Figures 6.5(a,b) that the threshold signal strength *difference* is a manifestation of the *absolute* threshold signal strength observed for the blanketing range of frequencies of any given sporadic-E layer (cf. Figures 5.3(a,b)). In §5.4, the ‘partial transparency’ range of frequencies was statistically determined to be at least  $\sim 30\%$  of the *ftEs* magnitude. Presuming a typical *ftEs* magnitude of  $22.5$  MHz, for the current data set, the equivalent vertical frequency extent of the ‘partial transparency’ range is  $\sim 1.46$  MHz. This is almost a factor of three times greater than the *vftEs* growth rate at which the signal strength *difference* tends to a threshold magnitude. It is therefore highly unlikely that the Probing Frequency falls outside the ‘partial transparency’ range of frequencies, for any but the largest *vftEs* growth rates. The MSS difference threshold is therefore confirmed to be a feature of the sporadic-E *vftEs* growth rate itself.

### *Summary*

Combining the results from Figure 6.4 and Figures 6.5(a,b), and considering whole bins of data from the *vftEs* growth rates distribution plot (cf. Figure 6.2), it may be concluded that for a fixed Probing Frequency, within the ‘*common*’ range of frequencies, the received signal strength increases with *vftEs*, as described by the signal strength-*ftEs* relationship in Chapter 5, but only for *vftEs* growth rates  $\leq 0.6$  MHz per 5 minutes. This accounts for  $\sim 75\%$  of all *vftEs* growth rates. For *vftEs* growth rates between  $\sim 0.6$  and  $\sim 1.0$  MHz per 5 minutes, the MSS *difference* remains fairly static for increasing *vftEs* growth rates. And for *vftEs* growth rates  $\geq 1.2$  MHz per 5 minutes, little or no change in signal strength is observed, within the ‘*common*’ range of frequencies, between the constituents of a given pair of sporadic-E layers. Clearly, the signal strength-*ftEs* relationship analysed in Chapter 5 and summarised by Equation 5.1, does not adequately define the signal strength characteristics of sporadic-E layers arising from *vftEs* growth rates in excess of  $\sim 0.6$  MHz per 5 minutes.

Finally, it is of benefit to consider whether the time interval between consecutive ionograms is significant. For data pertaining to this Chapter, the maximum time resolution of *ftEs* recordings is one every five minutes. However, fluctuations in *ftEs* have been noted over shorter time scales e.g. *Goodwin and Summers* (1970) observed changes in *vftEs* of greater than  $0.2$  MHz in less than 2 minutes. It is therefore instructive to repeat the plots within Figures 6.5(a,b) for an arbitrarily large ionogram (*ftEs*) resolution of one per hour. Analysis by this author demonstrated that the resulting plots resemble Figure 5.1 i.e. they essentially

depict the *vftEs growth rate independent* relationship defined by Equation 5.1. The resolution of *ftEs* recordings for this study may thus be considered arbitrary to a degree, but it is of a sufficiently high magnitude to highlight tangible *vftEs* growth rate characteristics.

#### 6.4.5. Signal Strength Observations of the Sporadic-E ‘Growth’ Region

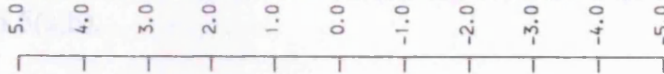
##### *Introduction*

To conclude the observations of sporadic-E *vftEs* growth rates, it is appropriate to consider the signal strength characteristics of the so-defined ‘*growth*’ range of frequencies, as introduced in Figure 6.3. For each sporadic-E observation, signal strength measurements may be determined over a range of Probing Frequencies. To enable comparisons of signal strength characteristics, between consecutive sporadic-E layers, a ‘*common*’ frequency range needs to exist between the two consecutive layers. For all previous signal strength comparisons within this Chapter, only this ‘*common*’ frequency range has been considered, the Probing Frequency being selected to be coincident with this range.

Beyond the ‘*common*’ frequency range however, and by definition, unique to the ‘*higher-ftEs*’ Es-layers, an *ftEs* ‘*growth*’ range is defined as the range of frequencies *between* the top frequencies of the ‘*higher-*’ and the ‘*lower-ftEs*’ Es-layers (cf. Figure 6.3). For a finite *vftEs* growth rate, each sporadic-E pair considered must by definition have a ‘*growth*’ range of frequencies. Note that as for the *vftEs* growth rate, the ‘*growth*’ range is a generic term; for negative *ftEs* growth, the ‘*growth*’ range represents a decrease in the *ftEs* value. It is the purpose of this Section to briefly consider the average signal strength characteristics pertinent to this ‘*growth*’ range of frequencies.

The ‘*growth*’ range by its nature is very variable, in terms of its range of frequencies and the absolute magnitude of those frequencies. It is thus difficult to select an appropriate, single Probing Frequency, for signal strength diagnostics, that will intersect a significant number of sporadic-E ‘*growth*’ ranges, without potentially biasing the results. An alternative data analysis approach was thus adopted. The Representative Signal Strength (RSS) of the ‘*growth*’ range was thus defined to be the median signal strength measurement determined for the whole ‘*growth*’ range of Probing Frequencies. The RSS of *each* ‘*higher-ftEs*’ Es-layer, is consequently determined by a potentially unique range and number of Probing Frequencies. The validity of this approach is demonstrated in Figure 6.6, by applying the analysis method

MEDIAN "REPRESENTATIVE SIGNAL STRENGTH" (RSS) DIFFERENCE FOR THE "COMMON RANGE" OF CONSECUTIVE SPORADIC-E LAYERS



MEDIAN "REPRESENTATIVE SIGNAL STRENGTH" (RSS) FOR THE "GROWTH RANGE" OF CONSECUTIVE SPORADIC-E LAYERS

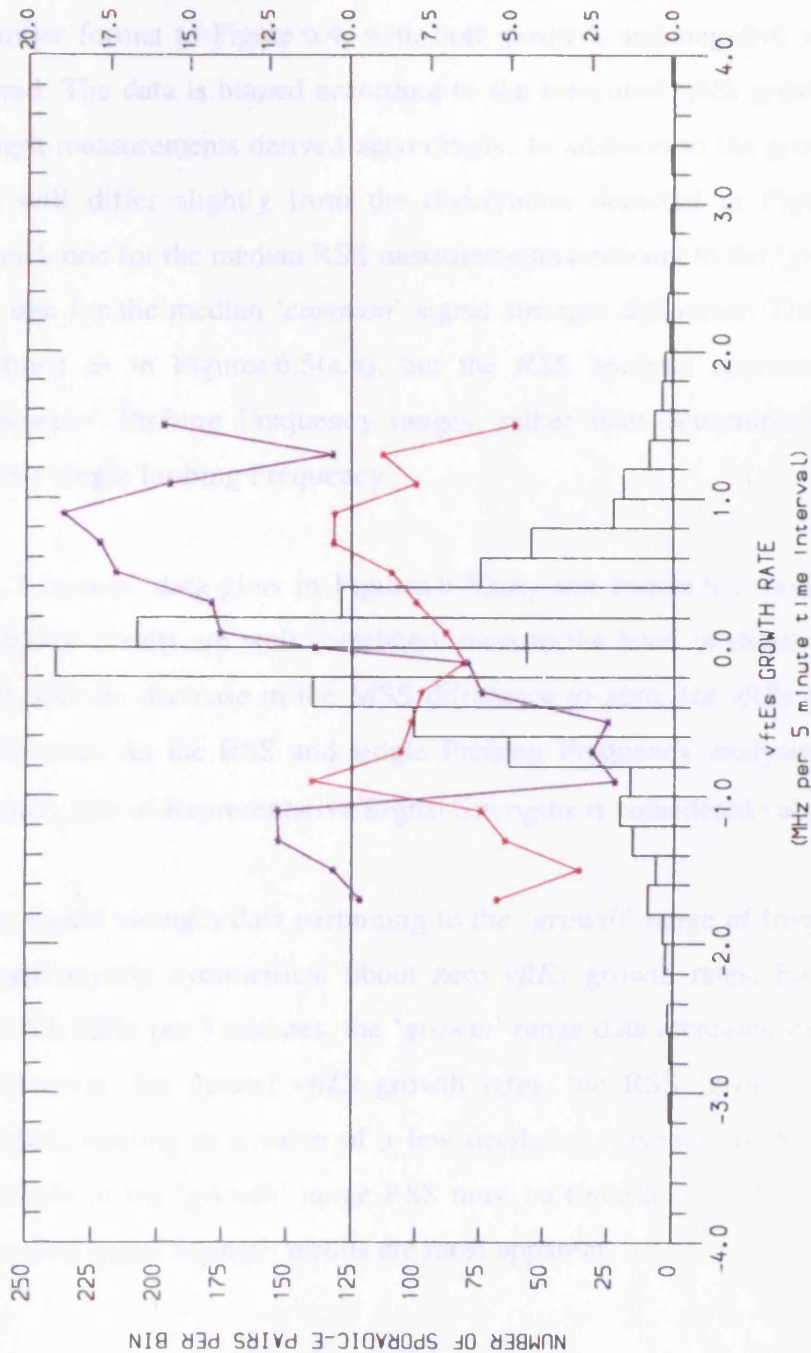


FIGURE 6.6 The "Representative Signal Strength" (RSS) of the "growth" range of Probing Frequencies, plotted with respect to the *vftEs* growth rate. The RSS is noted to vary in a similar manner to the signal strength difference plots compiled for the "common" range of Probing Frequencies. This is exemplified by the RSS representation of this "common" range data. Note that by definition, the "growth" range RSS must always be positive.

to the ‘*common*’ range of Probing Frequencies, and making comparisons with the data depicted in Figures 6.5(a,b).

#### *‘Growth’ range median RSS observations*

Figure 6.6 has a similar format to Figure 6.4, with both positive and negative *vftEs* growth rates being considered. The data is binned according to the measured *vftEs* growth rate, and median signal strength measurements derived accordingly. In addition to the growth rate bin distribution, which will differ slightly from the distribution depicted in Figure 6.2, two ordinates are presented, one for the median RSS measurements pertinent to the ‘*growth*’ range of frequencies, and one for the median ‘*common*’ signal strength *difference*. This latter data set is similarly defined as in Figures 6.5(a,b), but the RSS analysis approach has been adopted, across ‘*common*’ Probing Frequency ranges, rather than determining the signal strength difference at a single Probing Frequency.

Comparison of the ‘*common*’ data plots in Figures 6.5(a,b) and Figure 6.6, reveals that the signal strength difference results are well correlated, even to the level of detail of the MSS difference threshold, and the decrease in the MSS difference to zero, for *vftEs* growth rates  $\geq 1.2$  MHz per 5 minutes. As the RSS and single Probing Frequency analysis approaches give such similar results, use of Representative Signal Strengths is considered valid.

Considering now the signal strength data pertaining to the ‘*growth*’ range of frequencies, the median RSS is approximately symmetrical about zero *vftEs* growth rates. For increasing growth rates, up to  $\sim 0.9$  MHz per 5 minutes, the ‘*growth*’ range data increases steadily, up to a value  $\sim 11$  dB. However, for greater *vftEs* growth rates, the RSS ‘*growth*’ range data *decreases* from its peak, tending to a value of a few decibels or even zero. Noting that by definition, the magnitude of the ‘*growth*’ range RSS must be finite and positive, similarities with previously presented signal strength results are most apparent.

## **6.5 Discussion**

The signal strength characteristics of the ‘*growth*’ range of frequencies are thus similar to those of the ‘*common*’ range of frequencies. For relatively small *vftEs* growth rates ( $\leq 0.6$  MHz per 5 minutes), the signal strength within the ‘*common*’ range appears to increase for most or all Probing Frequencies pertinent to the ‘*partial transparency*’ range, as

determined by Equation 5.1. The signal strengths associated with the '*growth*' range of frequencies also increase proportionately, so as to maintain the generally observed signal strength profile structure (cf. Figure 5.3(a,b)).

For greater *vftEs* growth rates, between  $\sim 0.6$  MHz per 5 minutes and  $\sim 1.0$  MHz per 5 minutes, an approximate *threshold* signal strength difference, between the '*lower-*' and '*higher-ftEs*' Es-layers is apparent, within the '*common*' range of frequencies. Some semblance of a signal strength threshold is also noted for the '*growth*' range RSS results. The signal strength at a given Probing Frequency thus still increases for the said *vftEs* growth rates, but the increase is approximately independent of the *vftEs* growth rate magnitude.

For even greater *vftEs* growth rates, the signal strength *difference* between the '*lower-*' and '*higher-ftEs*' Es-layers is noted to *decrease* i.e. increasing magnitudes of *ftEs* actually results in lower signal strength magnitudes being received at a given Probing Frequency, than observed for smaller *vftEs* growth rates. The RSS of the '*growth*' range also decreases, even though the difference between the top frequencies of the '*lower-*' and '*higher-ftEs*' Es-layers is increasing. For *vftEs* growth rates greater than  $\sim 1.2$  MHz per 5 minutes, the signal strength difference between the '*lower-*' and '*higher-ftEs*' Es-layers, within the '*common*' range of frequencies, is approximately zero, as is the RSS of the '*growth*' range of frequencies. This is an indication of an almost identical signal strength-frequency profile for the '*higher-ftEs*' Es-layer, as compared to the '*lower-ftEs*' layer, despite a large increase in the top frequency.

### 6.5.1 Schematic Representation of Sporadic-E *vftEs* Growths

The observations above are summarised in the schematic representations of sporadic-E *vftEs* growth per unit time, depicted in Figures 6.7(a,h). Figures 6.7(b,h) each depict a signal strength profile, with respect to Probing Frequency, both before and after a given *vftEs* growth. All *vftEs* growths are with respect to the '*base*' signal strength profile depicted in Figure 6.7a. As positive *vftEs* growth is depicted throughout, Figure 6.7a is always defined as the initial or '*lower-ftEs*' layer, for each of the growth rates represented by Figures 6.7(b,h). The '*base*' signal strength profile is thus shaded, the signal strength profile arising from a given *vftEs* growth, is depicted by a continuous line, and as a means of comparison, the dotted line within each Figure gives the signal strength profile from the preceding Figure, arising from a lower magnitude of *vftEs* growth rate.

# Signal Strength-Probing Frequency Profiles for Differing $\nu ftEs$ Growth Rates

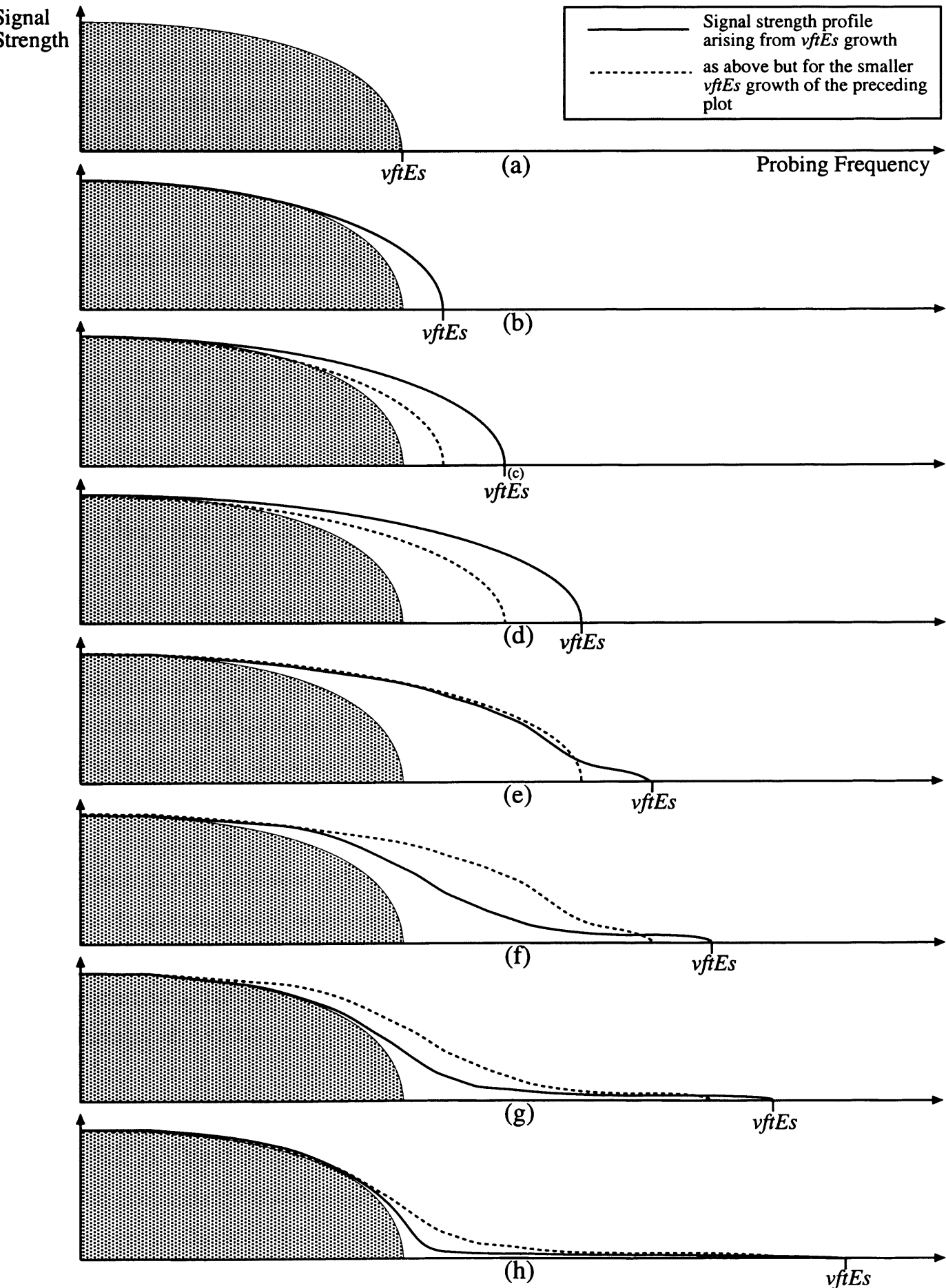


FIGURE 6.7 Schematic of signal strength versus Probing Frequency profiles, for increasing  $\nu ftEs$  growth rates, with respect to the 'base' profile (a). Note that for the smaller growth rates ((b) to (d)) the general profile 'shape' is maintained and the signal strength increases over a greater range of 'common' Probing Frequencies. At the larger  $\nu ftEs$  growth rates ((e) to (h)), the converse situation prevails, such that for the greatest  $\nu ftEs$  growth rate (h), the signal strength increases little with respect to the common 'base' (a), and a low signal strength 'tail' defines the  $\nu ftEs$  growth.

It is emphasised that the series of Figures, from (b) to (h), do *not* represent a chronological sequence, but are independent of each another. Though the Figures pertain to positive  $\nu ftEs$  growth, the observations may similarly be interpreted for negative  $\nu ftEs$  growth rates. For the purpose of this discussion, it is assumed that the ‘common’ range of Probing Frequencies extends over at least the ‘partial transparency’ range of frequencies, of the ‘lower- $ftEs$ ’ layer (Figure 6.7a).

$\nu ftEs$  growth rates of increasing magnitude, up to  $\sim 0.6$  MHz per 5 minutes, are represented by Figures 6.7(b,d). The signal strength profiles are noted to maintain their ‘shape’ for the differing rates of  $\nu ftEs$  growth, and resemble the empirical profile depicted in Figure 5.3a. Note that the signal strength increases over an increasing range of Probing Frequencies, within the ‘partial transparency’ frequency range, with increasing  $\nu ftEs$  growth rate, and that the increase is greatest for Probing Frequencies of closest proximity to the  $ftEs$  of the ‘lower- $ftEs$ ’ Es-layer (i.e. the  $ftEs$  of Figure 6.7a). Note also that the RSS of the ‘growth’ frequency range also increases with increasing  $\nu ftEs$  growth rate.

Figure 6.7e approximates to the ‘transitional’ range of  $\nu ftEs$  growth rates, between  $\sim 0.6$  MHz per 5 minutes and  $\sim 1.0$  MHz per 5 minutes. The signal strengths for the ‘partial transparency’ range of Probing Frequencies are noted to be independent of  $\nu ftEs$  growth rate, i.e. no increase in signal strength is observed. The signal strength profile of the sporadic-E layer as a whole, is also noted to be deviating from the initial profile ‘shape’ defined in Figure 6.7a and determined empirically in Figure 5.3a.

Figures 6.7(f,h) represent  $\nu ftEs$  growth rates greater than  $\sim 1.0$  MHz per 5 minutes. Note that the signal strengths are *decreasing* for *all* Probing Frequencies, with respect to those noted for lower  $\nu ftEs$  growth rates (cf. the dotted lines). The ‘growth’ range signal strengths are also tending to a ‘tail-like’ profile, of decreasing RSS magnitude, similar to those observed by *Turunen et al.* (1980).

### 6.5.2 A Cloud Model Explanation of the $\nu ftEs$ Growth Characteristics

The ‘cloud model’ plasma structure of sporadic-E was introduced in Chapter 2 (§2.4.2.1) and invoked in Chapter 5 (§5.6.1) to explain the signal strength profile of Es-layers, described by Equation 5.1. The model is thus equally applicable to the current observations and provides a ready explanation of the  $\nu ftEs$  growth characteristics noted throughout this Chapter, and specifically, those modelled in Figures 6.7(a,h).

The signal strength received at a given Probing Frequency may be considered as proportional to the total cross-sectional area of clouds, of plasma density greater than the equivalent Probing Frequency plasma density (cf. §5.6.1). Considering equal cloud scale sizes, the schematics in Figures 6.7(a,h) may be interpreted in terms of plasma cloud *number* density expressed as a function of cloud *plasma* density. The cloud(s) of maximum plasma density define the sporadic-E top frequency (cf. §5.6.1).

For relatively small *vftEs* growth rates ( $\lesssim 0.6\text{MHz}$  per 5 minutes), depicted by Figures 6.7(b,d), the cloud *number* density is observed to increase, over an increasing range of ‘partial transparency’ frequencies, for increasing *vftEs* growth rates. Further, clouds of increased *plasma* density are noted within the ‘*growth*’ range of frequencies, with corresponding number densities, so as to maintain the statistically ‘typical’ signal strength profile ‘shape’, depicted in Figure 5.3a.

For the ‘transitional’ growth rates, between  $\sim 0.6\text{MHz}$  per 5 minutes and  $\sim 1.0\text{MHz}$  per 5 minutes (cf. Figure 6.7e), the cloud number densities within the ‘partial transparency’ range of Probing Frequencies, vary little with respect to magnitudes noted for lower *vftEs* growth rates (cf. the comparison of the solid and broken lines in Figure 6.7e). Further, cloud *number* densities, within the ‘*growth*’ range of Probing Frequencies, are noted to be *less than* those observed at lower *vftEs* growth rates.

At even higher *vftEs* growth rates,  $\gtrsim 1.0\text{MHz}$  per 5 minutes (Figures 6.7(f,h)), there is increasingly little difference between the cloud number densities, prior to and after a given *vftEs* growth, for both the ‘partial transparency’ and ‘*growth*’ range of frequencies. In the latter case, this is interpreted as very low, and increasingly similar, cloud *number* densities, extending over an increasingly greater range of cloud *plasma* densities. For the largest *vftEs* growth rates, the cloud structure thus varies little within the ‘partial transparency’ range of Probing Frequencies, but an extended range of low *number* density, but high *plasma* density clouds, is observed to form a ‘tail-like’ signal strength profile.

Clearly, Figures 6.7(e,h) do not conform with the signal strength profiles implied by Equation 5.1 and depicted in Figure 5.3a. Again however it is emphasised that the proportion of growth rates greater than  $0.6\text{MHz}$  per 5 minutes is  $\sim 25\%$ . The great majority of sporadic-E top frequency growth rates still conform to the signal strength profiles depicted by Figures 6.7(b,d), for which Equation 5.1, derived independent of growth rate considerations, is applicable. The ‘modified’ signal strength-frequency profiles, depicted in Figures 6.7(e,h),

arise from the increasingly ‘non-typical’ plasma cloud distributions being generated due to the relatively high top frequency growth rates ( $\geq 0.6\text{MHz}$  per 5 minutes).

From a logical interpretation of the plasma cloud model, the existence of a threshold *vftEs* growth rate is perhaps not surprising. Statistically speaking, the increase in plasma cloud *number* densities (proportional to signal strength) over a range of cloud *plasma* densities (proportional to top frequency), will be increasingly curtailed, the larger the extent of the plasma density range, within the limits of a constant or slowing increasing *total* plasma content within the Es-layer. Either the extent of the plasma density range is restricted i.e. restricting the top frequency growth rate potential, or the cloud *number* densities at the higher cloud *plasma* densities are restricted, resulting in an increasingly ‘tail-like’ signal strength-frequency profile. From the distribution of *vftEs* growth rates, depicted in Figure 6.2, the former scenario is obviously more prevalent.

#### *Practical Considerations of the Cloud Model Interpretation of vftEs Growth*

The nature of *vftEs* growth has been interpreted in terms of the sporadic-E plasma cloud model: the signal strength reflected from a given sporadic-E layer, at a given Probing Frequency, will be determined by the number distribution, and size, of the plasma clouds, with respect to their plasma density. Each of these parameters may vary depending on the characteristics of the cloud generation mechanism. To fully explain the variability of these parameters, noted for different rates of *vftEs* growth, it is instructive to consider the nature of the possible generation mechanisms.

In §2.4.2.1, various plasma cloud generation mechanisms were considered. The interference of gravity waves with the solar semidiurnal tide (e.g. *Nygrén et al.*, 1990) and indeed, instabilities within the waves themselves (*Fritts et al.*, 1988), both contribute to a spectrum of wavelengths which may thus generate a spectrum of plasma clouds, through varying horizontal and vertical convergence magnitudes. This mechanism however describes the relatively low *vftEs* growth rates ( $\leq 0.6\text{MHz}$  per 5 minutes) depicted in Figures 6.7(b,d).

To account for the relatively large growth rates ( $\geq 1.0\text{MHz}$  per 5 minutes), represented in Figures 6.7(f,h), the generation or enhancement of plasma cloud densities must pertain to low *number* density, high *plasma* density clouds. ‘Critical levels’ of gravity waves (*Hines*, 1968) may account for such specific requirements. The resulting plasma convergence will be intense and localised and hence be of low number density (*Miller and Smith*, 1978). Further, the conditions for the convergence of plasma at a ‘critical level’ (the excitation of the gravity

wave for an extended time by a coherent source) are very specific and rare. This satisfies the infrequent nature of relatively large  $\nu ftEs$  growth rates.

The convergence of ionisation, by the windshear mechanism, from ablating meteors, is also a possible means by which a few intense clouds of ionisation may be generated, independent of the number distribution of other existing plasma clouds. Again, this mechanism is characterised by its infrequency and its low cloud numbers, resulting in a rapid enhancement of the top plasma frequency, yet of a low signal strength nature. This mechanism is also likely to generate short-lived plasma clouds. *Miller and Smith (1978)* observed such clouds for periods of just 10 minutes (~ 2 Bodø/Wick ionogram recordings).

Both of the above mechanisms result in the generation of plasma clouds *within* the existing radar field of view. It is also possible that  $\nu ftEs$  growth arises from plasma clouds *drifting into* (or out of) the field of view. Plasma clouds, within sporadic-E layers, have generally been observed to drift with the E-region neutral wind (e.g. *Kolawole and Derblom, 1978*). Typical wind speeds of between  $\sim 50 \text{ m s}^{-1}$  and  $\sim 100 \text{ m s}^{-1}$  are observed at E-region heights (*Bedinger et al., 1968*). In a time interval of five minutes, a plasma cloud may thus drift between  $\sim 15 \text{ km}$  and  $\sim 30 \text{ km}$ . From Equation 5.3 (§5.6.1) the first Fresnel Zone for HF propagation over the Bodø/Wick path, approximates to between  $\sim 20 \text{ km}$  and  $\sim 25 \text{ km}$ . Plasma structures consistent with scale sizes approximating to the first Fresnel Zone, may thus drift into the radar field of view, between consecutive ionogram recordings. These may then be responsible for abrupt changes in the observed sporadic-E top frequencies.

The main potential difference between plasma clouds drifting into the radar field of view, and clouds forming in-situ, is the time required for generation. Drifting clouds may be generated over much longer periods of time, external to the field of view, and be stable structures. However, the drifting of plasma structures within sporadic-E layers is a common feature, as indicated above, and hence the drifting into view of an enhanced plasma cloud, will most probably be accompanied by further drifts of enhanced, or otherwise, plasma clouds. The sudden, low signal strength growth in the  $\nu ftEs$ , will possibly be transformed into a high signal strength, high top frequency feature, as the whole spectrum of plasma clouds drifts into view. Indeed, the degree of infrequency of rapid growths in  $\nu ftEs$ , would solely be a manifestation of the randomness as to which density clouds *initially* drifted into the radar field of view. Note that irrespective of subsequent plasma cloud drifts, the Bodø/Wick field of view is large, and a drifting cloud will potentially be the source of reflected signals, over an

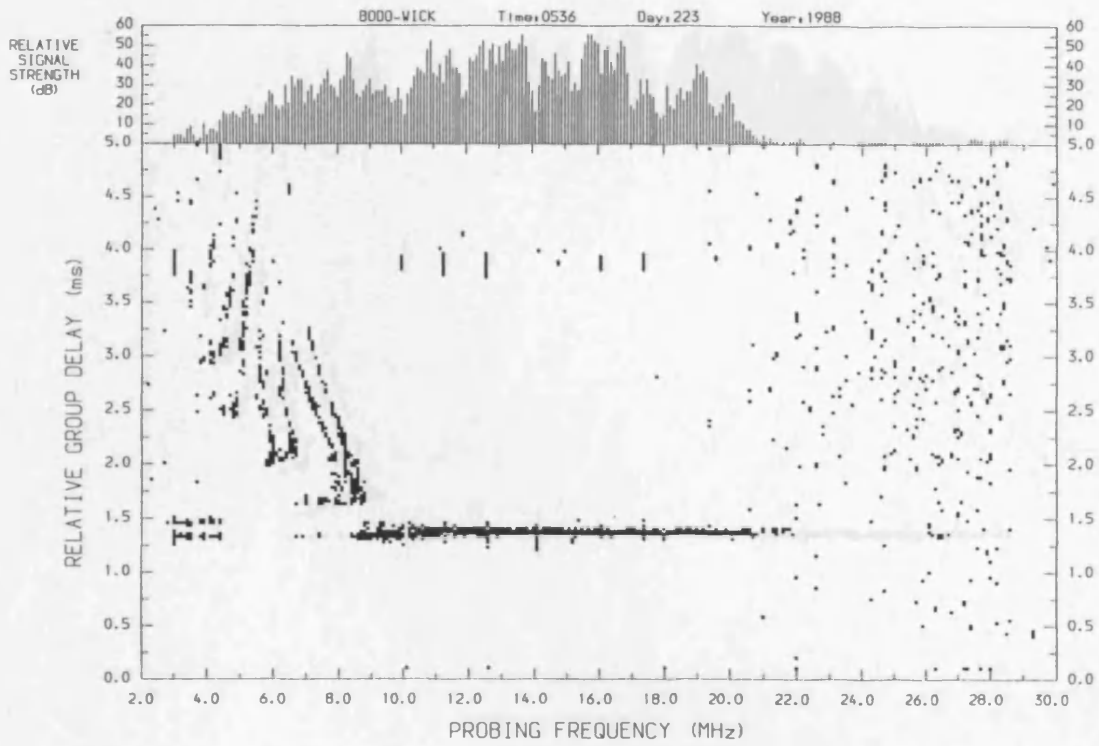
extended period of time. This is in contrast to the intrinsically transient nature of the gravity wave ‘critical level’, and meteor ablation, plasma cloud generation mechanisms.

### *Ionogram Observations of $\nu ftEs$ Growth*

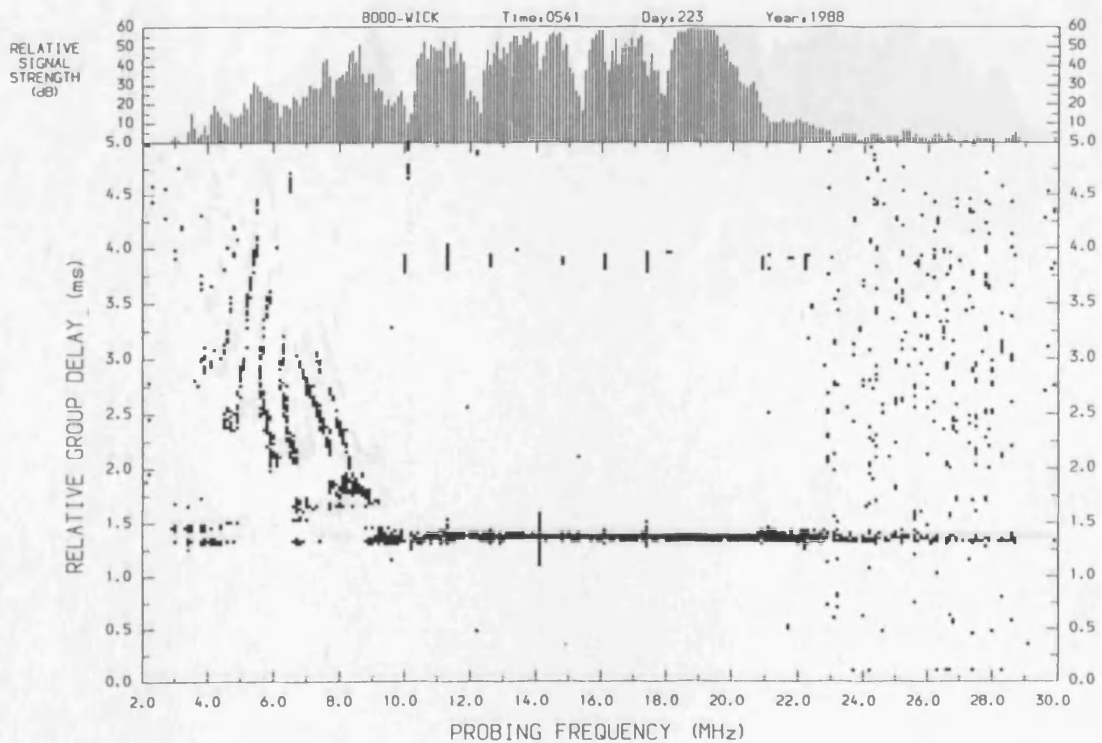
It is instructive to refer back to Figure 6.1. Several instances of relatively large  $\nu ftEs$  growth rates are noted, at 00:41 UT, 05:41 UT, 20:46 UT and 22:06 UT. The example at 05:41 UT, day 223, is presented in Figures 6.8(a,d). The main panel of each of the Figures 6.8(a,d), depicts the ionogram. Each ionogram is dimensioned by relative group delay (ms) versus oblique Probing Frequency (MHz), as described in §3.3.2. The upper panel of each Figure represents the signal strength (dB) received by the scanning Probing Frequency. The frequency-extended, constant group delay sporadic-E trace is clearly identifiable within each ionogram. The time interval between each of the ionograms is noted to vary, so as to highlight the different features of the  $\nu ftEs$  growth, rather than to analyse the actual *rate* of growth.

It is immediately apparent from both Figures 6.8(a,d) and Figure 6.1, that this initially, relatively large  $\nu ftEs$  growth ( $\sim 1.7$  MHz) is not temporary but rather transforms into a stable, high signal strength sporadic-E layer. Figure 6.8a depicts a typical Es-layer of  $ftEs$  equal to 21.0 MHz. In Figure 6.8b, the top frequency is noted to have extended to 28.8 MHz, but such that a low signal strength, Probing Frequency ‘tail’ has developed, within a five minute time interval. Figure 6.8c depicts the Es-layer 15 minutes later. In the intervening 15 minutes, the lower signal strengths of the Probing Frequency ‘tail’ have gradually increased. The Es-layer depicted in Figure 6.8c is now noted to have a ‘typical’ signal strength profile (cf. Figure 5.3a). Figure 6.8d depicts the Es-layer a further 15 minutes later. This generally high signal strength Es-layer is noted to have a top frequency greater than 29.9 MHz.

This latter example of *stable*  $\nu ftEs$  growth, suggests the influence of drifting plasma clouds. In contrast, Figures 6.9(a,d) depict a very large ( $\geq 3.2$  MHz), but *temporary*  $\nu ftEs$  growth. The example is taken from day 220, for the time range of 05:36 UT to 05:41 UT (cf. Figure 3.8). The four ionograms in Figures 6.9(a,d) represent a 15 minute time interval, all ionograms being consecutive. Figures 6.9(a,b) depict an Es-layer of oblique top frequency equal to 15.2 MHz. In both ionograms, a low signal strength, potential extension to the Es-layer top frequency is noted, but in accordance with the ‘mostly continuous’ scaling rule for Es-layers (Piggott and Rawer, 1961), this section of trace is disregarded. In contrast, the Es-layer depicted in Figure 6.9c, is now noted to be ‘mostly continuous’, with a low but measurable signal strength, extending over a Probing Frequency ‘tail’, to over 29.9 MHz. But in Figure 6.9d, the transient ‘tail’ has dispersed and the top frequency has reduced back to

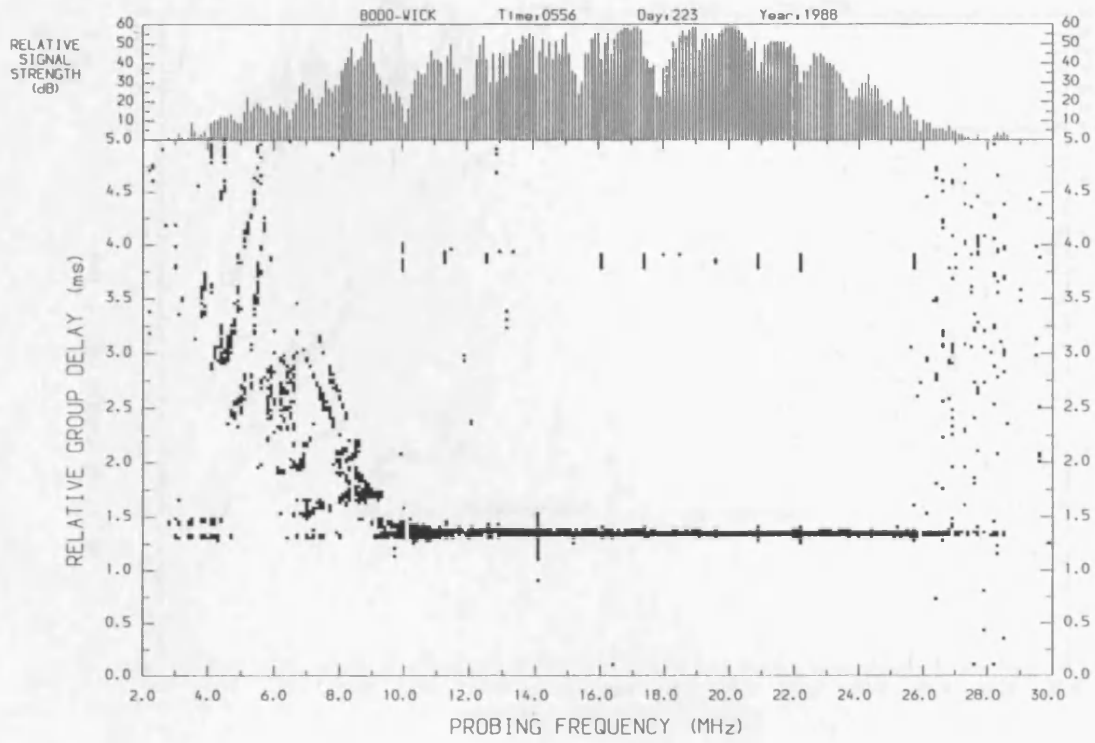


(a)

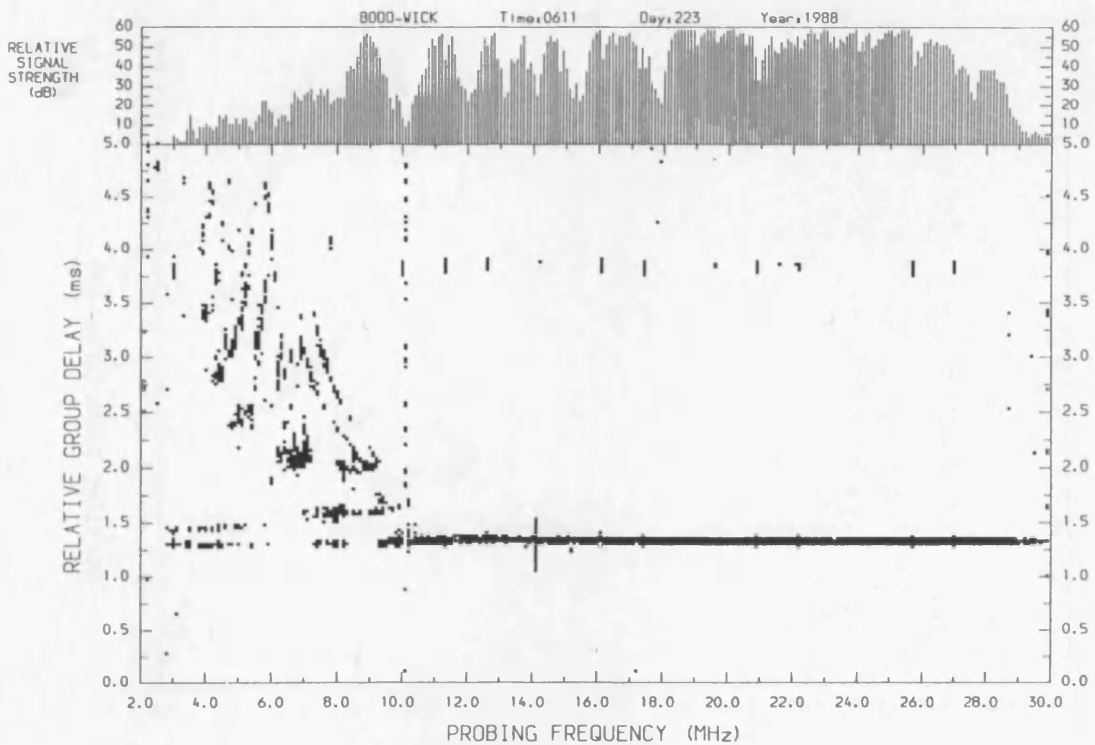


(b)

FIGURES 6.8(a,d) A case example of a rapid growth in the sporadic-E top frequency, transforming from a low signal strength "tail" of Probing Frequencies, into a stable, high signal strength, high top frequency sporadic-E layer. The series of four ionograms are not consecutive in time, but span 40 minutes, highlighting the important signal strength profile changes. The data was recorded over the Bodø/Wick propagation path, on day 223, 1988.

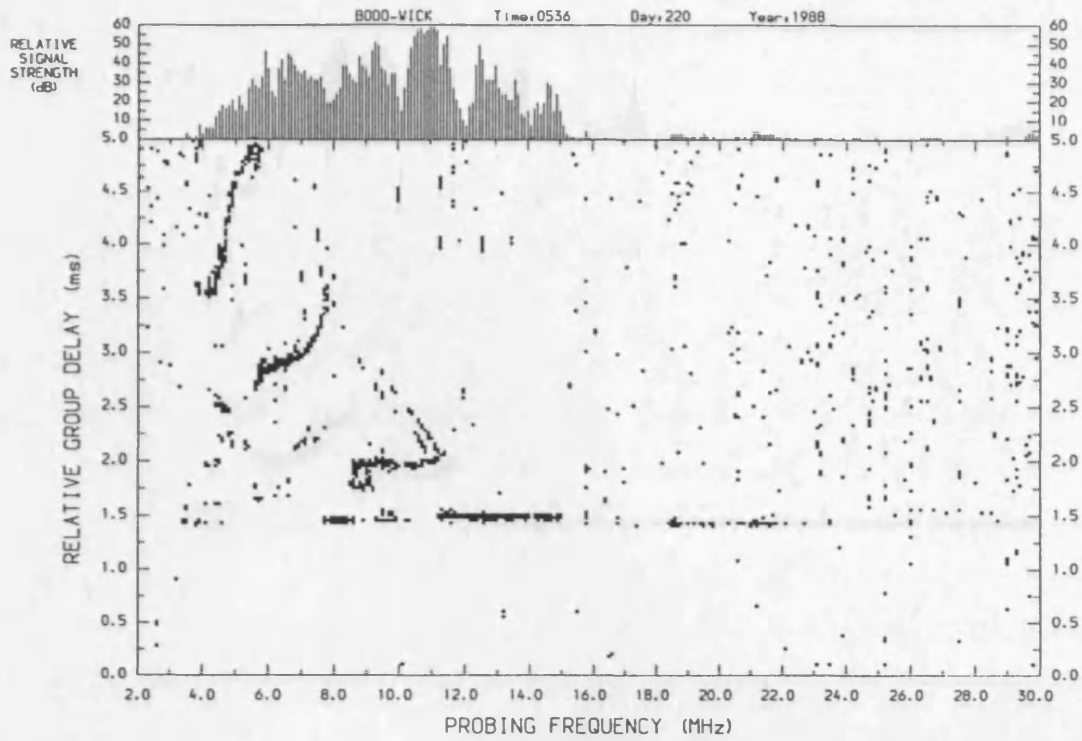


(c)

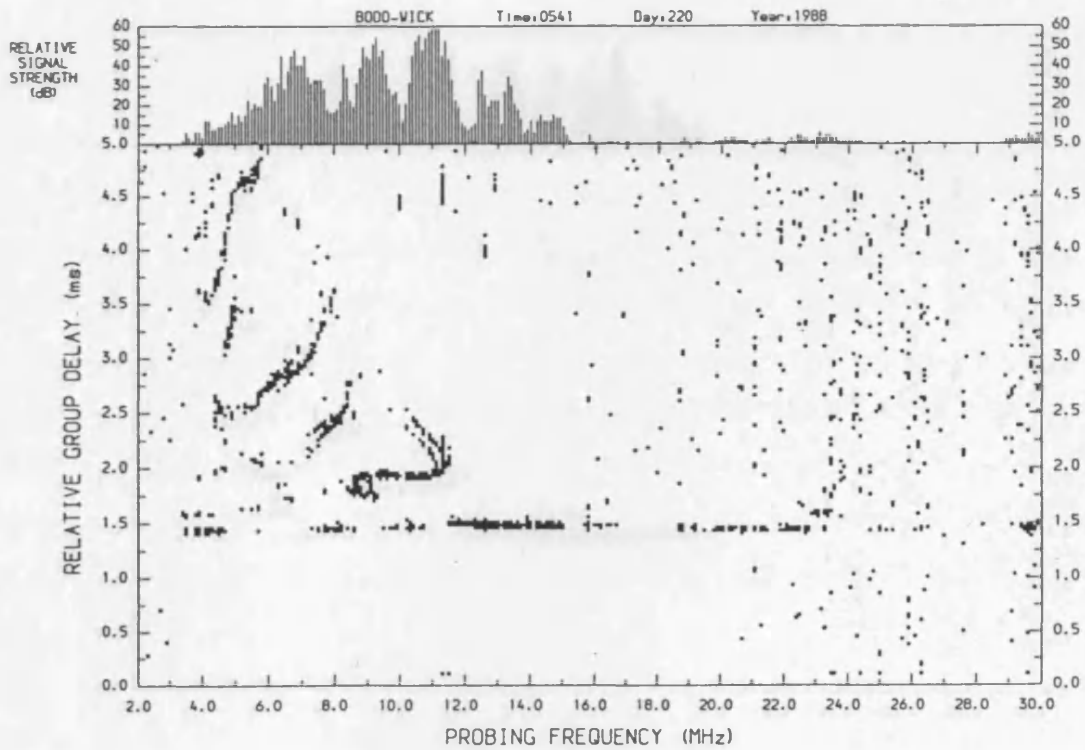


(d)

PROBING (c) and (d) show the relative group delay and signal strength of the signals from the BODO-WICK station. The group delay is plotted in milliseconds (ms) and the signal strength is plotted in decibels (dB). The group delay is generally low, around 1.5 ms, but increases sharply at approximately 10 MHz, reaching about 4.0 ms. This increase is consistent across both time slots, 0556 and 0611. The signal strength is generally high, between 30 and 50 dB, with some fluctuations. The BODO-WICK station is located at Bodo, India, and is used for ionospheric sounding.

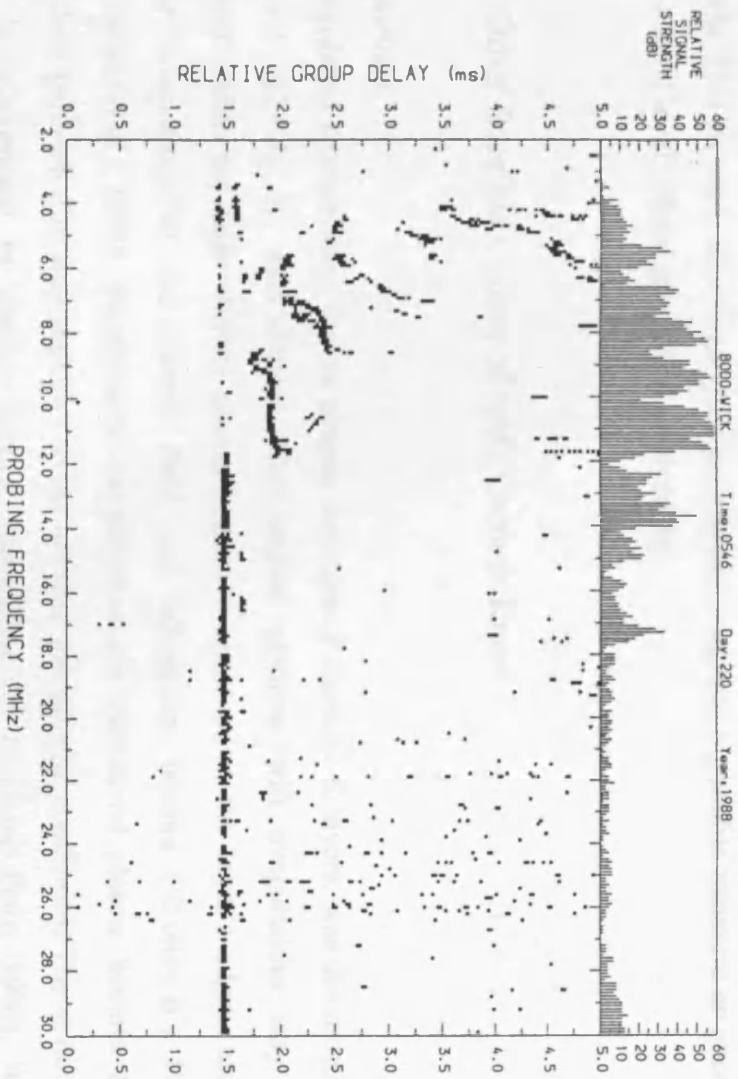


(a)

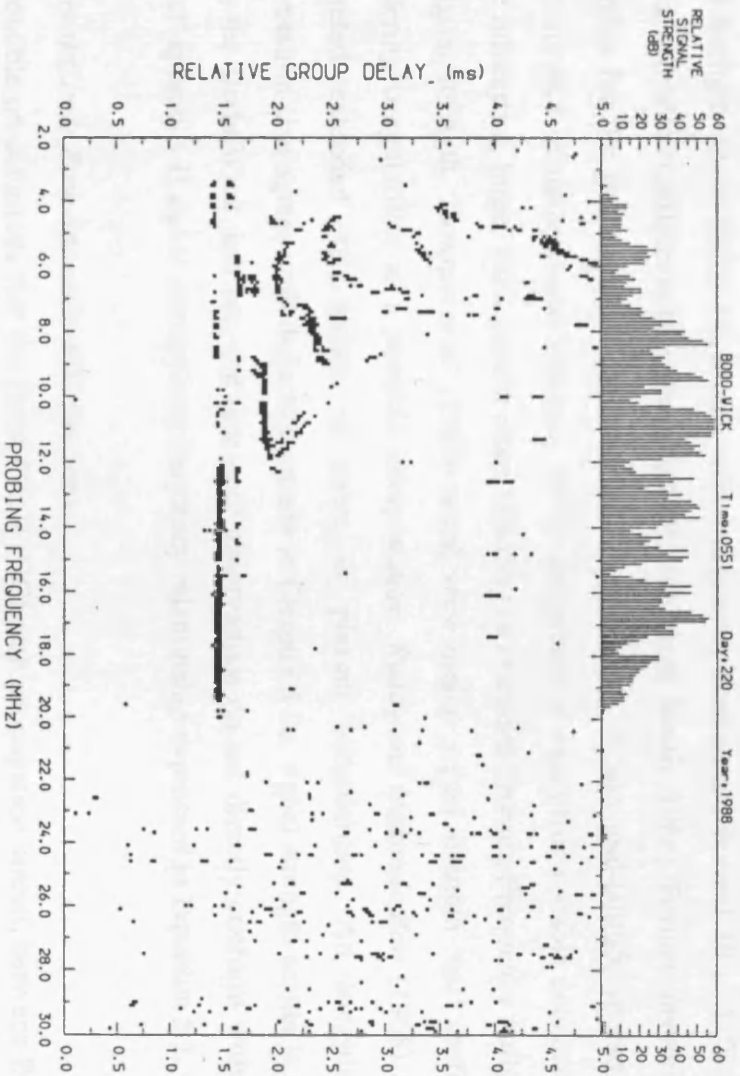


(b)

FIGURES 6.9(a,d) A case example of a *temporary* rapid growth in the sporadic-E top frequency, the Es-layer being of very low signal strength within the “growth-range” of Probing Frequencies. The major part of the top frequency growth, fades within the 20 minute time span of the four consecutive ionograms. The data was recorded over the Bodø/Wick propagation path, on day 220, 1988.



(c)



(d)

19.8MHz. This example of a large *vftEs* growth rate, suggests a possible meteoric or gravity wave ‘critical level’, cloud generation mechanism.

### 6.5.3 Other Possible Causes of *vftEs* Growth Rates

#### *Irregularities*

An irregularity interpretation for the plasma structure of sporadic-E layers, was discussed in Chapter 2 (§2.4.2). At mid-latitudes, field-aligned gradient drift irregularities may be generated within the large density plasma gradients observed at the layer’s edges, under suitable orientations of the electric field and subsequent plasma (‘E cross B’) flow (e.g. *Ecklund et al.*, 1981). Intrinsically, irregularities are short-lived plasma features and hence their generation is very sensitive to the ambient ionospheric conditions. The scattered power is proportional to plasma density fluctuations (cf. *Fejer and Kelly*, 1980), with favourable scattering conditions being related to the relationship between the radar and irregularity wavelengths (cf. §3.4.1).

Signal strength observations associated with irregularity scatter, are several 10’s of dB less than for sporadic-E reflection (e.g. *Booker*, 1959; *Miya and Sasaki*, 1966). Further, favourable conditions for the generation of gradient drift irregularities, within mid-latitude sporadic-E layers, are rare (*Haldoupis and Schlegel*, 1993). Irregularities thus offer a viable explanation for the infrequent, large, *vftEs* growth rates, resulting in extended Probing Frequency ‘tails’ of low signal strength. *Turunen et al.* (1980) noted very similar signal strength ‘tail’ profiles, considering irregularities as a possible interpretation. *Reddy and Mukunda Rao* (1968) also interpreted extended *ftEs* values in terms of plasma irregularities. An irregularity interpretation also agrees with deductions made in Chapter 5 i.e. signal strength scatter is rare within the Bodø/Wick data set, and that such observations do not directly conform with the ‘typical’ sporadic-E signal strength-top frequency relationship expressed in Equation 5.1.

#### *Off-Great Circle Path Sporadic-E Reflections*

It is possible on occasions that the Great Circle (GC) path propagation circuit, between Bodø and Wick, does not sustain the most favourable signal strength link, and that the oblique sounder preferentially receives from greater azimuth angles, with respect to the direct Bodø/Wick path. Such circumstances may arise from so called ionospheric ‘tilts’. From Secant Law considerations (cf. §3.2.3), the received oblique radar frequency will be greater than that received directly over a GC path, for a given sporadic-E plasma density. Such

'off-azimuth' reflections will thus manifest themselves as (sudden) variations in the scaled  $\nu f E_s$  values, and without azimuth angle data, be interpreted as variations in the sporadic-E plasma density and structure. The signal strength determinations will however be weaker, with respect to GC path propagation, with the signal strength decreasing with greater azimuth angles, and hence greater apparent top frequencies, all plasma parameter considerations being considered equal. These deductions are in agreement with the observations above, for apparent relatively large  $\nu f E_s$  growths, noting also that 'off-azimuth' reception is only probable for a small minority of sporadic-E recordings.

### *Sequential Es*

Sequential sporadic-E is observed to descend in altitude, with the descent of a solar, semidiurnal tidal convergent node (cf. §2.1). During this descent, windshear theory predicts an increase in the ion convergence term (§2.3.3), resulting in greater sporadic-E top frequencies. The descent speeds however are only  $\sim 1\text{-}2\text{ m s}^{-1}$  (e.g. *Smith*, 1970; *Turunen et al.*, 1988) i.e.  $\sim 300$  to  $600$  m descent in a five minute time interval. Such reductions in altitude are unlikely to give the observed variations in  $\nu f E_s$ . Further, sequential-Es is only pertinent to *increases* in  $\nu f E_s$  magnitudes, and hence in no way accounts for the equally likely negative  $\nu f E_s$  growths, noted herein (e.g. Figure 6.5a). Sequential-Es is thus not considered to be significant with respect to deliberations within this Chapter.

## 6.6 Summary

In Chapter 5, it was determined that the relationship between the sporadic-E signal strength, measured at a given Probing Frequency, and the top frequency of the layer, may be expressed in terms of Equation 5.1, for values of ' $n$ ' between  $\sim$  zero and  $\sim 20$ . The investigations within this Chapter demonstrate that the  $\nu f E_s$  growth rate is also an important determinant with respect to the said signal strength relationship, a factor not considered within Equation 5.1. Only  $\nu f E_s$  growth rates  $\geq 0.6$  MHz per 5 minute time interval, have an impact on the sporadic-E signal strength characteristics statistically predicted by Equation 5.1, and it is noted that only  $\sim 25\%$  of  $\nu f E_s$  growth rates, for the Bodø/Wick data set, are greater than this magnitude. However, for  $\nu f E_s$  growth rates that *are* greater than  $\sim 0.6$  MHz per 5 minutes, the impact on the sporadic-E signal strength characteristics is very significant.

Considering the ‘*common*’ Probing Frequency range between pairs of consecutively recorded sporadic-E traces (cf. Figure 6.3), the signal strength *difference* is observed to be independent of *vftEs* growth rate, for top frequency growth rates between  $\sim 0.6$  MHz per 5 minutes and  $\sim 1.0$  MHz per 5 minutes. And for *vftEs* growth rates  $\geq 1.2$  MHz per 5 minutes, the *absolute* signal strength is observed to be independent of the resulting top frequency magnitude. Similar characteristics are noted within the ‘*growth*’ range of frequencies (cf. Figure 6.3), such that at *vftEs* growth rates greater than  $\sim 1.0$  MHz per 5 minutes, this ‘*growth*’ range takes the form of a low signal strength ‘tail’ (cf. *Turunen et al.*, 1988). These characteristics result in signal strength-Probing Frequency profiles that differ substantially from the growth rate independent (‘typical’) profiles derived in Chapter 5 and depicted in Figures 5.3(a,b). Schematic profiles for increasing rates of *vftEs* growth, are depicted in Figures 6.7(a,h), and fully depict the observations described above.

The *vftEs* growth rate properties of sporadic-E may be interpreted in terms of the plasma ‘cloud’ structure (cf. §2.4.2.1), the number distribution of different plasma density clouds, directly corresponding signal strength-frequency profile. The most commonly espoused generation mechanism for the cloud structure, is gravity waves, and their interference with each other and the semidiurnal solar tide (e.g. *Nygrén et al.*, 1990). This generation mechanism is however unlikely to account for the relatively large *vftEs* growth rates. ‘Non-typical’ cloud number distributions most likely arise from the random drifting of ‘clouds’ into the radar field of view. Alternatively, and particularly for the largest *vftEs* growth rates, the generation of a low number of high plasma density clouds, due to meteor ablation or the coincident presence of gravity wave ‘critical levels’, is a possibility.

The generation of field-aligned irregularities *within* sporadic-E layers, offers an alternative interpretation of the observations. However, the signal strength characteristics determined from irregularity scattering, differ markedly from those associated with reflection from a cloud structure. Irregularities are thus considered to only account for the signal strength determinations arising from the largest *vftEs* growth rates. Non great circle path propagation is another potential source of pseudo large *vftEs* growth rates, but sequential-Es is not considered to have an important influence.

# Chapter 7

## Correlation Studies of Sporadic-E Layers and E-Region Plasma Irregularities

### 7.1 Introduction

The generation of E-region, field-aligned, plasma irregularities was introduced in Chapter 2 (cf. §2.4.2.2). Several mechanisms are responsible for these instabilities, the most prominent being the ‘two-stream’ (e.g. *Farley*, 1963) and ‘gradient-drift’ (e.g. *Rogister and D’Angelo*, 1970). Both types may be observed at all latitudes but the ‘two-stream’ instability is most prominent within the auroral zone, where the higher plasma ( $\sim$  electron) drift velocities required for generation ( $\geq 300 \text{ m s}^{-1}$ ), are present. Gradient drift irregularities may be excited at much lower plasma drift velocities. They are thus the most prominent type observed at mid-latitudes. E-region irregularities are most commonly observed at heights between  $\sim 100 \text{ km}$  and  $\sim 130 \text{ km}$  (e.g. *Fejer and Kelley*, 1980), the altitude range where sporadic-E generation is most prolific (e.g. *Smith and Metchley*, 1972).

Coincident observations of sporadic-E layers and field-aligned, E-region irregularities, have been observed or deduced at both mid-latitudes (e.g. *Riggin et al.*, 1986; *Tanaka and Venkateswaran*, 1982a) and high-latitudes (e.g. *Dudeney and Roger*, 1985; *Haldoupis et al.*, 1992). At mid-latitudes, the lower plasma drift velocities determine that the associated irregularities are most likely generated by the gradient-drift mechanism, promoted by the high density gradients found within sporadic-E layers. The irregularities are thus considered to be embedded *within* the upper and lower boundaries of the sporadic-E layer (*Ecklund et al.*, 1981).

Sporadic-E at high-latitudes is most often associated with substorms and magnetically disturbed conditions (e.g. *Turunen*, 1977; *Weber et al.*, 1977). Auroral-Es (cf. §3.3.2) takes the form of a thick, diffuse, range-spread trace on ionograms, and is associated with scattering from field-aligned irregularities, both gradient-drift *and* two-stream types. Flat-type Es (cf. §3.3.2) is also observed at high latitudes, though its plasma structure is determined solely by the converging action of a *uniform* electric field (e.g. *Bristow and Watkins*, 1994;

Nygrén *et al.*, 1984) (cf. §2.3.5). Such layers are observed as thin, flat, discrete traces on ionograms, similar to Windshear generated layers at mid-latitudes.

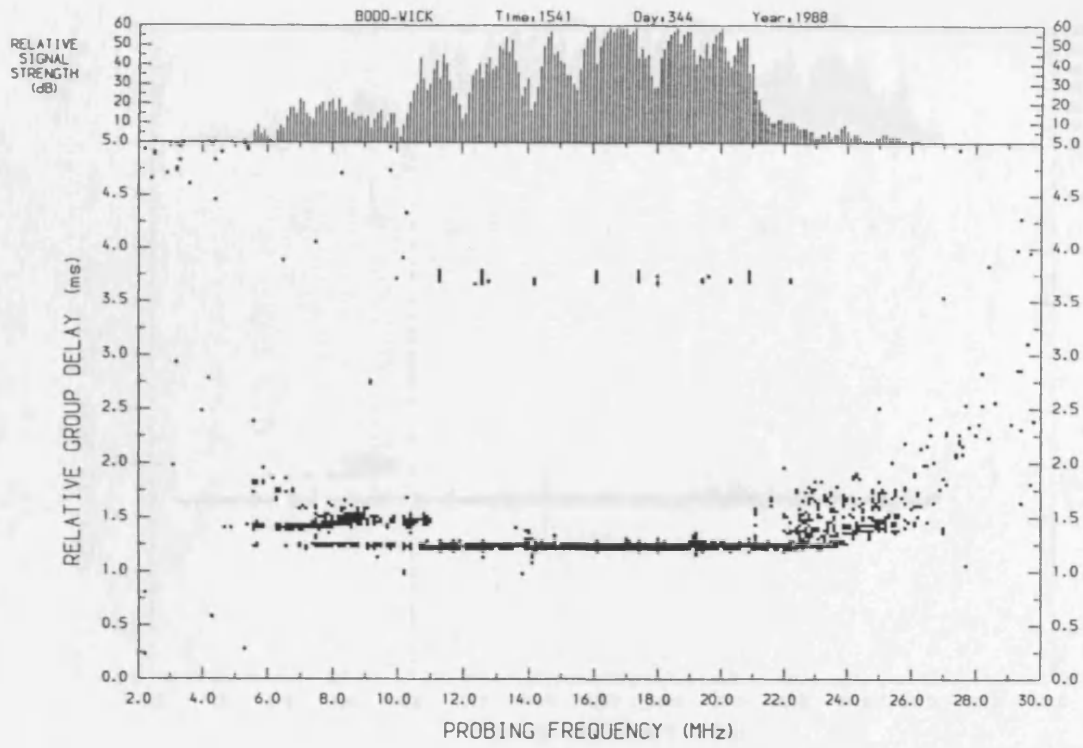
In previous Chapters, sporadic-E has largely been studied under fairly quiet magnetic conditions ( $K_p \lesssim 2.0$  on average). The following study is specifically concerned with sporadic-E observations at times of disturbed magnetic conditions and in particular, during times of substorm activity. Such studies are important for sub-auroral propagation paths, such as the Bodø/Wick path, whose propagation characteristics may change adversely in a short period of time. Conversely, the generation of evening and night-time sporadic-E layers, as a direct or indirect consequence of enhanced electric fields and plasma flows, may *enable* an E-region propagation circuit. These circuits would otherwise be unavailable, at times when the E-region densities reduce by up to two orders of magnitude with respect to midday peak densities (cf. Figure 1.8).

In this Chapter, coincident observations of sporadic-E layers, and E-region irregularities are analysed, as recorded by an HF oblique sounder, and by SABRE, a monostatic VHF coherent backscatter radar (cf. §3.4.1). Several time intervals are considered, within the context of five case studies (a-e), with the degree of occurrence correlation being noted in each case. Further, and unique to this study, the relationship between the backscatter intensity and the sporadic-E top frequency is also examined.

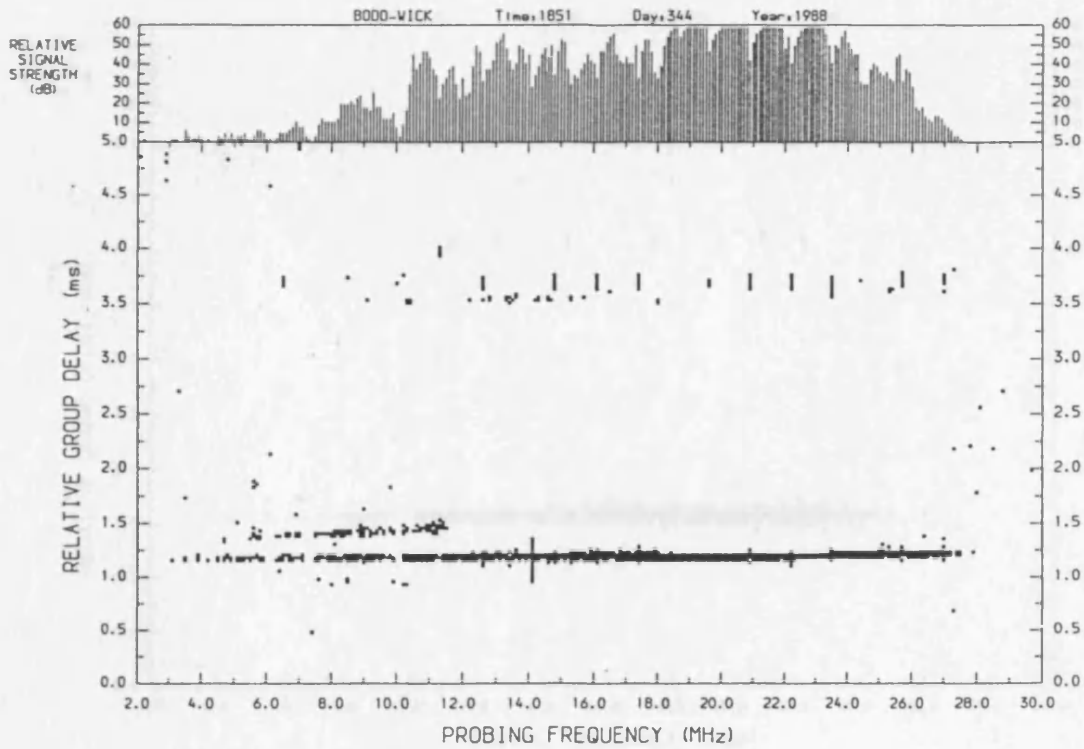
## 7.2 Ionogram Observations of Sporadic-E Layers

It is instructive to observe some typical sporadic-E layers as recorded by the oblique HF sounder during the December campaign, and at times of SABRE backscatter. Four examples are depicted in Figures 7.1(a-d). In each Figure, the main panel depicts the ionogram, the ordinate representing relative group delay (ms) with the abscissa depicting oblique Probing Frequency, from 2.0 MHz to 30.0 MHz. The upper panel displays relative signal strength, pertinent to each Probing Frequency. Each sporadic-E trace has a clearly defined top frequency, greater than or equal to 24.0 MHz. However the  $f^oE_s$  value is not always so clear and may lead to scaling ambiguities.

Figure 7.1a presents a thin, flat-type  $E_s$  trace with what appears like irregularity scatter at the higher Probing Frequencies. Characteristics of both the flat- and auroral-type  $E_s$ -layers are thus displayed. Figure 7.1b presents a typical mid-latitude flat-type  $E_s$  trace, with no

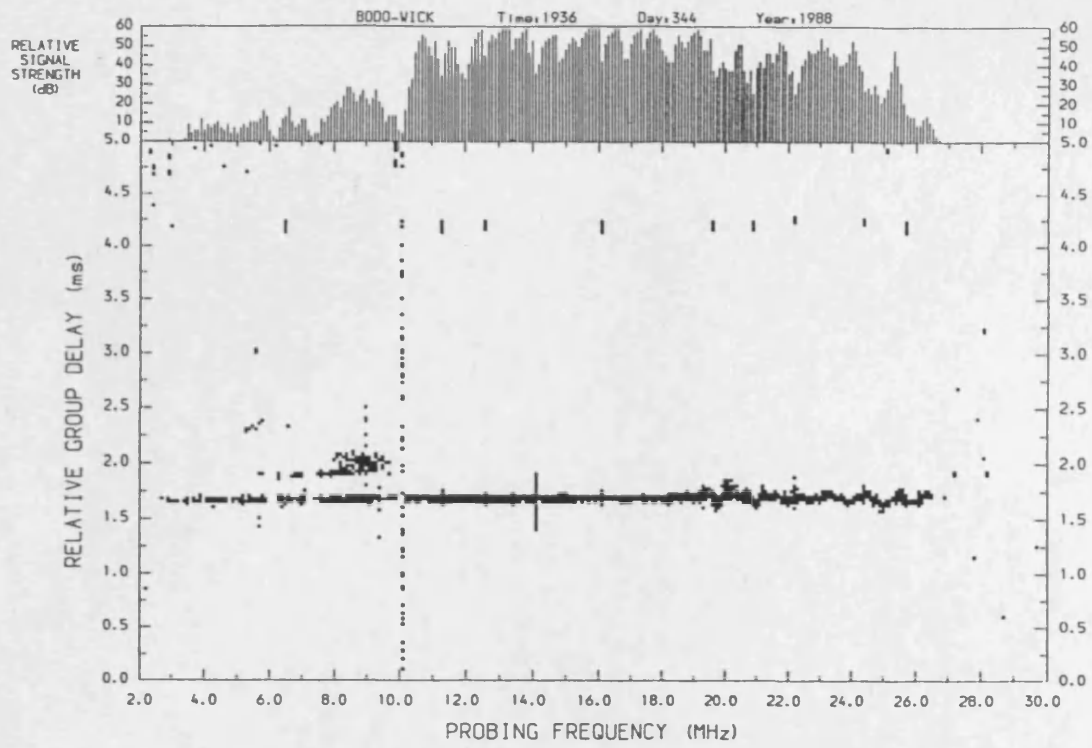


(a)

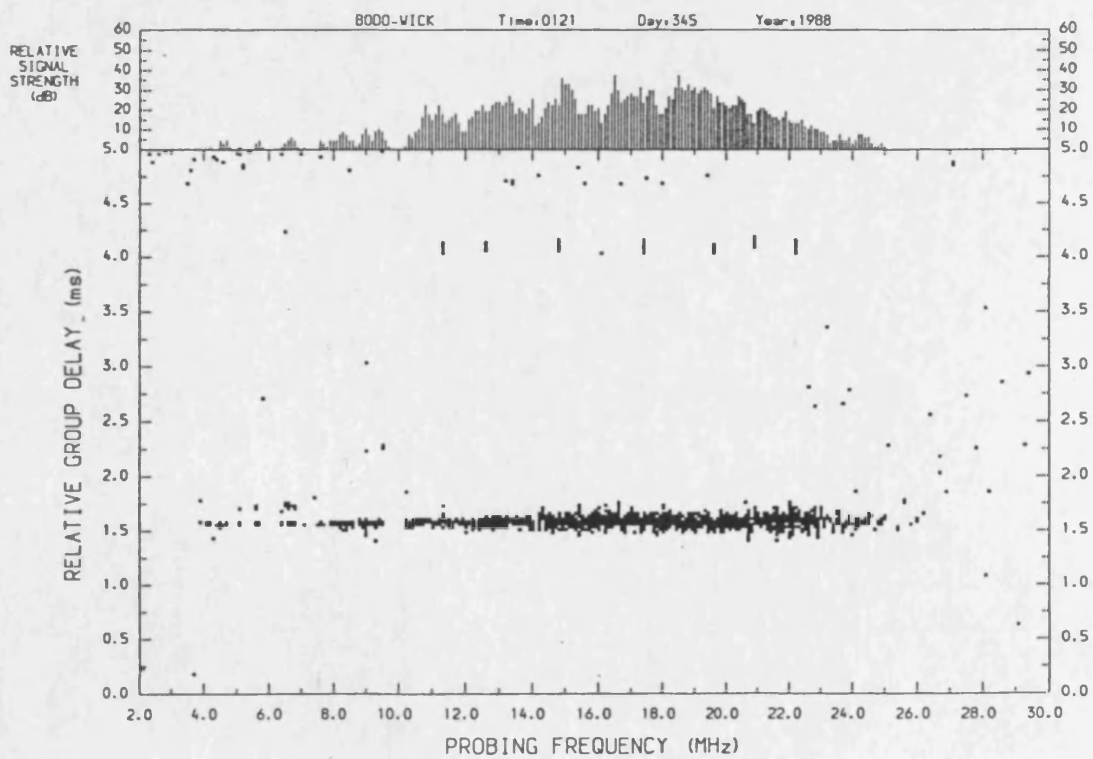


(b)

FIGURE 7.1(a,d) Examples of sporadic-E as recorded on Bodø/Wick oblique ionograms, during magnetically active periods of the December Campaign, specifically during case studies (a) and (b). Figure 7.1a depicts essentially 'flat' type Es but with diffuse scatter (of low signal strength) observed at the higher Probing Frequencies. Figure 7.1b depicts exclusively 'flat' type Es.



(c)



(d)

FIGURE 7.1(a,d) (cont) Figure 7.1c depicts an oscillation in the sporadic-E group delay, at the higher Probing Frequencies and Figure 7.1d presents a diffuse sporadic-E trace, termed 'auroral' type Es.

auroral-type Es characteristics. Figure 7.1c depicts an interesting feature noted throughout these case studies, i.e. an oscillation in the group delay. This feature is only observed at the higher Probing Frequencies and is sometimes correlated or anti-correlated with the signal strength. The amplitude of the oscillations are also often much greater and less clearly defined. It is considered to arise from some kind of propagation path or mode interference, or maybe an ionosonde interpretation of doppler shifts (cf. §3.3.2). It may also be a signature of gradient drift irregularities (cf. *Kelley et al.*, 1995). Further analysis is left to later studies.

The final ionogram is depicted in Figure 7.1d and may be termed diffuse. It has characteristics similar to the auroral-type Es, noted on vertical ionograms, and is the most prevalent type observed during the following case studies. Again, this example is well defined and fairly typical of its type, but much more distorted examples are also observed. It may also be considered, and is often observed to be, an obscured, less well defined, oscillatory group path type, as depicted in Figure 7.1c.

Various types of sporadic-E traces are thus recorded during the following case studies, reflecting the range of structures and characteristics noted previously for high latitude sporadic-E layers. Figures 7.1(c,d) represent the most commonly observed traces, together with distortions of each. It is thus inferred that a relationship between high-latitude sporadic-E layers and irregularities may exist for some of the proceeding observations. Flat-type sporadic-E layers are however also observed throughout all the case studies, but are more prevalent during the relatively quiet magnetic periods e.g. between 21:00 UT, day 344 and 00:30 UT, day 345 and also between 02:30 UT and 04:00 UT, day 345 (case studies (a) and (b), §7.4).

### **7.3 Analysis Procedure**

The ionogram data analysed in this Chapter pertains to recordings made over the oblique Bodø/Wick propagation path, during the December 1987 and March 1988 campaigns (cf. Table 4.1). The HF oblique sounder instrumentation was identical to that employed during the August, 1988 campaign, but for logistical reasons, the data volumes recorded were much more sparse. Several periods of disturbed magnetic activity, particularly during December, are noted, with ionogram recordings specifically concentrated at these times.

In conjunction with the HF oblique sounder, data was recorded by SABRE, the Sweden and Britain Radar-aurora Experiment. During the December and March campaigns, SABRE operated as a single, monostatic radar, with the transmitter and receiver being co-located at Wick. The SABRE radar frequency ( $\sim 150$  MHz) is sensitive to unstable electrostatic plasma waves  $\sim 1$  m in wavelength (cf. §3.4.1), which give rise to field-aligned plasma irregularities. Such small scale wavelengths bias observations towards irregularities generated by ‘primary’ two-stream instabilities, though ‘secondary’ gradient-drift irregularities (*Sudan, 1973*) may also be observed (*Mattin and Jones, 1987*), depending on the radar *flow angle*, the acute angle between the radar propagation vector and the plasma drift direction. The theory of irregularity *detection* is discussed more fully later.

This Chapter studies coincident observations of sporadic-E layers and E-region irregularity backscatter, during periods of magnetic activity and particularly substorm events (cf. §1.2.5). The observations are thus naturally biased towards the evening and night-time auroral zone sectors, where enhanced electrojets flow during substorm activity (*Akasofu, 1964*). Further, *Waldock et al. (1985)* observed that the probability of irregularity backscatter being detected by the SABRE radar, increased significantly between  $\sim 16:00$  UT and  $\sim 04:00$  UT, the probability of detection being greater than 20%. This is a consequence of the enhanced plasma flows mentioned above, but also due to the favourable flow angles.

The following analysis concentrates on a few case studies, which satisfy the above criteria, and is not intended to provide general occurrence statistics on either sporadic-E or backscatter data. For each specific case, the degree of correlation between the *occurrence* of sporadic-E and irregularity backscatter is determined over varying time intervals, as deemed meaningful and appropriate. Further, the correlation of the backscatter Signal-to-Noise (S/N) ratio (decibels) and the sporadic-E top frequency, measured at equivalent vertical incidence, (*vfEs*), is also analysed. Factors that influence these two measurements are then discussed.

Backscatter S/N ratio data is recorded at 50 range gates, along each of the 8 beams of the SABRE radar, as described in §3.4.1. Beam 7 (cf. Figure 3.9) is the beam most closely co-located with the Bodø/Wick propagation path, and hence the data presented herein is restricted to this single beam. Range gate 12 is located at a slant range of 660 km from the Wick transmitter and hence approximates to the nominal Bodø/Wick path midpoint. Range gate 30 is located at a slant range of 930 km from Wick, where the *magnetic aspect angle*, the angle between the radar propagation vector and the geomagnetic field, approximates to  $90^\circ$ . As the plasma instabilities propagate orthogonal to the magnetic field line, backscatter

intensity statistically maximises at this range. Backscatter data pertaining to both ranges, is preferentially considered below.

*Feldstein and Starkov* (1967) determined an empirical model of the visual auroral oval, relating its poleward and equatorward boundaries to the planetary K-index ( $K_p$ ). *Holzworth and Meng* (1975) developed a mathematical model of these results and by utilising this latter model, the statistical position of the oval may be determined for given Universal Time (UT) and  $K_p$  parameters. These parameters are used in the case studies below, to depict the oval position with respect to the SABRE field of view and the nominal Bodø/Wick propagation path.

## **7.4 Correlation Studies of SABRE Backscatter and Sporadic-E Top Frequency Data**

### **7.4.1 Introduction**

Five case studies are presented below, four pertaining to the December campaign and one to the March campaign. Each describes the characteristics of sporadic-E and E-region backscatter data, recorded during periods of magnetic activity and primarily, substorm events. In each case, data from the ground magnetometer, SAMNET network (cf. §3.4.2) assists in determining the nature, and localised timings, of the magnetic disturbances. The Feldstein (visual) auroral oval is also utilised to provide a statistical prediction of the location and extent of (backscatter) radar auroras, noting that the latter is approximately co-located within the statistical boundaries of the Feldstein oval (e.g. *Chestnut*, 1972).

### **7.4.2 Case Study (a): 12:00 – 24:00 UT, Day 344**

Figures 7.2(a,b) compare SABRE backscatter S/N ratio data with sporadic-E  $\nu f E_s$  values, recorded on day 344, 1987, between 12:00 UT and 24:00 UT. Both Figures are identical in format and indeed the sporadic-E data is identical in both. The S/N ratio data however, is depicted for range gates 12 and 30, for Figures 7.2(a,b) respectively. Four, three hour panels are presented in each of Figures 7.2(a,b). Each has two ordinates, measuring Wick (SABRE) S/N ratio and  $\nu f E_s$  magnitudes. The abscissa depicts Universal Time. On the upper border of each panel is 'data/no data' information, indicating the on/off times of both the oblique sounder and SABRE radars; white space indicates that the respective radar was off. It is noted

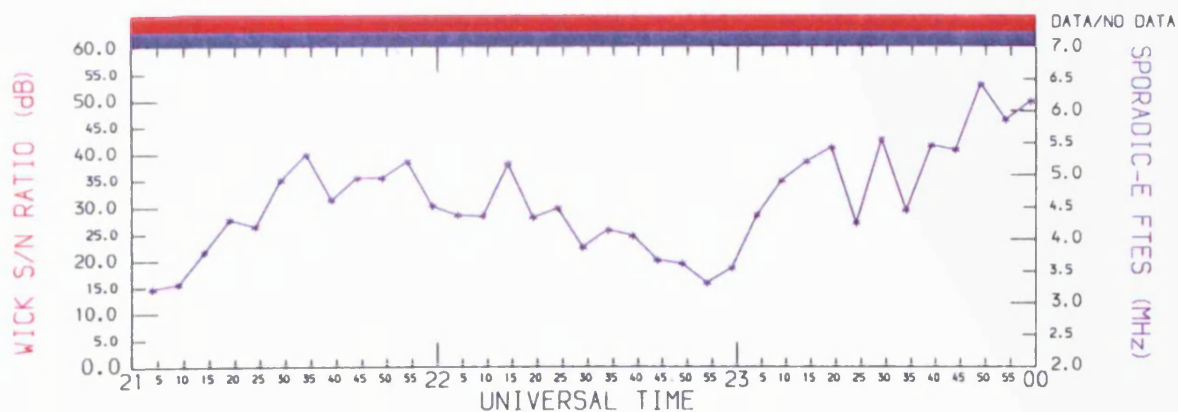
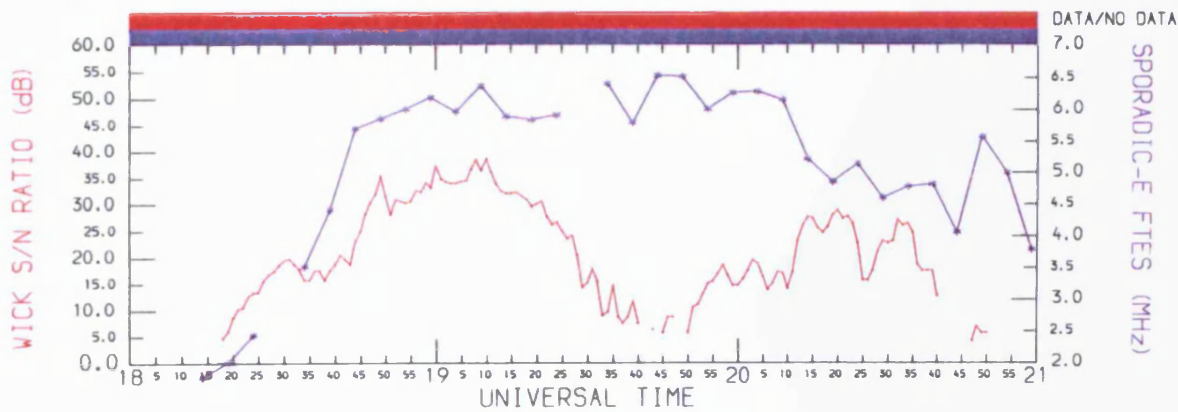
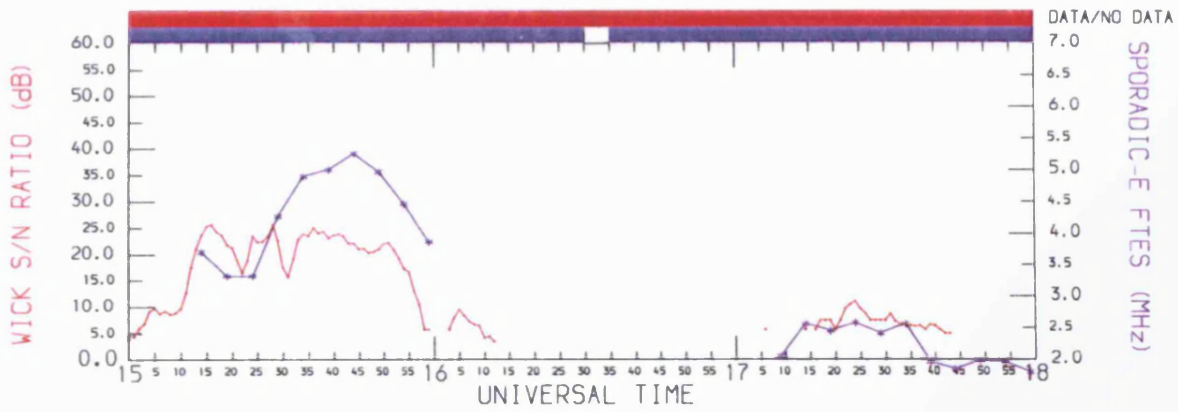
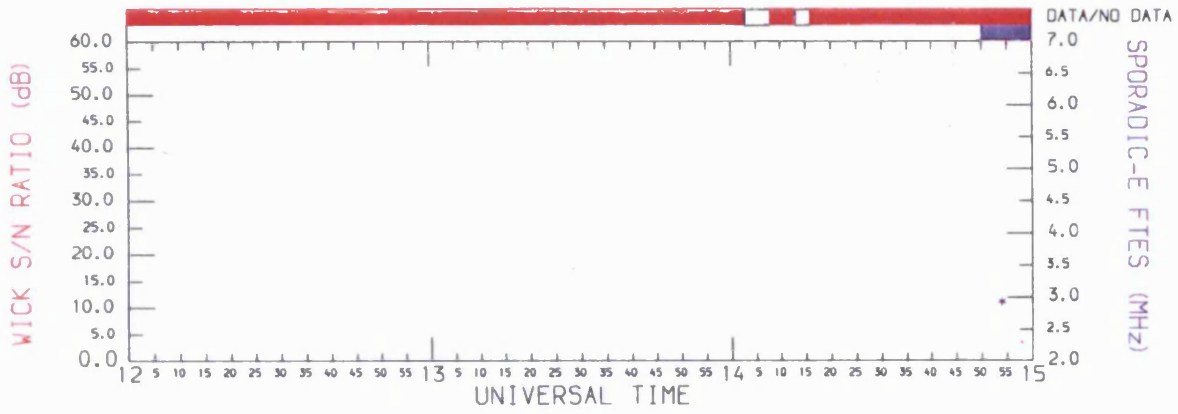


FIGURE 7.2a Case Study (a): A comparison of the SABRE coherent backscatter Signal-to-Noise (S/N) ratio, with the sporadic-E equivalent vertical top frequency (*v<sub>f</sub>E<sub>s</sub>*), observed over the Bodø/Wick propagation path. The SABRE irregularity backscatter was recorded from beam 7, at range gate 12 (660 km). The data pertains to a 12-hour period from day 344, 1987.

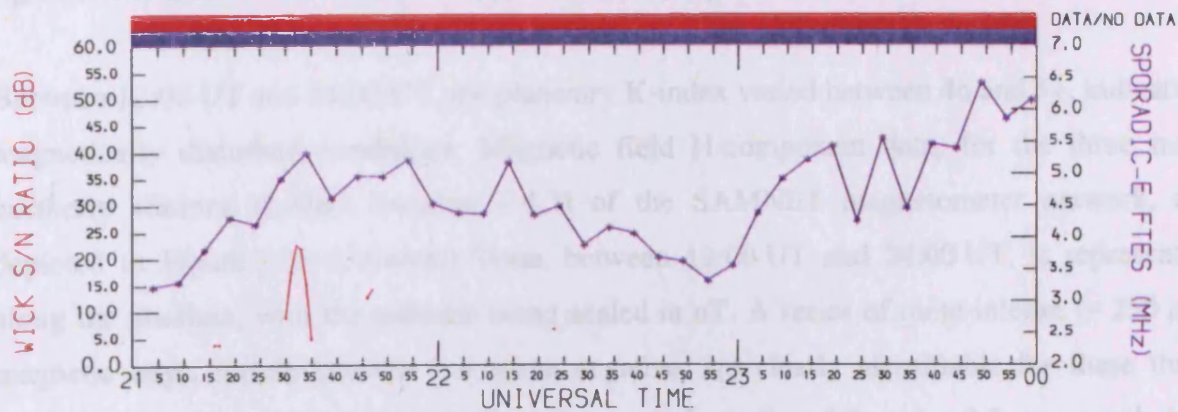
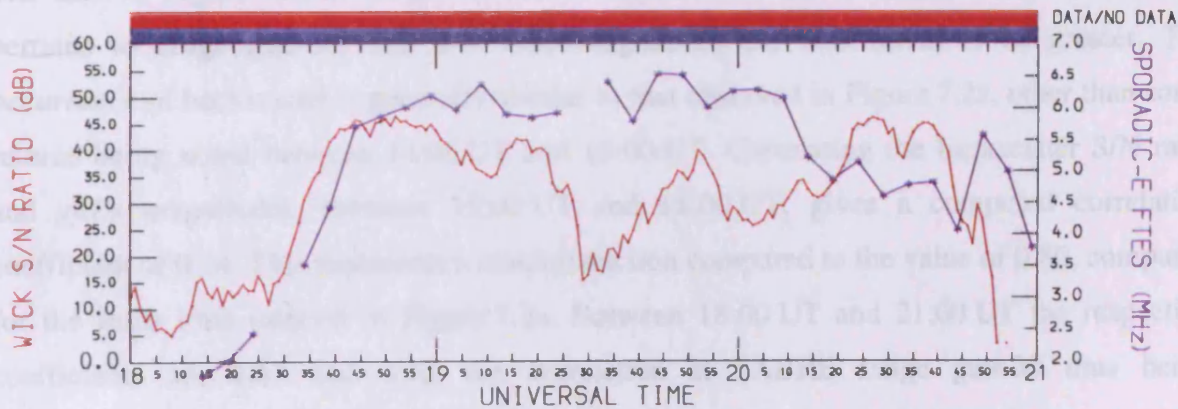
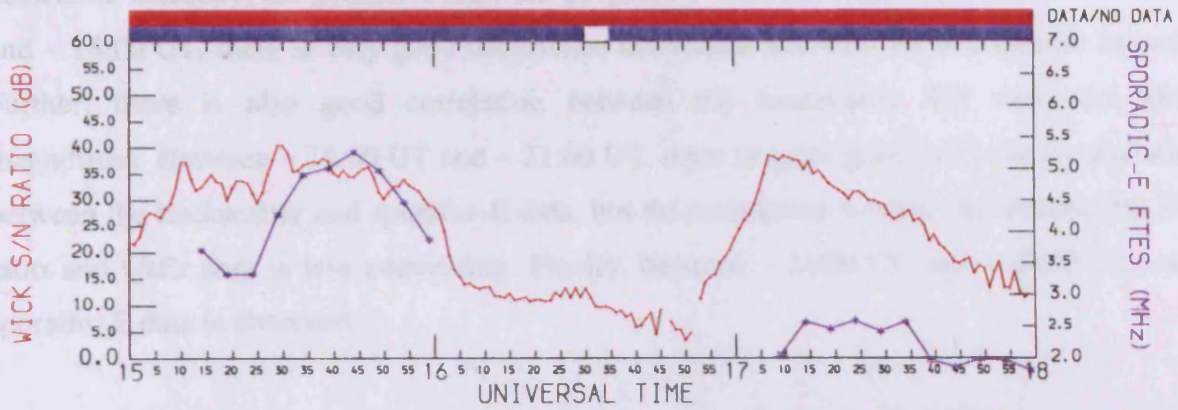
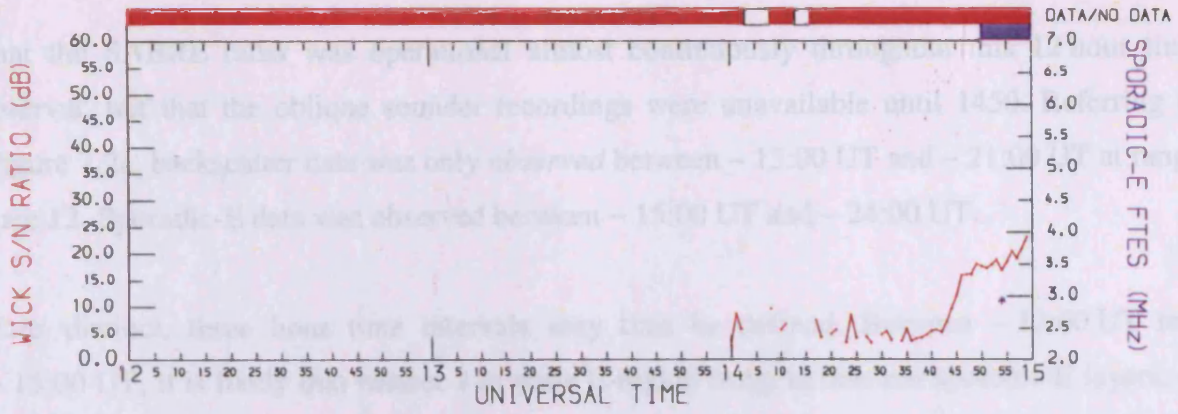


FIGURE 7.2b Case Study (a): As for Figure 7.2a, but with the SABRE backscatter being recorded at range gate 30 (930 km).

that the SABRE radar was operational almost continuously throughout this 12 hour time interval, but that the oblique sounder recordings were unavailable until 1450. Referring to Figure 7.2a, backscatter data was only *observed* between ~ 15:00 UT and ~ 21:00 UT at range gate 12. Sporadic-E data was observed between ~ 15:00 UT and ~ 24:00 UT.

Four distinct, three hour time intervals may thus be defined. Between ~ 12:00 UT and ~ 15:00 UT, it is likely that neither 1 m scale E-region irregularities nor sporadic-E layers, of detectable intensity, are present within the geographic viewing region. Between ~ 15:00 UT and ~ 18:00 UT, there is very good occurrence correlation between the two plasma features. Further, there is also good correlation between the backscatter S/N ratio and *vftEs* magnitudes. Between ~ 18:00 UT and ~ 21:00 UT, there is again good occurrence correlation between the backscatter and sporadic-E data, but the correlation between the backscatter S/N ratio and *vftEs* data is less convincing. Finally, between ~ 21:00 UT and ~ 24:00 UT, only sporadic-E data is observed.

The data in Figure 7.2b is similar to that in Figure 7.2a, but the SABRE backscatter data pertains to range gate 30. The S/N ratio magnitudes are thus noted to be greater. The *occurrence* of backscatter is generally similar to that observed in Figure 7.2a, other than some returns being noted between 14:00 UT and 15:00 UT. Correlating the backscatter S/N ratio and *vftEs* magnitudes, between 15:00 UT and 18:00 UT, gives a computed correlation coefficient of 0.74. This represents a small reduction compared to the value of 0.80, computed for the same time interval in Figure 7.2a. Between 18:00 UT and 21:00 UT the respective coefficients are 0.63 and 0.42, the correlation at SABRE range gate 30 thus being significantly greater. All coefficients are statistically significant at the 1% level.

Between 12:00 UT and 24:00 UT, the planetary K-index varied between 4<sub>o</sub> and 5<sub>+</sub>, indicating magnetically disturbed conditions. Magnetic field H-component data, for the three most northerly stations (L-shell location ~ 4.3) of the SAMNET magnetometer network, are depicted in Figure 7.3a. Universal Time, between 12:00 UT and 24:00 UT, is represented along the abscissa, with the ordinate being scaled in nT. A series of quite intense (~ 250 nT) magnetic bays, mostly positive but some negative, are clearly identifiable for these three stations. The lower magnetic latitude stations, on L-shells ~ 3.2 and ~ 2.5, are much less disturbed ( $\leq 100$  nT) but distinct Pi2 pulsations, the signature of substorm onset, are noted at approximate times of 17:50 UT, 19:05 UT and 20:50 UT.

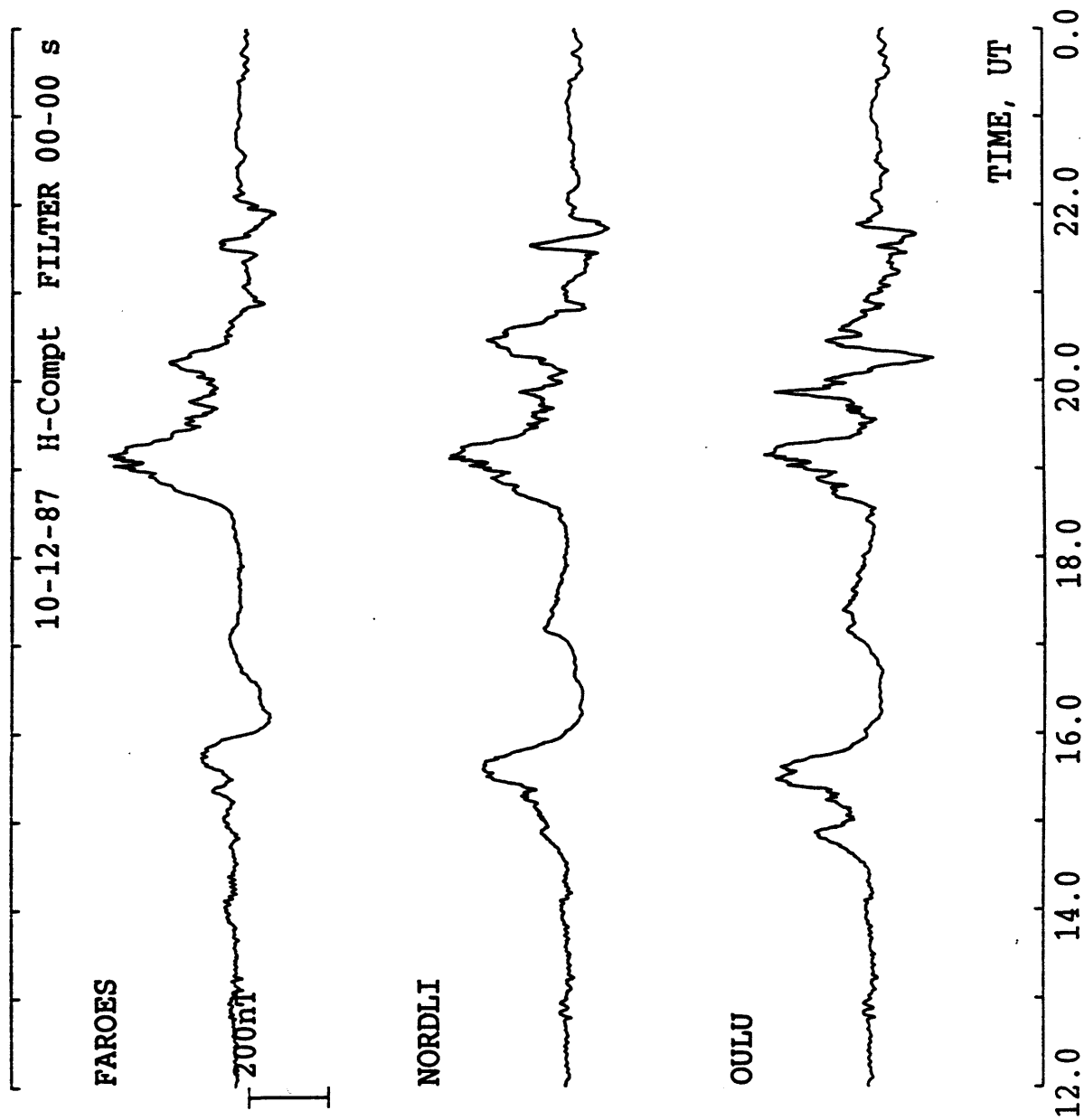


FIGURE 7.3a Case Study (a): SAMNET H-component magnetometer data from the three most northerly stations ( $L$ -shell  $\sim 4.3$ ), recorded over the same time interval as represented within Figures 7.2(a,b). Multiple onset substorm activity is noted between approximately 18:00 UT and 22:00 UT.

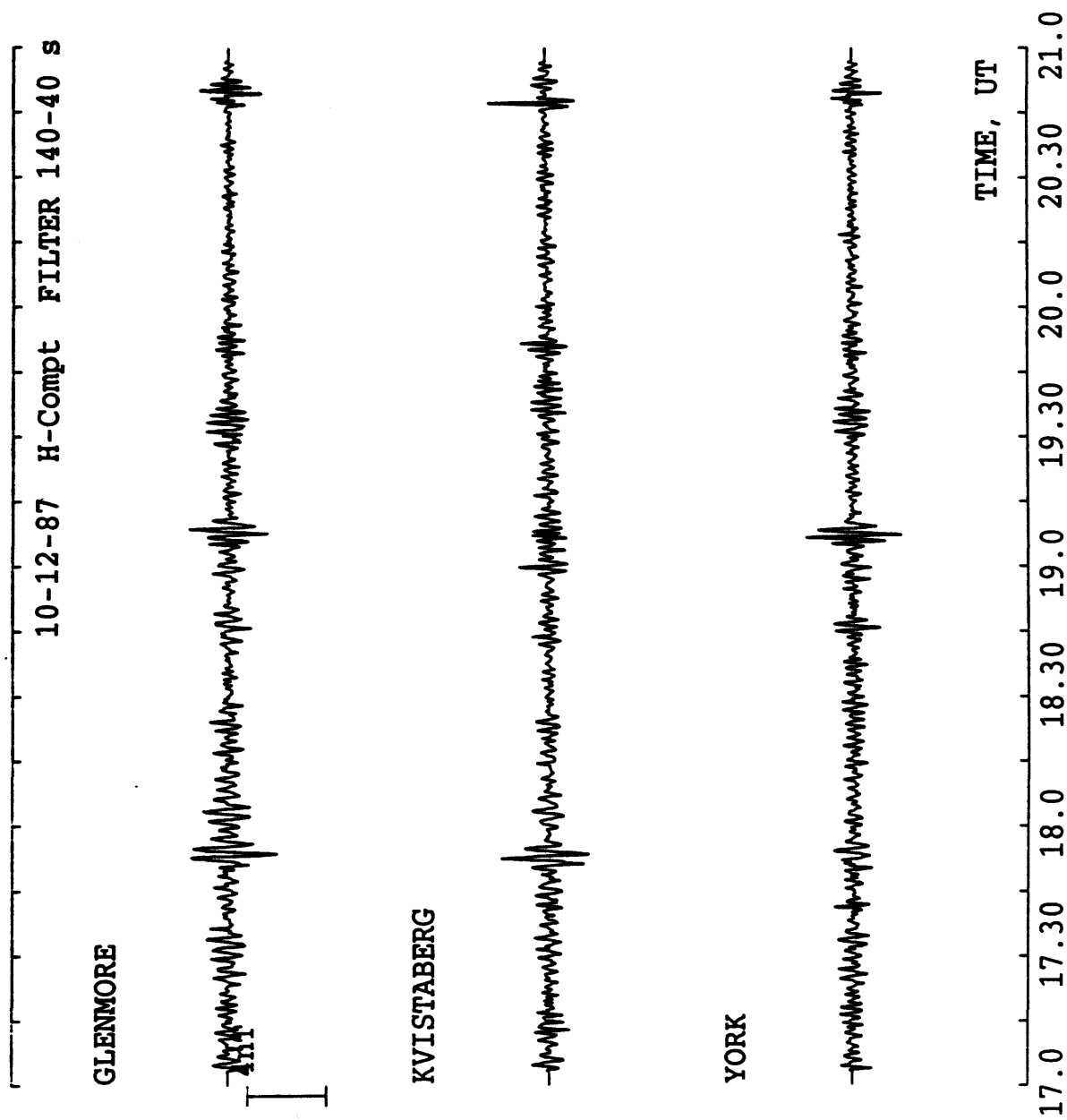


FIGURE 7.3b Case Study (a): Spectrally filtered SAMNET magnetometer data from three lower magnetic latitude stations (with respect to Figure 7.3a), i.e. at L-shells  $\sim 3.2$  and  $\sim 2.5$ . The data was recorded between 17:00 UT and 21:00 UT, day 344, 1987, and filtered for periods between 140 s and 40 s. Pi2 pulsations may thus be observed and are noted at approximate times of 17:50 UT, 19:05 UT and 20:50 UT.

These latter observations are depicted in Figure 7.3b, which presents selectively filtered, H-component data, for spectral periods between 140 seconds and 40 seconds, this being a nominal range for observing Pi2 pulsations. For the 12 hour temporal range under consideration, Pi2 signatures were not observed outside of the hours presented in Figure 7.3b, between 17:00 UT and 21:00 UT. It is thus deduced that the magnetic disturbance noted between ~ 14:00 UT and ~ 16:30 UT, is not substorm activity, while that between ~ 17:45 UT and ~ 22:00 UT depicts a series of substorm intensifications (*Pytte et al.* 1976). The positive H-component bay structure, depicted in Figure 7.3a, suggests an association with the eastward electrojet (*Rostoker et al.*, 1980).

Figure 7.4 depicts the Feldstein auroral oval at 20:00 UT, for  $K_p$  equal to 4o, these parameters being pertinent to the magnetic substorm data depicted in Figures 7.3(a,b). It is noted that the nominal Bodø/Wick propagation path midpoint is indicated in Figure 7.4 and indeed is located within the predicted auroral oval, as is the SABRE field of view (cf. Figure 3.9). With reference to the geographic location of the SAMNET magnetometer stations (cf. Figure 3.11), it is noted that the three, higher magnetic latitude stations are also located within the oval. The fact that significantly greater magnetic activity was noted at these stations, confirms the predicted positioning of the auroral oval in Figure 7.4.

#### *Observation Summary*

For a period of six hours, coincident observations of 1 m scale irregularities and sporadic-E data, are noted. Throughout the time interval, magnetic activity was disturbed. During the first three hours (15:00 UT to 18:00 UT), good correlation is observed between the backscatter S/N ratio and  $\nu f_i E_s$  magnitudes, the maximum correlation coefficient (0.82) being noted at range gate 13, just beyond the nominal Bodø/Wick propagation path midpoint. Substorm activity is not considered to be present.

During the latter three hours (18:00 UT to 21:00 UT), results not presented herein demonstrate that the correlation between backscatter S/N ratio and  $\nu f_i E_s$  magnitudes, initially increases approximately with SABRE range gate, i.e. with increasing SABRE beam magnetic aspect angle. The correlation maximises at range gate 25, with a coefficient value of 0.64. During *this* time interval, substorm activity was noted.

Good correlations are thus observed between the irregularity backscatter S/N ratio and  $\nu f_i E_s$  magnitudes, at different range gates and at different observation times. A common factor is magnetic disturbance, some pertaining to substorm activity.



### 7.4.3 Case Study (b): 00:00 – 06:00 UT, Day 345

This time interval follows on from case study (a) and is of interest because the sporadic-E observations are continuous from that time interval and because further substorm-type magnetic activity is noted. Figure 7.5 presents the backscatter S/N ratio and  $\nu f_i E_s$  magnitude data in the format of Figures 7.2(a,b). Twelve hours of observations are depicted but the two upper panels, for 00:00 UT to 06:00 UT, are of most interest.

Figure 7.6a presents magnetic field H-component data for the Faroes, Nordli and Oulu SAMNET stations (as in Figure 7.3a), between 00:00 UT and 06:00 UT. The negative H-component bay is typical of a westward electrojet associated substorm. In Figure 7.6b however, there is little indication of Pi2 pulsations at this time, though a Pi2 signature may be present at ~01:00. This would approximately coincide with the onset of irregularity backscatter, and a small but sudden rise in  $\nu f_i E_s$  values. Note that at low latitudes, the amplitude of Pi2 pulsations may be fractions of nT and hence may fall below the detection threshold level of the magnetometer (*Rostoker et al.*, 1980). Planetary K-indices of 4+ and 3o are respectively noted for the 00:00 UT and 06:00 UT time interval, followed by a value of 1+ between 06:00 UT and 09:00 UT.

No correlation exists between the S/N ratio and  $\nu f_i E_s$  magnitudes, at any SABRE range gate. Figure 7.5 depicts data for range gate 30, solely because the magnetic aspect angle, and hence backscatter intensity (cf. §2.4.2.2), maximises at this range gate, the former approximating to orthogonality conditions. Neither can it be stated that the occurrence of irregularity backscatter and sporadic-E is correlated, with sporadic-E observations extending prior to and beyond the backscatter recordings. There is thus the suggestion that while irregularity backscatter is closely correlated to the lifetimes of substorm and magnetic bay activity (cf. case study (a) also), on some occasions, the correlation of sporadic-E layers with these specific magnetic disturbances is weaker. The long lifetimes of the metallic ion constituents of sporadic-E layers (cf. §2.3.7) may be contributing to the extended duration of these layers, both between and beyond durations of magnetic activity. This said, it is interesting to note that the  $\nu f_i E_s$  values, depicted in Figure 7.5, decrease steadily between ~01:25 UT and ~04:00 UT, as the depressed H-component value is restored back to quiet time magnetic field magnitudes (cf. Figure 7.6a).

In conclusion, it is instructive to note the position of the Feldstein oval during this latter period of time. Figure 7.7 depicts the auroral oval for a  $K_p$  value of 4o and at a time of 02:00 UT. Note that neither the Bodø/Wick great circle path, nor beam 7 of the SABRE radar,

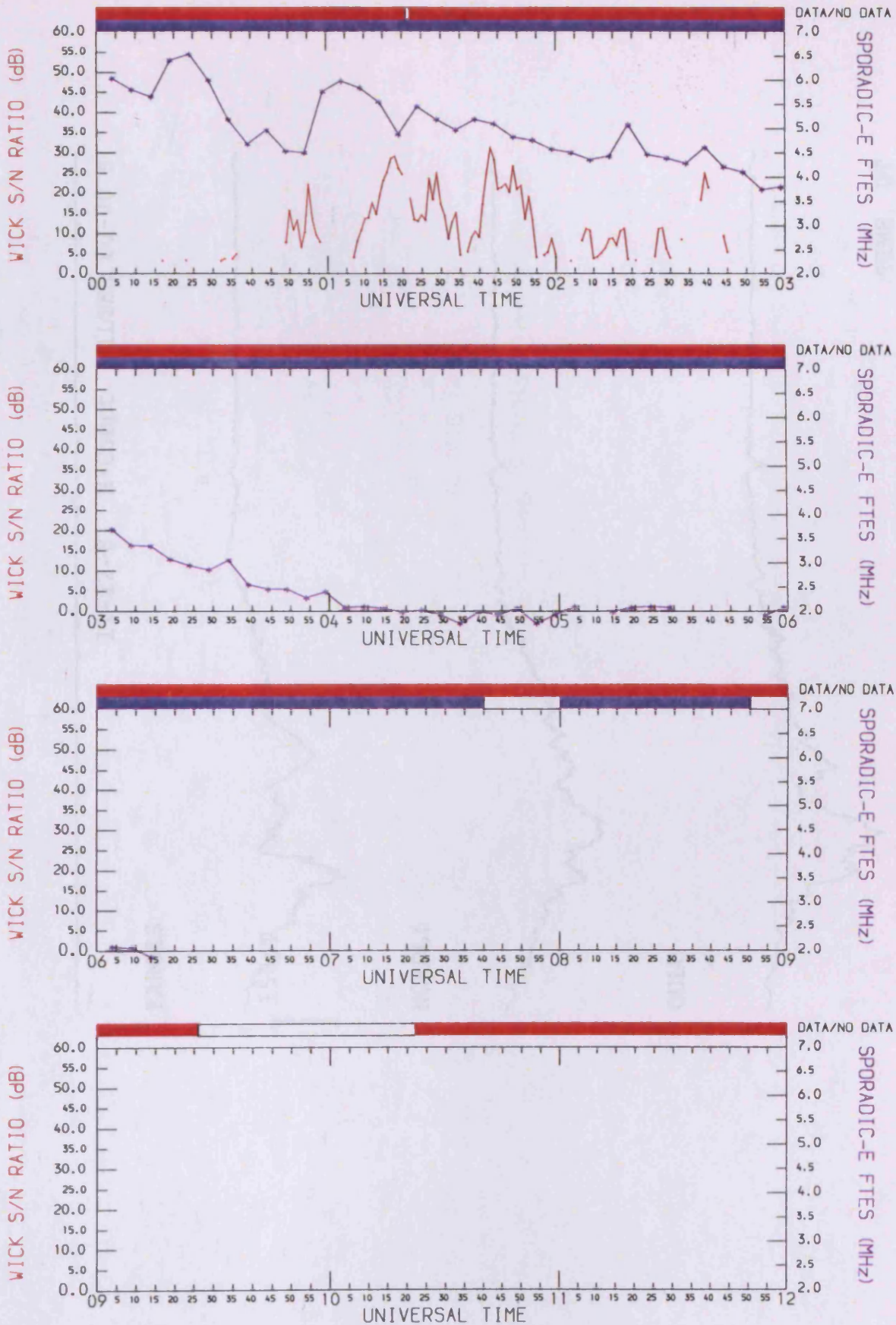
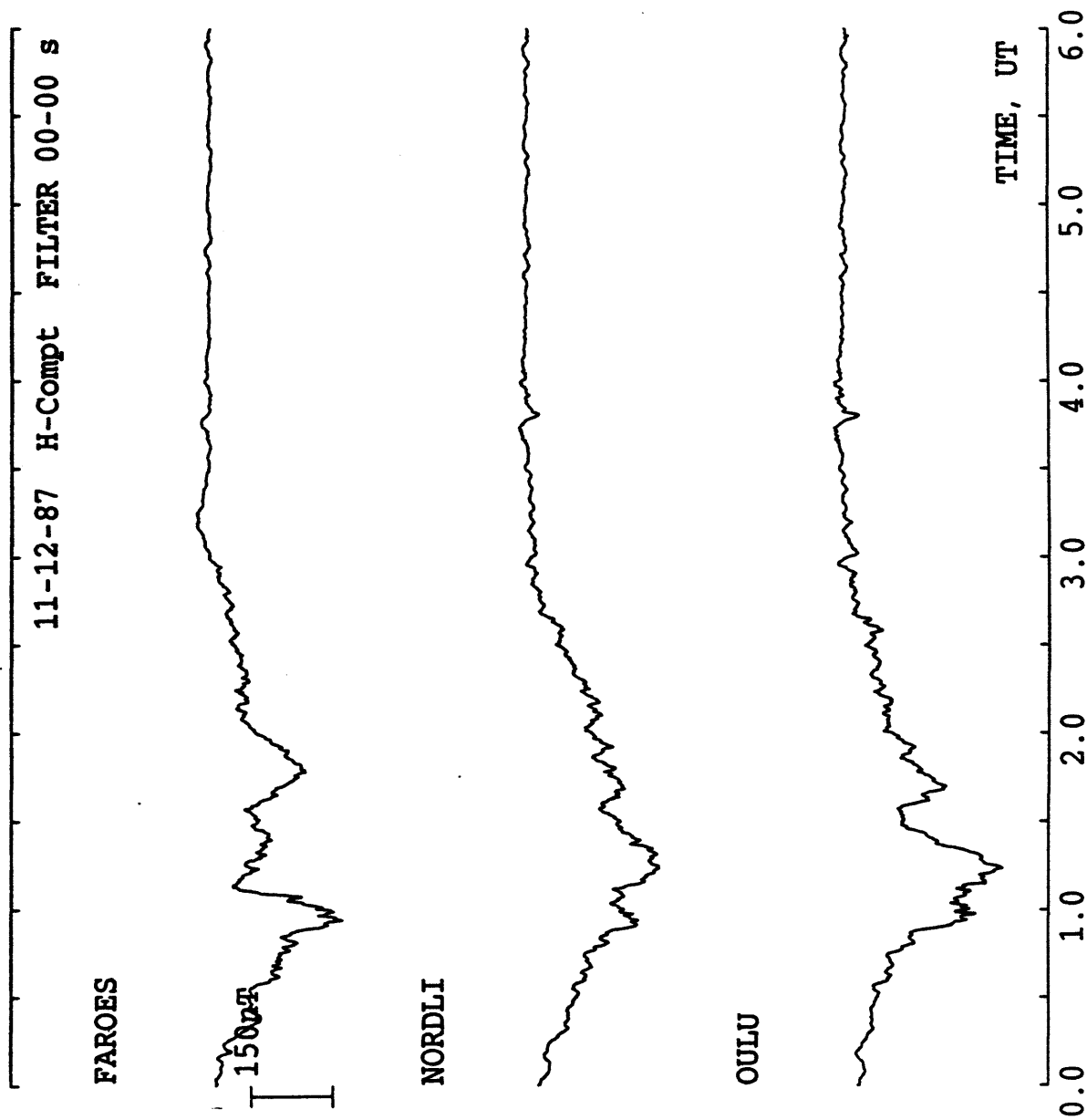


FIGURE 7.5 Case Study (b): SABRE backscatter S/N ratio, and sporadic-E *vftEs* data, as recorded for Figure 7.2b (range gate 30) but for the December Campaign period between 00:00 UT and 12:00 UT, day 345, 1987.



**FIGURE 7.6a** Case Study (b): SAMNET data as for Figure 7.3a, but recorded between 00:00 UT and 06:00 UT, day 345, 1987. Substorm activity is noted between approximately 00:00 UT and 03:00 UT.

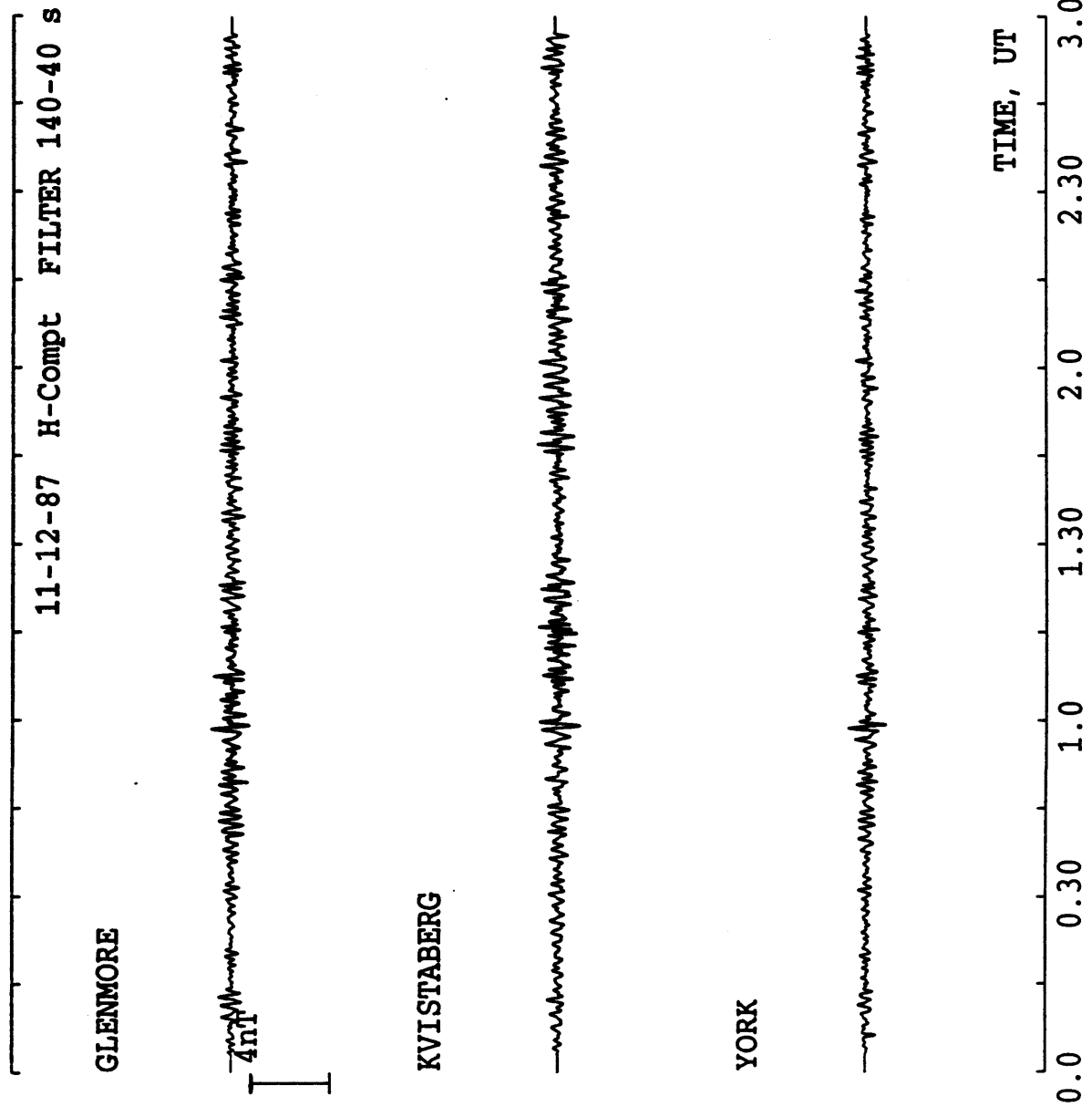


FIGURE 7.6b Case Study (b): SAMNET data as for Figure 7.3b, but recorded between 00:00 UT and 03:00 UT, day 345, 1987. Pi2 pulsations are difficult to identify, but an observation at ~ 01:00 UT appears probable.

are located within this predicted zone, the equatorward boundary of the oval having drifted northwards at this post-midnight stage.

UT = 2.0       $K_p = 4$

#### 7.4.4 Case Study (b): 22:00 UT, Day 338 – 02:00 UT, Day 339

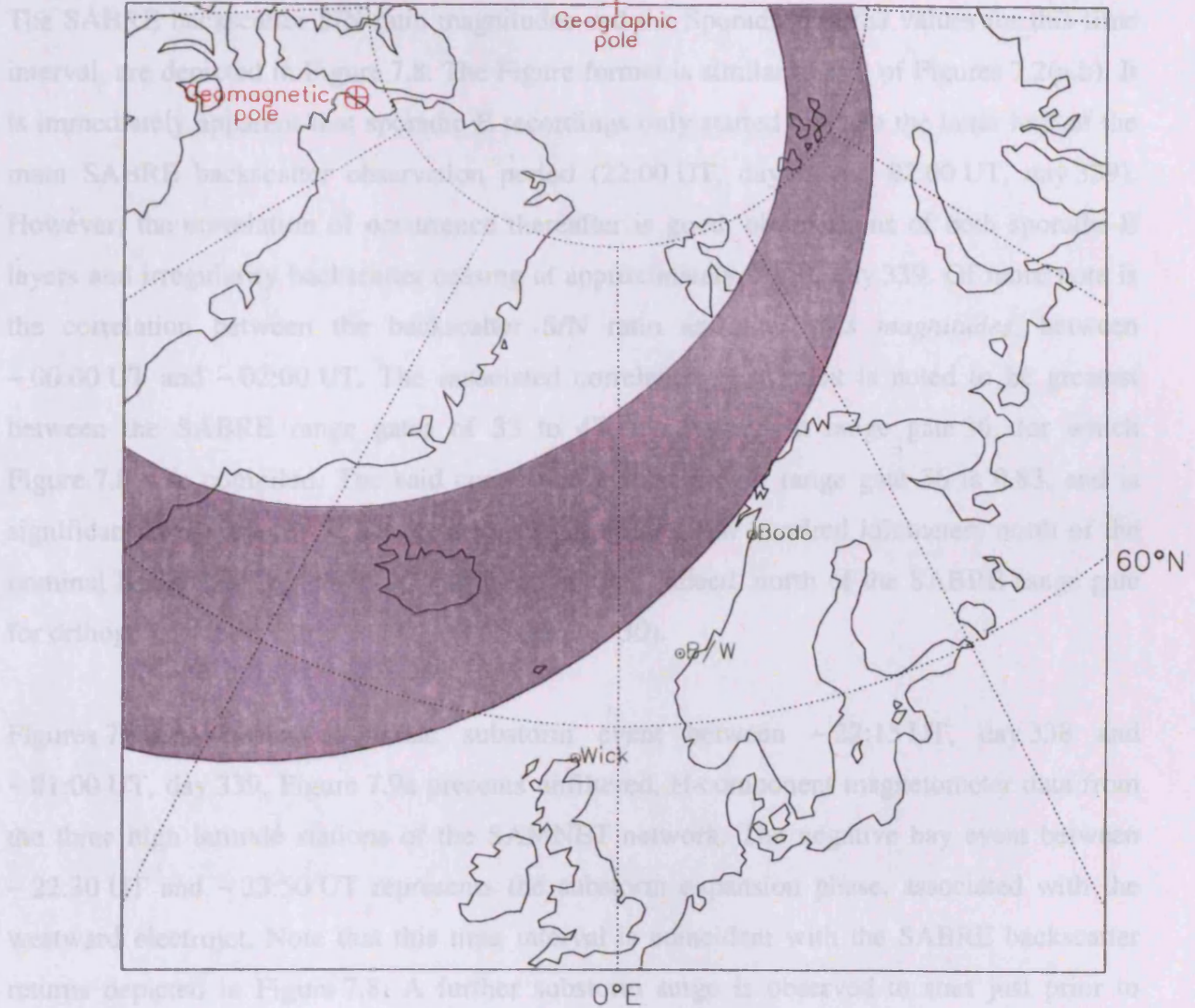


Figure 7.7a confirms the substorm activity, with  $Pf_2$  pulsations being noted at ~22:20 UT, ~22:30 UT and ~23:50 UT. Planetary  $K$  indices for the period from 21:00 UT, day 338 to 03:00 UT, day 339 are 4+ and 4o respectively. The model Feldstein oval for 24:00 UT and a  $K_p$  value of 4o, is presented in Figure 7.10. Again, as in Figure 7.4, the nominal Bodo/Wick propagation path midpoint and a significant proportion of the higher SABRE range gates (cf. Fig.

Figure 7.9b confirms the substorm activity, with  $Pf_2$  pulsations being noted at ~22:20 UT, ~22:30 UT and ~23:50 UT. Planetary  $K$  indices for the period from 21:00 UT, day 338 to 03:00 UT, day 339 are 4+ and 4o respectively. The model Feldstein oval for 24:00 UT and a  $K_p$  value of 4o, is presented in Figure 7.10. Again, as in Figure 7.4, the nominal Bodo/Wick propagation path midpoint and a significant proportion of the higher SABRE range gates

**FIGURE 7.7** Case Study (b): Feldstein oval data as described for Figure 7.4 ( $K_p = 4o$ ), but for 02:00 UT. Note that the Bodø/Wick nominal propagation path midpoint lies outside of the predicted zone.

are located within this predicted zone, the equatorward boundary of the oval having drifted northwards at this post-midnight time.

#### 7.4.4 Case Study (c): 22:00 UT, Day 338 – 02:00 UT, Day 339

The SABRE backscatter S/N ratio magnitudes and the Sporadic-E *vfiEs* values for this time interval, are depicted in Figure 7.8. The Figure format is similar to that of Figures 7.2(a,b). It is immediately apparent that sporadic-E recordings only started towards the latter half of the main SABRE backscatter observation period (22:00 UT, day 338 to 02:00 UT, day 339). However, the correlation of occurrence thereafter is good, observations of both sporadic-E layers and irregularity backscatter ceasing at approximately 01:50, day 339. Of more note is the correlation between the backscatter S/N ratio and the *vfiEs* magnitudes, between ~ 00:00 UT and ~ 02:00 UT. The associated correlation coefficient is noted to be greatest between the SABRE range gates of 33 to 47, maximising at range gate 36, for which Figure 7.8 was compiled. The said correlation coefficient, at range gate 36 is 0.83, and is significant at the 1% level. All these range gates are a few hundred kilometers north of the nominal Bodø/Wick propagation path midpoint and indeed, north of the SABRE range gate for orthogonal aspect angle conditions (range gate 30).

Figures 7.9(a,b) depict a classic substorm event between ~ 22:15 UT, day 338 and ~ 01:00 UT, day 339. Figure 7.9a presents unfiltered, H-component magnetometer data from the three high latitude stations of the SAMNET network. The negative bay event between ~ 22:30 UT and ~ 23:50 UT represents the substorm expansion phase, associated with the westward electrojet. Note that this time interval is coincident with the SABRE backscatter returns depicted in Figure 7.8. A further substorm surge is observed to start just prior to midnight, with recovery to quiet time magnetic conditions at approximately 02:00 UT. This second expansion surge is closely correlated with the SABRE backscatter and sporadic-E data presented in Figure 7.8.

Figure 7.9b confirms the substorm activity, with Pi2 pulsations being noted at ~ 22:20 UT, ~ 22:30 UT and ~ 23:30 UT. Planetary K-indices for the period from 21:00 UT, day 338 to 03:00 UT, day 339 are 4+ and 4o respectively. The model Feldstein oval for 24:00 UT and a  $K_p$  value of 4o, is presented in Figure 7.10. Again, as in Figure 7.4, the nominal Bodø/Wick propagation path midpoint and a significant proportion of the higher SABRE range gates (cf. Figure 3.9) are sited within this statistically active zone.

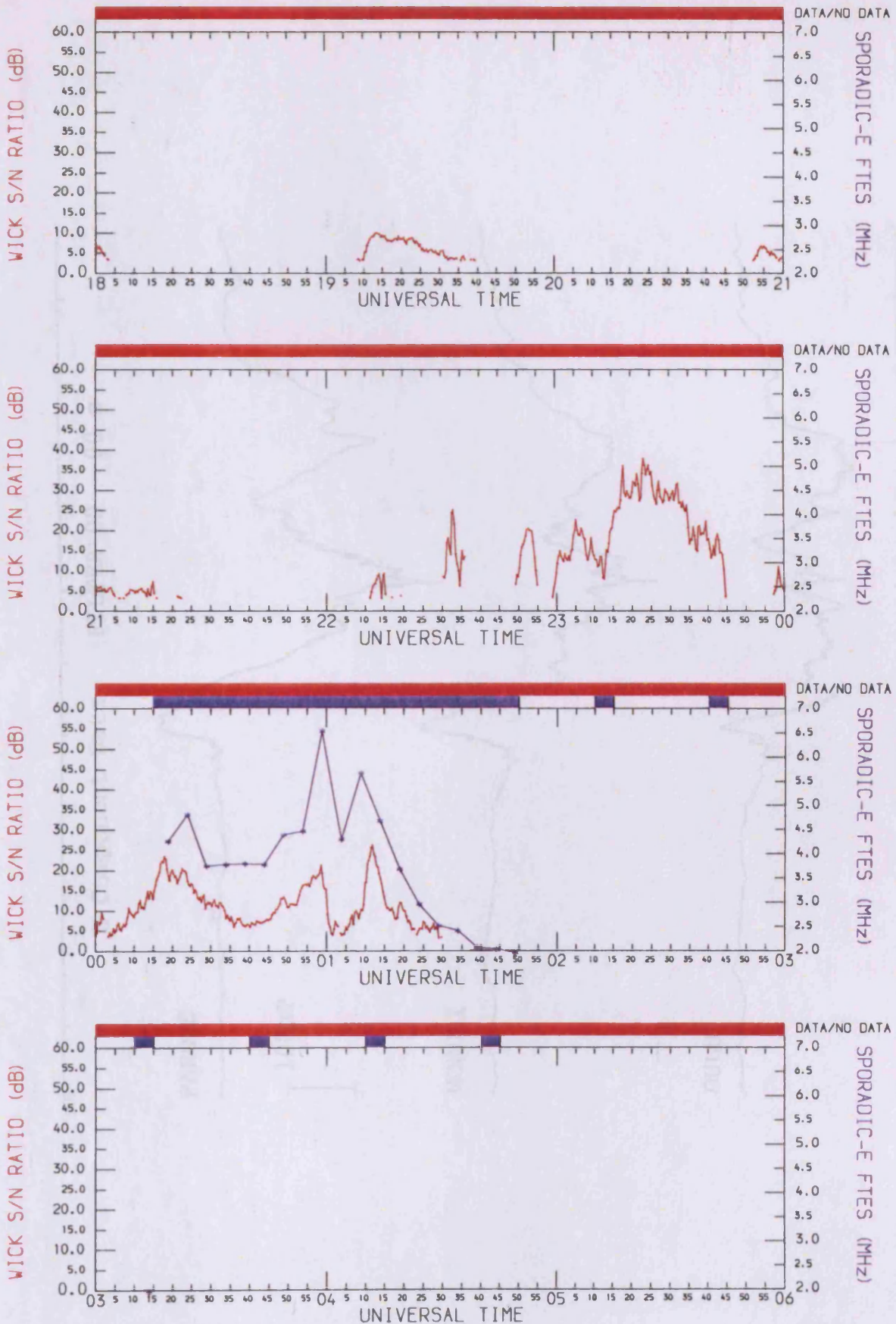


FIGURE 7.8 Case Study (c): SABRE backscatter S/N ratio, and sporadic-E  $\nu fE_s$  data, as recorded for Figure 7.2a, but for the December Campaign period between 18:00 UT, day 338, and 06:00 UT, day 339, 1987, and for range gate 36.

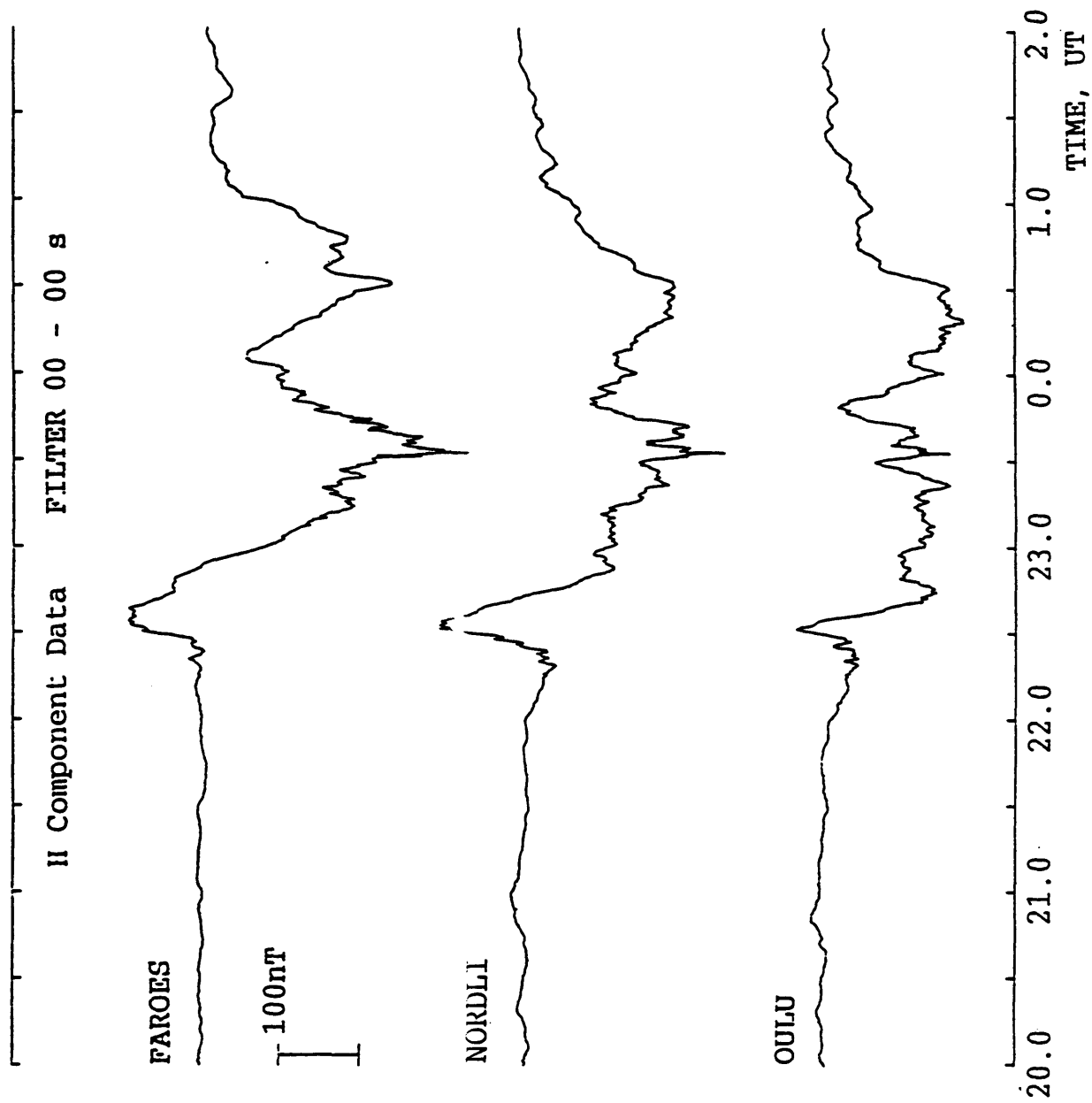
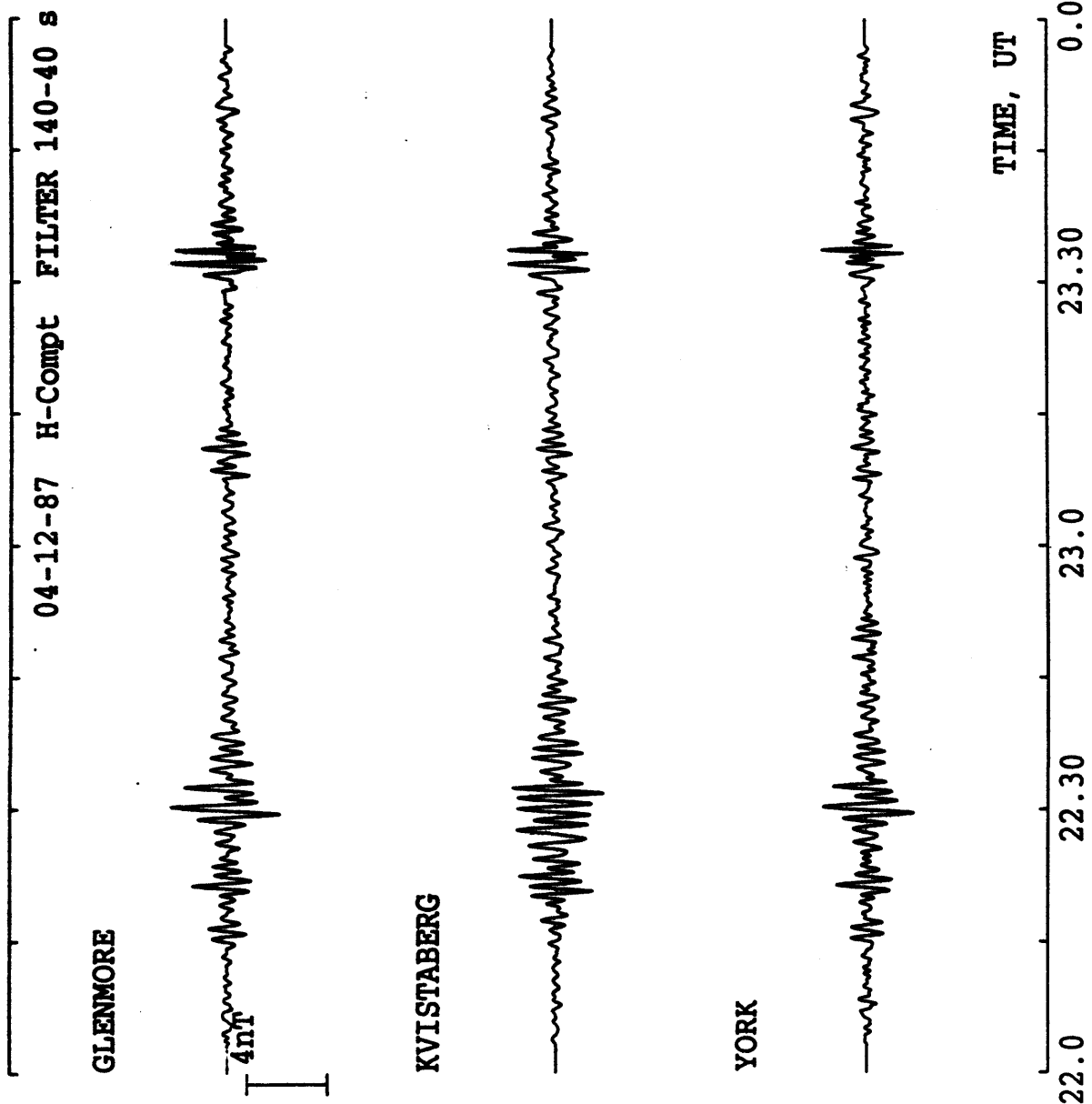


FIGURE 7.9a Case Study (c): SAMNET data as for Figure 7.3a, but recorded between 20:00 UT, day 338, and 02:00 UT, day 339, 1987. Substorm activity is noted between approximately 22:30 UT and 02:00 UT.

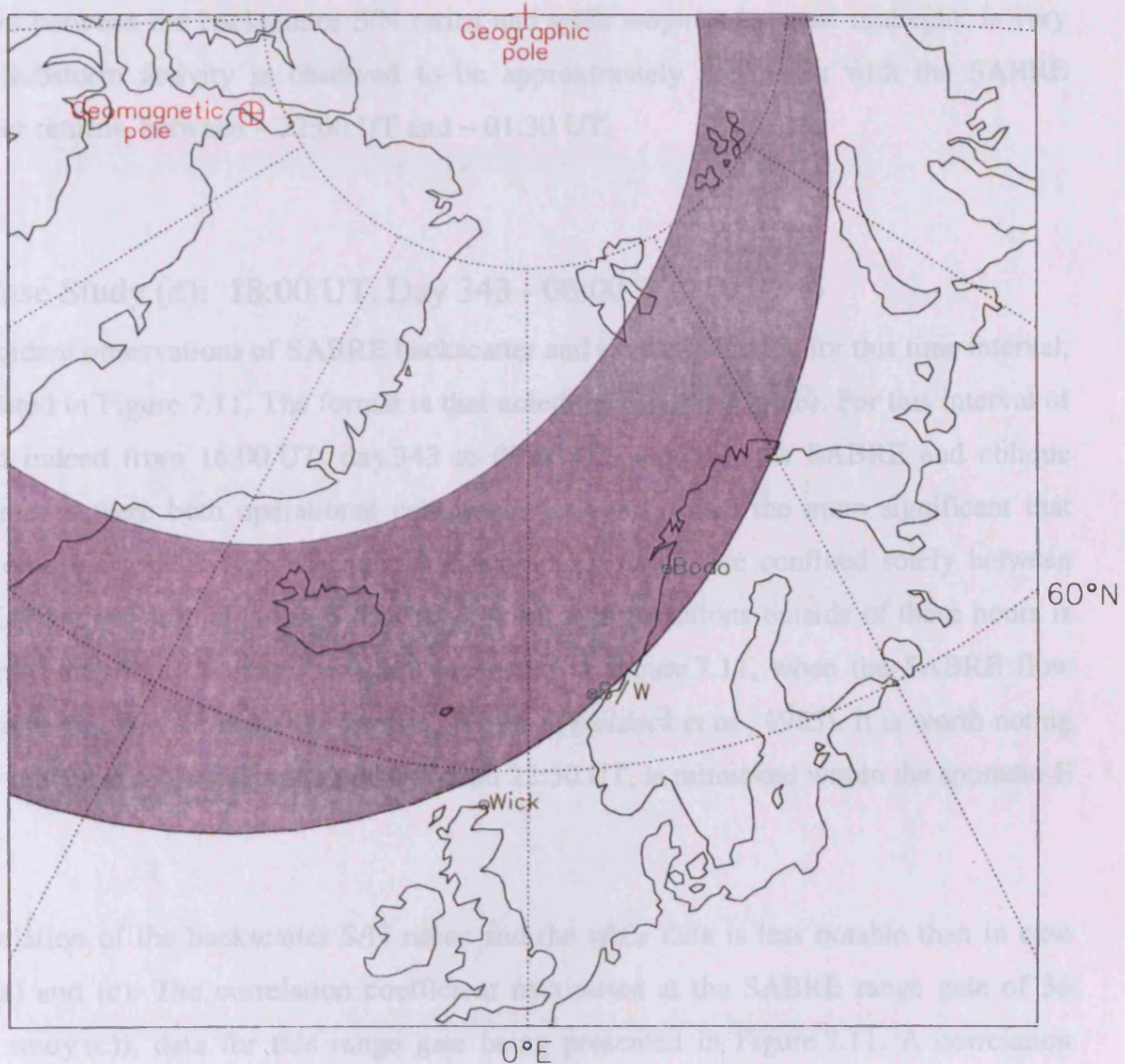


**FIGURE 7.9b** Case Study (c): SAMNET data as for Figure 7.3b, but recorded between 22:00 UT and 24:00 UT, day 338, 1987. Pi2 pulsations are clearly observed at ~ 22:20 UT, ~ 22:30 UT and ~ 23:30 UT.

### Observation Summary

The current case study concentrates on a magnetically disturbed time interval of four hours, straddling midnight, when substorm activity is prominent. The correlation of occurrence analysis between the SABRE backscatter data for day 343, 00:00 UT, is significantly affected by the absence of recordings of the latter prior to midnight on day 338. However, the correlation is still significant.

UT = 24.0      K<sub>p</sub> = 4



The correlation of the backscatter data for day 343, 00:00 UT, is less notable than in the studies (a) and (c). The correlation coefficient is 0.22, which is only significant at the 10% level. The backscatter data for range gate 30 is in fact very similar to that presented in Figure 7.11, although no backscatter data was recorded at range gate 12.

The significance of this 3-hour time period is demonstrated in Figure 7.12a. The data presented pertains to the unfiltered magnetic field H-component, as measured by the three highest latitude stations of the MANNET magnetometer network. A magnetic disturbance is clearly noted between ~ 21:00 UT, day 343 and ~ 00:30 UT, day 344, though the 50-nT scale bar indicates that the magnitude of this disturbance is significantly less than those noted in

**FIGURE 7.10** Case Study (c): Feldstein oval data as described for Figure 7.4 ( $K_p = 4$ ), but for 00:00 UT. Note that the Bodø/Wick nominal propagation path midpoint lies just inside the predicted zone.

### *Observation Summary*

The current case study concentrates on a magnetically disturbed time interval of four hours, straddling midnight, where substorm activity is prominent. The correlation of occurrence analysis between the SABRE backscatter data and sporadic-E layers, is significantly affected by the absence of recordings of the latter prior to midnight on day 338. However, the correlation between the backscatter S/N ratios and *vftEs magnitudes*, post midnight, is very notable. Substorm activity is observed to be approximately coincident with the SABRE backscatter returns, between ~ 22:00 UT and ~ 01:30 UT.

#### 7.4.5 Case Study (d): 18:00 UT, Day 343 - 06:00 UT, Day 344

The coincident observations of SABRE backscatter and sporadic-E data, for this time interval, are presented in Figure 7.11. The format is that noted for Figures 7.2(a,b). For this interval of time, and indeed from 16:00 UT, day 343 to 09:00 UT, day 344, the SABRE and oblique sounder radars were both operational continuously. It is thus all the more significant that observations of irregularity backscatter and sporadic-E data were confined solely between ~ 21:00 UT and ~ 24:00 UT, day 343. The absence of observations outside of these hours is significant, particularly during the hours presented in Figure 7.11, when the SABRE flow angles are favourable for detecting backscatter data (*Waldock et al.*, 1985). It is worth noting that even the absence of backscatter data around 22:50 UT, is mimicked within the sporadic-E data set.

The correlation of the backscatter S/N ratios and the *vftEs* data is less notable than in case studies (a) and (c). The correlation coefficient maximises at the SABRE range gate of 36 (cf. case study (c)), data for this range gate being presented in Figure 7.11. A correlation coefficient of 0.32 is calculated for the time interval of 21:00 UT to 24:00 UT, which is only significant at the 10% level. The backscatter data for range gate 30 is in fact very similar to that presented in Figure 7.11, though no backscatter data was recorded at range gate 12.

The significance of this 3-hour time period is demonstrated in Figure 7.12a. The data presented pertains to the unfiltered magnetic field H-component, as measured by the three highest latitude stations of the SAMNET magnetometer network. A magnetic disturbance is clearly noted between ~ 21:00 UT, day 343 and ~ 00:30 UT, day 344, though the 50 nT scale bar indicates that the magnitude of this disturbance is significantly less than those noted in

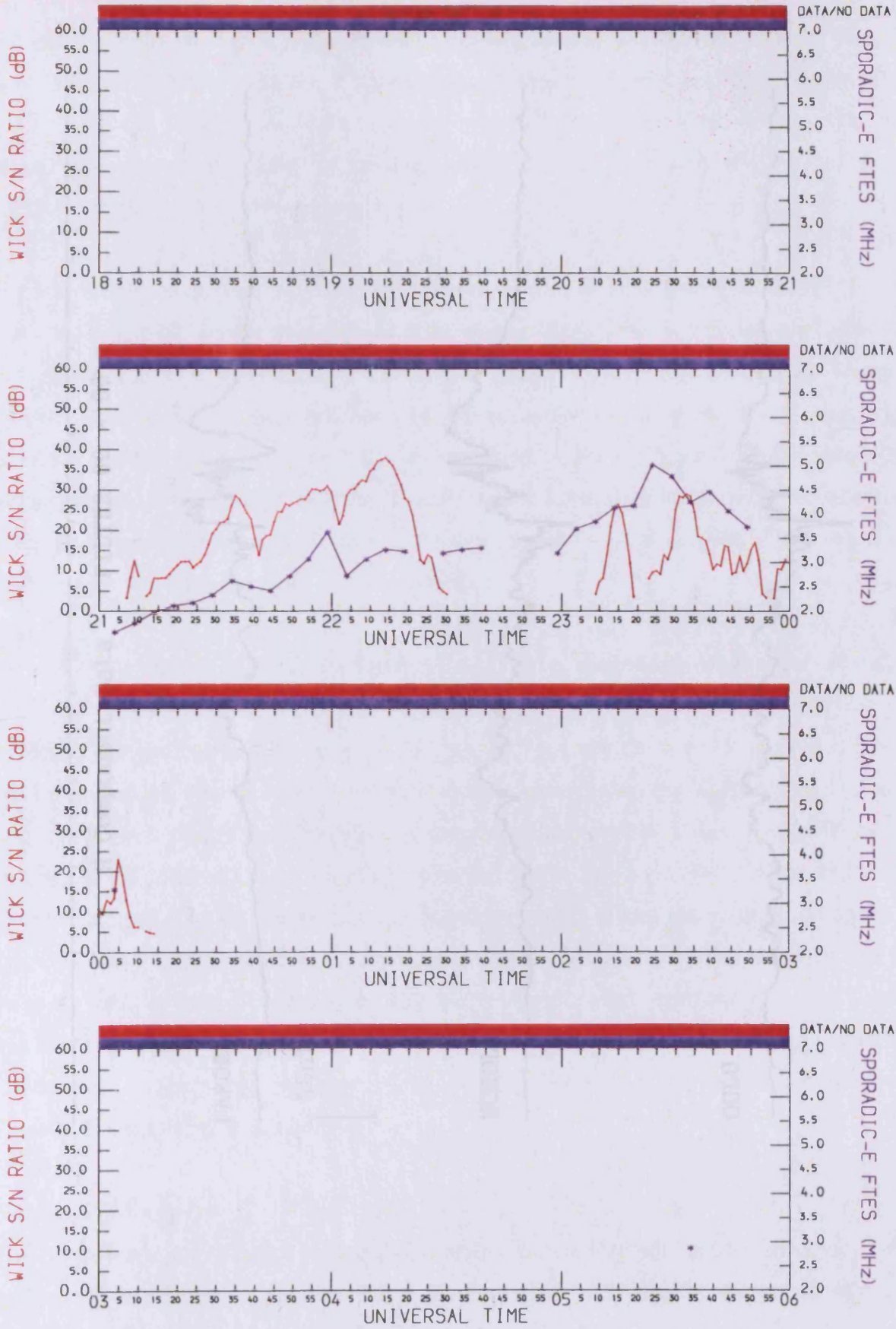


FIGURE 7.11 Case Study (d): SABRE backscatter S/N ratio, and sporadic-E *ftEs* data, as recorded for Figure 7.2a, but for the December Campaign period between 18:00 UT, day 343, and 06:00 UT, day 344, 1987, and for range gate 36.

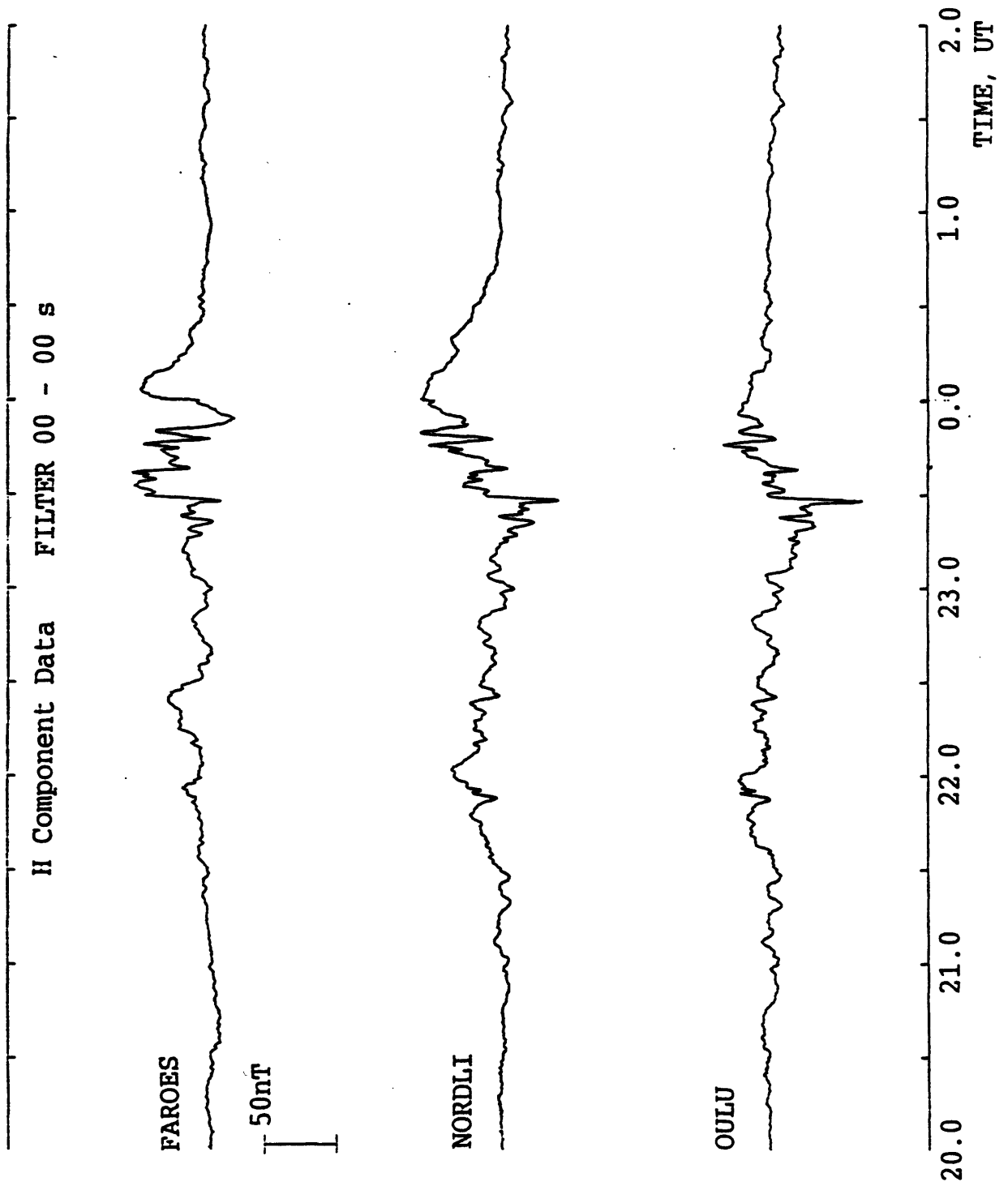


FIGURE 7.12a Case Study (d): SAMNET data as for Figure 7.3a, but recorded between 20:00 UT, day 343, and 02:00 UT, day 344, 1987. Substorm activity (confirmed by Pi2 pulsations) is observed between approximately 21:00 UT and 00:30 UT.

case studies (a) to (c). Figure 7.12b presents spectrally filtered H-component data, for three lower latitude SAMNET stations. Pi2 pulsations are clearly observable at approximate times of 19:40 UT and 21:55 UT, indicating that the magnetic disturbance noted in Figure 7.12a, is indeed substorm activity, albeit of relatively small intensity, or maybe not proximal to the SABRE/oblique sounder viewing area.

It is interesting to note that the planetary K-index for the period 21:00 UT to 24:00 UT is 4-. The local magnetic activity thus appears to be similar to that observed during case study (c), with the position of the Feldstein auroral oval, depicted in Figure 7.10, being similarly located. This deduction does not however correspond with the significantly lower *local* magnetic activity noted in Figure 7.12a, as compared to that in Figure 7.9a. It is thus often more appropriate to consider the local K-index values rather than the planetary K-index, the latter being generally more applicable to planetary magnetic storm activity (*Gonzalez et al.*, 1994) than to the more localised substorm events.

Lerwick is the nearest station to the SABRE field of view, providing local K-index values. As this was not considered sufficiently 'local', pseudo K-indices were compiled for the SAMNET stations, as described in §3.4.2. Figure 7.13 presents the three H- and D-component pseudo K-indices, for the three SAMNET stations surrounding the SABRE radar viewing area, i.e. Nordli, Faroes and Glenmore. Each station depicts the pseudo K-indices for the duration of the December campaign i.e. from day 335 to day 345, 1987. The ordinates are scaled in nT. Of note are the increases in magnetic activity during the evening and nights of days 339 and 344, the time periods pertinent to case studies (a) to (c). But also note that the magnetic activity around midnight on day 343, pertinent to this case study, is significantly less than for the previous three case studies, despite similar  $K_p$ -index values being calculated. Given these observations, positioning the Feldstein oval, with respect to the *planetary* K-index, is inappropriate in this case.

### *Observation Summary*

The *occurrence* correlation between the E-region backscatter and sporadic-E data is very striking. Over a period of time extending for more than 18 hours, the only observations of either data type was between 21:00 UT and 24:00 UT on day 343. This time interval was characterised by a substorm event and generally increased magnetic activity, though of a lesser magnitude than observed in the previous case studies.

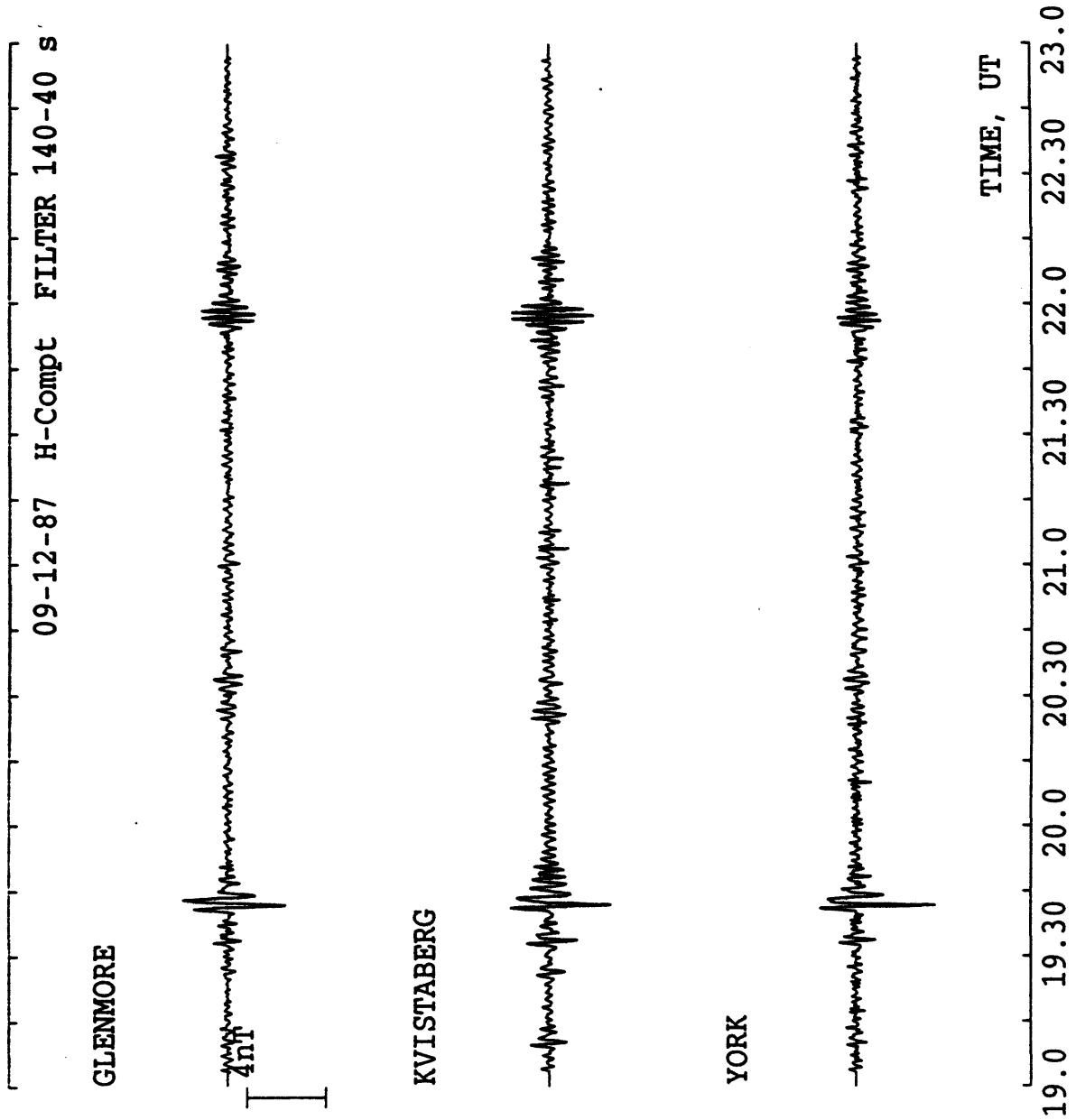


FIGURE 7.12b Case Study (d): SAMNET data as for Figure 7.3b, but recorded between 19:00 UT and 23:00 UT, day 343, 1987. Pi2 pulsations are clearly observed at ~ 19:40 UT and ~ 21:55 UT.

DAY, 335 TO DAY, 345 YEAR, 1987

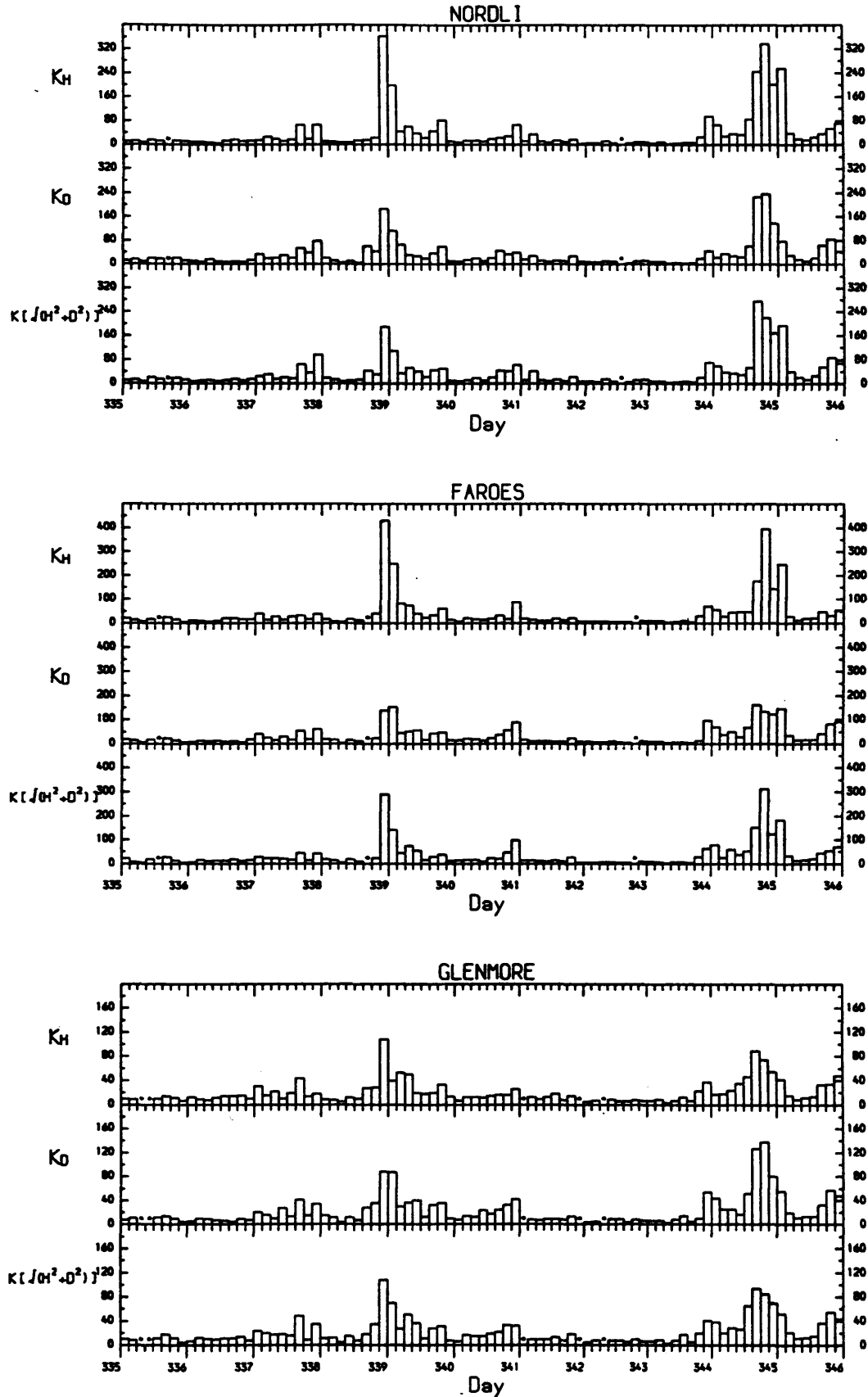


FIGURE 7.13 Case Study (d): Pseudo K-index values derived from SAMNET magnetometer data as described in §3.4.2. The three stations represented are those of closest proximity to the Bodø/Wick nominal propagation path midpoint. Note the relatively quiet magnetic activity between 18:00 UT, day 343 and 06:00 UT, day 344, the hours pertinent to this case study.

#### 7.4.6 Case Study (e): 18:00 UT, Day 75 – 03:00 UT, Day 76

The following case study is derived from the March, 1988 campaign data set (cf. Table 4.1). Figures 7.14(a,b) present the SABRE backscatter S/N ratio and oblique sounder *vfiEs* data, in the format of Figures 7.2(a,b), for range gates 12 and 30 respectively. Referring to Figure 7.14a, irregularity backscatter and sporadic-E layers are both detected almost simultaneously at 18:35 UT. As in case study (b), the sporadic-E layer persists long after the backscatter returns cease, though a significant coincident recurrence is noted at ~ 02:00 UT. In Figure 7.14b, the coincident occurrence of both backscatter and sporadic-E data is significantly more notable, though sporadic-E is still observed to persist when backscatter returns have ceased (cf. ~ 21:00 UT to ~ 23:00 UT).

To put the results in context, the oblique sounder was in continuous operation from 12:00 UT, day 75, with no sporadic-E being detected until 18:30 UT, as depicted in Figures 7.14(a,b). Similarly, the SABRE radar was in continuous operation from 12:34 UT, detecting no backscatter from any range until 17:35 UT. Sporadic-E layer and irregularity generation are thus initiated at approximately the same time, after a prolonged period of inactivity.

Figure 7.15a presents the unfiltered H-component magnetic field data, recorded by the Nordli and Oulu SAMNET magnetometer stations (Faroes data being unavailable). Substorm activity, associated with the westward electrojet, is noted between ~ 18:00 UT to ~ 21:00 UT and between ~ 23:00 UT to 04:00 UT. Significant Pi2 pulsations are observed at ~ 18:45 UT, ~ 18:55 UT and ~ 19:40 UT (Figure 7.15b) and also at ~ 23:30 UT, ~ 00:05 UT, ~ 00:30 UT and ~ 01:05 UT. This is clearly a time interval of multiple substorm onsets. The  $K_p$  indices for this case study are 4+, 4o and 4-. Appropriate Feldstein auroral ovals are thus depicted in Figures 7.4, 7.7 and 7.10.

##### *Observation Summary*

Three distinct substorm events are noted throughout the time period of this case study, with onsets being at approximately 18:30 UT, 23:30 UT and 01:00 UT. The SABRE backscatter returns are closely correlated with these events, as are observations of sporadic-E layers, though the latter is noted to persist after the first substorm event for a duration of approximately 1.5 hours. A few data gaps also interfere with correlation determinations. The *vfiEs* value is noted to increase at each of the substorm onset times.

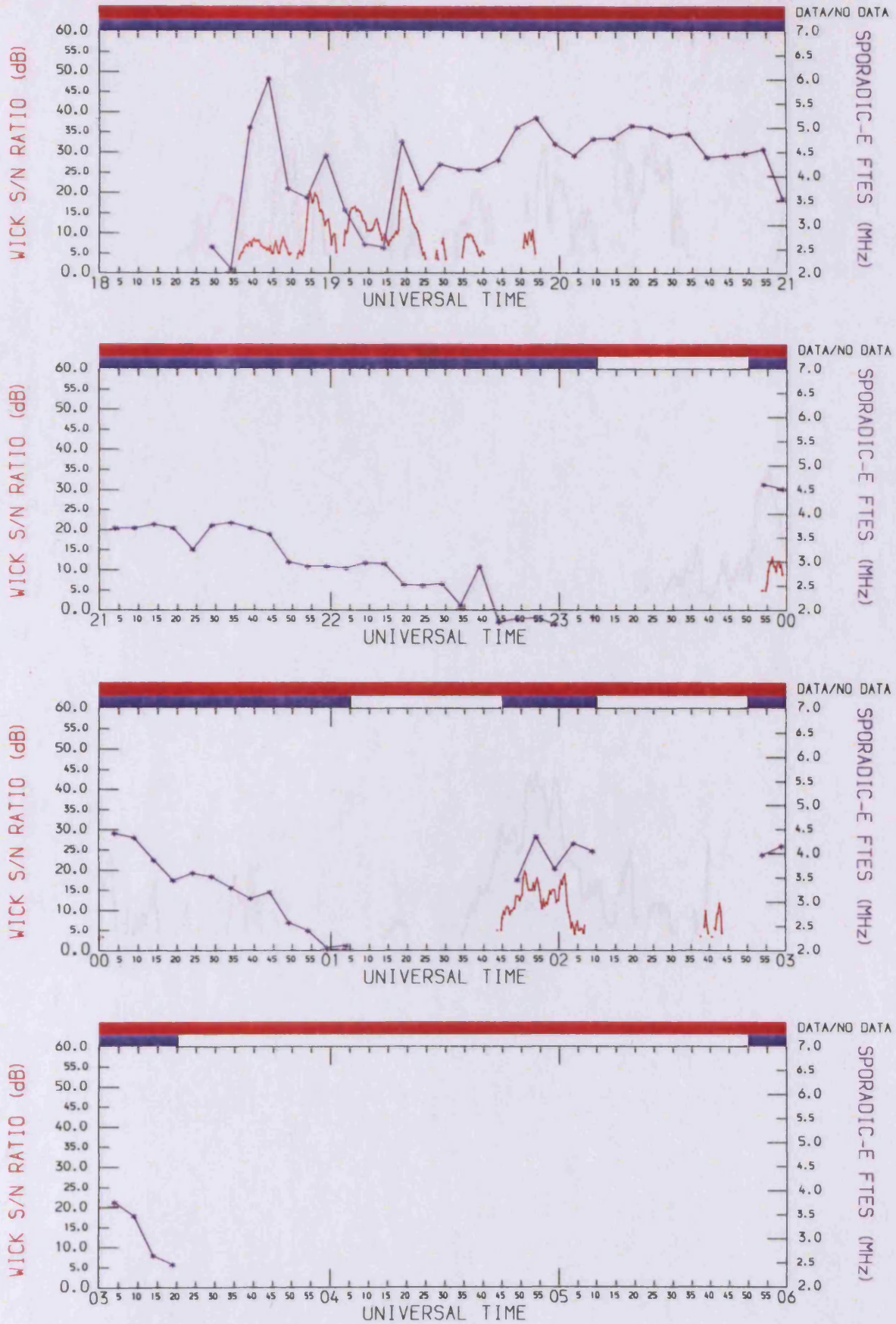


FIGURE 7.14a Case Study (e): SABRE backscatter S/N ratio, and sporadic-E *vftEs* data, as recorded for Figure 7.2a, but for the March Campaign period between 18:00 UT, day 75, and 06:00 UT, day 76, 1988, and for range gate 12.

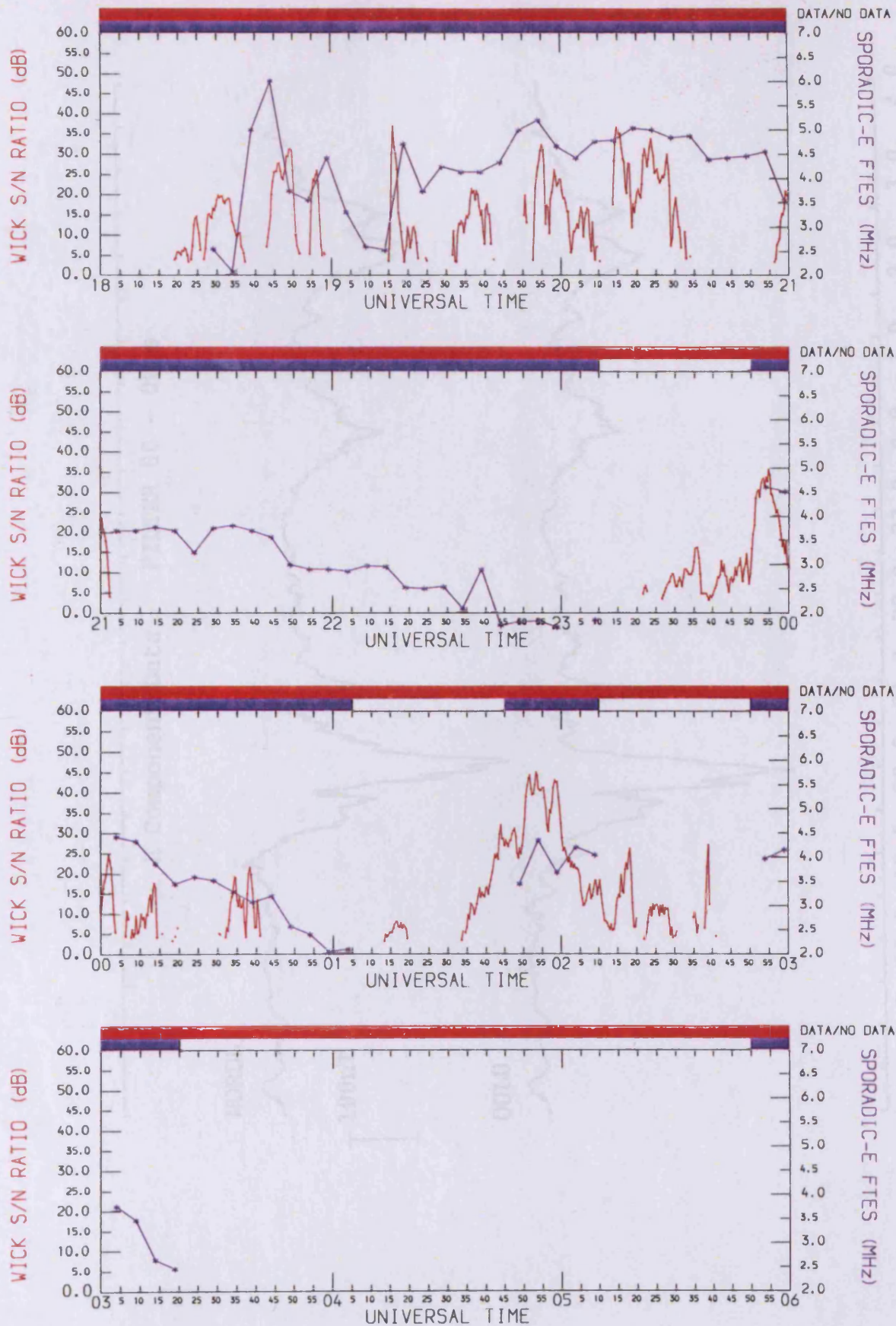


FIGURE 7.14b Case Study (e): SABRE backscatter S/N ratio, and sporadic-E *vftEs* data, as recorded for Figure 7.14a, but for range gate 30.

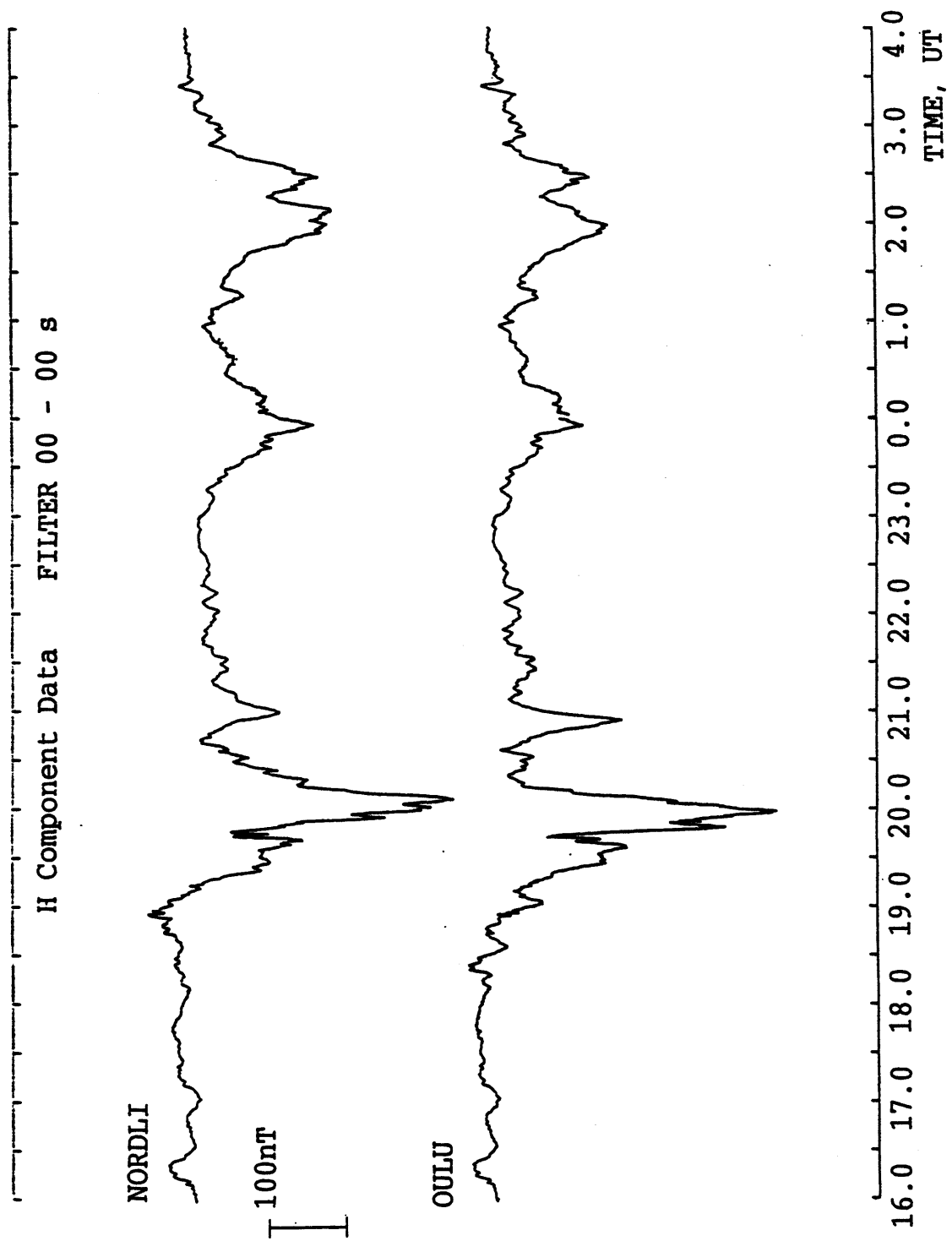


FIGURE 7.15a Case Study (e): SAMNET data as for Figure 7.3a, but recorded between 16:00 UT, day 75, and 04:00 UT, day 76, 1988, and with the Faroes data omitted. A classic substorm onset is observed at approximately 18:30 UT. Further substorms are noted between approximately 23:00 UT and 01:00 UT, and also between ~ 01:00 UT and ~ 03:30 UT.

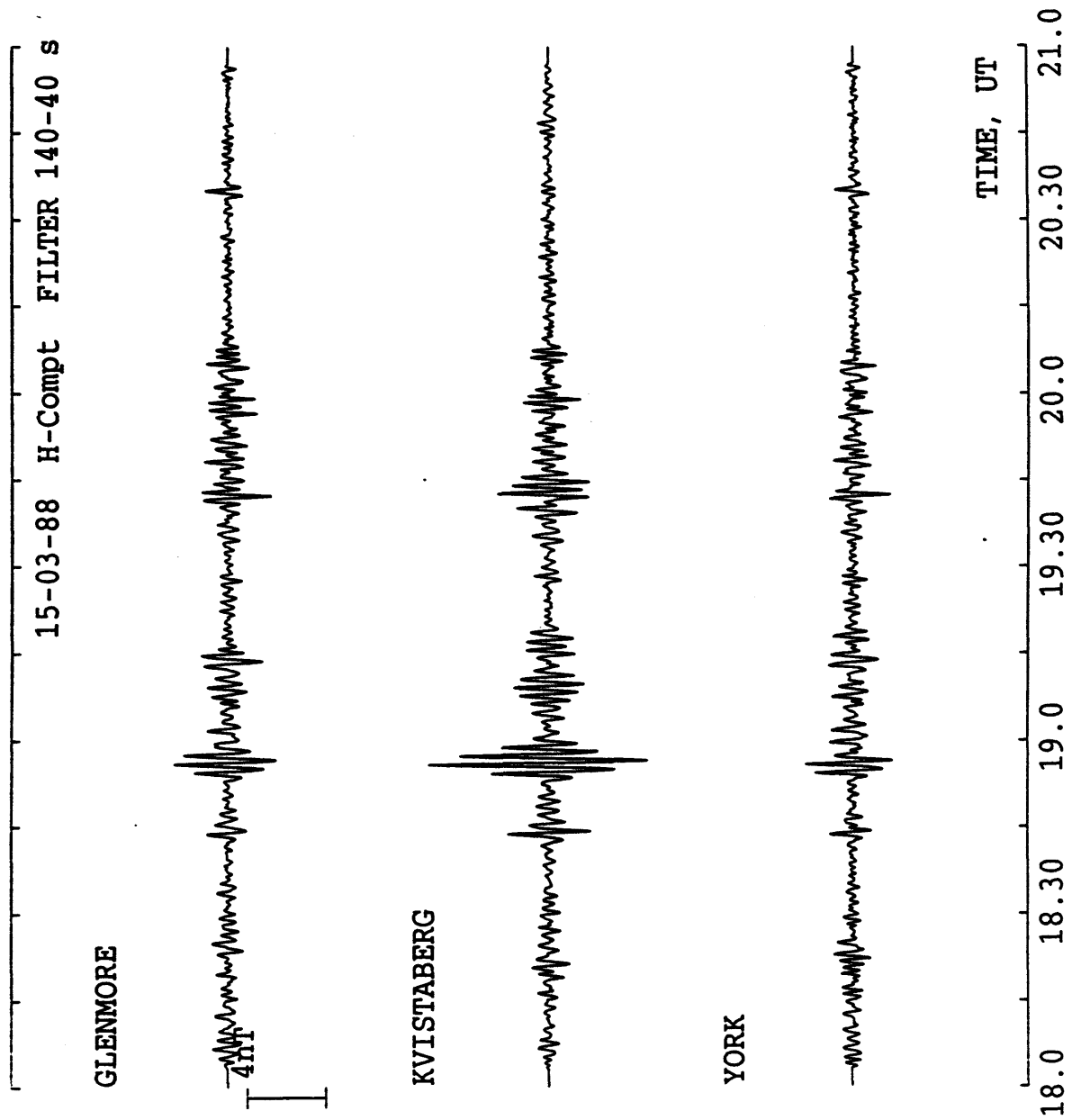


FIGURE 7.15b Case Study (e): SAMNET data as for Figure 7.3b, but recorded between 18:00 UT and 21:00 UT, day 75, 1988. Pi2 pulsations are observed throughout the period of the case study, but notably in this Figure, at ~ 18:45 UT, ~ 18:55 UT and ~ 19:40 UT.

## 7.5 Summary of the Case Study Observations

In §7.4, sporadic-E  $vfiEs$  values were observed with respect to E-region irregularity backscatter data, primarily during substorm activity. The five case studies presented represent all *types* of observations and correlations noted during the December and March campaigns. A summary of the collective observations is thus instructive.

Without exception, all substorm activity is accompanied by irregularity backscatter and sporadic-E layer observations. The backscatter data is generally closely correlated with the time interval of the substorm, whereas on several occasions, the sporadic-E observations extended beyond the substorm interval. An example is the time interval between ~ 21:00 UT, day 344 and ~ 00:45 UT, day 345 (case studies (a) and (b)) (Figures 7.2(a,b) and Figure 7.5). This period of time falls between two significant substorm events and indeed the sporadic-E observations extend beyond the second substorm, for a time of about 1 hour (~ 03:00 UT to ~ 04:00 UT, day 345) (Figure 7.5). Case study (e) is another example (Figure 7.14(a,b)), with these Figures demonstrating the need to consider data from a variety of SABRE range gates.

In contrast, Figure 7.8 and Figure 7.11 depict sharp, coincident cut-offs of the sporadic-E data with respect to the backscatter data. Further, Figure 7.11 is very notable for coincident initiation of sporadic-E and backscatter data, after many previous hours of continuous radar operation with no returns. Figures 7.14(a,b), in case study (e) similarly depict a coincident initiation of the two data sets, and also following several hours of no returns.

Of particular interest are the correlated  $vfiEs$  and irregularity backscatter S/N ratio magnitudes. Significant correlations are noted between 00:00 UT and 00:02 UT, day 339 (Figure 7.8), between 15:00 UT and 18:00 UT, day 344 (Figure 7.2(a,b)) and to a lesser extent between 18:00 UT and 21:00 UT, day 344 (Figure 7.2(b)). For each the correlation coefficient maximises at a different SABRE range gate, i.e. gates 36, 13 and 25. The example between 15:00 UT and 18:00 UT, day 344 is of further note in that this time period is the only time period from all five case studies, that does not occur during a substorm event, though magnetically disturbed bays are still noted (Figure 7.3a). From henceforth, the ionospheric conditions pertinent to substorms are presumed to apply to this magnetically disturbed period. All of these observations contrast with other occasions of correlated *occurrence* between the two data sets, where little or no correlation is noted between the  $vfiEs$  and backscatter S/N ratio *magnitudes*.

## 7.6 Discussion

The ionospheric signature of a magnetospheric substorm, is characterised by high energy particle precipitation into the high latitude auroral E-region (*Akasofu, 1964*). The subsequent increase in conductivities (e.g. *Horwitz et al., 1978*), together with enhanced auroral electric fields (e.g. *Rino et al., 1974*), lead to augmented plasma flows within the auroral electrojets. These characteristic substorm features are directly responsible for the generation of plasma irregularities and sporadic-E layers. Coincident observations of both are thus linked by the substorm event. The relationships between substorm activity and separately, SABRE irregularity backscatter and sporadic-E layers, are discussed below, in light of the observations noted in §7.4 and §7.5. A discussion of the correlation of SABRE backscatter S/N ratio and  $\nu f E_s$  magnitudes then follows.

### 7.6.1 The Correlation of SABRE backscatter observations with Substorm Events

The enhanced plasma drifts and ambient densities, resulting from substorm activity, are favourable to the generation of small scale irregularities, for example those of wavelengths  $\sim 1$  m, which may be observed by the SABRE radar (cf. §3.4.1). During substorm events, the auroral oval is also noted to broaden, with the equatorward boundary drifting to lower latitudes (*Feldstein and Starkov, 1967*). This oval broadening increases with the degree of magnetic disturbance. Sub-auroral radars such as SABRE (and the Bodø/Wick oblique HF sounder) are thus increasingly influenced by these ionospheric responses.

The correlation of substorm activity and SABRE irregularity backscatter observations is thus to be expected. However, with reference to the observations described in §7.4, the degree of correlation is noted to vary with the exact onset and recovery times of the substorms. For example, Pi2 observations are rarely coincident with backscatter intensifications. Disturbed magnetic activity as indicated by the unfiltered magnetic field H-component, is though noted to approximately correlate with the SABRE backscatter observations. The best correlation is noted in case study (c). Comparing Figure 7.8 with Figure 7.9a, substorm related magnetic bays are observed between just after 22:00 UT to approximately 01:30 UT, day 338 to day 339. Coincident observations of SABRE irregularity backscatter match exactly.

A more typical example is noted for case study (e). Referring to Figure 7.15a, significant substorm activity is deduced between  $\sim 18:00$  UT and  $\sim 21:30$  UT, day 075, and between

~ 23:00 UT and ~ 03:30 UT, days 75 to 76. Corresponding SABRE backscatter is noted in Figure 7.14b, between ~ 18:20 UT and ~ 21:00 UT, and between ~ 23:25 UT and ~ 02:40 UT. Small discrepancies are thus noted between the time intervals, and significantly, the backscatter observations are confined *within* the magnetic disturbance times. It thus appears that there is a time delay between the onset of a magnetic disturbance, and the sufficient enhancement of the plasma drift, required to excite plasma instabilities. Similarly, the plasma drift reduces below the excitation threshold before the end of the magnetic disturbance. Comparison with the other case studies reveals this to be a general observation, but with the time delays tending to zero on occasions, e.g. case study (b). These observations contrast with the sporadic-E correlations with magnetic (substorm) activity, discussed below.

Factors influencing the exact correlation of SABRE backscatter with magnetic disturbances, are firstly the range gate considered (cf. Figures 7.14(a,b)) but also a variety of intrinsic factors discussed later e.g. flow and magnetic aspect angles, and the amplitude (and hence detectability) of the irregularities, which is determined by the magnitude of the plasma drift. Each of these factors depend on the relative location of the substorm to the SABRE field of view, and hence on the associated enhanced electrojets and plasma flow vectors. An *exact* correlation between the substorm magnetic signature and the occurrence of SABRE backscatter is thus unlikely.

## 7.6.2 The Correlation of Sporadic-E Occurrence with Substorm Events

The substorm induced, increased particle precipitation and enhancements of the auroral electric fields, are both favourable to the generation of *different types* of sporadic-E layers at high latitudes. Auroral sporadic-E (e.g. *Besprozvannaya et al.*, 1980; *Turunen*, 1977; *Weber et al.*, 1977) is sometimes directly associated with scattering from irregularities i.e. independent of any ionisation compression mechanism (cf. equatorial sporadic-E (e.g. *Cohen*, 1967)). The enhanced electric fields may thus promote the generation of intense gradient drift irregularities, with wavelengths ~ 10 m, which may be detected by an HF radar e.g. an ionosonde.

The associated irregularities of auroral-Es are, however, often considered to be embedded *within* the sporadic-E layer, the layer itself being generated through the converging action of uniform electric fields (*Nygrén et al.*, 1984), acting directly or indirectly, on the enhanced ionisation arising from the substorm induced particle precipitation (cf. §2.3.7). Gradient-drift instabilities are excited when a component of the ambient electric field is oriented both

parallel to and in the same direction as the electron density gradient, given sufficient magnitudes of each (*Ecklund et al.*, 1981). This type of instability is presumed for coincident observations of sporadic-E layers and plasma irregularities at mid-latitudes (e.g. *Haldoupis and Schlegel*, 1993; *Keys and Andrews*, 1984), but is equally applicable, and more easily excited, at high latitudes, particularly during substorm activity.

Further, *Haldoupis et al.* (1992) have observed Type III irregularities within sub-auroral sporadic-E layers. Type III irregularities resemble the two-stream, Type I irregularities, with respect to doppler power spectra, but have phase velocities well below 'typical' ion acoustic velocities. It is suggested that these reduced velocities may result from the large electron density gradients within sporadic-E layers, and also that the ion acoustic velocity itself may be reduced due to the presence of heavier ions, i.e. the metallic ions noted within Es-layers (e.g. *Huuskonen et al.*, 1988). Similar observations and deductions were made by *Riggin et al.* (1986).

Mechanisms thus exist to explain the presence of both gradient-drift *and* two-stream related irregularities, *within* sporadic-E layers at high-latitudes, both types being generated more readily during substorm activity.

Sporadic-E at high-latitudes may however exist independent of an irregularity structure. Thin, flat-type sporadic-E layers are also observed at high latitudes (e.g. *Rodger et al.* 1983; *Turunen*, 1977), similarly generated through the action of uniform electric fields. The electric field has been noted to intensify about an hour before substorm onset (*Mozer*, 1971), with 'flat-type' Es-layers being noted specifically at this time (*Schaeffer*, 1967). The electric field and precipitation characteristics associated with substorm events, are thus equally favourable to generating mid-latitude-type Es-layers at high-latitudes.

#### *Further Data Observations*

It was noted in §7.5 that while sporadic-E was always observed *during* the substorm activity, observations sometimes extended *beyond* the time interval of magnetic disturbances (cf. SABRE observations in §7.6.1). Various explanations for these observations are possible. Firstly, the generation mechanisms for both the auroral and flat-type Es-layers, observed at high latitudes, relate either directly or indirectly to the enhanced electric fields. It is noted that plasma irregularities are very short-lived features (~ ms) and hence the observation of irregularities is very sensitive to the instantaneous magnitude of the plasma drift. The fact that SABRE irregularity backscatter is always noted to be confined within the time periods of

magnetic disturbance (cf. §7.6.1), indicates that the substorm induced, enhanced electric field and hence plasma drift, does not maintain its magnitude after substorm recovery. However, flat-type sporadic-E may be generated at much reduced electric field magnitudes, ~ a few mV's (*Morton and Mathews, 1993*) and hence may persist beyond irregularity backscatter observations.

Further, the threshold excitation plasma drift velocity, is inversely proportional to the irregularity wavelength (*Farley, 1963*). Larger wavelength irregularities (i.e. gradient-drift type) are thus more easily excited and hence observable, during periods of reduced electric fields and plasma drifts. The generation of these larger scale irregularities, and possibly the Type III irregularities, within auroral-Es, may thus be possible beyond the recovery phase of the substorm.

But perhaps most importantly, mid-latitude type sporadic-E layers are generally associated with long lifetime, metallic ion constituents (cf. §2.3.7). Sporadic-E layers generated by the plasma-compressing action of uniform electric fields (*Nygrén et al., 1984*), may thus exist beyond the lifetime of the generating source.

It is noted that the sporadic-E observed between ~ 21:00 UT, day 344 and ~ 00:45 UT, day 345 (Figures 7.2(a,b) and Figure 7.5) and between ~ 03:00 UT to ~ 04:00 UT, day 345 (Figure 7.5), is generally classified as flat-type i.e. independent of an irregularity structure. These time intervals are notable for the absence of SABRE backscatter and substorm activity. However, a similarly classified time period, between ~ 21:00 UT and ~ 23:00 UT, day 75, is associated with diffuse, auroral-Es type layers. It appears that at least on some occasions, the HF sounder may detect larger scale irregularities (~ 10 m) at times when smaller scale irregularities (~ 1 m) are not excited, or at least not detectable by SABRE.

### 7.6.3 The Correlation of SABRE Backscatter S/N Ratio and $\nu f_i E_s$ Magnitudes

In §7.4 and §7.5, several instances of the correlation of SABRE backscatter S/N ratio and  $\nu f_i E_s$  magnitudes were noted. To discuss possible mechanisms and scenarios to account for these correlations, it is first necessary to briefly review the theory associated with backscatter intensity magnitudes. Typical enhancements to the auroral electric fields observed during substorm and auroral activity, are then employed to deduce the corresponding irregularity backscatter intensities and the magnitudes and variations of  $\nu f_i E_s$  values. In deducing typical

*vftEs* magnitudes and variations, both electric field and irregularity aspects of sporadic-E layers are considered separately.

### *E-Region Irregularity Backscatter Intensity Theory*

The received backscatter intensity, or power,  $P_r$ , is determined by both radar and ionospheric factors, and is defined as (Haldoupis, 1989):-

$$P_r = P_t \frac{L_t L_r G_t G_r g_r \lambda^2 \sigma(k) c \tau T \Delta \delta}{2(4\pi R)^3} \quad (7.1)$$

where  $P_t$  is the transmitted power,  $L_{t,r}$  and  $G_{t,r}$  are the transmitter and receiver ohmic loss factors and antenna gains,  $g_r$  is the receiver gain,  $\lambda$  is the radar wavelength,  $c$  is the free space velocity,  $\tau$  is the radar pulse length,  $T$  is the scattering layer thickness,  $\Delta \delta$  is the antenna beam width and  $R$  is the slant range to the scattering target. Presuming constant radar parameters and a fixed, homogenous, scattering layer thickness, the power is determined solely by the scattering cross-section,  $\sigma$ , defined in terms of the mean square of the electron density fluctuation  $\langle (\Delta N_e / N_e)^2 \rangle$ , i.e.:-

$$\sigma(k) \sim \langle N_e^2 \rangle \left\langle \left( \frac{\Delta N_e}{N_e} \right)^2 \right\rangle F(\theta, \phi) \quad (7.2)$$

where  $k$  is the radar wave number,  $N_e$  is the ambient electron density, and  $F(\theta, \phi)$  is a function of the *flow angle*,  $\theta$ , and the magnetic *aspect angle*,  $\phi$ .

The attenuation of backscatter intensity with magnetic aspect angle, is very sensitive to angular deviations from orthogonality. Magnitudes between ~ 3 dB/degree to ~ 10 dB/degree have been observed (e.g. *Leadabrand et al.*, 1967; *Nielsen*, 1988), differences being noted with respect to radar frequency (*Haldoupis*, 1989) and backscatter intensity (*Waldock et al.*, 1985).

The dependence of backscatter intensity on the irregularity flow angle, varies significantly with the irregularity type. Backscatter from gradient-drift irregularities is largely independent of flow angle, these irregularities propagating isotropically in the plane perpendicular to the magnetic field (*Fejer and Kelly*, 1980). Backscatter from two-stream irregularities however, is

sensitive to the cone of instability, defining the angular range for which the relative electron-ion drift ( $V_d$ ) exceeds the ion-acoustic velocity, the condition required for excitation of two-stream instabilities. The backscatter intensity is thus very anisotropic with respect to flow angle and may vary by a few 10's of dB between angles of  $0^\circ$  and  $90^\circ$  (André, 1983).

The relationship between the backscatter intensity and  $\langle N_e^2 \rangle \langle (\Delta N_e / N_e)^2 \rangle$  is complex, such that other factors, e.g. the electron-ion drift velocity and indeed the ambient electron density, influence the magnitude of the electron density fluctuation  $\langle (\Delta N_e / N_e)^2 \rangle$ . Studies suggest a non-linear relationship with respect to the electron-ion drift velocity (Haldoupis *et al.*, 1990). At auroral latitudes,  $\Delta N_e / N_e$  varies between  $\sim 5\%$  to  $\sim 15\%$  (Fejer and Kelly, 1980), with the ambient electron density,  $N_e$ , varying by an order of magnitude or more during intense precipitation events (Robinson and Vondrak, 1985). It follows that the backscatter intensity increases with  $K_p$  (cf. SABRE results in Waldock *et al.*, 1985).

#### *Observed Magnitudes and Variations of SABRE Irregularity Backscatter Intensity*

To analyse the correlated variations of the irregularity backscatter S/N ratio and  $v_{ftEs}$  magnitudes, it is instructive to consider some typical auroral E-region characteristics during substorm activity. The electron drift velocity is noted to approximate to the plasma (relative electron-ion) drift velocity, presuming small ion drifts. As the electrons 'E cross B' drift, this approximation is employed in coherent backscatter studies to derive electric field vectors (Nielson and Schlegel, 1985).

The scattering cross-section of irregularities,  $\sigma$ , was noted above to vary non-linearly with plasma drift velocity,  $V_d$ . Haldoupis *et al.* (1990) derived the following relationship:-

$$\sigma = V_d^m \tag{7.3}$$

where  $m$  was noted to be 2.2 and 3.9 for the westward and eastward electrojets. During substorm activity, the electric field may increase by an order of magnitude e.g. from  $4 \text{ mV m}^{-1}$  to  $40 \text{ mV m}^{-1}$  (e.g. Steen *et al.*, 1988). The plasma drift thus approximately increases to a similar degree and hence from Equation 7.3, the scattering cross-section will increase by three orders of magnitude, presuming an average value of 'm' of 3.0. The scattering cross-section is proportional to the backscatter intensity (cf. Equation 7.1) and hence it follows that an order of magnitude increase in the auroral electric field, may typically enhance the S/N ratio

magnitude by ~ 30dB, particularly when increasing from a quiet time, 0 dB level. Increases of this order are generally noted in the previous SABRE backscatter plots in §7.4, within the required time scales of a few ionogram recordings (cf. Figures 7.2(a,b)). It is now necessary to demonstrate that the  $\nu fE_s$  magnitudes can also vary by several MHz within the same time interval, given a typical electric field magnitude  $\sim 40 \text{ mV m}^{-1}$ .

#### *Correlation Interpretation for Electric Field Dominated Sporadic-E Layers*

Variations in  $\nu fE_s$  magnitudes may be interpreted directly in terms of the enhanced electric fields noted during substorm activity, the related enhancements of the E-region ionisation densities, arising from particle injection (Akasofu, 1964), and the subsequent charge-exchange processes with metallic atoms (cf. §2.3.7). For the examples from the case studies where the  $\nu fE_s$  and backscatter S/N ratio magnitudes were reasonably well correlated (cf. Figures 7.2(a,b) and Figure 7.8), the sporadic-E layer was generated from the ambient electron density over a time interval equivalent to several, 5 minute ionogram recordings.

Kirkwood and Von Zahn (1991) modelled the generation of sporadic-E layers for a variety of electric field vectors. The Es-layer characteristics varied considerably with respect to the resulting thickness, height and  $\nu fE_s$  values, primarily depending on whether a metallic (e.g.  $\text{Fe}^+$ ,  $\text{Mg}^+$ ) or molecular (e.g.  $\text{NO}^+$ ,  $\text{O}_2^+$ ) ion composition was assumed, and also on the orientation of the electric field (cf. Nygrén *et al.*, 1984, and Figure 2.6(a,b)). They calculated that sporadic-E layers with  $\nu fE_s$  values typically between  $\sim 3 \text{ MHz}$  and  $\sim 6 \text{ MHz}$  would be generated in an 18 minute time interval, presuming an electric field magnitude of  $40 \text{ mV m}^{-1}$ . These model results were confirmed through observation, with similar observations being noted by various authors e.g. Turunen *et al.* (1985).

From these calculations and the approximate variations of backscatter intensity derived previously, it may be deduced that typical enhancements of the electric field, noted during substorm events (i.e.  $\sim 40 \text{ mV m}^{-1}$ ), may be employed to explain correlated variations in backscatter S/N ratio and  $\nu fE_s$  magnitudes. The degree of correlation is however very sensitive to a range of factors. Backscatter intensity fluctuations may occur independent of the electric field, and hence independent of  $\nu fE_s$  magnitudes, an example being variations in backscatter intensity arising from fluctuations in the radar beam magnetic aspect angle (e.g. Waldock *et al.*, 1983). Further, variations in the magnitude and orientation of the electric field vector will have different perturbing influences on the generation of irregularities and sporadic-E layers (cf. plasma flow angle factors versus ion compression efficiency factors (cf. §2.4.2) respectively).

The feasibility of the correlation of backscatter S/N ratio and  $\nu f E_s$  magnitudes has thus been demonstrated for  $\nu f E_s$  magnitudes dependent solely on the electric field characteristics. It has also been highlighted that the degree of correlation will be very sensitive to a variety of common perturbing factors.

#### *Correlation Interpretation for Irregularity Dominated Sporadic-E Layers*

In the previous Section, the correlation of irregularity backscatter S/N ratio and  $\nu f E_s$  magnitudes, was interpreted solely in terms of the electric field. An interpretation based on intrinsic irregularity characteristics is now discussed. For a given electric field magnitude and associated electron drift velocity, plasma instabilities are generated over a spectrum of wavelengths, all propagating in a plane perpendicular to the magnetic field. If the plasma drift is greater than the ion acoustic velocity, then both gradient drift and two-stream irregularities may be detected, depending on for example, the radar flow angle and wave vector.

The latter parameter is particularly significant to the current study. SABRE operates at  $\sim 150$  MHz and is thus sensitive to irregularities  $\sim 1$  m in wavelength (cf. §3.4.1). The HF oblique sounder however, will be sensitive to irregularities with wavelengths between  $\sim 5$  m and  $\sim 75$  m. These larger wavelengths are most likely generated by gradient-drift instabilities, whilst SABRE may detect both two-stream and ‘secondary’ gradient drift irregularities.

The relationship between the backscatter scattering cross-section,  $\sigma$ , and the irregularity wavelength,  $\lambda$ , has been empirically and theoretically derived for the HF and VHF bands, i.e.:-

$$\sigma \propto \lambda^j \quad (7.4)$$

where  $j$  equals 3 (Chestnut *et al.*, 1968; Oksman *et al.*, 1979) or 3.5 (Farley *et al.* 1981; McDonald *et al.*, 1974). The backscatter intensity thus increases approximately with the third power of the irregularity wavelength. Alternatively, the minimum wavelength irregularity detectable by a frequency scanning radar (e.g. the HF oblique sounder), will depend on the signal strength sensitivity of the radar. All other parameters being equal (cf. Equations 7.1 and 7.2), Equation 7.4 thus determines the *spectrum* of irregularities that the HF sounder may detect. For an irregularity dominated sporadic-E layer, the top frequency thus represents the smallest wavelength irregularity detectable by the radar within the E-region, presuming of course that it is greater than 5 m (equivalent to a the maximum Probing Frequency of 30 MHz).

If again it is presumed that the electric field increases by an order of magnitude during substorm activity, and that the backscatter cross-section correspondingly increases by three orders of magnitude (cf. Equation 7.3) (i.e. 1000 times), then a spectrum of irregularity wavelengths, previously below the intensity detectability level of the ionosonde, may now be observed. From Equation 7.4, the minimum, observable irregularity wavelength, will increase by a factor of approximately  $\sqrt[3]{1000}$  i.e. 10. The sporadic-E top frequency will thus increase approximately ten-fold for a ten-fold increase in the auroral electric field. Referring to Figures 7.2(a,b) and Figure 7.8, sporadic-E is noted to grow from very low  $\nu f_i E_s$  values and such a large multiplying factor may well be required to give the peak  $\nu f_i E_s$  values noted (~ 6 MHz). Note that for a value of 'j' equal to 3.5 (cf. Equation 7.4), the factorial increase is reduced to ~ 7.2. Note also that for a doubling of the auroral electric field, the backscatter cross-section increases by a factor of only ~ 8 and hence for a value of 'j' equal to 3, the factorial increase in the  $\nu f_i E_s$  value is only 2. This gives some possible guide to  $\nu f_i E_s$  variations *during* a substorm disturbance.

An alternative explanation for the correlation of  $\nu f_i E_s$  with backscatter intensity, may be deduced from Equation 7.2. For a constant mean square electron density fluctuation and constant flow and magnetic aspect angles, the backscatter cross-section is proportional to the square of the electron density. From simple plasma relationships (cf. Equation 1.10), the backscatter cross-section is proportional to the fourth power of the equivalent Probing Frequency. If this Probing Frequency is taken as  $\nu f_i E_s$  then  $\sigma \propto (\nu f_i E_s)^4$ . For a three orders of magnitude increase in the backscatter cross-section,  $\sigma$ , (due to a presumed order of magnitude increase in the electric field (see above)),  $\nu f_i E_s$  would increase by a factor of ~ 5.6. Considering a doubling of the auroral electric field magnitude, and hence an 8-fold increase in the backscatter cross-section, the factorial change in  $\nu f_i E_s$  would be ~ 1.7.

Both of the above irregularity interpretations, for the correlation of  $\nu f_i E_s$  with the SABRE S/N ratio magnitude, are based on a variety of assumptions. In particular, with respect to the latter hypothesis, the mean electron density is not easily de-coupled from the mean square electron density fluctuation, the relationship being very complex (Haldoupis *et al.*, 1990). Nevertheless, both demonstrate in principle how the  $\nu f_i E_s$  value, may vary correspondingly with the SABRE backscatter intensity, given a very realistic increase in the auroral electric field, during a substorm or other magnetic disturbance.

### *Magnetic Orthogonality Considerations*

One of the problems with an irregularity explanation for the sporadic-E observations, is the requirement for orthogonal or near orthogonal aspect angle conditions, the scattering cross-section being very sensitive to deviations of just a few degrees in the magnetic aspect angle, as described above. To satisfy magnetic orthogonality conditions, the Bodø/Wick propagation path, would need to be severely deviated from the great circle path. For magnetic aspect angles near  $90^\circ$ , the single hop reflection point is up to several hundred km magnetically north-west of Bodø (IGRF model), and located within the westerly beams of the SABRE field of view (e.g. beam 1).

Neither of these facts however, greatly detract from the deductions described above. Both the transmitter and receiver beam widths of the HF oblique sounder were very large ( $>90^\circ$ ). The radar may thus transmit and receive over a wide range of azimuth angles. It is also generally noted that the backscatter returns from the eight SABRE beams, do not differ substantially from each other at a given range gate, i.e. the plasma instabilities are operative over large areas simultaneously. To demonstrate this fact, Figures 7.2(a,b) are reproduced in Figures 7.16(a,b), utilising backscatter data from SABRE beam 1, for range gates 12 and 30 respectively. Comparison of the plots reveals only minor variations in the backscatter S/N ratio magnitudes.

It may thus be concluded that the backscatter intensity variations with range gate, are solely a manifestation of the significant influence of magnetic aspect angle factors (cf. Equation 7.2). Within reasonable spatial limitations, determined by the prevailing ionospheric conditions, correlations between different backscatter data that is geographically spaced, are valid provided that similar aspect angle criteria are met. Correlations between SABRE and Bodø/Wick backscatter data, determined utilising SABRE beam 7, are thus equally applicable for large deviations of the Bodø/Wick circuit from the great circle path, presuming similar magnetic aspect angle characteristics.

### *Concluding Remarks*

The latter point highlights an interesting aspect to all the case studies analysed in §7.4. When correlation calculations between the SABRE backscatter S/N ratio and  $\nu fE_s$  magnitudes, were deemed appropriate, the maximum coefficients were noted at a variety of different SABRE range gates, i.e. 13, 25 and 36. Gate 13 approximates to the nominal Bodø/Wick path midpoint, while gate 36 approximates to a 2-hop reflection point. Gate 25 has no obvious propagation path significance, though the data presented is very similar to that noted in range

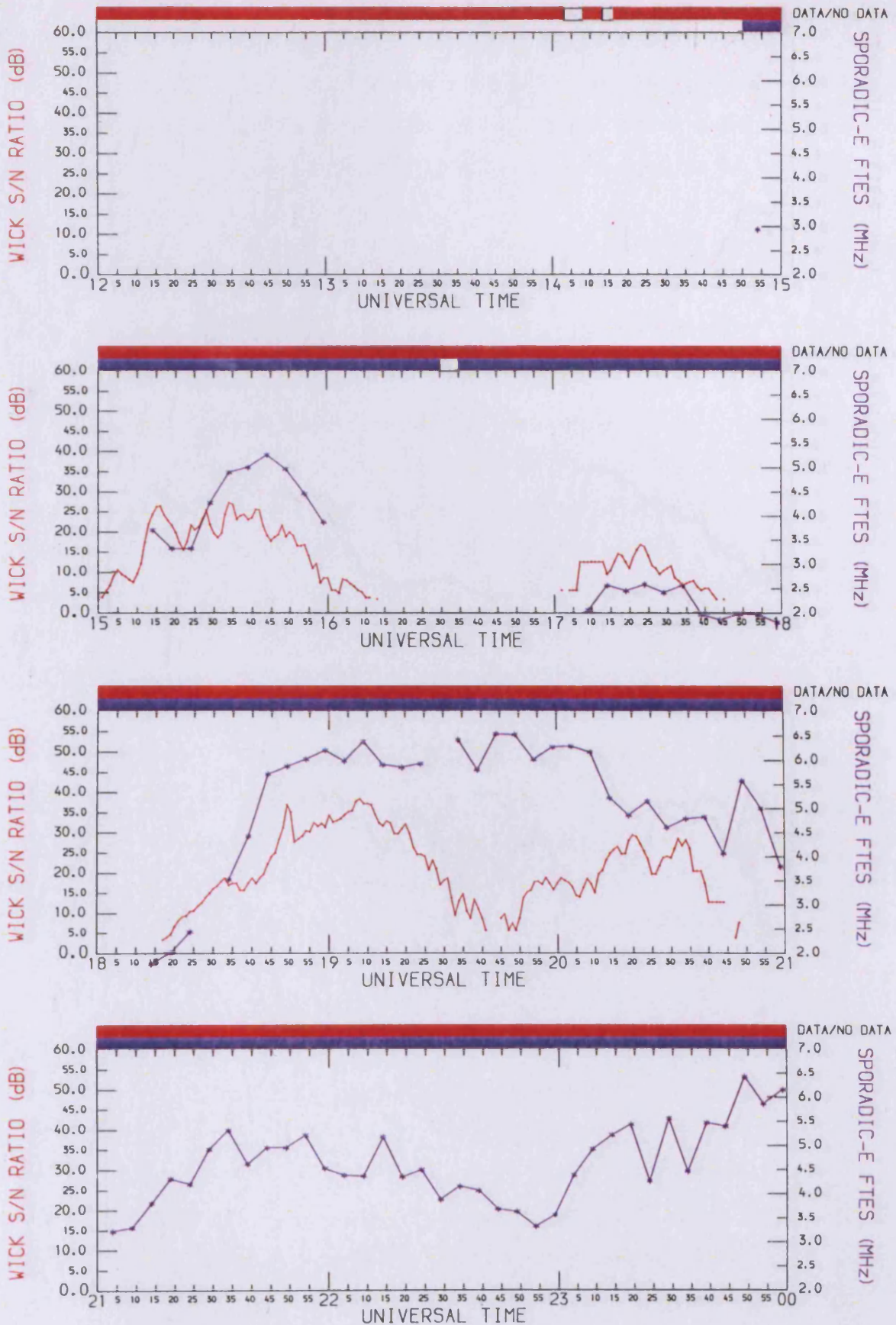


FIGURE 7.16a SABRE backscatter S/N ratio, and sporadic-E *vtEs* data, as recorded for Figure 7.2a (range gate 12), but presenting backscatter data detected within SABRE beam 1, the most westerly beam. Few differences are noted between the backscatter observed within beam 1 and beam 7.

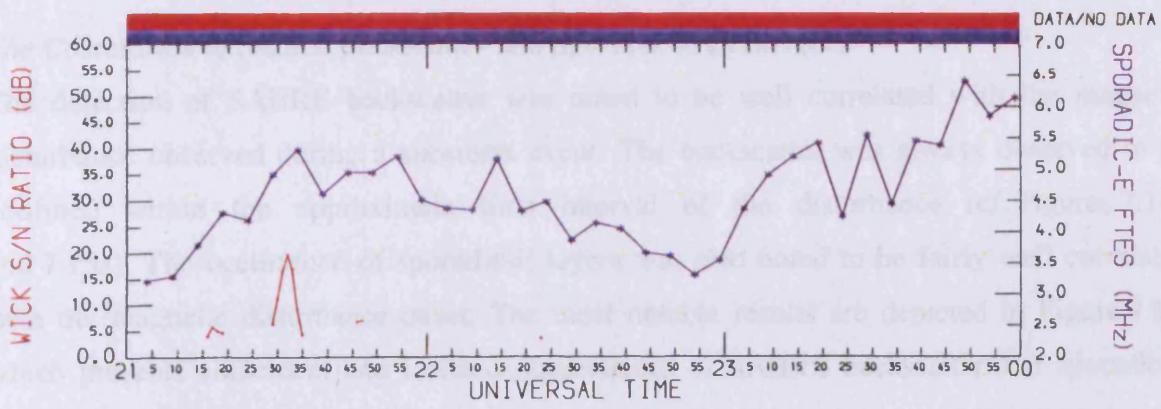
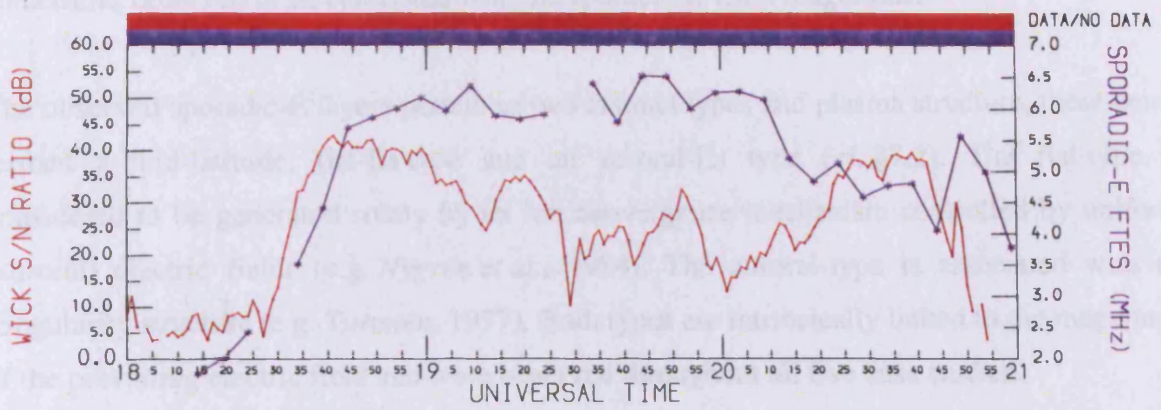
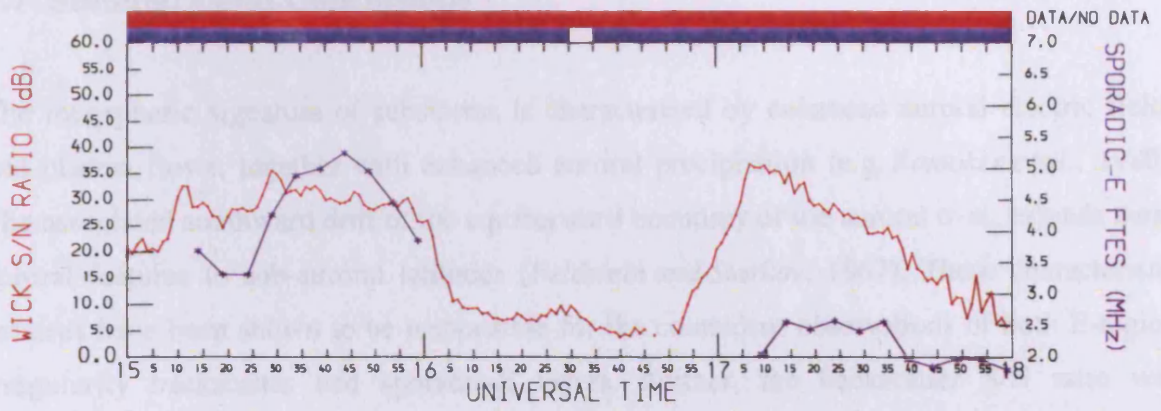
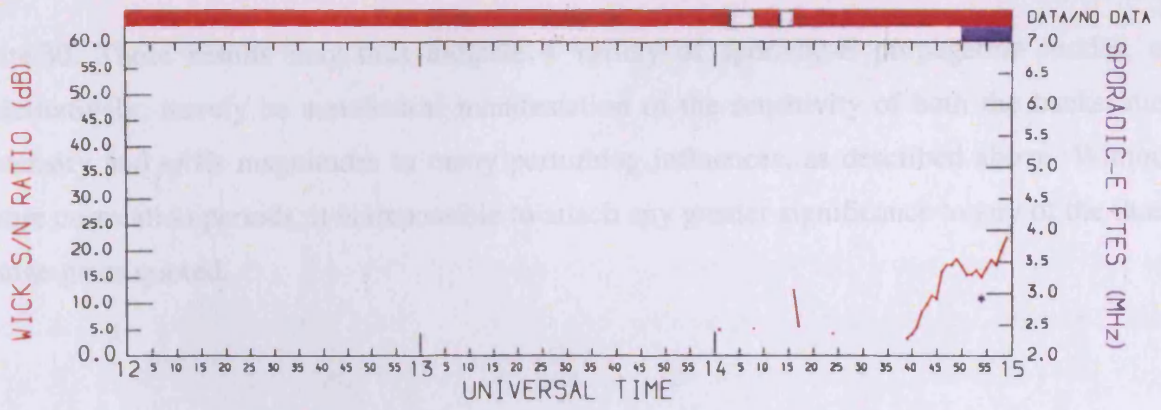


FIGURE 7.16b SABRE backscatter S/N ratio, and sporadic-E *νfEs* data, as for Figure 7.16a, but for range gate 30. At this range also, few differences are noted between the backscatter observed within beam 1 and beam 7.

gate 30. These results may thus indicate a variety of sporadic-E propagation modes, or alternatively, merely be a statistical manifestation of the sensitivity of both the backscatter intensity and  $\nu f_i E_s$  magnitudes to many perturbing influences, as described above. Without more correlation periods, it is impossible to attach any greater significance to any of the three range gates quoted.

## 7.7 Summary and Conclusions

The ionospheric signature of substorms is characterised by enhanced auroral electric fields and plasma flows, together with enhanced auroral precipitation (e.g. *Rostoker et al.*, 1980). The associated southward drift of the equatorward boundary of the auroral oval, extends these auroral features to sub-auroral latitudes (*Feldstein and Starkov*, 1967). These characteristic features have been shown to be responsible for the coincident observations of both E-region irregularity backscatter and sporadic-E layers. Further, the backscatter S/N ratio was sometimes observed to be correlated with the sporadic-E  $\nu f_i E_s$  magnitude.

The observed sporadic-E layers pertain to two distinct types and plasma structure, these being termed a mid-latitude, flat-Es type and an auroral-Es type (cf. §7.2). The flat-type is considered to be generated solely by an ion convergence mechanism controlled by uniform (auroral) electric fields (e.g. *Nygrén et al.*, 1984). The auroral-type is associated with an irregularity structure (e.g. *Turunen*, 1977). Both types are intrinsically linked to the magnitude of the prevailing electric field and were observed throughout all five case studies.

### *The Correlation of SABRE Backscatter and Sporadic-E Occurrence*

The detection of SABRE backscatter was noted to be well correlated with the magnetic disturbance observed during a substorm event. The backscatter was always observed to be confined within the approximate time interval of the disturbance (cf. Figures 7.14b and 7.15a). The occurrence of sporadic-E layers was also noted to be fairly well correlated with the magnetic disturbance onset. The most notable results are depicted in Figure 7.11, which presents coincident and isolated observations of SABRE backscatter and sporadic-E layers, during a brief period of substorm activity amid an otherwise extended quiet magnetic time interval.

However, on occasions, sporadic-E layers were observed to prevail *after* a period of magnetic disturbance and associated 1 m scale irregularity backscatter observations

(e.g. Figure 7.2(a,b)). This may be explained for both electric field generated, or irregularity structured, sporadic-E layers. During the return to quiet magnetic conditions (e.g. during the recovery phase of a substorm), the auroral electric fields and currents diminish in magnitude relatively slowly, as compared to 'onset'. While irregularity generation may thus be inhibited, the magnitude of the electric field may still be sufficient to force ion convergence (e.g. *Morton and Mathews*, 1993). Further, the presence of long lifetime metallic ions (e.g. *Huuskonen et al.*, 1988) within the flat-type sporadic-E layers, may prolong their lifetimes beyond that of the generating force.

For sporadic-E layers with an irregularity structure, it is noted that lower excitation plasma (~ 'E cross B') drifts are pertinent to the larger scale irregularities (~ 10 m), detected by the HF sounder, as compared to the ~1 m irregularities detected by SABRE (e.g. *Fejer and Kelley*, 1980). It thus follows that the *generation* of the larger scale (~ 10 m) irregularities may persist *after* the 1 m scale irregularities.

Examples of *both* flat- and auroral-type sporadic-E layers were observed during these extended periods of sporadic-E occurrence, giving credence to each of the possible explanations above. Note that while the above arguments may apply both prior to, as well as after a magnetic disturbance, disturbance onsets, and in particular substorm onsets, are significantly more rapid than the corresponding recovery time scales. Coincident 'onsets' of irregularity backscatter and sporadic-E layer observations, are thus more likely than coincident 'terminations'.

#### *The Correlation of SABRE Backscatter S/N ratio and $v_{ft}E_s$ Magnitudes*

The correlation of SABRE backscatter S/N ratio and  $v_{ft}E_s$  magnitudes was noted on a few occasions, with two notable periods of correlation being observed (~ 17:00 UT to ~ 21:00 UT, day 344 (Figures 7.2(a,b)) and ~ 00:00 UT to ~ 02:00 UT, day 338 (Figure 7.8)). Both periods are characterised by the predicted auroral oval (*Feldstein and Starkov*, 1967) being positioned over the nominal Bodø/Wick propagation path midpoint. By assuming a realistic (order of magnitude) enhancement of the auroral electric field magnitude at substorm onset (e.g. *Steen et al.*, 1988), the correlated observations of backscatter S/N ratio and  $v_{ft}E_s$  values were interpreted, for both flat-type Es and auroral-type Es.

For flat-type Es-layers, deductions were based on modelling work developed by *Kirkwood and Von Zahn* (1991). For auroral-type Es-layers, Equations 7.2 and 7.4 were both employed independently to deduce possible factorial increases in  $v_{ft}E_s$  magnitudes, for the

typical order of magnitude increase in the auroral electric field at substorm onset. The factors determined ranged between  $\sim 5.6$  and  $\sim 10$ . In contrast, for a doubling of the electric field, *during* a substorm disturbance, the factorial increase in *vftEs* magnitudes was determined to be  $\leq 2$ , for both equations. These factorial increases closely match observed variations in *vftEs* magnitudes, during times of substorm activity.

### ***Concluding Remarks***

It is noted that the ionogram sporadic-E traces observed during the correlation time intervals, are of a diffuse, as well as a discrete, flat nature (cf. Figures 7.1(a,d)). Diffuse traces however, may not indicate the presence of an irregularity structure, but may instead be a manifestation of the disturbed propagation conditions and hence a distortion of the nominal propagation path. Ionosondes are not ideally suited to determining detailed plasma structure and it is thus impossible to state with certainty, the true plasma nature of the sporadic-E layers during these periods of correlation.

Finally, it is poignant to note that a weakly compressed or uncompressed plasma layer, arising respectively from electric fields or auroral precipitation, may be incorrectly classified as a sporadic-E layer (or particle E in the latter case). What constitutes a sporadic-E layer, as opposed to a 'normal' E-layer enhancement, is thus open to a degree of subjectiveness, particularly for ionosonde studies at high-latitudes. Incorrect classifications may thus influence the degree of correlation observed between backscatter S/N ratios and *vftEs* magnitudes. It is believed that such misinterpretations have been avoided in this study.

In conclusion, it is emphasised that irregularity backscatter intensity is very sensitive to numerous ionospheric influences e.g. flow and magnetic aspect angles, and ambient and relative fluctuation electron densities (cf. Equation 7.2). The *vftEs* values may *also* be sensitive to these perturbing factors, if an irregularity interpretation of *vftEs* is determined, but otherwise, will be sensitive to amongst other things, variations in the ambient electric field, attenuation influences and the internal plasma structure of the sporadic-E layers (cf. Chapters 5 and 6). Exact correlations between the backscatter S/N ratio and *vftEs* magnitude are thus unlikely to be observed frequently, nor for prolonged periods of time.

# Chapter 8

## Summary and Suggestion for Further Work

### 8.1 Introduction

The deployment of HF oblique 'Chirp' sounders has proved an effective and relatively cheap means of studying the plasma structure of sporadic-E layers. Predicting and understanding such characteristics is important for the effective implementation of oblique HF propagation circuits. And unlike more complex means of study (e.g. the EISCAT incoherent scatter radar (*Rishbeth and Williams, 1985*)), oblique sounders, by definition, enable signal strength determinations to be measured directly over the desired propagation path.

Sporadic-E observations and associated interpretations were derived from the Bodø/Wick propagation path, during the December, March and, most significantly, August campaign (cf. Table 4.1). The latter campaign is characterised by predominantly quiet geomagnetic conditions, with occasional disturbed intervals (cf. Figure 4.7), and is identified with the most extensive sporadic-E data set. Statistical plasma structure studies, pertaining to typical mid-latitude Es-layers, were thus pursued within Chapter 5 and Chapter 6.

During the December and March campaigns, sporadic-E recordings were less frequent, arising from both morphological and logistical factors. Significant observations were however noted during times of geomagnetic and in particular, substorm activity. A number of case studies were undertaken, correlating the HF sporadic-E observations with coincident irregularity backscatter data, derived from the SABRE VHF coherent radar. Details of this study are presented in Chapter 7 and together with all important data observations, are summarised below.

### 8.2 Summary of Results

#### 8.2.1 Morphological Characteristics

Sporadic-E observations collated from the Bodø/Wick propagation path during the August campaign, were noted to display typical mid-latitude morphological characteristics. The

diurnal occurrence statistics are dominated by a broad, pre-midday maximum, defining a greater than 50% probability of occurrence, for equivalent vertical top frequencies ( $\nu f_i E_s$ ) in excess of 6 MHz (e.g. *Dyer*, 1972). A less well defined early evening maximum is also observed (e.g. *Smith*, 1957). These maxima are most distinct for  $\nu f_i E_s$  magnitudes greater than 4 MHz. The representative nature of the data, with respect to mid-latitude characteristics, is further confirmed by its conformity to Phillips' Rule (*Phillips*, 1947).

Additional occurrence maxima are observed post-midnight, for top frequencies  $\leq 5$  MHz, and pre-midnight, for top frequencies  $\geq 5$  MHz. Both of these maxima are observed under all the prevailing, predominantly quiet, geomagnetic conditions of the August campaign: they are not a manifestation of auroral activity. Intermediate layers (e.g. *Mathews et al.*, 1997), arising from plasma driven down from the F-region (*Rowe*, 1974) may account for these night-time sporadic-E observations. Alternatively, or in association with, tidal components generated by the passage of the F-region trough during quiet geomagnetic conditions, may be responsible for their generation (*Turunen et al.*, 1993), and may explain the apparent latitudinal dependence of the pre-midnight Es-layers.

### 8.2.2 The Sporadic-E Signal Strength Profile

The relationship between the sporadic-E signal strength, SS, and top frequency,  $f_i E_s$ , was studied with respect to the *normalised* Probing Frequency,  $(PF/f_i E_s)$ , during predominantly 'quiet' or 'moderately disturbed' magnetic conditions, at sub-auroral latitudes (i.e. the Bodø/Wick propagation path). It was determined that:-

$$SS \propto \left( \frac{f_i E_s}{PF} \right)^n \quad (8.1)$$

for values of 'n' varying between zero, for normalised Probing Frequencies pertinent to the 'blanketing' frequency range, up to ~20 for normalised Probing Frequencies ~1.0. These values are applicable to 'overdense' sporadic-E reflections, from High Frequency obliquely propagating radio waves.

The determined values of 'n' were validated with respect to similar determinations in the literature, in particular those predicted by the empirical model derived by *Miya and Sasaki* (1966) and *Miya et al.* (1978). This latter signal strength model, in principle applicable to HF

propagation circuits, predicted lower values of 'n' for the Bodø/Wick propagation path. The model, however, was derived from VHF propagation circuits and as a consequence was compiled from both 'overdense' sporadic-E reflections and 'underdense' sporadic-E scatter. For the 'typical' sporadic-E layers most likely observed on the Bodø/Wick or similar HF propagation paths, consideration of Es-scatter, from a field-aligned irregularity structure, or intense plasma density gradients, is considered inappropriate. It was thus concluded that its inclusion in the VHF signal strength model accounts for the said discrepancies in the values of 'n'. Values of 'n' empirically determined by *Booker (1959)* and *Bramley (1972)* supported these conclusions.

With emphasis on the 'partial transparency' range of *normalised* Probing Frequencies, the sporadic-E signal strength profile may be interpreted in terms of the plasma 'cloud' model (cf. §2.4.2.1). By utilising either incoherent *or* coherent scatter theories, the received signal strength may be modelled by a gaussian number distribution of plasma cloud densities, all clouds having an identical size. The received signal strength is thus characterised by relatively strong, 'overdense' reflections via refractive processes alone, as compared to weaker Es scatter (e.g. *Booker, 1959*). Density gradients between the sporadic-E layer and the 'normal' E-region are considered to have little impact on the received signal strength.

The *relative* extent of the 'partial transparency' range of frequencies, with respect to *fEs*, was investigated by the effective superposition of *oblique* signal strength-Probing Frequency profiles, each profile being scaled with respect to the *normalised* Probing Frequency. For nominal daytime (06:00-18:00) and night-time (18:00-06:00) data, the 'partial transparency' frequency range was determined to be ~30% and ~40% of the sporadic-E top frequency respectively, a significantly greater extent than accounted for by O- and X-mode characteristics. The daytime results were in agreement with *vertically* incident observations made by *Reddy and Mukunda Rao (1968)* and *Miller and Smith (1978)*.

### 8.2.3 *vftEs* Growth Rate Factors affecting the Sporadic-E Signal Strength

By observing the change in sporadic-E top frequency between consecutively recorded ionograms, it was determined that the larger *vftEs* growth rates have a significant impact on the signal strength-normalised Probing Frequency characteristics summarised by Equation 8.1. Approximately 75% of equivalent vertical top frequency (*vftEs*) growth rates, both positive and negative, are less than ~0.6 MHz per 5 minute time interval. For these magnitudes, the relationship defined by Equation 8.1 *is* applicable. However, for growth rates

greater than  $\sim 0.6$  MHz per 5 minute interval, the ‘typical’ signal strength-Probing Frequency profile, presented in Figure 5.3a, adopts an increasingly modified form.

Considering the ‘common’ Probing Frequency range between pairs of consecutively recorded sporadic-E traces (cf. Figure 6.3), the signal strength *difference* is observed to be independent of *vftEs* growth rate, for top frequency growth rates between  $\sim 0.6$  MHz per 5 minutes and  $\sim 1.0$  MHz per 5 minutes. And for *vftEs* growth rates  $\geq 1.2$  MHz per 5 minutes, the *absolute* signal strength is observed to be independent of the resulting top frequency magnitude. Similar characteristics are noted within the ‘growth’ range of frequencies (cf. Figure 6.3), such that at *vftEs* growth rates greater than  $\sim 1.0$  MHz per 5 minutes, this ‘growth’ range takes the form of a low signal strength ‘tail’ (cf. *Turunen et al.*, 1988). These characteristics result in signal strength-Probing Frequency profiles that differ substantially from the growth rate independent (‘typical’) profiles derived in Chapter 5. Schematic profiles for increasing rates of *vftEs* growth, are depicted in Figures 6.7(a,h), and fully depict the observations described above. Particularly attention is drawn to the increasingly low signal strength ‘tail’ within the ‘growth’ range of frequencies, most noticeable at the highest *vftEs* growth rates (cf. Figure 6.7h).

Large growths in *vftEs* may have short temporal durations ( $\sim$  a few consecutive ionogram recordings) as depicted in Figures 6.9(a,d), or alternatively transform into high signal strength, high *vftEs*, stable sporadic-E layers. Both may be interpreted in terms of the sporadic-E plasma ‘cloud’ model, differences arising from the cloud generation mechanism. Transient, high plasma density, low number density clouds, may arise from the convergence of ionisation from meteor ablation (*Miller and Smith*, 1978). Gravity wave ‘critical levels’ (*Hines*, 1968) may also account for such cloud characteristics. The more stable sporadic-E layers, arising from large *vftEs* growth rates, are more likely the consequence of plasma clouds, of different plasma and number density, drifting into the radar field of view (e.g. *Kolawole and Derblom*, 1978).

Other, non cloud model interpretations of the signal strength features discussed above, are the generation of embedded gradient-drift irregularities within the Es-layers (*Ecklund et al.*, 1981) or more likely, off-great circle path transmissions (cf. the Secant Law (§3.2.3)). These alternative interpretations particularly relate to the large temporary *vftEs* growths (cf. Figures 6.9).

#### 8.2.4 The Correlation of Sporadic-E Observations and E-Region Irregularities

In Chapter 7, correlation studies of sporadic-E layers, observed by the HF sounder, and E-region field-aligned irregularities, observed by a VHF coherent backscatter radar, were undertaken. All observations were noted during geomagnetically disturbed time intervals and in particular, during magnetospheric substorm events.

In general, the *occurrence* of the two plasma features was correlated with the duration of the substorm, though sporadic-E was sometimes noted to persist beyond the recovery phase. The generation of irregularities and sporadic-E layers is a consequence of the enhanced auroral electric fields, an ionospheric signature of a substorm event (e.g. *Rostoker et al.* 1980). SABRE, the VHF coherent backscatter radar employed in this study (cf. §3.4.1), detects irregularities of wavelengths  $\sim 1$  m, excited by enhanced 'E cross B' plasma flows (*Nielsen et al.*, 1983). The sporadic-E layers may have a larger scale ( $\sim 10$  m) irregularity structure (auroral-Es), generated by similar enhanced flows (*Turunen*, 1977), or may arise from uniform electric field compression mechanisms (flat-type Es) (e.g. *Nygrén et al.*, 1984). Both types are observed throughout the different case studies.

The persistence of the sporadic-E layers beyond the substorm recovery phase, may thus be a consequence of the lower excitation thresholds of the larger (gradient drift) irregularity wavelengths, detected by the HF sounder and associated with the sporadic-E layers (e.g. *Farley*, 1963). Alternatively, the persistence of electric fields of only a few mV's, are sufficient to maintain the compression of ionisation in sporadic-E layers (*Morton and Mathews*, 1993). The long lifetime properties of the metallic ion composition of Es-layers may also be significant (*Huuskonen et al.*, 1988).

Less frequently observed was the correlation of the SABRE backscatter S/N ratio with the sporadic-E top frequency. It has been demonstrated that for both the auroral- and flat-type, auroral zone sporadic-E layers, realistic enhancements in the auroral electric fields, may account for the observed, correlated variations in the sporadic-E top frequency and the backscatter S/N ratio. The magnitude of the latter in particular, is however very sensitive to plasma flow and magnetic aspect angles (*Waldock et al.*, 1985), and also ambient and relative fluctuation electron densities (e.g. *Haldoupis et al.*, 1990). Frequent correlations are thus not expected to be observed.

### 8.3 Suggestions for Further Work

The oblique 'Chirp' sounder has proved itself to be a very reliable and flexible radar system for oblique propagation path studies, via sporadic-E reflections. Various limitations are however apparent. The Secant factor (§3.2.3) for the Bodø/Wick propagation path limits the maximum equivalent vertical top frequency to approximately 6.5 MHz. For sporadic-E studies, this upper limit for the Probing Frequency is often too low, as can be ascertained from Figure 3.8. A greater frequency scanning range is thus desirable. Conversely, the signal strength studies in Chapter 5 and Chapter 6 were also influenced by the *E/F-region cut-off frequency*, as a consequence of the single signal strength determination per discrete Probing Frequency. This issue has already been addressed by the Radio Oblique Sounder Equipment (ROSE) programme (*Dickson et al.*, 1991). The ROSE system allows for individual signal strength determinations for all received ionospheric traces, and would enable sporadic-E signal strength profiles to be determined at significantly lower Probing Frequencies than presented herein. Azimuth and elevation angle information would also reduce some of the uncertainties with respect to the exact nature of the propagation mode. Such information is particularly useful for field-aligned irregularity studies. An adapted oblique dynasonde (e.g. *Wright and Pitteway*, 1982) would prove very useful in all these regards.

This thesis has largely concentrated on data recorded over an 11 day period, on a single oblique propagation path. Though significant observations of sporadic-E were recorded, data from a variety of further paths, of equal or greater temporal resolution, is required to substantiate the observations presented herein. These should range between the mid-, sub-auroral and high-latitudes, to comprehensively account for any latitudinal influences on the sporadic-E plasma structure and morphology. In this respect, coincident studies with the CUTLASS, HF coherent backscatter radars (*Milan et al.*, 1997) would be beneficial, providing direct observations of E-region irregularities pertinent to the HF wavelength band. Further, this bistatic facility allows for electric field determinations and discrimination between types of irregularity doppler spectrum (*Fejer and Kelley*, 1980), allowing for more precise interpretations of auroral and mid-latitude sporadic-E plasma structure.

Sporadic-E has been observed and analysed for many decades and yet continues to manifest new and exciting plasma features. This thesis has demonstrated that the study of such features need not be the reserve of expensive, high power equipment, and that significant observations of the sporadic-E plasma structure may be combined with oblique propagation path studies.

# References

AKASOFU, S. -I., The main phase of magnetic storms and the ring current, *Space Sci. Rev.*, **2**, 91, 1963

AKASOFU, S. -I., A source of energy for geomagnetic storms and auroras, *Planet. Space Sci.*, **12**, 801, 1964

ANDRÉ, D., The dependence of the relative backscatter cross section of 1-m density fluctuations in the auroral electrojet on the angle between electron drift and radar wave vector, *J. Geophys. Res.*, **88**, 8043, 1983

APPLETON, E. V., The propagation of radio waves over the Earth, *Nature*, **115**, 382, 1925

APPLETON, E. V. and M. A. F. BARNETT, Local reflection of wireless waves from the upper atmosphere, *Nature*, **115**, 333, 1925a

APPLETON, E. V. and M. A. F. BARNETT, On some direct evidence for downward atmospheric reflection of electric rays, *Proc. Royal Soc.*, **190**, 621, 1925b

APPLETON, E. V. and G. BUILDER, The ionosphere as a doubly-refracting medium, *Proc. Physical Soc.*, **45**, 208, 1932

APPLETON, E. V. and W. R. PIGGOTT, Ionospheric absorption measurements during a sunspot cycle, *J. Atmos. Terr. Phys.* **5**, 141, 1954

AXFORD, W. I., Note on a mechanism for the vertical transport of ionisation in the ionosphere, *Can. J. Phys.*, **39**, 1393, 1961

AXFORD, W. I., The formation and vertical movement of dense ionized layers in the ionosphere due to neutral wind shears, *J. Geophys. Res.*, **68**, 769, 1963

AXFORD, W. I. and C. O. HINES, A unifying theory of high latitude geophysical phenomena and geomagnetic storms, *Can. J. Phys.*, **39**, 1433, 1961

BAGGALEY, W. J., Seasonal characteristics of daytime Es occurrence in the southern hemisphere, *J. Atmos. Terr. Phys.*, **47**, 611, 1985

BAGGALEY, W. J., Structure in the seasonal variations of ionospheric Es occurrence in the South Pacific, *J. Atmos. Terr. Phys.*, **50**, 855, 1988

BARNES, R. I., Spread-Es structure producing apparent small scale structure in the F-region, *J. Atmos. Terr. Phys.*, **54**, 373, 1992

BARNES, R. I., Full wave determination of oblique incidence reflection coefficients for model Es-layers, *J. Atmos. Terr. Phys.*, **56**, 377, 1994

BARNES, R. I., Analysis of Es traces from a calibrated oblique ionosonde, *J. Atmos. Terr. Phys.*, **57**, 1753, 1995

BARRY, G. H., A low power vertical-incidence ionosonde, *IEEE Trans.*, **GE-9**, 86, 1971

- BEDINGER, J. F. and H. B. KNAFLICH, Observed characteristics of ionospheric winds, *Radio Sci.*, **1**, 156, 1966
- BEDINGER, J. F., H. B. KNAFLICH, E. MANRING and D. LAYZER, Upper atmosphere winds and their interpretation-1, *Planet. Space Sci.*, **16**, 159, 1968
- BESPROZVANNAYA, A. S., A. V. SHIROCHKOV and T. I. SHCHUKA, The dynamics of the high latitude ionospheric E-region, *J. Atmos. Terr. Phys.*, **42**, 115, 1980
- BOOKER, H. G., Radio scattering in the lower ionosphere, *J. Geophys. Res.*, **64**, 2164, 1959
- BOWLES, K. L. and R. COHEN, N.B.S. equatorial region VHF scatter research program, *QST*, **41**, 1957
- BRAMLEY, E. N., Very-high-frequency wave propagation by the temperate-latitude sporadic-E layer, *J. Atmos. Terr. Phys.*, **34**, 1495, 1972
- BREIT, G. and M. A. TUVE, A radio method of estimating the height of the conducting layer, *Nature*, **116**, 357, 1925
- BREIT, G. and M. A. TUVE, A test of the evidence of the existence of the conducting layer, *Phys. Rev.*, **28**, 554, 1926
- BRISTOW, W. A. and B. J. WATKINS, Numerical simulation of the formation of thin ionization layers at high latitudes, *Geophys. Res. Lett.*, **18**, 404, 1991
- BRISTOW, W. A. and B. J. WATKINS, Effect of the large-scale convection electric field structure on the formation of thin ionization layers at high latitudes, *J. Atmos. Terr. Phys.*, **56**, 401, 1994
- BROWN, T. L., The chemistry of metallic elements in the ionosphere and mesosphere, *Chem. Rev.*, **73**, 645, 1973
- BUDDEN, K. G. and E. COOPER, Ionospheric equivalent heights of reflection calculated by a full wave method and by the phase integral method, *J. Atmos. Terr. Phys.*, **24**, 609, 1962
- BUNEMAN, O., Excitation of field aligned sound waves by electron streams, *Phys. Rev. Lett.*, **10**, 285, 1963
- BURCH, J. L., P. H. REIFF, J. D. MENIETTY, R. A. HEELIS, W. B. HANSON, S. D. SHAWHAN, E. G. SHIELLEY, M. SUGIURA, D. R. WEIMER and J. D. WINNINGHAM, IMF B<sub>y</sub> dependent plasma flow and Birkland currents in the dayside magnetosphere 1., Dynamic Explorer Observations, *J. Geophys. Res.*, **90**, 1577, 1985
- CHAPMAN, S., The absorption and dissociative or ionizing effect of monochromatic radiation in the atmosphere on a rotating Earth, *Proc. Phys. Soc.*, **43**, 26, 1931
- CHESEL, C. I., J. A. THOMAS and I. A. BOURNE, Experimental observations of the amplitudes of Es and F-region reflections and their comparison with the thin-layer model for Es, *J. Atmos. Terr. Phys.*, **35**, 545, 1973

CHESTNUT, W. G., J. C. HODGES and R. L. LEADABRAND, Auroral backscatter wavelength dependence studies, *Fin. Rep. SRI Proj. 5535*, Stanford Research Institute, Menlo Park, California, 1968

CHESTNUT, W. G., Polar propagation effects on VHF-UHF radars, in *Radar propagation in the Arctic*, edited by J. Frihagan, *AGARD Conf. Proc. No. 97*, Advisory Group for Aerospace Research and Development, NATO, 5-1, 1972

CHIMONAS, G., Enhancement of sporadic E by horizontal transport within the layer, *J. Geophys. Res.*, **76**, 4578, 1971

CHIMONAS, G. and W. I. AXFORD, Vertical movement of temperate-zone sporadic E layers, *J. Geophys. Res.*, **73**, 111, 1968

COHEN, R., The equatorial ionosphere, *Phys. Geomagn. Phenomena*, **1**, 561, 1967

COWLEY, S. W. H., Solar wind control of magnetospheric convection, *Proc. Conf. Achievements of the IMS*, 483, ESA SP-217, September, 1984

K. DAVIES, Ionospheric radio propagation, *National Bureau of Standards Monograph 80*, 1965

K. DAVIES, Ionospheric radio, *Peter Peregrinus Ltd*, 1990

DICKSON, A. H., P. C. ARTHUR and P. S. CANNON, ROSE – A DSP enhancement to the Barry ionospheric sounder, *IEE 5th International Conference, Edinburgh*, 1991

DUDENEY, J. R. and A. S. RODGER, Spatial structure of high latitude sporadic E, *J. Atmos. Terr. Phys.*, **47**, 529, 1985

DUNGEY, J. W., The influence of the geomagnetic field on turbulence in the ionosphere, *J. Atmos. Terr. Phys.*, **8**, 39, 1956

DUNGEY, J. W., Effect of a magnetic field on turbulence in an ionized gas, *J. Geophys. Res.*, **64**, 2188, 1959

DUNGEY, J. W., Interplanetary magnetic field and the auroral zones, *Phys. Rev. Lett.*, **6**, 47, 1961

DYER, P. J., Fifty-megahertz Es, 1964-1970, *Radio Sci.*, **7**, 351, 1972

ECKLUND, W. L., D. A. CARTER and B. B. BALSLEY, Gradient drift irregularities in mid-latitude sporadic E, *J. Geophys. Res.*, **86**, 858, 1981

EGELAND, A., Ø. HOLTER and A. OMHOLT, *Cosmical Geophysics, Scandinavian University Books*, 1973

EGLITIS, P., Radar studies of small scale E-region plasma irregularities, *Ph.D. Thesis, University of Leicester*, 1994

EYKEN, A. P. VAN, P. S. J. WILLIAMS, A. D. MAUDE and G. MORGAN, Atmospheric gravity waves and sporadic-E, *J. Atmos. Terr. Phys.*, **44**, 25, 1982

- FARLEY, D. T., A plasma instability resulting in field-aligned irregularities in the ionosphere, *J. Geophys. Res.*, **68**, 6083, 1963
- FARLEY, D. T., H. M. IERKIC and B. G. FEJER, The absolute scattering cross section at 50MHz of equatorial electrojet irregularities, *J. Geophys. Res.*, **86**, 1569, 1981
- FEJER, B. G. and M. C. KELLY, Ionospheric irregularities, *Rev. Geophys. Space Phys.*, **18**, 401, 1980
- FELDSTEIN, Y. I., Some problems concerning the morphology of auroras and magnetic disturbances at high latitudes, *Geomag. Aeron.*, **3**, 183, 1963
- FELDSTEIN, Y. I. and Yu. I. GALPERIN, The auroral luminosity structure in the high-latitude upper atmosphere: Its dynamics and relationship to the large-scale structure of the Earth's magnetosphere, *Rev. Geophys.*, **23**, 217, 1985
- FELDSTEIN, Y. I. and G. V. STARKOV, Dynamics of auroral belt and polar geomagnetic disturbances, *Planet. Space Sci.*, **15**, 209, 1967
- FEJER, B. G. and M. C. KELLY, Ionospheric Irregularities, *Rev. Geophys.*, **18**, 401, 1980
- FORMICHEV, V. I. and G. M. SHVED, Height and probability of formation on an Es Layer at temperate latitudes, *Geomagn. Aeron.*, **21**, 470, 1981
- FRANK, L. A., Several observations of low-energy protons and electrons in the Earth's magnetosphere with OGO 3, *J. Geophys. Res.*, **72**, 1905, 1967
- FRITTS, D. C., S. A. SMITH, B. A. BALSLEY and C. R. PHILBRICK, *J. Geophys. Res.*, **93**, 7015, 1988
- FROM, W. R., Sporadic E movement followed with a pencil beam high frequency radar, *Planet. Space Sci.*, **31**, 1397, 1983
- FROM, W. R., Ionospheric reflection coefficient for television signals, *J. Atmos. Terr. Phys.*, **46**, 705, 1984
- FROM, W. R. and J. D. WHITEHEAD, On the peculiar shape of sporadic-E clouds, *J. Atmos. Terr. Phys.*, **40**, 1025, 1978
- FUJITAKA, K., T. TOHMATSU, A tidal theory of the ionospheric intermediate layer, *J. Atmos. Terr. Phys.*, **35**, 425, 1973
- GONZALEZ, W. D., J. A. JOSELYN, Y. KAMIDE, H. W. KROEHL, G. ROSTOKER, B. T. TSURUTANI and V. VASYLIUNAS, What is a magnetic storm?, *J. Geophys. Res.*, **99**, 5771, 1994
- GOODWIN, G. L. and R. N. SUMMERS, Es-layer characteristics determined from spaced ionosondes, *Planet. Space Sci.*, **18**, 1417, 1970
- GOODWIN, G. L. and J. A. THOMAS, Field-aligned irregularities in the Es-region, *J. Atmos. Terr. Phys.*, **27**, 777, 1965

- GORDEN, W. E. and H. C. CARLSON, The excitation of plasma lines in blanketing sporadic E, *J. Geophys. Res.*, **81**, 4016, 1976
- GOSLING, J. T., J. R. ASBRIDGE, S. J. BAME and W. C. FELDMAN, Solar wind speed variations 1962-1974, *J. Geophys. Res.*, **81**, 5061, 1976
- GREENHOW, J. S., E. L. NEUFELD, Winds in the upper atmosphere, *Q. I. R. met. Soc.*, **87**, 472, 1961
- GREENWALD, R. A., W. WEISS, E. NEILSEN and N. R. THOMSON, STARE: A new radar auroral backscatter experiment in northern Scandinavia, *Radio Sci.*, **13**, 1021, 1978
- HALDOUPIS, C., A review of radio studies of auroral E region ionospheric irregularities, *Ann. Geophys.*, **7(3)**, 239, 1989
- HALDOUPIS, C., E. NIELSEN and K. SCHLEGEL, Dependence of radar scattering cross section on the ambient electron density and the destabilizing electric field, *Ann. Geophysicae*, **8**, 195, 1990
- HALDOUPIS, C. and K. SCHLEGEL, A 50-MHz radio doppler experiment for midlatitude E region coherent backscatter studies: System description and first results, *Radio Sci.*, **28**, 959, 1993
- HALDOUPIS, C., K. SCHLEGEL and E. NIELSEN, On Type 3 auroral VHF coherent radar backscatter, *J. Geophys. Res.*, **97**, 4109, 1992
- HARGREAVES, J. K., The solar-terrestrial environment, *Camb. Univ. Press*, 1992
- HARPER, R. M., R. H. WAND, C. J. ZAMLUTTI and D. T. FARLEY, E-region ion drifts and winds from incoherent scatter measurements at Aricibo, *J. Geophys. Res.*, **81**, 25, 1976
- HARRIS, R. D. and R. TAUR, Influence of the tidal wind system on the frequency of sporadic-E occurrence, *Radio Sci.*, **7**, 405, 1972
- HEAVISIDE, O., Telegraphy: Theory, *Encyclopedia Britannica*, **33**, 215, 1902
- HEISLER, L. H. and J. D. WHITEHEAD, Longitude effects in temperate zone sporadic E and the Earth's magnetic field, *Nature*, **187**, 676, 1960
- HEELIS, R. A. and W. B. HANSON, Ion convection velocity reversals in the dayside cleft, *J. Geophys. Res.*, **81**, 3803, 1976
- HEPPNER, J. P. and N. C. MAYNARD, Empirical high-latitude electric field models, *J. Geophys. Res.*, **92**, 4467, 1987
- HINES, C. O., Internal atmospheric gravity waves at ionospheric heights, *Can. J. Phys.*, **38**, 1441, 1960
- HINES, C. O., Some consequences of gravity-wave critical layers in the upper atmosphere, *J. Atmos. Terr. Phys.*, **30**, 837, 1968
- HOLZWORTH, R. H. and C. -I. MENG, Mathematical representation of the auroral oval, *Geophys. Res. Lett.*, **2**, 377, 1975

- HORWITZ, J. L., J. R. DOUPNIK and P. M. BANKS, Chatanika radar observations of latitudinal distributions of auroral zone electric fields, conductivities, and currents, *J. Geophys. Res.*, **83**, 1463, 1978
- HUNSUCKER, R. D., Atmospheric gravity waves generated in the high-latitude ionosphere, *Rev. Geophys. Space Phys.*, **20**, 293, 1982
- HUUSKONEN, A., T. NYGRÉN, T. L. JALONEN, N. BJORNA, T. L. HANSEN, A. BREKKE and T. TURUNEN, Ion composition in sporadic E layers measured by the EISCAT UHF radar, *J. Geophys. Res.*, **93**, 14603, 1988
- IJIMA, T. and T. A. POTESRA, The amplitude distribution of field-aligned currents at northern high latitudes observed by TRIAJ, *J. Geophys. Res.*, **81**, 2165, 1976
- ISTOMIN, V. G., Ions of extra-terrestrial origin in the earth's ionosphere, *Space Res.*, **3**, 209, 1963
- JALONEN, L., T. NYGRÉN and T. TURUNEN, On the partial transparency of sporadic E-layers at high latitudes, *J. Atmos. Terr. Phys.*, **44**, 731, 1982
- JOHANNESSEN, A., NDRE report no. 64, *Norwegian Defence Research Establishment, Kjeller, Norway*, 1974
- KATO, S., Theoretical basis of the formation of sporadic-E due to wind motion in the ionosphere, *Radio Sci.*, **11**, 823, 1966
- KATO, S., T. ASO, T. HORIUCHI, J. NAKAMURA and T. MATSUOKA, Sporadic-E formation by wind shear, comparison between observation and theory, *Radio Sci.*, **7**, 359, 1972
- KELLY, M. C., *The Earth's Ionosphere, Academic Press*, 1989
- KELLY, M. C., D. RIGGIN, R. F. PFAFF, W. E. SWARTZ, J. F. PROVIDAKES and C. -S. HUANG, Large amplitude quasi-periodic fluctuations associated with a mid-latitude sporadic E layer, *J. Atmos. Terr. Phys.*, **57**, 1165, 1995
- KENNELLY, A. E., *Electrical World*, **39**, 473, 1902
- KERBLAY, T. S., G. N. NOSOVA, R. G. MINULLIN and R. KURGANOV, M factor during radiowave reflection from an Es-layer on a 1050 km long path, *Geomag. Aeron*, **16**, 51, 1976
- KERBLAY, T. S., G. N. NOSOVA, L. PALASIO and B. MELENDES, The intensity of reflections from the Es layer according to the data of an experiment on the Santiago De Cuba-Havana link, *Geomag. Aeron*, **26**, 464, 1986
- KEYS, J. G. and M. K. ANDREWS, Gravity wave and sporadic-E echo signatures on VHF backscatter radar systems, *Planet. Space Sci.*, **32**, 1455, 1984
- KING, J. H., Solar wind parameters and magnetospheric coupling studies, *Solar Wind-Magnetospheric Coupling*, edited by Y. Kamide and J. A. Slavin, *Terra Scientific Publishing Company*, 495, 1986

- KIRBY, S. S. and E. B. JUDSON, *Proc. IRE*, **23**, 733, 1935
- KIRKWOOD, S. and U. VON ZAHN, On the role of auroral electric fields in the formation of low altitude sporadic-E and sudden sodium layers, *J. Atmos. Terr. Phys.*, **53**, 389, 1991
- KIRKWOOD, S. and U. VON ZAHN, Formation mechanisms for low-altitude Es and their relationship with neutral Fe layers: Results from the METAL campaign, *J. Geophys. Res.*, **98**, 21549, 1993
- KNUDSEN, W. C., Magnetospheric convection and the high latitude F2 ionosphere, *J. Geophys. Res.*, **79**, 1046, 1974
- KOCHANSKI, A., Atmospheric motions from sodium cloud drifts, *J. Geophys. Res.*, **69**, 3651, 1964
- KOLAWOLE, L. B. and H. DERBLOM, Skywave backscatter studies of temperate latitude Es, *J. Atmos. Terr. Phys.*, **40**, 785, 1978
- KOPP, E., On the abundance of metal ions in the lower ionosphere, *J. Geophys. Res.*, **102**, 9667, 1997
- LANCHESTER, B. S., H. RISHBETH, T. NYGRÉN, L. JALONEN and T. TURUNEN, Wave activity, F1-layer disturbance and a sporadic E-layer over EISCAT, *J. Atmos. Terr. Phys.*, **51**, 179, 1989
- LEADABRAND, R. L., A. G. LARSON and J. C. HODGES, Preliminary results on the wavelength dependence and aspect sensitivity of radar auroral echoes between 50 and 3000 MHz, *J. Geophys. Res.*, **72**, 3877, 1967
- MACDOUGALL, J. W., 110km neutral zonal wind patterns, *Planet. Space Sci.*, **22**, 545, 1974
- MACDOUGALL, J. W., Seasonal variation of semi-diurnal wind in the dynamo region, *Planet. Space Sci.*, **26**, 705, 1978
- MACLEOD, M. A., Sporadic-E theory, 1, Collision-geomagnetic equilibrium, *J. Atmos. Sci.*, **23**, 96, 1966
- MACLEOD, M. A., T. J. KENESHEA and R. S. NARCISI, Numerical Modelling of a metallic ion sporadic-E layer, *Radio Sci.*, **10**, 371, 1975
- MANRING, E. R., J. F. BEDINGER and H. KNAFLICH, *Space Res. 2nd, Proc. Int. Space Sci. Symp.*, Florence, 1961
- MASLIN, N., *HF Communications - A Systems Approach*, 1986
- MATHEWS, J. D., Sporadic E: current views and recent progress, *J. Atmos. Terr. Phys.*, **60**, 413, 1998
- MATHEWS, J. D., Y. T. MORTON and Q. ZHOU, Observations of ion layer motions during the AIDA campaign, *J. Atmos. Terr. Phys.*, **55**, 447, 1993

- MATHEWS, J. D., M. P. SULZER and P. PERILLAT, Aspects of layer electrodynamics revealed by high-resolution ISR observations of the 80-270 km ionosphere, *Geophys. Res. Lett.*, **24**, 1411, 1997
- MATTIN, N. and T. B. JONES, Propagation angle dependence of radar auroral E-region irregularities, *J. Atmos. Terr. Phys.*, **49**, 115, 1987
- MAYAUD, P. N., Derivation, meaning and use of geomagnetic indices, *American Geophysical Union, Washington D.C.*, 1980
- McDONALD, B. E., T. P. COFFREY, S. OSSAKOW and R. N. SUDAN, Preliminary report on numerical simulation of type 2 irregularities in the equatorial electrojet, *J. Geophys. Res.*, **79**, 2551, 1974
- McPHERRON, R. L., Growth phase of magnetospheric substorms, *J. Geophys. Res.*, **75**, 5592, 1970
- McPHERRON, R. L., C. T. RUSSELL and M. P. AUBRY, Satellite studies of magnetospheric substorms on August 15, 1968, 9. Phenomenological model for substorms, *J. Geophys. Res.*, **78**, 3131, 1973
- MILAN, S. E., T. K. YEOMAN, M. LESTER, E. C. THOMAS and T. B. JONES, Initial backscatter occurrence statistics from the CUTLASS HF radars, *Ann. Geophys.*, **15**, 703, 1997
- MILLER, K. L. and L. G. SMITH, Horizontal structure of midlatitude sporadic-E layers observed by incoherent scatter radar, *Radio Sci.*, **10**, 271, 1975
- MILLER, K. L. and L. G. SMITH, Midlatitude sporadic-E layers, *Aeronomy Report No.76*, 1976
- MILLER, K. L. and L. G. SMITH, Reflection of radio waves by sporadic-E layers, *J. Atmos. Terr. Phys.*, **39**, 899, 1977
- MILLER, K. L. and L. G. SMITH, Incoherent Scatter Radar Observations of irregular structure in mid-latitude sporadic E layers, *J. Geophys. Res.*, **83**, 3761, 1978
- MINULLIN, R. G., V. I. NAZARENKO and O. N. SHERSTYUKOV, Altitudes and coefficients of reflection from the Es layer, *Ionospheric Investigations, Moscow*, **44**, 48, 1988
- MIYA, K. and T. SASAKI, Characteristics of ionospheric Es Propagation and calculation of Es signal strength, *Radio Sci.*, **1**, 99, 1966
- MIYA, K., K. SHIMIZU and T. KOJIMA, Oblique-incidence sporadic-E propagation and its ionospheric attenuation, *Radio Sci.*, **13**, 559, 1978
- MORTON, Y. T. and J. D. MATHEWS, Effects of the 13-14 March 1989 geomagnetic storm on the E region Tidal Ion Layer structure at Arecibo during AIDA, *J. Atmos. Terr. Phys.*, **55**, 467, 1993
- MOZER, F. S., Origin and effects of electric fields during isolated magnetospheric substorms, *J. Geophys. Res.*, **76**, 7595, 1971

- MOZER, F. S., Simultaneous electric-field measurements on nearby balloons, *J. Geophys. Res.*, **77**, 6129, 1972
- NARCISI, R. S. and A. D. BAILEY, Mass Spectrometer measurements of positive ions at altitudes from 64 to 112 kilometers, *J. Geophys. Res.*, **70**, 3687, 1965
- NATH, N., I. STEEN MIKKELSEN and T. STOCKFLET JØRGENSEN, On the formation of high latitude Es-layers, *J. Atmos. Terr. Phys.*, **42**, 841, 1980
- NESS, N. F., Initial results of the Imp 1 magnetic field experiment, *J. Geophys. Res.*, **69**, 3531, 1964
- NIELSEN, E., Aspect angle dependence of backscatter intensity of 1-m auroral plasma waves, *J. Geophys. Res.*, **93**, 4119, 1988
- NIELSEN, E., W. GÜTTLER, E. C. THOMAS, C. P. STEWART, T. B. JONES and A. HEDBERG, A new radar auroral backscatter experiment, *Nature*, **304**, 712, 1983
- NICHOLS, H. W. and J. C. SCHELLENG, The propagation of radio waves over the Earth, *Nature*, **115**, 334, 1925
- NIELSON, E. and K. SCHLEGEL, Coherent radar doppler measurements and their relationship to the ionospheric electron drift velocity, *J. Geophys. Res.*, **90**, 3498, 1985
- NYGRÉN, T., L. JALONEN, J. OKSMAN and T. TURUNEN, The role of electric field and neutral wind direction in the formation of sporadic E-layers, *J. Atmos. Terr. Phys.*, **46**, 373, 1984a
- NYGRÉN, T., L. JALONEN, A. HUUSKONEN and T. TURUNEN, Density profiles of sporadic E-layers containing two metal ion species, *J. Atmos. Terr. Phys.*, **46**, 885, 1984b
- NYGRÉN, T., B. S. LANCHESTER, A. HUUSKONEN, L. JALONEN, T. TURUNEN, H. RISHBETH and A. P. VAN EYKEN, Interference of tidal and gravity waves in the ionosphere and an associated sporadic E-layer, *J. Atmos. Terr. Phys.*, **52**, 609, 1990
- OKSMAN, J., H. G. MÖLLER and R. GREENWALD, Comparisons between strong HF backscatter and VHF radar aurora, *Radio Sci.*, **14**, 1121, 1979
- OSSAKOW, S. L. and P. K. CHATURVEDI, Current convective instability in the diffuse aurora, *GeoPhys. Res. Lett.*, **6**, 323, 1979
- OVEZGEL'DYYEV, O., Spacial structure of the Es-layer, *Geomag. Aeron.*, **12**, 803, 1972
- PARKER, E. N., Dynamics of the interplanetary gas and magnetic fields, *Astrophys. J.*, **128**, 664, 1958
- PARKER, E. N., Sudden expansion of the corona following a large solar flare and the attendant magnetic field and cosmic-rays, *Astrophys. J.*, **133**, 1014, 1961
- PIGGOTT, W. R. and K. RAWER, URSI handbook of ionogram interpretation and reduction, *Elsevier Publishing Company*, 1961

- PITTAWAY, M. L. V. and C. O. HINES, The reflection and ducting of atmospheric acoustic-gravity waves, *Can. J. Phys.*, **43**, 2222, 1965
- PHILLIPS, M. L., *Trans A.G.U.*, **28**, 71, 1947
- POOLE, A. W. V., Advanced sounding 1. The FMCW alternative, *Radio Sci.*, **20**, 1609, 1985
- POOLE, A. W. V. and G. P. EVANS, Advanced sounding 2. First results from an advanced chirp ionosonde, *Radio Sci.*, **20**, 1617, 1985
- PRIEST, E. R., The sun and its magnetohydrodynamics, *Introduction to Space Physics*, edited by M. G. Kivelson and C. T. Russell, *Camb. Univ. Press*, 1995
- PYTTE, T., R. L. McPHERRON and S. KOKUBUN, The ground signature of the expansion phase during multiple onset substorms, *Planet. Space Sci.*, **24**, 1115, 1976
- RATCLIFFE, J. A., An introduction to the ionosphere and magnetosphere, *Camb. Univ. Press*, 1972
- RATCLIFFE, J. A., and E. L. C. WHITE, *Proc. Phys. Soc. (London)*, **45**, 399, 1933
- RAWER, K., Structure of Es at temperate latitudes, *Ionospheric Sporadic E*, edited by E. K. SMITH and S. MATSUSHITA, *Pergamon*, New York, 292, 1962
- RCS-5 Chirpsounder Receiver, update#3, Operating and Service, Manual No. 0040-2540-15001, May 15, 1985.
- REDDY, C. A., Physical significance of the Es parameters  $fbEs$ ,  $fEs$  and  $FoEs$  – 2. Causes of partial reflections from Es, *J. Geophys. Res.*, **73**, 5627, 1968
- REDDY, C. A., M. MUKUNDA RAO, On the physical significance of the Es parameters  $fbEs$ ,  $fEs$ , and  $foEs$ , *J. Geophys. Res.*, **73**, 215, 1968
- REDDY, C. A., M. MUKUNDA RAO, S. MATSUSHITA and L. G. SMITH, Rocket observations of electron densities in the night-time auroral E-region at Fort Churchill, Canada, *Planet. Space Sci.*, **17**, 617, 1969
- REES, M. H., Physics and chemistry of the upper atmosphere, *Camb. Univ. Press*, 1989
- REES, D., E. B. DORLING, K. H. LLOYD and C. LOW, The role of neutral winds and ionospheric electric field in forming the stable sporadic E-layers, *Planet. Space Sci.*, **24**, 475, 1976
- RIGGIN, D., W. E. SWARTZ, J. PROVIDAKES and D. T. FARLEY, Radar studies of long-wavelength waves associated with mid-latitude sporadic E layers, *J. Geophys. Res.*, **91**, 8011, 1986
- RINO, C. L., V. B. WICKWAR, P. M. BANKS, S. -I. AKASOFU and E. REIGER, Incoherent scatter radar observations of westward electric fields, 2, *J. Geophys. Res.*, **79**, 4669, 1974
- RISHBETH, H. and O. K. GARRIOTT, Introduction to ionospheric physics, *Academic Press*, 1969

- RISHBETH, H. and P. J. S. WILLIAMS, 'The EISCAT ionospheric radar: the system and its early results', *Q. J. R. Astr. Soc.*, **26**, 478, 1985
- ROBINSON, R. M. and R. R. VONDRAK, Characteristics and sources of ionization in the continuous aurora, *Radio Sci.*, **20**, 447, 1985
- RODGER, A. S., C. MORRELL and J. R. DUDENEY, Studies of sporadic E (Es) associated with the main ionospheric trough, *Radio Sci.*, **18**, 937, 1983
- ROGISTER, A. and N. D'ANGELO, Type II irregularities in the equatorial electrojet, *J. Geophys. Res.*, **75**, 3879, 1970
- ROSTOKER, G., S. I. AKASOFU, J. FOSTER, R. A. GREENWALD, Y. KAMIDE, K. KAWASAKI, A. T. Y. LUI, R. L. McPHERRON and C. T. RUSSELL, Magnetospheric Substorms-Definitions and Signatures, *J. Geophys. Res.*, **85**, 1663, 1980
- ROWE, J. F., Jr., Downward transport of nighttime Es-layers into the lower E-region at Aricibo, *J. Atmos. Terr. Phys.*, **36**, 225, 1974
- ROWE, J. F. Jr. and G. F. GIERALTOWSKI, Ion layer formation by uniform neutral winds in the nighttime E region, *J. Geophys. Res.*, **79**, 2917, 1974
- SCHAEFFER, R. C., The relation of auroral 'flat-type' sporadic-E to magnetic disturbance, *J. Atmos. Terr. Phys.*, **29**, 1511, 1967
- SCHUNK, R. W. and A. I. NAGY, Ionospheres of the terrestrial Planets, *Rev. Geophys. Space Phys.*, **15**, 429, 1980
- SCHUTZ, S., G. J ADAMS and F. S. MOZER, Probe electric field measurements near a midlatitude ionospheric barium release, *J. Geophys. Res.*, **78**, 6634, 1973
- SMITH, E. K., Worldwide occurrence of sporadic E, *NBS Circular 582, U.S. Govt. Printing Office, Washington D.C.*, 1957
- SMITH, E. K., Some unexplained features in the statistics for intense sporadic E, *Second Seminar on the Cause and Structure of Temperate Latitude Sporadic-E*, Paper 12, Vail, Colorado, 1968
- SMITH, E. K., Temperate zone sporadic-E maps ( $foEs > 7$  MHz), *Radio Sci.*, **13**, 571, 1978
- SMITH, L. G., A sequence of rocket observations of night-time sporadic-E, *J. Atmos. Terr. Phys.*, **32**, 1247, 1970
- SMITH, L. G. and E. A. MECHTLY, Rocket observations of sporadic-E layers, *Radio Sci.*, **7**, 367, 1972
- SMITH, L. G. and K. L. MILLER, Sporadic-E layers and unstable wind shears, *J. Atmos. Terr. Phys.*, **42**, 45, 1980
- SPENCER, P. S. J., Oblique Propagation by Sporadic-E, *Ph.D. Thesis, University of Aberystwyth*, 1991

- SPIRO, R. W., R. A. HEELIS and W. B. HANSON, Ion convection and the formation of the mid-latitude F region ionization trough, *J. Geophys. Res.*, **94**, 6739, 1989
- SPIZZICHINO, A. and A. GIRAUD, Experimental study of the structure of sporadic E, *Radio Sci.*, **1**, 145, 1966
- STEEN, A., P. COLLIS and I. HAGGSTROM, On the development of folds in auroral arcs, *J. Atmos. Terr. Phys.*, **50**, 301, 1988
- SUDAN, R. N., J. AKINRIMISI and D. T. FARLEY, Generation of small-scale irregularities in the equatorial electrojet, *J. Geophys. Res.*, **78**, 240, 1973
- TANAKA, T., Sky-wave scatter observations of sporadic-E over Japan, *J. Atmos. Terr. Phys.*, **41**, 203, 1979
- TANAKA, T. and S. V. VENKATESWARAN, Characteristics of field-aligned E-region irregularities over Iioka (36°N), Japan-I, *J. Atmos. Terr. Phys.*, **44**, 381, 1982a
- TANAKA, T. and S. V. VENKATESWARAN, Characteristics of field-aligned E-region irregularities over Iioka (36°N), Japan-II, *J. Atmos. Terr. Phys.*, **44**, 395, 1982b
- TANAKA, T. and S. V. VENKATESWARAN, Gradient-drift instability of nighttime mid-latitude Es-layers, *J. Atmos. Terr. Phys.*, **44**, 939, 1982c
- TASCIONE, T. F., W. H. KROEHL and B. A. HAUSMAN, A technical description of the ionospheric conductivity and electron density profile model (ICED, version 196-II), *Syst. Doc. Vol. VII, Air Weather Serv., U.S. Air Force, Scott Air Force Base, Ill.*, 1987
- TASCIONE, T. F., W. H. KROEHL, R. CREIGER, J. W. FREEMAN, R. A. WOLF, R. W. SPIRO, R. V. HILMER, J. W. SHADE and B. A. HAUSMAN, New ionospheric and magnetospheric models, *Radio Sci.*, **23**, 1988
- TITHERIDGE, J. E., Ionogram Analysis with the Generalised program POLAN, *UAG-93, WDC A, Boulder, Colorado, USA*, 1985
- TURUNEN, T., Properties of the sporadic E layer at Sodankylä, *Ph.D. Thesis, Sodankylä Geophysical Observatory, Sodankylä, Finland*, 1977
- TURUNEN, T., T. NYGRÉN, A. HUUSKONEN and L. JALONEN, Incoherent scatter studies of sporadic-E using 300m resolution, *J. Atmos. Terr. Phys.*, **50**, 277, 1988
- TURUNEN, T., T. NYGRÉN and L. JALONEN, Observations of the reflection coefficient of the sporadic E-layer at high latitudes, *J. Atmos. Terr. Phys.*, **42**, 147, 1980
- TURUNEN, T., J. SILEN, T. NYGRÉN and L. JALONEN, Observation of a thin Es-layer by the EISCAT radar, *Planet. Space Sci.*, **33**, 1407, 1985
- VILLANTE, U., Some remarks on the structure of the distant neutral sheet, *Planet. Space Sci.*, **23**, 723, 1975
- VILLARD, O. G., The ionospheric sounder and its place in the history of radio science, *Radio Sci.*, **11**, 847, 1976

- VIRDI, T. S., G. O. L. JONES and P. J. S. WILLIAMS, EISCAT observations of the E-region semidiurnal tide, *Nature*, **324**, 354, 1986
- WALDOCK, J. A. and T. B. JONES, Statistics of 1-m wavelength plasma irregularities and convection in the auroral E region, *Radio Sci.*, **20**, 709, 1985
- WEBER, E. J., J. A. WHALEN, R. A. WAGNER and J. BUCHAU, A 12-hour case study of auroral phenomena in the midnight sector: electrojet and precipitating particle characteristics, *J. Geophys. Res.*, **82**, 3557, 1977
- WHALEN, J. A., A quantitative description of the spatial distribution and dynamics of the energy flux in the continuous aurora, *J. Geophys. Res.*, **88**, 7155, 1983
- WHITEHEAD, J. D., The formation of the sporadic-E layer in the temperate zones, *J. Atmos. Terr. Phys.*, **20**, 49, 1961
- WHITEHEAD, J. D., Production and Prediction of sporadic E, *Rev. Geophys. Space Sci.*, **8**, 65, 1970
- WHITEHEAD, J. D., Difficulty with wind-shear theory of sporadic E, *J. Geophys. Res.*, **76**, 3127, 1971
- WHITEHEAD, J. D., The structure of sporadic E from a radio experiment, *Radio Sci.*, **7**, 355, 1972
- WHITEHEAD, J. D., Recent work on mid-latitude and equatorial sporadic-E, *J. Atmos. Terr. Phys.*, **51**, 401, 1989
- WILLIAMS, P. J. S., G. CROWLEY, K. SCHLEGEL, T. S. VIRDI, I. McCREA, G. WATKINS, N. WADE, J. K. HARGREAVES, T. LACHLAN-COPE, H. MÜLLER, J. E. BALDWIN, P. WARNER, A. P. VAN EYKEN, M. A. HAPGOOD and A. S. RODGER, The generation and propagation of atmospheric gravity waves observed during the Worldwide Atmospheric Gravity-wave Study (WAGS), *J. Atmos. Terr. Phys.*, **50**, 323, 1988
- WILLIAMS, P. J. S. and T. S. VIRDI, EISCAT observations of tidal modes in the lower thermosphere, *J. Atmos. Terr. Phys.*, **51**, 569, 1989
- WOODMAN, R. F., M. YAMAMOTO and S. FUKAO, Gravity wave modulation of gradient drift instabilities in mid-latitude sporadic E irregularities, *Geophys. Res. Lett.*, **18**, 1197, 1991
- WRIGHT, J. W. and L. S. FEDOR, The interpretation of ionospheric radio drift measurements - II. Kinesonde observations of microstructure and vertical motion in sporadic-E, *J. Atmos. Terr. Phys.*, **31**, 925, 1969
- WRIGHT, J. W., and L. S. FEDOR, Errata, *J. Atmos. Terr. Phys.*, **32**, 451, 1970
- WRIGHT, J. W. and M. L. V. PITTEWAY, Data processing for the dynasonde, *J. Geophys. Res.*, **87**, 1589, 1982
- YEOMAN, T. K., M. D. BURRAGE, M. LESTER, T. R. ROBINSON and T. B. JONES, Long-term variation of radar auroral backscatter and the interplanetary sector structure, *J. Geophys. Res.*, **95**, 21123, 1990a

YEOMAN, T. K., D. K. MILLING and D. ORR, Pi2 polarisation patterns on the UK sub-auroral magnetometer network (SAMNET), *Planet. Space Sci.*, **38**, 589, 1990b

VON ZAHN, U. and T. L. HANSEN, Sudden neutral sodium layers: a strong link to sporadic E layers, *J. Atmos. Terr. Phys.*, **50**, 93, 1988